THÈSE

Pour obtenir le grade de

Docteur

Délivré par l'**Università degli Studi dell'Insubria**

et par l'**Université de Montpellier**

Préparée au sein de l'école doctorale **Information, Structures et Systèmes (I2S)**
Et de l'unité de recherche **Laboratoire Charles Coulomb**

Spécialité: **Physique de la matière condensée**

Présentée par **Silvia Bonfanti**

LOW TEMPERATURE THEORETICAL AND NUMERICAL STUDY OF STRUCTURAL GLASSES

Directeur de thèse: **Prof. Giancarlo Jug**
Co-Directeur de thèse: **Prof. Walter Kob**

Soutenue le 25 Janvier 2016 devant le jury composé de:

Prof. Giulio Monaco	University of Trento (Italy)
Prof. Stefan Kettemann	Jacobs University Bremen (Germany)
	POSTECH (South Corea)
Prof. Walter Kob	University of Montpellier (France)

UNIVERSITÉ FRANCO ITALIENNE | UNIVERSITÀ ITALO FRANCESE

Contents

List of acronyms

1D	One Dimensional
2D	Two Dimensional
2LS	Two-Level System
3D	Three Dimensional
3ND	$3N$ Dimensional
AB	Aharonov-Bohm
ATS	Anomalous Tunneling System
BFA	Biased Flattest Ascent
BGSD	Biased Gradient Square Descent
BMLJ	Binary Mixture Lennard-Jones
CG	Conjugate Gradient
CRN	Continuous Random Network
DOS	Density of States
DWP	Double-Well Potential
EIS	Effective Isopotential Surface
ETM	Extended Tunneling Model
FCC	Face-Centered-Cubic
GCF	Good Crystal Former
HRTEM	High Resolution Transmission Electron Microscopy
KFS	Kettemann-Fulde-Strehlow
IS	Inherent Structure
LJ	Lennard-Jones
LJ13	13 atoms Lennard-Jones cluster
MB	Müller-Brown
MD	Molecular Dynamics
NF	Network Former
NM	Network Modifier
NMR	Nuclear Magnetic Resonance
PBC	Periodic Boundary Conditions
PEL	Potential Energy Landscape
RER	Regions of Enhanced Regularity
SP	Saddle Point
STM	Standard Tunneling Model

TS	Tunneling System
TFWP	Tetrahedral Four-Well Potential
TWP	Three-Well Potential

Introduction

Glasses are an important, versatile class of materials in modern society that are useful for their interesting physical and chemical properties. In applications ranging from those typical of the construction all the way down to the electronic industries, the ease and low cost of fabrication and deployment are as important as their mechanical strength and chemical inertia. However, contrary to the case of crystalline solid materials, basic knowledge about the intermediate- and long-range atomic structure of amorphous solids is still lacking and represents serious hindrance for the progress of systematic theoretical research in the physics of these solids. Indeed, solid state physics textbooks remain limited to the description of crystals. This work is a contribution to the furthering of knowledge about the nature of glasses as can be deduced from experiments, theory and computer simulation in the low temperature range. Like in the case of the physics of crystals, the aim is to start at the low temperatures end and work up towards some improved understanding of the nature of glass and of the glass transition.

At low temperature, i.e. in the 1 K regime or so, glasses show properties that are remarkably different from those of the corresponding crystalline counterparts: e.g., the heat capacity depends approximately linearly and the thermal conductivity almost quadratically on temperature (in crystals one finds a cubic dependence for both properties). Many of these observations can be rationalized by the so-called "Standard Tunneling Model" (STM) whose basic assumption is the existence of local double-well potentials (DWPs), or two-level systems (2LSs), in the potential energy landscape (PEL), where localized excitations (a particle or rather a cluster of particles) undergo quantum tunneling through the potential barrier. An active area of research in the 1970s and 1980s, in recent times, the physics of tunneling systems (TSs), has attracted considerable renewed attention, also for the aim of fabricating coherent qubits for quantum computers, involving amorphous barrier superconducting Josephson junctions.

Despite the success of the STM, however, many features of the model are still unclear in that, e.g., the microscopic nature of the TSs remains unknown. In addition, unexpected magnetic effects have been discovered in non magnetic multicomponent glasses, like e.g. the non-monotonous changes of the dielectric constant and of the specific heat in the presence of weak magnetic fields. A possible explanation of these observations is the so-called "Extended Tunneling Model" (ETM) in which one assumes the presence of better-ordered tiny regions, hosting TSs in their interstitials that

have to be described by three-well potentials (TWPs), in the intermediate-range structure of glasses. As a result the effective tunneling particles can couple to the magnetic field orbitally, via an enhanced Aharonov-Bohm (AB) effect.

Since the early days of X-ray scattering investigations, different schools of thought about the structure of glasses have been developing: roughly speaking, the "Russian" school that views glass as a mosaic of small crystalline-like regions (though, not necessarily micro-crystals), and the "Western" school of thought that views glass as a continuously-disordered network where the atomic structure is that of a liquid both at the intermediate- and at the long-range. Scattering and other methods have been unable to resolve the controversy between the two schools of thought and one of the ambitions of the present research is that the physics of glasses at the low temperatures might be of help in deciding between the two scenarios using the TSs as probes, much as the nuclei are in NMR structural investigation. In this perspective, the magnetic and compositional effects discovered in glasses at low temperatures might become the basis of a new type of (amorphous) solid state spectroscopy.

This work consists of two parts: In the first one we carry out analytical calculations that extend the ETM model to the explanation of SQUID paramagnetic magnetization data for a number of non-magnetic multi-silicate glasses from 4 to 300 K. Our theoretical fits for these data are a further test for the validity of the ETM, also beyond the 1 K regime. We have also considered the case of a four-welled tetrahedral trapping potential in a magnetic field: our calculations show that in fact the TWP ETM can be considered as the simplest working model to describe real glasses. Our derived contribution to the SQUID magnetization from the TWPs of our model results in good fits of the experimental data and an improved estimate for the concentration of trace paramagnetic impurities. We show that only by taking into account such TWPs, magnetic-field sensitive TSs, we get a good agreement between the impurity concentrations extracted from the magnetization and those extracted from low temperature heat capacity measurements. Moreover, we show that the determination of the concentration of impurities from the sole assumption of a Langevin paramagnetic contribution results in a serious overestimate of it.

The goal of the second part is to elucidate the nature of the TSs via computer simulations. For this we first develop new algorithms to study the geometry of the minima and barriers of a simple two-dimensional model of a PEL. This study is the starting point for a novel method, the so-called "Effective Isopotential Method", that we introduce to perform a local and systematic analysis of the energy landscape close to the bottom of the local minimum (or inherent structure (IS)). We apply this method to a test case, a Lennard-Jones FCC crystal, and then to a binary mixture Lennard-Jones glass at low temperature. We find that the geometric shape of the IS at low temperature is not smooth, but characterized by internal valleys, i.e. points of the configuration space where the potential energy is lower than the immediate neighbourhood. In the case of the crystal we observe the presence of six symmetric valleys associated with a given particle, while in the case of the glass we find that most of the particles show only two valleys. Amongst them we find the geometries with the

right semi-quantitative features (in agreement with the phenomenological models) to be considered as possible TSs candidates, so that we finally know how they look like in reality. Moreover, we present some first numerical evidence for the existence of TWPs and also of so-called "crystallite" regions in the intermediate-range structure of our model glass. This somewhat corroborates the assumptions made for the setting up of the ETM and supports features of the better-ordered regions, non-homogeneous mosaic atomic structure of glasses. Further work in this directions is in progress.

Chapter 1

Theoretical background

1.1 General considerations on glasses

According to P.W. Anderson [1], the nature of glass and the glass transition are two of the most interesting unsolved problems of solid state physics. This statement seems to be a contradiction since glassy materials have been known and utilized by humans for more than ten millennia (glassy relics dating back to 12000 B.C. have been discovered in Egypt) and nowadays they continue to play a central role for commercial, industrial, scientific and technological applications. Since the publication of that remarkable interview by P.W. Anderson in 1995, despite two decades of intensive research in this field, our understanding of glasses is still incomplete, yet much progress has been made to improve our knowledge in view of a full understanding of these issues.

Glass is an inorganic (or organic, polymeric: plastics) substance that is typically produced by cooling a liquid to a rigid consistency without the occurrence of crystallization. However there are many alternative routes for making a glass, such as sol-gel process, vapor-phase deposition or chemical reactions (a good review of the glass formation process is presented in [2]).

Glassy materials are difficult to classify since they are solids with similar features to their corresponding crystals, but at the same time isotropic resembling liquids. The main feature of glasses (and amorphous solids) is indeed the lack of the periodic order typical of the crystalline arrangement. This is the reason why vitreous materials are often referred as “noncrystalline” or “disordered” solids. The main difference compared to crystals is that glasses do not show a well-defined melting point; they are in fact characterized by a narrow, but continuous region (of temperature), the so-called “glass transition”, over which the system “falls out of equilibrium”. By analogy with their crystalline counterparts, one talks about insulating, semiconducting, metallic and polymeric glasses.

The beginning of this Chapter deals with the fundamental aspects of glasses, starting from the description of the volume-temperature diagram and the glass transition phenomena (Section 1.1.1) and ending with some considerations on the atomic structure depending on the different glass families (Section 1.1.2) and the respective glass-

forming abilities (Section 1.1.3). In Section 1.2 we address the phenomenology of glasses at low temperature; as we shall see, the surprising quasi universality in the properties of different glasses, and overall the recent important applications in this temperature regime, make this an attractive field of research. The widely accepted theoretical model to describe these phenomena is presented in Section 1.2.1, while the main experimental deviations and the attempts to provide an adequate explanation for them are reported in Section 1.2.2 and 1.2.3. Within this context we will introduce the basis of the new cellular theory of the atomic structure of glasses at intermediate-range that is capable to explain the major experiments on amorphous solids at intermediate and low temperatures in a magnetic field (Section 1.3).

1.1.1 The glass transition

When a liquid is cooled down (or compressed) below its melting temperature T_m (or pressure), sufficiently fast to avoid its crystallization, it is said to be in a supercooled state. The dramatic slow down of the diffusive motion that characterizes this process does not allow the system to visit all the energetically accessible parts of the configuration space. This corresponds to a fast increment of relaxation time τ with decreasing temperature, so that, when the laboratory timescale is exceeded, the system falls out of equilibrium and the glass transition occurs. The supercooled liquid therefore results frozen in a solid amorphous state, which is called glass, and the relaxation process stops (over geological timescale [4]).

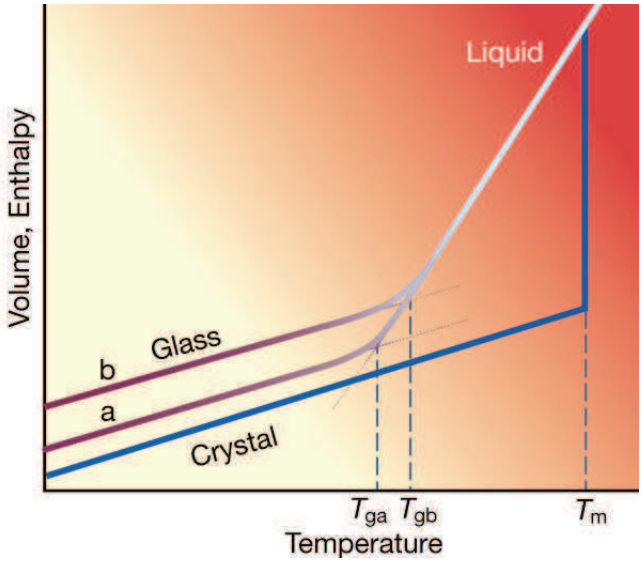

Figure 1.1: Comparison of the $V-T$ diagram for a crystalline solid and a glass forming liquid; the bold solid lines represent the equilibrium curves, which separate at T_m. The supercooled liquid curve does not show a sharp discontinuity as for the crystal case. The cooling rate dependence of the curve is also shown: a fast cooling rate produces the glass transition at high T, T_{gb}, while a slow cooling rate at T_{ga}. From [3].

In the characteristic volume-temperature (V-T) diagram of a glass (shown in Figure 1.1), this situation corresponds to a decrease of the volume with respect to the temperature; the smooth curve between the onset of departure from the supercooled liquid line to the solid glassy state line, shown in figure 1.1, represents the glass transition region, and, the intersection of the two extrapolated lines defines the glass transition temperature T_g. Since there is no evidence of discontinuities in the physical

properties (except for a smooth sudden change for example in heat capacity, thermal expansion and shear modulus), this is not a first order phase transition, which is instead the case of the liquid-crystal transition, where the system undergoes an abrupt change at T_m.

Experiments provide another definition of T_g, that is, the temperature at which the viscosity η, the resistance to flow of a system, reaches 10^{13} Poise. Figure 1.2 reports the behavior of $\log(\eta)$ as a function of the inverse temperature for several supercooled liquids. As can be noted, the viscosity increases up to 15 orders of magnitude when the temperature is changed only by a factor of 2-3. These data are in equilibrium, i.e. do not depend on cooling rate. The characteristic value of 10^{13} Poise is chosen because it is difficult to equilibrate samples with larger viscosities. The pronounced slowing down of the macroscopic quantity η, reflects the fact that the relaxation time becomes longer and longer with decreasing temperature.

Experimentally (via neutron or X-ray scattering) the relaxation dynamics of glass forming liquids can be described by the intermediate scattering function $F(\vec{k},t)$, which measures the decay of density fluctuations [6]; by defining the local density

$$\rho(\vec{r}) = \sum_{i=1}^{N} \delta(\vec{r} - \vec{r}_i) \tag{1.1}$$

and taking its Fourier transform

$$\rho_{\vec{k}} = \int d\vec{k}\, \exp(-i\vec{k}\cdot\vec{r})\rho(\vec{r}) = \sum_{j=1}^{N} \exp(-i\vec{k}\cdot\vec{r}_j) \tag{1.2}$$

we obtain

$$F(\vec{k},t) = \frac{1}{N}\langle \rho_{\vec{k}}(t)\rho_{-\vec{k}}\rangle \tag{1.3}$$

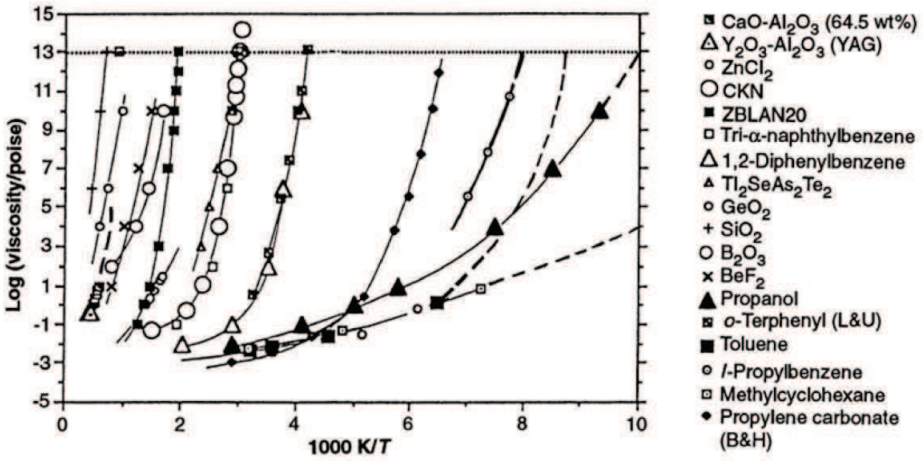

Figure 1.2: Temperature dependence of the viscosity for different glass forming liquids (from [5]).

where $\vec{k}$ is the wave vector, N is the total number of particles in the system and the time t is obtained from the time Fourier transform of the energy transfer. The average $\langle ... \rangle$ is taken with respect to thermal fluctuations.

For normal liquids $F(\vec{k},t)$ decays exponentially in time as shown in Figure 1.3 (left); the relaxation dynamics of glass forming liquids instead is strongly non-exponential, as depicted in Figure 1.3 (right). In particular, during the cooling process we observe a separation of relaxation timescales:

- at very short times (range I) the usual ballistic motion takes place and $F(\vec{k},t)$ initially decreases.
- at intermediate times (range II), the motion of the particles begins to be hampered by the interaction with neighbors through the presence of *cages* [8], where only small rearrangements can occur. This is the β-relaxation regime, that corresponds to a plateau in the correlation function, constant over two or more decades in time.
- at long times (range III), particles leave their cages and global rearrangement processes occur. In this case $F(\vec{k},t)$ decays to zero, in a stretched exponential fashion (α-relaxation regime), usually described by the Kohlrausch-Williams-Watts function:

$$f(t) = \exp\left[-\left(\frac{t}{\tau}\right)^{\beta}\right] \quad (\beta < 1) \tag{1.4}$$

  where the exponent β is found to be material and wave number dependent [6].

The slowing down in the decay of time dependent correlation functions when decreasing the temperature has been confirmed extensively in numerical simulations [9] and appears to be a signature of glassy behavior. In this sense, another important discovery has been achieved from both experiments and simulation analysis in the last decade: this relaxation of the system is accompanied by local spatial fluctuations which are

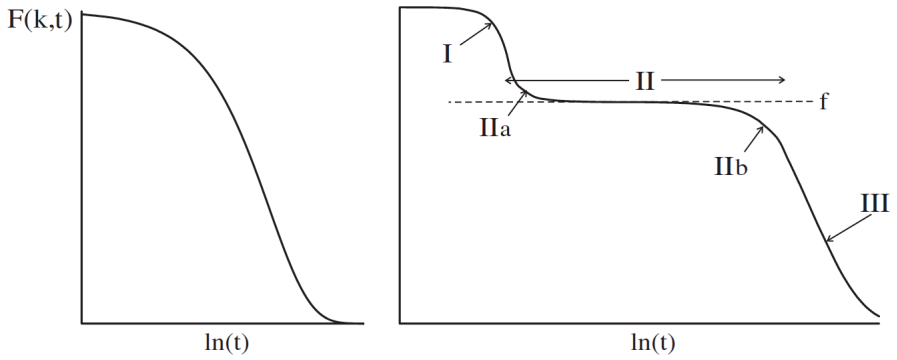

Figure 1.3: Intermediate scattering function $F(\vec{k},t)$ for (left) normal liquids (or glass forming liquids at high T) characterized by an exponential decay with t, and (right) supercooled liquids, distinguished by a strongly non-exponential decay [7]. Note that t is plotted on logarithmic scale.

related to different relaxing ways and rates. The observed spatial fluctuations in the local dynamical behavior are termed *dynamical heterogeneities* (DHs) and they can be visualized through simulations by looking at the temporal displacement of the individual particle trajectories. A possible way to describe such inhomogeneous behavior, and thus try to quantify the features of the dynamical heterogeneity, is the concept of mobility; basically what is observed is the extreme behavior which correspond to the fastest (or *mobile*) and the slowest (or *immobile*) particles. For example, in [10], to identify the most 5% of mobile and immobile particles, the average fluctuation of the particle from its average position was estimated:

$$d_i^2 = \overline{|\vec{r}_i(t) - \overline{\vec{r}_i(t)}|^2} \tag{1.5}$$

where $\vec{r}_i(t)$ indicates the positions at time t and the bar is intended as an average over the whole time of the production run. In particular the most important result that comes from this study regards the organization of mobile and immobile particles in clusters, which are usually defined by setting a proximity threshold between the considered particle and its neighbors. The origin of this phenomenon is not yet clear (though probably related to the nucleation of non-crystalline clusters[11] but what we know about the relation between mobile and immobile particles when decreasing the temperature towards and then below the glass transition is that the slower regions increase in size [12]. At the end of this Chapter we will discuss the hypothesis regarding a possible connection of the DHs at high temperatures with the real structure of glasses, investigated and understood thanks to a theoretical model which was developed to explain the low temperatures magnetic anomalies of glasses [13].

1.1.2 Atomic scale structures of glasses

The atomic structure can be investigated through the analysis of the static structure factor $S(\vec{k})$ which can be measured in X-ray and neutron scattering experiments:

$$S(\vec{k}) = \frac{1}{N}\langle \rho_{\vec{k}} \rho_{-\vec{k}} \rangle = \sum_{j=1}^{N}\sum_{l=1}^{N} \langle \exp(-i\vec{k}\cdot(\vec{r}_j - \vec{r}_l)) \rangle \tag{1.6}$$

note that $S(k) \equiv F(\vec{k},t)$ at $t = 0$. As an example we can consider the simplest glass, vitreous silica SiO_2, which, combined with other constituents like alkali oxides (soda and potash), boric oxide and lead oxide, forms glasses with features suitable for commercial purposes. Figure 1.4 presents the comparison between the X-ray diffraction spectra obtained for crystalline materials (in this case cristobalite, a high-temperature polymorph of silica) and the respective glassy material (vitreous silica). While for the first one, one can clearly distinguish intense diffraction peaks associated with the crystalline lattice spacing as described by Bragg's law, for the second one finds a rounding and spreading out of the peaks, due to the absence of periodicity of the elementary cell. Nevertheless, the broad peak for amorphous SiO_2 does occur at the very same

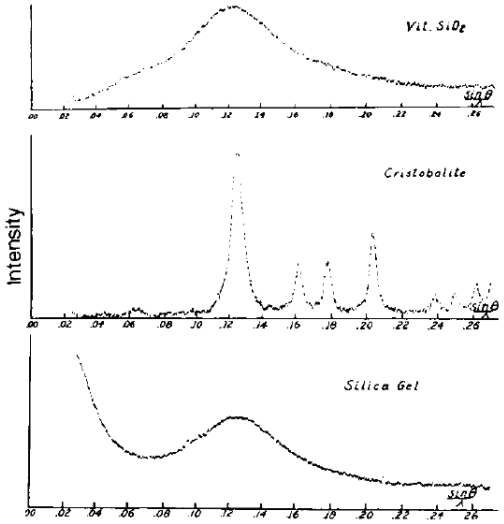

Figure 1.4: X-ray diffraction spectra of vitreous silica, cristobalite, and silica gel [14].

wavevector as for the sharpest crystalline peak. (The figure reports also the spectra for the silica gel).

The degree of disorder in glasses is indeed associated to different length scales: for distances comparable to the atomic bond there is a local (short-range) order which is given by the basic atomic building blocks (SiO_4 tetrahedra in silica, schematically shown in Figure 1.5) and corresponds to that of crystals. It is actually at intermediate-range length scales that the disordered structure takes form due to the way tetrahedra connect together: the angles and bonds are not fixed as in crystals. In vitreous silica for example (Figure 1.6(a)), the measured bond angle distribution, indicated with β, varies between 120° and 180°; α_1 and α_2 are the torsion angles [15]. Finally at long-range length scales (>10 Å) not much can be deduced by looking at the structure factor and by performing ring structure statistics (Figure 1.6(b)). However, which is the actual degree of intermediate-range disorder is still a matter of controversy, since the present experimental techniques do not allow yet to visualize directly the distributions of the adjacent rings.

There are in essence two main different schools of thought regarding the structural arrangement of glasses [15] which developed separately: the Western School that supports the random network theory of Zachariasen and Warren which is currently the most accepted view, and the Russian School, that follows the crystallite theory of Lebedev and other Russian workers.

Before Zachariasen, Randall attempted to explain the broadening of the diffraction peaks with the assumption that the structure of glass consisted of a very large assembly of real tiny microcrystals like those displayed in Figure 1.7 (marked by ellipsoids). Nevertheless, the density of glasses is around 10% less than that of poly-crystalline aggregates and the thermal properties of glasses have no explanation within this picture; furthermore the absence of small-angle scattering in fused silica was used to confirm

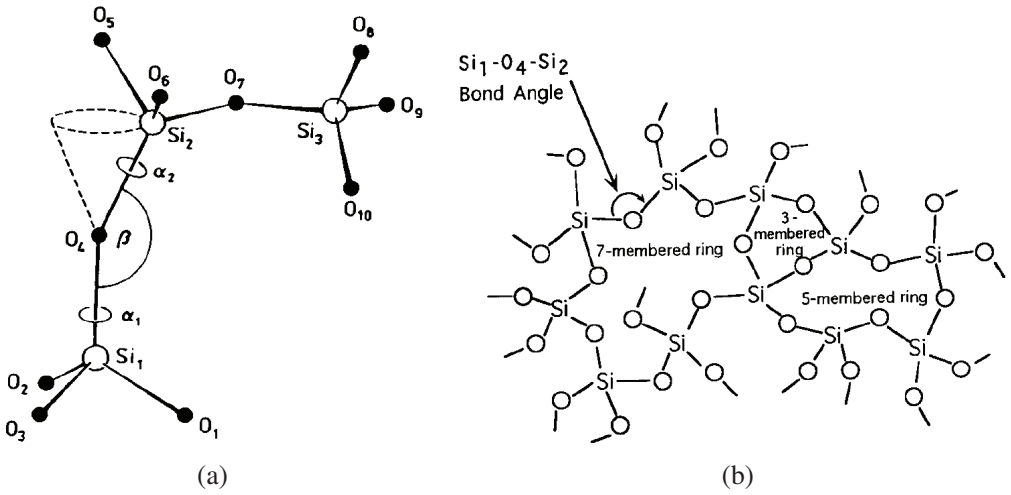

(a) (b)

Figure 1.6: a) Definition of the oxygen bond angle β and torsion angles α_1, α_2, between two linked tetrahedra [15]. (b) Sketch of the silica glass network where the bond angle and the ring structures are highlighted (from [14]).

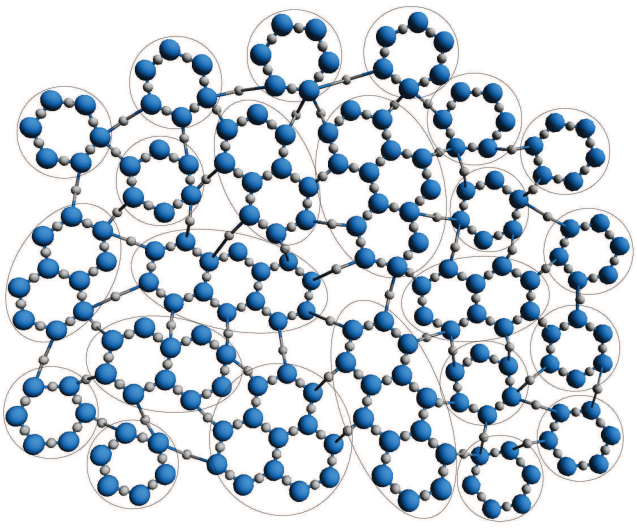

Figure 1.7: Schematic representation of the glass structure according to Randall; the micro-crystals are are enclosed by ellipsoids.

the absence of any microcrystals such as those that can be found in silica gel [14].

In 1932 Zachariasen proposed his well-known continuous random network (CRN) model [16] where he extended the concept of disorder in the broadest sense, having in mind a completely random intermediate-range structure (like those sketched in the left part of Figure 1.8). Support for the random network model came subsequently from Warren that extended the theory to modified oxides systems. In 1921, before Zachariasien's model and then more precisely in 1937, Lebedev came up with a different vision: instead of considering the glass structure as a CRN, he conceived a sort of intermediate-range ordering. He coined the word "crystallites" meaning small undefined subcrystalline regions in which the atomic structure is more ordered than the rest. The main difference with Randall's microcrystal is indeed that the crystallites are embedded in an amorphous matrix and the disorder increases with the distance from these regions. The sketch of the glass structure postulated by the Russian school is shown in Figure 1.8 (right); the crystallites can be distinguished with red circles amidst the surrounding disordered random network. The famous Bell Labs physicist J.C. Phillips also did not support the Zachariasen construction, to the point that he published a paper entitled: "Realization of a Zachariasen glass" [17] (the first page is reported in Appendix B), where he admitted the presence of paracrystals in generic glasses. Other criticisms to the Zachariasien-Warren model comes from Wright [18] who, through an analysis of data from many covalently bonded and network glasses, states that *cybotactic groupings*, or simply, better-ordered regions, should be present and frozen-in in most glasses, particularly in the multi-component ones. The most recent proposal of the Russian thought introduces the concept of *polyclusters* [11, 19], instead of crystallites, that can outbeat thermodynamically and kinetically crystal nucleation during a rapid quench.

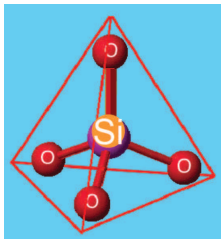

Figure 1.5: The silica glass basic building block: a SiO_4 tetrahedron; the four oxygen atoms act as a bridge between neighboring tetrahedra.

The discovery of the existence of a rich variety of glasses which are characterized by different nanocrystals sizes (such as the ceramic glasses) is in favor of the model of Lebedev; however, the presence of such structures in single component glasses has never been proven. Therefore the idea seems to emerge that the range of extension of random disorder depends on the considered type of glass, thus it could be somehow related to the chemical composition.

1.1.3 Glass formation ability

On the other hand, from neutron scattering and X-ray spectroscopy it is now known that the chemical composition affects precisely the glass-forming ability. This is indeed a prerogative of the so-called Network Former (NF) type constituents, cations that combine with oxygen atoms, giving rise to the glassy network. NFs are p-group elements, in particular Si^{4+}, B^{3+}, P^{3+}, P^{5+}, As^{3+}, As^{4+}, Ge^{4+}, which are characterized

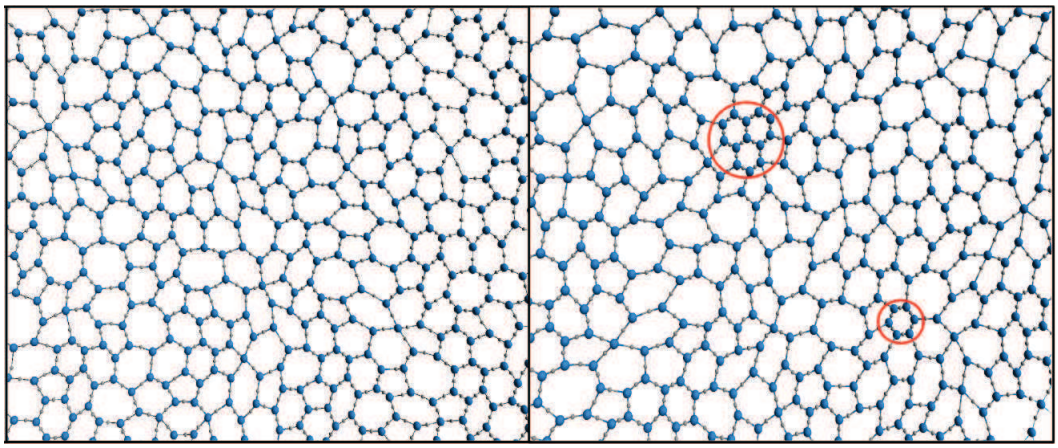

Figure 1.8: Representation of the atomic structure of vitreous silica for left) Zachariasien and right) Lebedev (the crystallites are marked with red circles).

by covalent bonds to oxygen and tend to favor tetrahedral coordination; this therefore leads to a well defined coordination. However the glass constituents can also be Network Modifiers (NMs), other cations (typically ionic) types that support and change the shape of the silicate network with their flexible coordination geometries. NFs are directly incorporated into the network of bonds, while NMs are not: they introduce cavities within the glassy network rather than becoming part of that. NMs in fact tend to cluster together: at small concentration they are "mixed" in the glassy network forming their own clusters in the holes of the amorphous matrix, while at large content they can form "channels". NMs are s-group elements (but not Be, Mg), e.g. Na^{+}, K^{+}, Ca^{2+}, Ba^{2+}, Al^{3+}; their coordination number is not precisely defined since they have a broad distribution of bond lengths. Table 1.1 lists the main glass former and NM oxides; a third group, the intermediate oxide, is classified, describing the inability to form a glass by itself but the possibility of being incorporated into the glass former network [20].

Typically NMs combined alone with oxygen atoms tend to form a crystal, this is why they are also called good crystal formers. The structure of a silicate glass constituted by NM species is characterized by a network of silica tetrahedra (linked by bridging oxygens) broken by the network modifiers, which are usually large and form ionic bonds with non-bridging oxygens (O^{-}).

Glass Formers	Intermediates	Modifiers
B_2O_3	TiO_2	Y_2O_3
SiO_2	ZnO	MgO
GeO_2	PbO_2	CaO
P_2O_5	Al_2O_3	PbO
V_2O_3	BeO	Na_2O

Table 1.1: Division of the oxides into glass formers, intermediates, and modifiers [21].

By means of molecular dynamics (MD) simulations it is possible to visualize the structure of the mixed glasses network; Figure 1.9 presents a MD snapshot of the sodium-silicate melt $Na_2O{\cdot}3SiO_2$ at temperature T=2100 K ([22]). The network contains the silica tetrahedra, formed by

oxygen (red spheres) and Si atoms (yellow spheres), and many irregular pockets and channels which are constituted by Na atoms (big blue spheres and their oxygens).

Another important (and still unexplained, though entropy increase is certainly involved) feature that characterizes the mixed glasses formation, is that adding modifiers reduces the mixture's melting temperature with respect to that of the individual components; of course this is a great advantage exploited by industries to make glasses cheaply. Recent research has remarked that glasses form more easily near the eutectic because there are freezing depression regions that bring the liquid to reach higher viscosities at lower temperatures [24]. The effect of adding Na_2O NMs produces indeed an eutectic with lower melting temperature. Moreover, as shown in Figure 1.10, adding calcium oxide causes a further change in the glassy structure, e.g., the mixture CaO-Na_2O-SiO_2 vitrifies at around T=750-850 K while the melting points of each components are: 1900 K for SiO_2, 2886 K for CaO and 1405 K for Na_2O. At present, current nucleation theories still cannot explain why the beginning of the crystalline growth (with the associate ordering), for example within the channels formed by CaO and Na_2O within the SiO_2 network, is stopped when cooling the melt. The contention in this work is that all glasses - especially the multi-component ones - are inhomogeneous and are made up of regions characterized by enhanced, though not complete, ordering and with more mobile particles in the interstitials between the better-ordered regions.

Examples of such mixed or multi-component glasses are those that are mainly considered in this Thesis, namely, a-Al_2O_3-BaO-SiO_2 (BAS in short), Duran (a complex

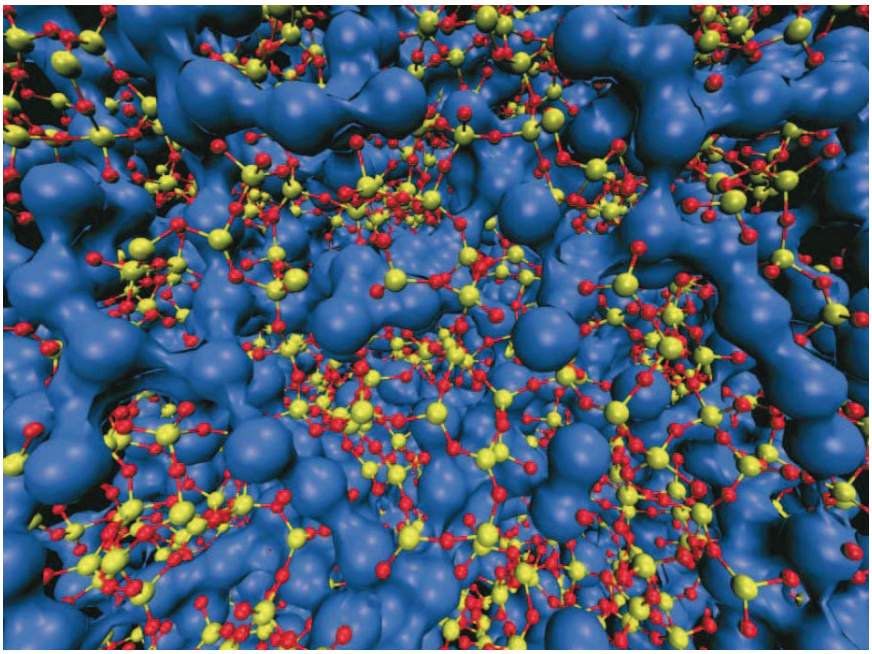

Figure 1.9: Molecular dynamics snapshot (from [22]) of the structure of sodium-silicate melt $Na_2O{\cdot}3SiO_2$ at T=2100 K and density 2.2 $\frac{g}{cm^3}$: Na atoms are represented with blue spheres. The SiO_4 tetrahedra network is displayed as yellow (Si) and red (O) spheres, connected by covalent bonds (shown by sticks).

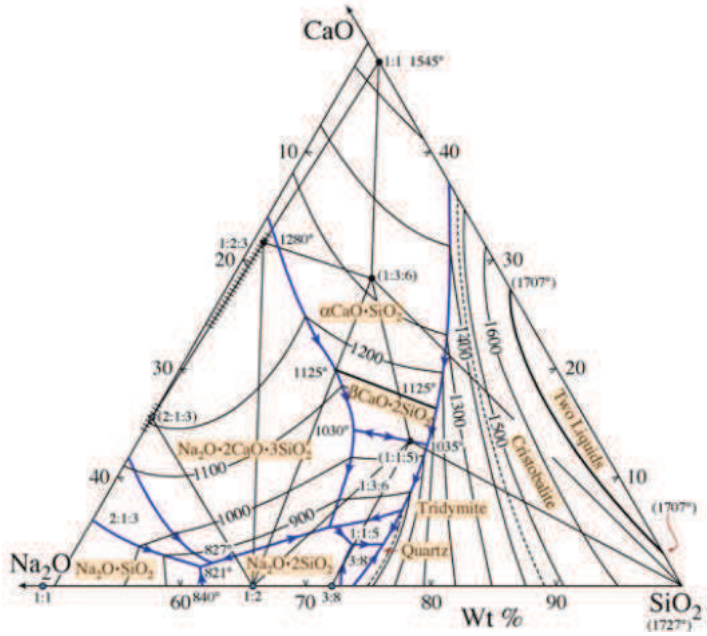

Figure 1.10: CaO-Na_2O-SiO_2 phase diagram (from [23]).

borosilicate commercial glass) and the BK7 optical glass. In the following Section we will review the low temperature properties of glasses and discuss about their possible dependence on the microscopic structure.

1.2 Low temperature physics of glasses

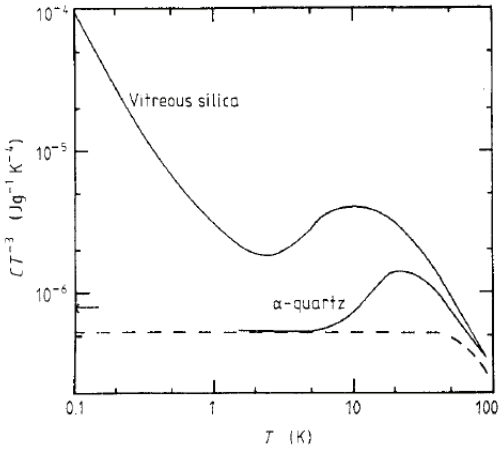

Figure 1.11: The heat capacity of vitreous silica and crystalline quartz as a function of temperature [25], displayed as $\frac{C_p}{T^3}$ versus T.

At low temperatures ($T < 1$ K), glasses display quasi universal thermal, acoustic, and dielectric properties which are very different from those of their crystalline counterparts. Figure 1.11 shows the difference of the heat capacity C_p between an amorphous material and the corresponding crystal: C_p in glasses is much larger and depends approximately linearly on temperature T below 1 K. This is in contrast to the cubic dependence observed in crystals, well understood in terms of the Debye theory of lattice vibrations. Furthermore, the thermal conductivity κ is orders of magnitude lower than the crystal one and depends almost quadratically on temperature. The real part of the dielectric constant ε'

and the sound velocity in glasses show instead a universal logarithmic dependence on temperature T at low frequencies.

These thermal, dielectric and acoustic universal properties of amorphous solids can be understood in broad terms in the framework of the two-level system standard tunneling model (2LS STM), which has become the conventional approach to describe glasses at very low temperatures. The fundamental postulate of the STM (described in Section 1.2.1) is that atomic tunneling systems (TS), till now held responsible for the low temperature universal behavior, are approximated by particles moving in a double-well potential, the parameters of which are widely distributed due to the irregular structure of these materials as described by the Zachariasen-Warren model of glass structure.

There are, however, several drawbacks with this approach; some are related to limitations in the formulation of the theory, like the still unknown microscopic nature of the tunneling systems, while others come from some recent experimental measurements that show qualitative and quantitative discrepancies from the behavior predicted by the model [26]. The relevant deviations beyond the STM are presented in Section 1.2.2, while the different theories developed to explain these phenomena, and their limitations, are summarized in Section 1.2.3. Finally in Section 1.3 we propose a picture for the amorphous solids that overcomes the *impasse* and is able to explain all the reported new experimental features.

1.2.1 The Standard Tunneling Model

According to the STM, introduced by W.A. Phillips [27] and, independently by, Anderson, Halperin and Varma [28] in 1972, in amorphous materials some atoms or small groups of atoms can occupy one of two (or more) local potential minima, contrary to perfect crystals, where the atoms are forced by symmetry to occupy a single minimum. At low temperatures (below 1 K) the transition between these states is possible only via quantum-mechanical tunneling; thermally activated processes are in fact highly improbable. A tunneling system can be thought of as a particle that moves by tunnel effect in a potential of the form depicted in Figure 1.12(a), where the abscissa does not represent necessarily the spatial coordinate, but it could also be related to the angular separation of two positions where the particles can rest in two energetically favored configurations [29]. In this justification of the TSs, clearly the tunneling "particle" cannot be typically a real atom/ion of the glass, but rather an effective, fictitious particle: jumps between contiguous minima of the potential energy landscape (PEL) correspond to the rearrangements of several atoms/ions.

The energy levels of the particle are calculated using as a starting point the solutions of the single-well problem. Since we are interested in the low temperature regime, we can consider only the ground states of the two approximately harmonic potential wells V_1 and V_2. In fact, the statistical population of the higher levels can be neglected, since they have an energy of $\hbar\Omega \gg \Delta$, where Δ is the energy difference between the two ground states and Ω is the single-well frequency. The simplest low-

energy single-well Hamiltonians, H_1 and H_2, of each independent TS are related to the total hamiltonian H in this way:

$$H = T + V_1 + V - V_1 = H_1 + (V - V_1) = H_2 + (V - V_2) \tag{1.7}$$

where T and V are respectively the kinetic energy and potential energy operators. H_1 and H_2 are the individual well Hamiltonians. Using the localized wave functions, $|\phi_1\rangle$ and $|\phi_2\rangle$, that correspond to the single harmonic local potentials V_1 and V_2, we can write

$$\begin{pmatrix} \langle\phi_1|H|\phi_1\rangle & \langle\phi_1|H|\phi_2\rangle \\ \langle\phi_2|H|\phi_1\rangle & \langle\phi_2|H|\phi_2\rangle \end{pmatrix} = \begin{pmatrix} E_1 + \langle\phi_1|V - V_1|\phi_1\rangle & \langle\phi_1|H|\phi_2\rangle \\ \langle\phi_2|H|\phi_1\rangle & E_2 + \langle\phi_2|V - V_2|\phi_2\rangle \end{pmatrix} \tag{1.8}$$

If we take into account the case where the barrier is high we can neglect the terms of the form $\langle\phi_i|V - V_i|\phi_i\rangle$ with respect to E_i; choosing the zero of the energy as the average between the two local ground state energies E_1, E_2 we can express the Hamiltonian matrix $\mathcal{H}_{2LS}$ of a 2LS system in the following way:

$$\mathcal{H}_{2LS} = \frac{1}{2}\begin{pmatrix} -\Delta & -\Delta_0 \\ -\Delta_0 & +\Delta \end{pmatrix} \tag{1.9}$$

where the tunneling splitting Δ_0 is given by:

$$\Delta_0 = -2\langle\phi_1|H|\phi_2\rangle \tag{1.10}$$

This quantity can be evaluated for specific potentials, however generally speaking we have that it depends on the barrier height and separation of the wells in an exponential fashion.

If for example we consider the double-well harmonic potential, thus

$$V(x) = \begin{cases} V_1(x) = \frac{1}{2}m\Omega^2(x+d)^2 & \text{if } x < 0 \\ V_2(x) = \frac{1}{2}m\Omega^2(x-d)^2 & \text{if } x > 0 \end{cases} \tag{1.11}$$

we can use the ground state functions (schematically shown in Figure 1.12(b)) and the WKB approximation to obtain an approximate form for Δ_0 (which can be thought as a good qualitative representation):

$$\Delta_0 \approx \hbar\Omega e^{-\lambda} = \hbar\Omega \exp\left[-d\left(\frac{2mV_0}{\hbar^2}\right)^{\frac{1}{2}}\right] \tag{1.12}$$

where m denotes the mass of the particle, V_0 is the barrier height between the two wells and $2d$ is the well separation along the configurational coordinate. Therefore we find that if m or d or V_0 is too large the tunneling is negligible. Each 2LS is characterized by two energy levels:

$$\mathcal{E}_{1,2} = \pm\frac{1}{2}\sqrt{\Delta^2 + \Delta_0^2} = \pm\frac{1}{2}E \tag{1.13}$$

where E represents the interlevel spacing between the two energy eigenstates. The delocalized wave functions (represented in Figure 1.12(b)) have the following form [25]:

$$\begin{aligned} \Psi_1 &= \phi_1 \cos\theta + \phi_2 \sin\theta \\ \Psi_2 &= \phi_1 \sin\theta - \phi_2 \cos\theta \end{aligned} \tag{1.14}$$

where $\tan(2\theta) = \frac{\Delta_0}{\Delta}$. The diagonalized Hamiltonian can be formulated in this form:

$$\mathcal{H}_{2LS} = \frac{1}{2} E \sigma_z \tag{1.15}$$

where σ_z is the Pauli matrix.

The way to include the disorder in the description (as a direct consequence of the Zachariasen-Warren model of glass structure) is to introduce a probability distribution for the physical quantities. Of course, the form of the chosen distribution function is critical in order to derive the properties of the main observables at low temperature. When the glass is cooled from the melt, its atoms or ions form a potential energy landscape in which the characteristic parameters of the double-well potentials (V_0, Δ) are widely spread, so they may have a very broad range of values. Making the assumption that the range of energy variation is much greater than that available at such low temperatures, one can consider a uniform distribution that does not depend on Δ. The other parameters of the standard model can be treated together using the λ parameter; as we know from Equation 1.12 a small variation of λ means a big variation of Δ_0, thus one can consider a constant distribution in λ as well:

$$P(\lambda, \Delta) d\lambda d\Delta = P_0 d\lambda d\Delta \tag{1.16}$$

where P_0 represents a phenomenological constant containing the density of the tunneling states. Thus, we obtain:

$$P(\Delta, V_0) d\Delta dV_0 \cong P(\Delta, \Delta_0) d\Delta d\Delta_0 \tag{1.17}$$

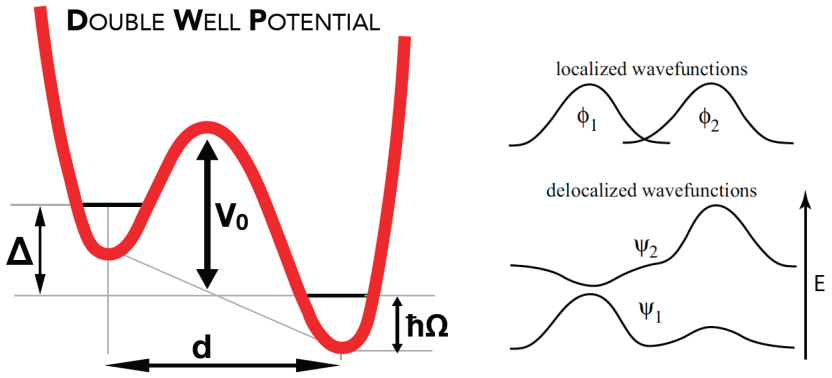

Figure 1.12: a) The potential of a two-level system (2LS) with a barrier height V_0, energy asymmetry Δ, well separation d and ground state energy $\hbar\Omega_0/2$. b) Representation of the two localized wave functions ϕ_1 and ϕ_2 of the particle in the two potential minima and the two lowest states of the delocalized system Ψ_1 and Ψ_2, in the STM description, from [30].

which leads to a distribution function that is uniform in Δ and $\ln\Delta_0$

$$\mathcal{P}_{2LS}(\Delta,\Delta_0) = P(\Delta,V_0)\frac{dV_0}{d\Delta_0} = \bar{P}\frac{1}{\Delta_0} \tag{1.18}$$

where $\bar{P}$ is a material-dependent constant, proportional to the volume concentration of the 2LSs, which has to be determined experimentally; for many of the dielectric glasses its value is in the range (0.5-3)$\times 10^{45}$ J^{-1}m^{-3} [31].

However, not all the states of the parameter space (Δ,Δ_0) count. Using the equation (1.13) and its Jacobian matrix, the above distribution function can be converted to a distribution in terms of the tunneling splitting Δ_0 and energy E:

$$P(E,\Delta_0)dEd\Delta_0 = \bar{P}\frac{E}{\Delta_0}\frac{1}{\sqrt{E^2-\Delta_0^2}}dEd\Delta_0 \tag{1.19}$$

This function diverges when $\Delta_0 = 0$ and thus it is convenient and physically meaningful to introduce the following cutoff limits: a minimal tunneling splitting Δ_{0min} and (eventually) a maximum energy splitting E_{max}.

This distribution of Equation 1.18 corresponds to an almost uniform density of states (DOS) $n(E)$, which is defined as:

$$n(E) = \int_{-\infty}^{+\infty} d\Delta \int_0^{+\infty} d\Delta_0 \mathcal{P}_{2LS}(\Delta,\Delta_0)\delta(E-\sqrt{\Delta^2+\Delta_0^2}) \tag{1.20}$$

Thus to evaluate

$$\left\langle \delta\left(E-\sqrt{\Delta^2+\Delta_0^2}\right)\right\rangle_{\Delta,\Delta_0} \tag{1.21}$$

where $\langle ...\rangle$ means the average, one can exploit

$$\delta(\varphi(x)) = \sum_i^N \frac{1}{|\varphi'(x_i)|}\delta(x-x_i) \tag{1.22}$$

where $\{x_i\}$ are the N zeroes of $\varphi(x)$=0 and $\varphi'(x) = \frac{d\varphi(x)}{dx}$. In this case $x = \Delta$ and $\varphi(\Delta) = E-\sqrt{\Delta^2+\Delta_0^2}$. For $\varphi(\Delta) = 0$ one can find the solutions:

$$\Delta_i = \pm\sqrt{E^2-\Delta_0^2} \tag{1.23}$$

thus by using Equation 1.22 one has:

$$\delta(E-\sqrt{\Delta^2+\Delta_0^2}) = \begin{cases} \frac{E}{\sqrt{E^2-\Delta_0^2}}\delta\left(\Delta-\sqrt{E^2-\Delta_0^2}\right) & \text{if } \Delta_0 \le E \\ 0 & \text{if } \Delta_0 > E \end{cases} \tag{1.24}$$

Since the distribution $\mathcal{P}_{2LS}(\Delta_0,\Delta)$ is symmetric in Δ, the DOS is

$$\begin{aligned} n(E) &= 2\int_0^{\infty} d\Delta_0 \int_0^{\infty} d\Delta \mathcal{P}_{2LS}(\Delta_0,\Delta)\delta\left(E-\sqrt{\Delta^2+\Delta_0^2}\right) \\ &= 2\int_0^{E} d\Delta_0 \frac{\bar{P}}{\Delta_0}\int_0^{\infty} d\Delta \frac{E}{\sqrt{E^2-\Delta_0^2}}\delta\left(\Delta-\sqrt{E^2-\Delta_0^2}\right) \\ &= 2\bar{P}\int_0^{E} d\Delta_0 \frac{E}{\Delta_0\sqrt{E^2-\Delta_0^2}} \end{aligned} \tag{1.25}$$

Therefore the integral reduces to

$$n(E) = \int_{\Delta_{0min}}^{E} \mathrm{d}\Delta_0 \frac{E}{\Delta_0 \sqrt{E^2 - \Delta_0^2}} \simeq 2\bar{P} \ln\left(\frac{E}{\Delta_{0min}}\right) \tag{1.26}$$

Since the energy variation is weak, $n(E) = n_0 =$constant can be considered energy independent.

Finally, by coupling the TSs with external acoustic and electric fields as perturbation of $\mathcal{H}_{2LS}$, the STM is capable to explain the majority of thermal, dielectric and acoustic properties of glasses at low temperature.

1.2.2 Significant experimental deviations from the STM predictions

In spite of the important contribution to the description of a wide range of physical properties of glasses at very low temperatures, the STM has some important limitations. As we have already mentioned, the very nature of the tunneling systems is still unclear [32]. The present experimental techniques in fact are able to detect the low temperature anomalous properties of amorphous solids, but still cannot measure the individual properties of the TS. Moreover, there is a full list of recent experimental measurements that cannot be explained by the STM. It is important to remark that the observed deviations from universality are found in multicomponent silicate and ceramic glasses, relevant for technology applications. Basically from the available experimental measurements one can group these kinds of "anomalies" in two subcategories, that we indicate as:

Composition effects It has been found that the heat capacity response shows a strong dependence on the different concentration of NMs; Figure 1.13 presents $\frac{C_p}{T^3}$ as a function of T for the mixed glasses $(SiO_2)_{1-x}(K_2O)_x$ and $(SiO_2)_{1-x}(Na_2O)_x$ for different composition x of potassium or sodium oxides [33]. In these data the heat capacity is larger than that of pure vitreous silica (a factor of 10 near 0.1 K) and the temperature behavior is very peculiar for different x: the heat capacity decreases and then increases again with increasing molar concentration of K_2O. A similar effect has been reported for a glass with different composition, Pyrex, as shown in Figure 1.14 where we can see that below 1 K the heat capacity deviates significantly from the expected linear T dependence and an almost temperature-independent "shoulder" is shown.

An even strongest response to the different concentration of NMs is found for the real part of the dielectric constant as a function of T as we can see in Figure 1.15(a), where the concentration x(K) has been varied from 0.05 to 0.20, and e.g. for the BAS glass, as shown in Figure 1.15(b) [34] where the expected behavior derived with the STM is shown with a dashed line.

Magnetic effects There are mainly three measurements in which one can observe a puzzling enhanced response to an external magnetic field:

- The heat capacity of multicomponent glasses, e.g. BAS and Duran, shown in Figure 1.16. We can see an anomalous T-dependence specific heat behavior for different B values: the maximum deviation from the STM+Debye type behavior (thus linear plus cubic with temperature) is found near $B = 0$. When increasing B, the heat capacity increases and then decreases again for higher values (vanishing above B=8 T). The same response has been obtained for Pyrex, as we can see from Stephens data [35]: when the magnetic field is switched on (in this case B=33 kG) the bump in the specific heat disappears.
- The dielectric constant: the multicomponent BAS, for example, presents at very low temperatures ($1< T <200$ mK), an unexpected enhanced dielectric response to very weak magnetic fields $B \sim 10\mu$T followed by slow decrease at higher fields [36], a behavior that was later discovered in the BK7 and Duran glasses [37]. Similar effects have been confirmed for the structural glass a-$SiO_{2+x}C_yH_z$ in the range $50< T <400$ mK at B=3 T [38].
- The polarization-echo experiments in both BAS, Duran and BK7 glasses have also revealed considerable sensitivity in the response of the echo amplitude to very weak magnetic fields [39], as shown in Figure 1.17; note that a remarkable result of such measurement is that Suprasil I (which is very pure a-SiO_2) shows no measurable magnetic field effect.

Often, these kind of unusual effects are ascribed to spurious agents or to trace of paramagnetic impurities; however this seems not to be the case, since for the composition experiments all samples used the same starting material and were subjected to the same treatment. Hence iron impurity cannot explain the variation of the magnitude of the hump with concentration x. Regarding the other experiments we conclude that the observed magnetic response does not scale with the declared paramagnetic impurity concentration. In addition, we will see that analogous effects have been measured in the a-$SiO_{2+x}C_yH_z$ glass that do not contain at all iron paramagnetic impurities. In Chapter 3 we will definitely show, by means of our model that the paramagnetic impurities do not represent the cause of these striking effects.

1.2.3 Proposed Theoretical Explanations

Several different models have been proposed in order to explain these unusual phenomena; in the following we summarize some of these. The first theory developed by Kettemann-Fulde-Strehlow (KFS) in [42] to explain the magnetic effects in glasses takes into account the tunneling of charged particles moving on closed paths in a three dimensional (3D) DWP, that couple to the magnetic field via the AB effect. As in the case of the STM, the ground and first excited state can be approximated (if $V_0 \gg \hbar\Omega > \Delta$) by the superposition of the harmonic single well potential. The energy levels are found to be periodic in the magnetic flux $\frac{\varphi}{\varphi_0}$ where φ_0 is the quantum flux unit, thus the TSs result in persistent tunneling currents. The derived energy gap and

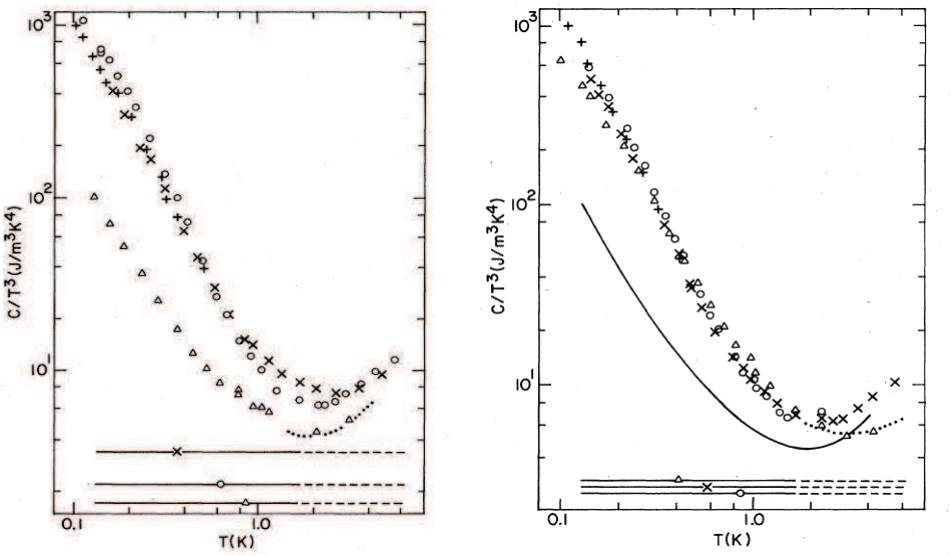

Figure 1.13: Specific heat of the silicate glasses divided by T^3 for the following compositions: a) x=0 (Δ), x(K)=0.05 ($\circ$), x(K)=0.20 ($\times$), x(K)=0.20 ($+$) measured with a different technique; the dotted line is the Vitreosil (x=0) from a different reference; b) x=0 (solid line), x(K)=0.08 ($\circ$), x(K)=0.10 ($\times$), x(K)=0.10 ($+$) measured with a different technique; the Na composition is also reported: x(Na)=0.27 (Δ) and x(Na)=0.25 (dotted line). In both figures the horizontal lines indicate the Debye phonon contribution. Data from [33].

the tunneling splitting now depends on the magnetic field and can be used to calculate the response of the electric permittivity to weak magnetic fields for BAS glass can be explained for $B = 0$. Note that the parameter distribution is the same ast that for the STM. This model requires a large value of q, the charge of the effective tunneling particle, to explain the magnetic effect in BAS glass, that leads to a big cluster of 2LSs (around 10^6). This approach, however, would also apply to the pure a-SiO_2 glass. KFS explain the absence of magnetic effects in pure SiO_2 through the role of the TS-TS interactions and the large variation of the parameter Δ_{0min} depending on the glass type. This parameter has been proposed by Yu and Legget [43, 44] and subsequent workers (Levitov [45, 46] and Burin [47, 48]) to be determined by the interactions between (nominal) 2LSs.

Some agreement with the experimental data of the polarization echo in vitreous glycerol ($C_3H_8O_3$) has been provided by the nuclear electric quadrupole approach of Würger-Fleischmann-Enss [49] that associates the observation of magnetic effects to tunneling atoms that carry electric quadrupole moments, based on the fact that a-SiO_2 does not have nuclei with spin greater that $\frac{1}{2}$ contrary to other glasses. By means of the interaction of the nucler quadrupole moment with the local electric field due to a 2LS it is possible to obtain an energy level splitting. However at present this approach is not capable to explain the magnetic effect for the dielectric constant. Furthermore there are recent echo experiments on defected crystals KCl:Li where both

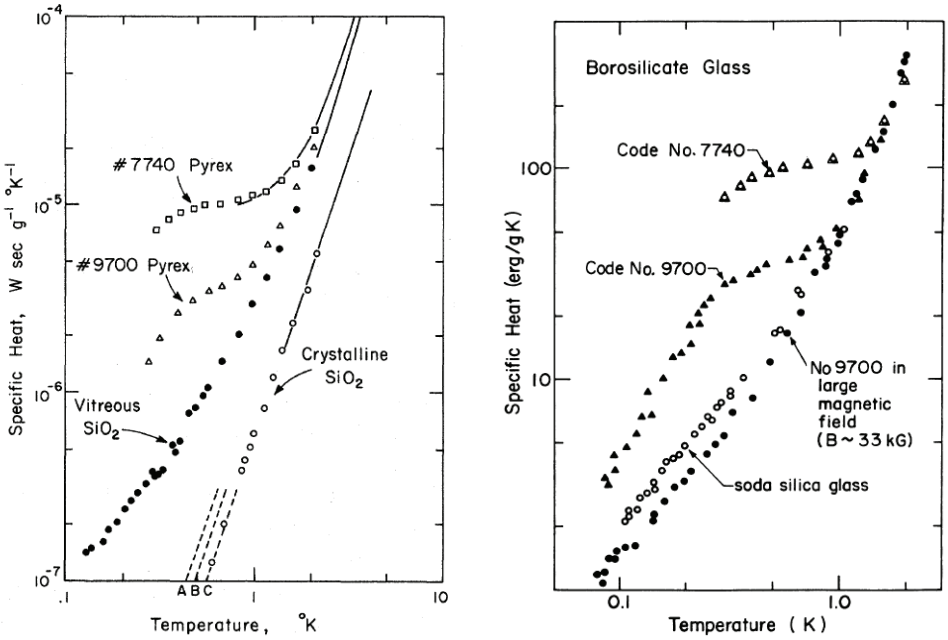

(a) (b)

Figure 1.14: a) Specific heat of vitreous SiO_2 (•), 9700 Pyrex (Δ), 7740 Pyrex (□); the solid lines are crystalline SiO_2. Data from [40]. b) Specific heat of 7740 Pyrex (Δ), 9700 Pyrex for magnetic field B=0 (△) and B=33 kG (•); soda-silica glass $(Na_2O)_{0.25}(SiO_2)_{0.75}$ (○). Data from [35].

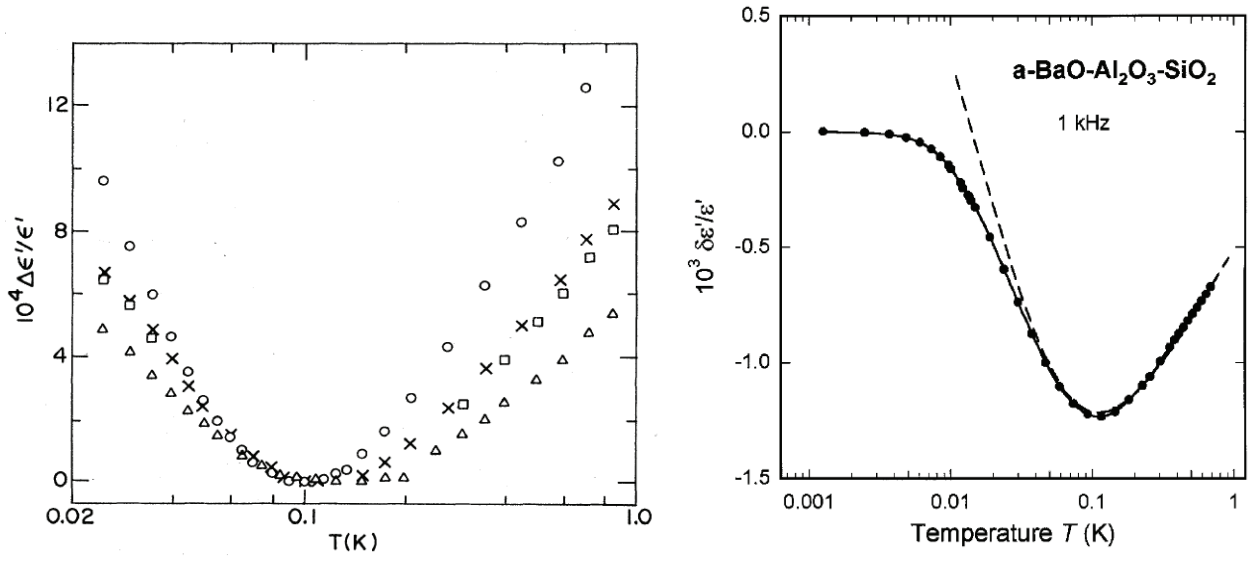

(a) (b)

Figure 1.15: Variation of the real part of the dielectric constant with T and composition x: a) for the silicate glasses [33], with x(K)=0.05 (△), x(K)=0.08 (□), x(K)=0.10 (×), x(K)=0.20 (○); b) for the BAS glass at 1 kHz [34], the dashed line represent the 2LS predicted behavior.

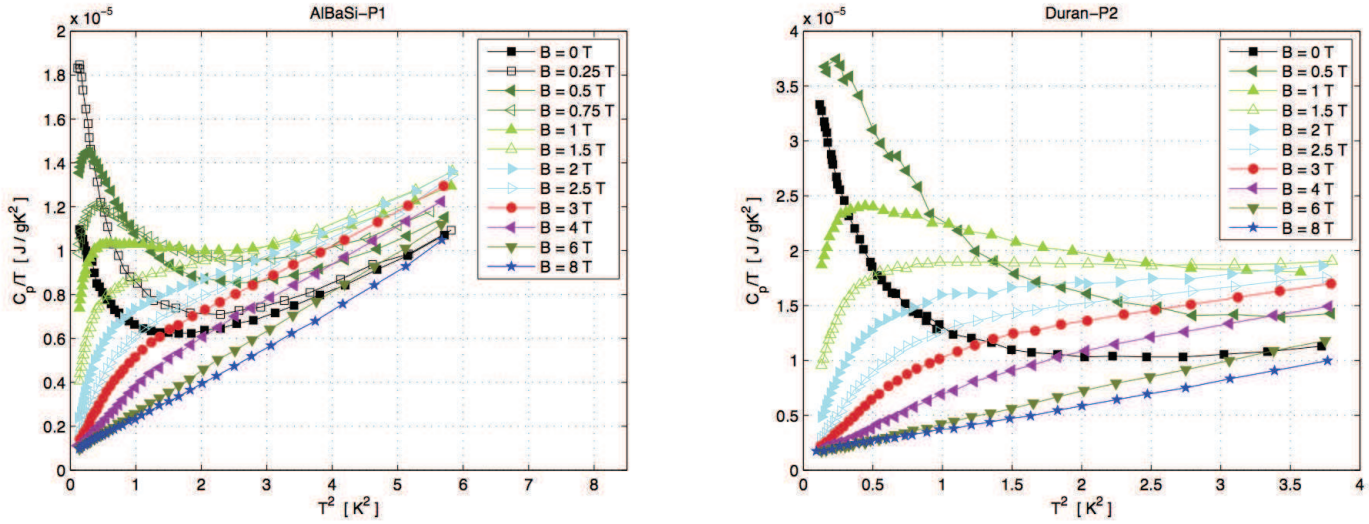

(a) (b)

Figure 1.16: Specific heat divided by T for a) BAS and b) Duran glasses for various applied magnetic field. The curve at B=8 T describes the linear temperature dependence of the specific heat. Data from M. Meissner (2000, private communication). Part of these data is reported in [41].

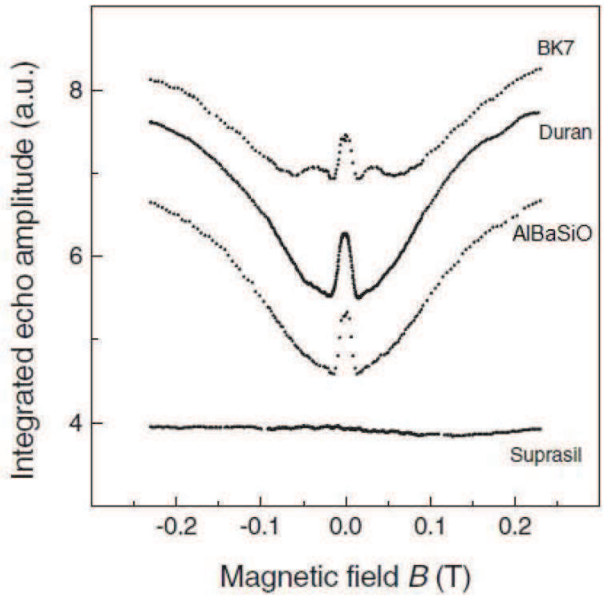

Figure 1.17: The integrated echo amplitude as a function of the magnetic field for different silicate glasses: BK7, Duran, AlBaSiO (BAS) and Suprasil I. All data were taken at T=12 mK, delay time τ_{12}=2 ms, and roughly 1 GHz, except for Duran, where τ_{12}=1.7 ms [39].

the ^{6}Li and ^{7}Li isotopes where studied. The most remarkable effects (oscillation in B and waiting time τ) where found to be stronger for the KCl:Li^6 specimen, rather than for KCl:Li^7. This is exactly the opposite of the expected behavior, since the magnitude of the nuclear quadrupole moment for ^{7}Li is around forty times bigger than that of ^{6}Li (Q(^{6}Li)=-0.001 barn with respect to Q(^{7}Li)=-0.040 barn). Moreover, the a-SiO_2+$_x$C$_y$H$_z$ glasses have nuclei with no nuclear quadrupole moments and yet show a marked magnetic effect in the dielectric constant.

Another attempt to explain the magnetic field effect for the dielectric constant for BAS is due to Borisenko and Bakai [50]. They made the hypothesis of the existence of paramagnetic TS that can exist due to paramagnetic (Fe) impurities which substitute the Si atoms and have different valence. Typically such defects are accompanied by charged particles (holes) that carry a spin-$\frac{1}{2}$ (therefore a magnetic moment) and tunnel in their own 2LS potential. By means of this description, the magnetic field effect for the heat capacity, dielectric constant and the polarization echo have been explained, but still there is no explanation for the effects in the amorphous glycerol and the borosilicate BK7. Moreover, the paramagnetic explanation does not explain why the magnetic effects do not scale with the impurities concentration. Indeed, the needed impurity concentrations are much higher than the nominal Fe concentrations and overestimate the % of Fe that can substitute Si in a glass. None of these models takes into account the fact that the most remarkable effects have been found in multicomponent glasses, which are characterized by a multiphase composition with crystalline-like regions in their microscopic structure. This, we think, represents a key aspect in order to understand and describe all of the above mentioned experimental deviations from the predictions of the STM. In the next Section we will present the picture of the cellular model for glasses.

1.3 The cellular model of glasses at intermediate and low temperatures

In this Section we propose a new picture for the atomic structure of glasses, the *cellular model*, which is the framework for the extended tunneling model (ETM), described in the next Chapter, that is capable to explain the unexpected behavior at low temperature (the composition and magnetic effects) for a big variety of amorphous insulators. Within the cellular model, the Zachariasen's hypothesis of the CRN, is considered only a useful idealization to apply mathematically highly appealing concepts. There are indeed several arguments in favor of the heterogeneous nature of the real glasses, which we believe is always characterized by the presence of regions (not so small in ceramic glasses, as previously discussed) that are better ordered where the atoms, ions or molecules are characterized by their own frozen dynamics, like the NM-regions that reduce the melting temperature in ternary glasses. Since the thermodynamically stable phase of a liquid that is cooled below the freezing temperature T_f would be the perfect crystal, following the concept of nucleation, we can imagine that,

the regions that have just begun to orient to form the crystal in the supercooled liquid, do not form a crystal nucleus but are therefore better ordered. In fact, not surprisingly, Lubchenko and Wolynes [51, 52], consider a glass well below T_g a "mosaic of aperiodic crystals". The behavior is in analogy with the phenomenon of the formation of droplets near the freezing temperature for certain substances. We name these regions in the glassy phase *regions of enhanced regularity* or RER which are like the Wright's cybotactic groupings deduced from a critical analysis of the X-ray and neutron scattering data in amorphous solids [18]. Other similar names have been proposed in the literature, e.g. the existence of *polymerized clusters* in both oxide and chalcogenide network glasses seems to be common, to the contrary of Zachariasen's glass which is rare to produce, almost an exception in nature, according to [17]. Again, *para-crystals* structures at the 10 to 20 nm lenght scale have been found in amorphous Si films, using combined electron diffraction and fluctuation microscopy [53]. Crystalline-like regions of sub-nanometer size embedded in the otherwise homogeneous amorphous mass have been found for some metallic glasses like $Zr_{50}Cu_{45}Al_5$ [54] or $Ni_{64}Zr_{36}$ alloys [55] using combined theoretical methods (such as reverse Monte-Carlo simulations) and different experimental techniques (e.g. electron fluctuation microscopy)

On the other hand, the evidence from X-ray analysis for real crystalline-like regions in network glasses is much more pronounced in the case of multi-component materials, like *ceramic glasses* [18] (e.g. $(MgO)_x(Al_2O_3)_y(SiO_2)_{1-x-y}$), which indeed are also termed as *crystallized glasses* [56]. Contrary to what one might expect, one of the current cutting-edge research in this field is the crystallization of glasses. Nowadays such hybrid materials are becoming more and more important for their attractive properties (mechanical, optical, electrical and so on) which are improved compared to those of glasses themselves. The final motivation is the realization of a new generation of glass-related materials through the crystallization of glasses; this is the reason why the understanding of the medium-range order structure is of primary importance. However, the attitude we will take in this Thesis is that only the purest mono-component glasses may obey to the Zachariasen-Warren random-network model, while the intermediate-range atomic structure of the majority of real glasses will contain RERs in some extent.

Moreover, we think that there is another indication that points to the direction of the presence of better ordered regions that facilitate the structural rearrangements: the DHs [57], that have characterized the research on glasses in the last twenty years and are nowadays well established both via experimental and numerical investigation. As previously discussed, the phenomenology of these fluctuations give rise to the appearance of cluster of faster and slower particles (represented in Figure 1.18(a)), with different size and distribution, whose nature and origin are however not yet explained, but we believe is linked to the nucleation of RERs. From simulation studies it has been found that the slower regions of immobile particles, that grow and increase in size as $T \to 0$, are also better ordered while the faster regions have a more liquid-like structure.

In our view the RERs are nothing more than the thermal history continuation of

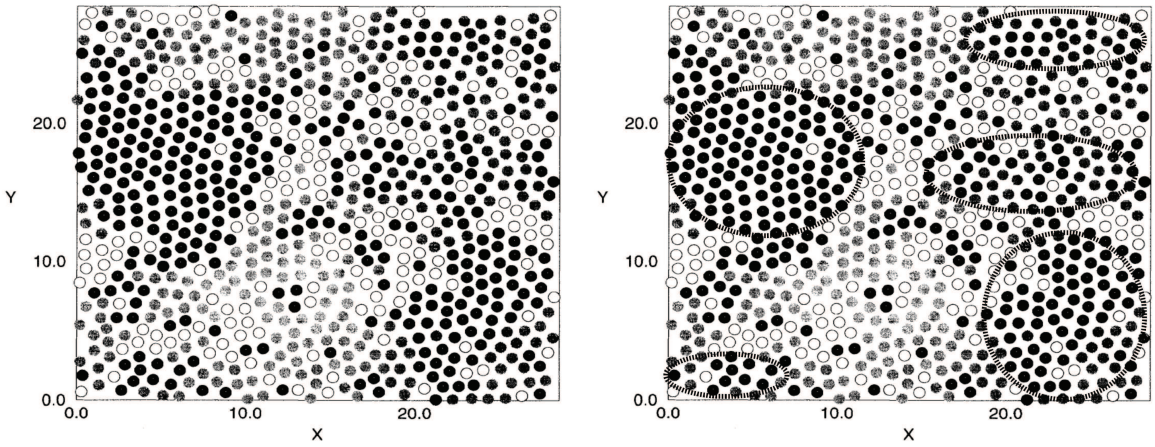

(a) (b)

Figure 1.18: a) Map of the relaxation times of one MD simulation run of a two dimensional (2D) system of 780 soft disks, interacting via a repulsive $1/r^{12}$ potential cut off at some distance [58]. The circles represent the position of the particles: the black are the 40% slowest while the shaded gray the 40% fastest and the unfilled cirlces are the intemediate 20%. Such different cluster represent the DH. b) The slower regions have been schematically highlighted to show the cellular structure.

the slower particle regions (or cells, which are highlighted with black bold circles in Figure 1.18(b)) in the forming glass down to the deep glassy region, with the remark that their average size does not diverge at any characteristic temperature.

Therefore, the picture that we have in mind is a cellular-type arrangement of RERs that can have complicated (perhaps fractal) compact morphology whose disorder in the arrangement give rise to the standard 2LS but also causes distortion in the bond angles between neighboring cations with the anions that can take up two nearly equivalent positions differing by a small energy. Therefore the RERs contain some of the 2LSs and the great majority of them will be located at the meeting point between these cells, since the cell boundary is where the bond/chemical discontinuity takes place [59].

Each interstitial between these cells is populated by a large number N (on average) of still fast-moving charged particles (the faster particles of the DHs at $T > T_g$), that, below T_g are constrained to move in a coherent fashion due to the high Coulomb repulsion between them. In this picture, the phonons propagate in the cells now jammed against each other and the remnant localized degrees of freedom act as TSs, which now are of two species: the DWPs which are located within the RER and at their points of contact, and the *anomalous tunneling systems* or ATSs. The latter are *effective* charged quasi-particles[1] that describe the coherent collective motion of the ions trapped in the interstices and which are subjected to an effective tunneling potential

[1]In the literature "additional" TS (beside the standard 2LS) were already proposed by MacDonald [33] and in earlier papers too. Black and Halperin [60] suggested a new type of TS from an estimate of tunneling parameters and from comparison of specific heat experimental measurements.

having four natural wells in the cell distorted tetrahedral configuration that is formed.

Fig. 1.19(a) shows in a schematic way how the atomic/ionic matter could be organized below T_g in a real glass. The RER are the bold black globular blobs which have increased their size to fill the space and contain the DWPs (blue spots, the boundary 2LSs are not shown for clarity in this cartoon); trapped, charged and faster particles of the DH existing above T_g are located in the cell interstices (yellow regions) and give rise to a coherent tunneling movement, that can be represented by a single fictitious quasi-particle, the ATS (orange central dot). The potential tetrahedral configuration is also separately highlighted in Figure 1.19(b).

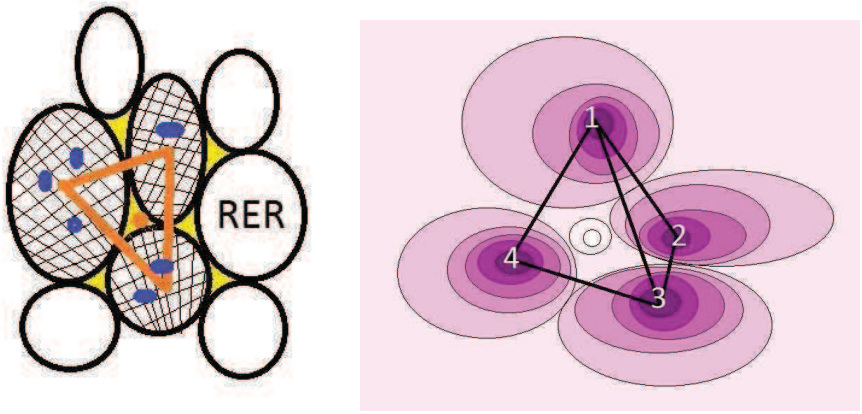

(a) (b)

Figure 1.19: (a) Sketch of the cell structure of a glass below T_g: the RER (bold black circles in this oversimplified draw for fractal-like but compact objects) have increased their size to completely fill the space and enclose the 2LS standard tunneling units (blue spots). At the same time, in the cell interstices (yellow colored regions, connecting to each other) the trapped, charged and faster particles of the DH existing above T_g (which are now probably charged dangling bonds) give rise to coherently tunneling large groups of ions that can be represented by a single fictitious quasi-particle, the ATS (orange central dot), which is subjected to an effective tunneling potential having four natural wells in the cell distorted tetrahedral configuration, which is separately represented, for clarity, in b) with the following color coding for the potential intensity: dark=deepest, light=highest.

The tetrahedral shape of the potential is constituted by four wells for each interstice, with a large barrier in the center. Actually, the tetrahedral four wells potential, or TFWP, can be replaced with four local 2D potentials for the four particles describing the coherent tunneling of the dangling-bond particles sitting near each face of the tetrahedron, close to a group of three (on average) quasi-ordered cells. Therefore the TFWP can be reduced to a triangular three-well version that has the advantage to simplify the mathematical description. Because of the better ordering implied in this model of the glassy intermediate-range atomic structure and in each cell, the three

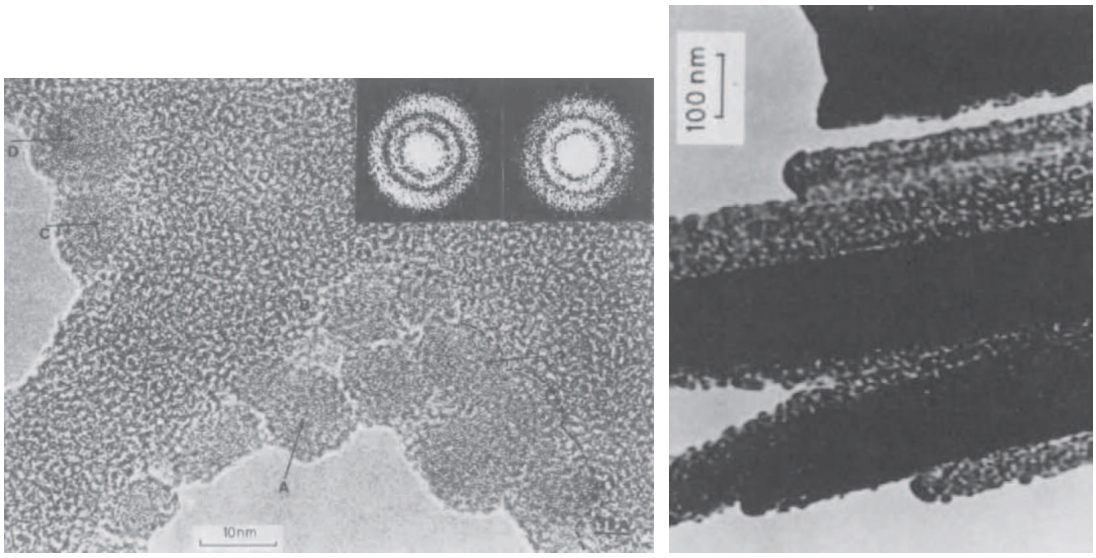

(a) (b)

Figure 1.20: a) High resolution transmission electron microscopy of a-SiO_2 obtained with sol-gel process; b) the cellular structure is clearly distinguishable. Images from [63].

wells of each effective 2D potential for the ATS will be near-degenerate in terms of their ground-state energy asymmetries: $E_1 \simeq E_2 \simeq E_3 \simeq 0$ [59].

In conclusion we propose a novel possible cellular scenario for the type of arrangement of the RERs below the glass transition temperature. Note that a cellular structure for glasses had already been proposed in the past by de Gennes [61] and, related to the low-temperature anomalies by Baltes [62] who explained in this way the linear in T behavior in C_p. As already discussed a very similar picture is that of the Bakai's polyclusters [11]. Lastly, the cluster nature of the TSs is also implicit in the approach by Lubchenko and Wolynes [51]) in their mosaic-structure inspired theory of the glass transition.

We can visualize a rare image for a real glass of such cellular structure in Figure 1.20 [63] where the intermediate-range atomic structure of a-SiO_2 was imaged by means of high resolution transmission electron microscopy, or HRTEM in short (Figure 1.20(a)); the cellular structure is clearly visible in Figure 1.20(b). In Figure 1.21 we present two other electron microscopy images where the cellular structure is clearly evident, for a $(B_2O_3)_{0.75}$-$(PbO)_{0.25}$ glass (Figure 1.21(a) from [64]) and a LiO_2-SiO_2 glass (Figure 1.21(b) from [65]).

Finally we remark that the 2LSs are consequences of the intrinsic and intracellular disorder, while the ATS exist only in glasses with ionic species, such as the BAS and other borosilicate (and glycerin contaminated with H_2O). E.g. interstices among the cells of the amorphous SiO_2 shown in Figure 1.20, are filled only with non-ionic particles (Si-O is a covalent bond) and therefore does not respond to the magnetic field (no ATS). It is the multiphase nature of real glasses and the better ordered regions in their microscopic structure that give rise to the unexplained composition and magnetic

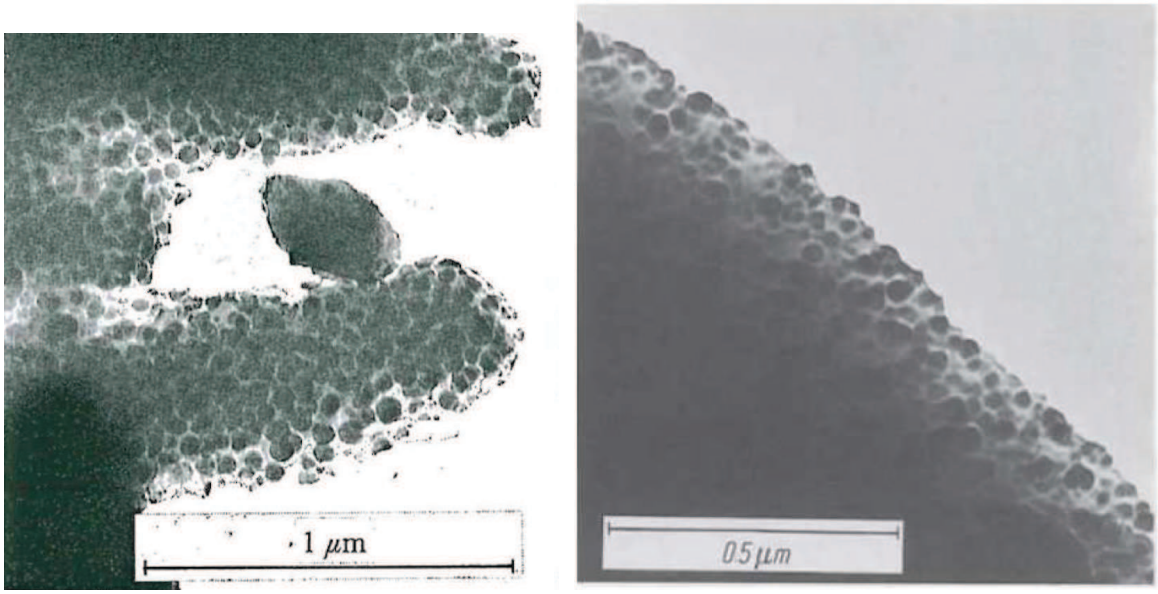

(a) (b)

Figure 1.21: Electron microscopy image of the cellular structure of a) $(B_2O_3)_{0.75}$-$(PbO)_{0.25}$ from [64], and b) LiO_2-SiO_2 from [65].

effects (section 1.2.2).

With this qualitative picture in mind, in the next Chapter we expose the mathematical description (the extended tunneling model), of our model of real glasses, capable to explain the above mentioned effects, not comprehensively explained by any other extensions of the STM. By construction the 2LS are more numerous than the new type of tunneling system, the ATS that give rise to the magnetic response.

Chapter 2

The Extended Tunneling Model

In the first Chapter of this Thesis it was mentioned how the thermal and dielectric universality of glasses at low temperatures ($T < 1\ K$) can be rather successfully described by the 2LS approach. However, numerous experimental deviations from the expected STM behavior (especially in the presence of a magnetic field in multicomponent glasses) were also presented and discussed. In the following we expose and detail a possible explanation of such phenomena through a suitable extension of the 2LS STM: the extended tunneling model, that was originally proposed in [13].

This model is based on the belief that glasses can be no longer considered as completely homogeneous disordered solids at the intermediate atomic length scales. As discussed in Section 1.3 there is indeed an increasing evidence, both through experimental and numerical investigations, that the structure of glassy solids is spatially heterogeneous with regions of enhanced atomic ordering (better ordered, the RERs) jammed against each other below T_g in an irregular closed-packed configuration and surrounded by still fluid particles in the interstices.

In favor of this statement we recall that the described composition dependent effects in the low temperature properties of mixed glasses have been found to be proportional to the concentration x of good crystal formers present in the sample under examination; no such unusual effects were indeed measured in the ultrapure SiO_2 and furthermore cannot be ascribed to spurious agents like paramagnetic impurities. The cellular picture has pointed out how the percolating cluster of RERs organizes within the homogeneous networked residual fluid background, giving rise to new, different tunneling potential morphology (with a tetrahedral configuration) where the ATSs are generated due to the collective tunneling of the good crystal forming ions in the interstices.

Recent studies demonstrated that the underlying concept that describes the phenomenology of glasses is the *potential energy landscape*, a function that depends on the spatial location of each particle of the system [66]. This is a useful paradigm that allows to relate an atomic configuration (consisting of $3N$ coordinates) to a state point $\vec{r}$ in the configuration space. The resulting multidimensional surface is characterized by stationary points at which the forces are zero: minima that correspond to mechanically stable arrangements of the particles in space, and saddle points which

are the transition states between minima. In this "topological" picture, the local minima or basins, correspond to metastable states that are sampled by the liquid phase above the melting temperature; the lowest global minimum correspond to the crystal phases (thus the thermodinamically stable state of the system). Figure 2.1 shows a highly schematic and speculative illustration of the PEL in a hardly realistic one dimensional (1D) representation.

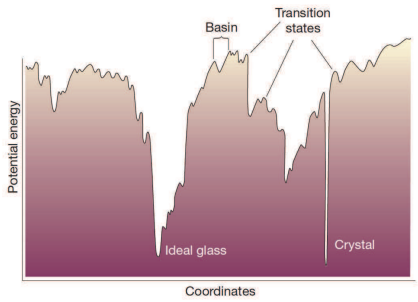

Figure 2.1: Schematic 1D representation of the potential energy landscape (from [3]); the horizontal axis represents all the configuration coordinates.

It has been stated in [67] that the 2LSs correspond to pairs of minima, i.e. DWPs of the PEL, with an energy asymmetry of max. 1 K. However, we will show in Chapter 6 by means of numerical investigations, that the important relation between the TSs and the PEL is much more complex. A more realistic description of the energy landscape should indeed identify more than two local wells, separated by shallow energy barriers. Within this approach, the density of states (DOS) and the related physical quantities have contributions from both the 2LSs and the additional ATSs. In particular, the latter in the PEL picture could be thought of as an effective representation of local displacements of the equilibrium position of some of the glass ions. Wells in the minima correspond to metastable configurations involving many NM atoms/ions, the jumps from one well to the next in a local multi-well potential corresponding to the rearrangement of many atomic groups. So long as their energy parameters obey the usual uniform distribution advocated by the STM, most of these n_w-well potentials (n_w is the number of the wells) present the very same physics as the n_w=2 case and thus in practice the n_w distribution cannot be resolved experimentally in a pure glass [68]. Therefore, in order to take into account some degree of devitrification the multi-well potentials should follow a new energy-parameters distribution that leads to a different physics.

This Chapter has therefore a twofold purpose: i) present the mathematical description that shows how the ETM provides a good explanation of the magnetic effects (basically through the motion of a fictitious charged particle in an effective TWP, as the simplest tetrahedral reduced potential, that couples to the magnetic field through the AB phase). ii) report previous results obtained within this theory for the different experimentally reported low temperature effects.

2.1 Theory in zero magnetic field

Instead of the standard 1D double-well (W-shaped) potential, which continues to describe the ordinary 2LS TSs inherent to the a-SiO_2 network, this model considers a fictitious particle of charge q moving in a n_w-well 3D potential of the type presented in figure 2.2 where n_w=3. The reduced Hamiltonian (well representation) for these local multi-well potentials can be written down as a generalization of eq. (1.9). For a TWP,

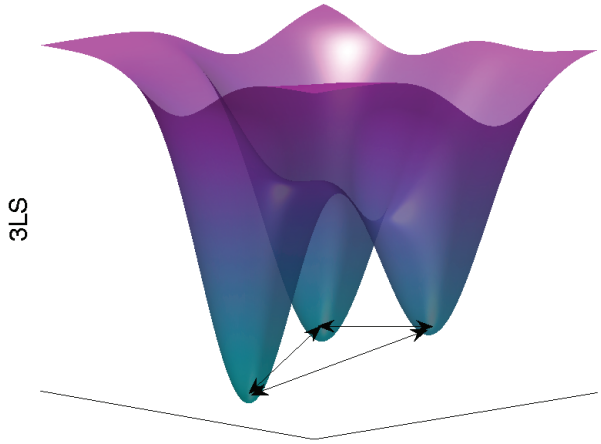

Figure 2.2: The particle moving in the 3WP.

thus n_w=3, it has the following form (when $B = 0$):

$$\mathcal{H}_{TWP}^{(B=0)} = \sum_{i=1}^{3} E_i C_i^{\dagger} C_i + D_0 \sum_{i,j=1}^{3} C_i^{\dagger} C_j \tag{2.1}$$

which can be visualized in the matrix representation as follows:

$$\mathcal{H}_{TWP}^{(B=0)} = \begin{pmatrix} E_1 & D_0 & D_0 \\ D_0 & E_2 & D_0 \\ D_0 & D_0 & E_3 \end{pmatrix} \tag{2.2}$$

where E_1, E_2, E_3 are the energy asymmetries between the wells (we have chosen a simplified potential, having three of the four possible tetrahedral wells) and D_0 is the most relevant tunneling amplitude (through saddles of the PEL, in fact). Here $D_0 > 0$ is the tunneling parameter, E_1, E_2, E_3 are random energy asymmetries between the wells chosen to satisfy $\sum_{i=1}^{3} E_i = 0$ and taken from a different distribution function which will be discussed later. The final and most important consideration is that the TSs appear to be rather diluted defects in the glass (indeed their concentration is of the order of magnitude of that for trace paramagnetic impurities, as we shall see), hence the tunneling "particles" are embedded in a medium otherwise characterized only by simple acoustic-phonon degrees of freedom (and 2LSs). This embedding, however, means that the rest of the material takes a part in the making of the tunneling potential for the ATS particle, which itself is not moving quantum-mechanically in a vacuum. Sussmann [69] has shown that this situation leads to local trapping potentials that (for the case of triangular and tetrahedral perfect symmetry) must be characterized by a degenerate ground state. This means that, as a consequence of this ATS embedding, our minimal model (2.16) must be chosen with a positive tunneling parameter [13]:

$$D_0 > 0 \tag{2.3}$$

where of course perfect degeneracy is always removed by weak disorder in the asymmetries.

As in the case of the standard 2LS STM, the tunneling parameter of the ATS is linked to the characteristic potential parameters through eq. (1.12). In the case of a square four-well potential (4LS): n_w=4, arranged on the vertices of a square, the Hamiltonian has the form (for $B = 0$):

$$\mathcal{H}_{4LS}^{(B=0)} = \begin{pmatrix} E_1 & D_1 & D_2 & D_1 \\ D_1 & E_2 & D_1 & D_2 \\ D_2 & D_1 & E_3 & D_1 \\ D_1 & D_2 & D_1 & E_4 \end{pmatrix} \tag{2.4}$$

where E_1, E_2, E_3, E_4 are random energy asymmetries and D_1 is the n.n. well hopping and D_2 n.n.n. hopping tunneling parameter ($|D_2| \ll |D_1|$). These are simple, possible choices [68]; other suitable generalizations of the 2LS matrix Hamiltonian are possible as the case of the four wells tetrahedral potential that we present in Appendix A.

As long as the energy parameters of the above multi-well effective Hamiltonians obey the usual uniform distribution (advocated by the STM as a realization of the Zachariasen-Warren description of glassy atomic structure), the DOS will remain a constant and then all these multi-well local potentials will give rise to the very same physics as in the n_w=2 case. In practice, the 2LS choice represents the appropriate minimal model for all of the extra low-energy excitation characterizing amorphous solids at low temperature.

The choice for the probability distribution of the parameters E_1, E_2, E_3 of the TWPs nesting in the proximity of a group of four RERs is dictated by the fact that near degeneracy ($E_1 = E_2 = E_3$) must be favored, yet not fully attained for the wells energy asymmetries. Assuming again the tunneling potential barriers to be broadly distributed, the new parameter distribution has the form:

$$P_{ATS}(E_i, D_0) = \frac{P^*}{(E_1^2 + E_2^2 + E_3^2) D_0} \tag{2.5}$$

where P^* is now a dimensionless material-dependent parameter.

Therefore for the Hamiltonian of eq. (2.2) it is still possible to calculate the three low-lying states:

$$\mathcal{E}_k = 2D_0 \sqrt{1 - \frac{\sum_{i \neq j} E_i E_j}{6D_0^2}} \cos\left(\frac{1}{3}\theta + \theta_k\right)\Bigg) \tag{2.6}$$

where

$$\cos\theta = \frac{E_1 E_2 E_3}{2D_0^3} \left(1 - \frac{\sum_{i \neq j} E_i E_j}{6D_0^2}\right)^{-\frac{3}{2}} \tag{2.7}$$

with k=0,1,2 and θ_k=+$\frac{2\pi}{3}$,-$\frac{2\pi}{3}$,0. In particular one finds that the relation among the three eigenvalues is $\mathcal{E}_0 < \mathcal{E}_1 \ll \mathcal{E}_2$, thus we can reduce the three level system to an *effective* two level state which has energy gap equal to

$$\Delta\mathcal{E} = |\mathcal{E}_1 - \mathcal{E}_0| \simeq D \tag{2.8}$$

by considering the $E_i \to 0$ limits and for the near degenerate situation $D \equiv \sqrt{E_1^2+E_2^2+E_3^2} \ll D_0$. In this way we can determine the *reduced* DOS:

$$g_{ATS}(E) = \int_{D_{0min}}^{\infty} \mathrm{d}D_0 \int_{-\infty}^{+\infty} \mathrm{d}E_1 \mathrm{d}E_2 \mathrm{d}E_3 P_{ATS}(E_1,E_2,E_3;D_0)\delta(E_1+E_2+E_3)\delta(E-\Delta\mathcal{E}) \tag{2.9}$$

The integration is now carried out with a change of variables which respects the condition $E_1+E_2+E_3=0$; we thus use the polar coordinates, expressing the old ones as a function of an angle Ψ and a distance $r=\frac{D}{D_0}$:

$$\begin{cases} E_1 = D\left(-\dfrac{1}{\sqrt{2}}\cos\Psi + \dfrac{1}{\sqrt{6}}\sin\Psi\right) \\ E_2 = D\left(-\dfrac{2}{\sqrt{6}}\sin\Psi\right) \\ E_3 = D\left(+\dfrac{1}{\sqrt{2}}\cos\Psi + \dfrac{1}{\sqrt{6}}\sin\Psi\right) \end{cases} \tag{2.10}$$

thus the DOS reduces to:

$$g_{ATS}(E) \simeq \int_0^{2\pi} \mathrm{d}\Psi \int_{D_{min}}^{\infty} \mathrm{d}D D \int_{D_{0min}}^{\infty} \mathrm{d}D_0 \frac{P^*}{D_0 D^2}\delta(E-\Delta\mathcal{E}) \tag{2.11}$$

Since the integrand does not depend on Ψ (due to symmetry), the first integral is equal to 2π. Then, recalling Eq. 2.8, one can perform the integration in D if $E > D_{min}$; therefore we have

$$g_{ATS}(E) \simeq \frac{2\pi P^*}{E}\int_{D_{0min}}^{\infty} \mathrm{d}D_0 \frac{1}{D_0} \tag{2.12}$$

We introduce an upper cutoff limit D_{0max} to the integral in order to remove the logarithmic divergence at $D_0 = \infty$ which which has no physical meaning. We can thus write:

$$g_{ATS} \simeq \begin{cases} 0 & \text{if } E < D_{min} \\ \frac{2\pi P^*}{E}\ln\frac{D_{0max}}{D_{0min}} & \text{if } E < D_{min} \end{cases} \tag{2.13}$$

where D_{min} is the lower cutoff. The main difference with the standard model is that here the DOS for the ATS is no longer a constant and this embodies the change from a Zachariasen-Warren description of glassy atomic structure to a Lebedev-Wright-Bakai approach.

2.2 Theory in the presence of a magnetic field

In this Section we present the derivation of the equations to describe the magnetic effects with the ETM model; we remark that currently this is the only approach able to reproduce theoretical curves matching the experimental data. We therefore believe this is the correct theoretical explanation for the observed magnetic field and composition dependent in multicomponent glasses. The magnetic field is introduced via the

AB effect; in particular the "effective" tunneling particle of charge q couples to the magnetic field B when tracing a loop among the wells. The presence of more than two potential wells is not the only way to allow the AB mechanism [42], however we have verified that the presence of more than two wells can afford a complete and consistent description of the experiments unexplained by the STM [70].

Therefore we can modify the Hamiltonian of Eq. 2.2 in this way:

$$\mathcal{H}_{TWP}^{B>0} = \sum_{i=1}^{3} E_i C_i^\dagger C_i + D_0 \sum_{i,j=1}^{3} \exp(i\varphi_{ij}) C_i^\dagger C_j + \text{h.c.} \tag{2.14}$$

where $\varphi/3$ is the Peierls phase for the tunneling particle through a saddle, and φ is the AB phase for a tunneling loop, which is given by the usual formula:

$$\varphi = 2\pi \frac{\Phi}{\Phi_0}, \qquad \Phi_0 = \frac{h}{|q|} \tag{2.15}$$

Φ_0 being the magnetic flux quantum (h is Planck's constant) and $\Phi = \vec{B} \cdot \vec{S_\triangle}$ the magnetic flux threading the area $\vec{S_\triangle}$ formed by the three tunneling paths. In the matrix representation the Hamiltonian for $B > 0$ can be written as follows:

$$\mathcal{H}_{TWP}^{(B>0)} = \begin{pmatrix} E_1 & D_0 e^{i\varphi/3} & D_0 e^{-i\varphi/3} \\ D_0 e^{-i\varphi/3} & E_2 & D_0 e^{i\varphi/3} \\ D_0 e^{i\varphi/3} & D_0 e^{-i\varphi/3} & E_3 \end{pmatrix} \tag{2.16}$$

In this case it is still possible to find the exact solutions for the eigenvalues (using the solution for cubic equations):

$$\mathcal{E}_k = 2D_0 \sqrt{1 - \frac{\sum_{i \neq j} E_i E_j}{6D_0^2}} \cos\left(\frac{1}{3}\theta + \theta_k\right) \tag{2.17}$$

where

$$\cos\theta = \left(\cos\varphi + \frac{E_1 E_2 E_3}{2D_0^3}\right) \left(1 - \frac{\sum_{i \neq j} E_i E_j}{6D_0^2}\right)^{-\frac{3}{2}} \tag{2.18}$$

but this time we can trace them as a function of φ (or B), as shown in Figure 2.3. In the limit $\varphi \to 0$ since $\mathcal{E}_0 < \mathcal{E}_1 \ll \mathcal{E}_2$, we can therefore consider again the TWP like an effective 2LS model, but this time the energy gap $\Delta\mathcal{E}$ depends on the magnetic field through the phase $\varphi(B)$, that can be derived in a similar way to the case of $B = 0$:

$$\Delta\mathcal{E} \simeq \sqrt{D_0^2 \varphi^2 + D^2} + \mathcal{O}\left(\frac{E_1 E_2 E_3}{D^2}\right) \tag{2.19}$$

We can therefore derive the DOS using the appropriate energy gap (Eq. 2.8):

$$g_{ATS}(E, \varphi) \simeq 2\pi \int_{D_{min}}^{\infty} \mathrm{d}D D \int_{-\infty}^{+\infty} \mathrm{d}D_0 \frac{P^*}{D_0 D^2} \delta\left(E - \sqrt{D_0^2 \varphi^2 + D^2}\right) \tag{2.20}$$

by introducing a change of variable ($D_0 \to D_0\varphi$), using the following relation:

$$\delta(f(x)) = \sum_a \frac{\delta(f - f_a)}{|f'(D_a)|} \tag{2.21}$$

where x_a are the zeroes of $f(x)$ (in this case $x = D$) to resolve the integral in D. We find

$$\begin{aligned} g_{ATS}(E,\varphi) \simeq 2\pi P^* \int_{-\infty}^{+\infty} \mathrm{d}D_0 \frac{1}{D_0} \frac{E}{\sqrt{E^2 - D_0^2\varphi^2}} \theta(D_0 - D_{0min}) \\ \times \theta(D_{0min} - D_0)\theta\left(\frac{1}{\varphi}\sqrt{E^2 - D_{min}^2} - D_0\right) \end{aligned} \tag{2.22}$$

To resolve this integral we have to consider three different intervals for E, which are delimited by $E_{c1} = \sqrt{D_{min}^2 + D_{0min}^2\varphi^2}$ and $E_{c2} = \sqrt{D_{min}^2 + D_{0max}^2\varphi^2}$. Therefore we have that:

$$g_{ATS}(E,\varphi) = \begin{cases} 0 & \text{if } E < E_{c1} \\ \frac{2\pi P^*}{E} \ln\left(\frac{\sqrt{(E^2 - D_{0min}^2\varphi^2)(E^2 - D_{min}^2)}}{D_{0min} D_{min}\varphi}\right) & \text{if } E_{c1} \le E \le E_{c2} \\ \frac{2\pi P^*}{E} \ln\left(\frac{D_{0max}}{D_{0min}} \frac{E^2 - D_{0min}^2\varphi^2}{E^2 - D_{0max}^2\varphi^2}\right) & \text{if } E < E_{c2} \end{cases} \tag{2.23}$$

Figure 2.4 presents the behavior of the DOS as a function of the energy E (for different values of φ, Figure 2.4(a)) and the phase φ (varying the energy, Figure 2.4(b)). In the first plot we see that the shape of the DOS at $B = 0$ is recovered; then increasing the magnetic field the peak vanishes and decreases according to a rapid shift of the states to a broader region at higher energies (Figure 2.5). In particular, we find that it is precisely the characteristic shape of the DOS (through its convolution) that influences

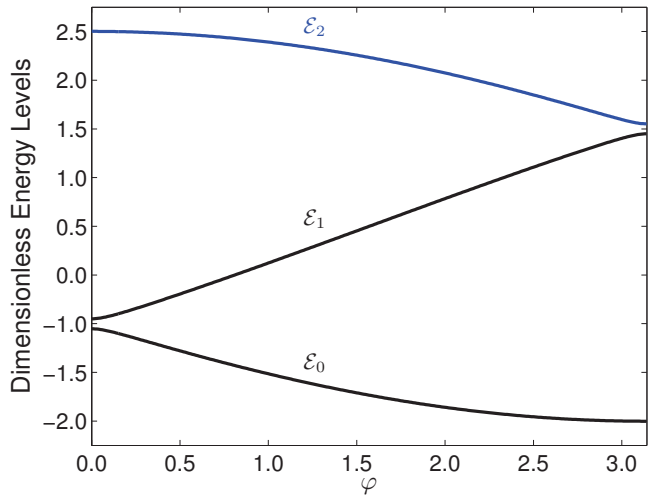

Figure 2.3: The energy spectrum ($D_0 = 1$ units) of the TWP ETM, in the limits of weak magnetic field and nearly degeneracy due to the embedding within the RER interstitials. On the horizontal axis the AB phase $\varphi \propto B$ is shown.

all of the observed anomalies at low temperature in the presence of a magnetic field. In the next Section we will indeed remark how the above mentioned experiments always reproduce the qualitative behavior of the DOS as a function of B.

A final remark of this Section regards the low field approximation of the energy gap $\Delta\mathcal{E} = |\mathcal{E}_1 - \mathcal{E}_0|$ that we have considered in this effective TWP model given by Eq. 2.19 in the limit $\varphi \to 0$. If we follow the gap as a function of the AB phase, for higher magnetic fields ($\varphi \leq 1$) we find that the curve starts to deviate from the linear behavior used in our description. Therefore this means that we have to use higher order corrections when considering higher magnetic fields. If we compute the next order expansion (referring again to the eigenvalue of Eq. 2.17) in φ we find the following dependence [70]:

$$\Delta\mathcal{E} = \sqrt{D_0^2\varphi^2 - \frac{1}{27}D_0^2\varphi^4 + D^2} \tag{2.24}$$

The most straightforward solution is to make the following replacement for the AB phase:

$$\varphi^2 \to \varphi^2\left(1 - \frac{1}{27}\varphi^2\right) \to \frac{1}{3}\varphi^2\left[1 - \frac{1}{45}\left(\frac{B}{B^*}\right)^2\right] \tag{2.25}$$

where the second relation follows from the orientation averaging $\overline{\cos^2\beta}=\frac{1}{3}$ and $B^* = \frac{\varphi_0}{\frac{q}{e}S_\triangle}$ represent the value at which the magnetic field dependence of the dielectric constant changes its curvature, and therefore also the energy gap, according to the experimental data. This approximation has been implemented to analyze the magnetic

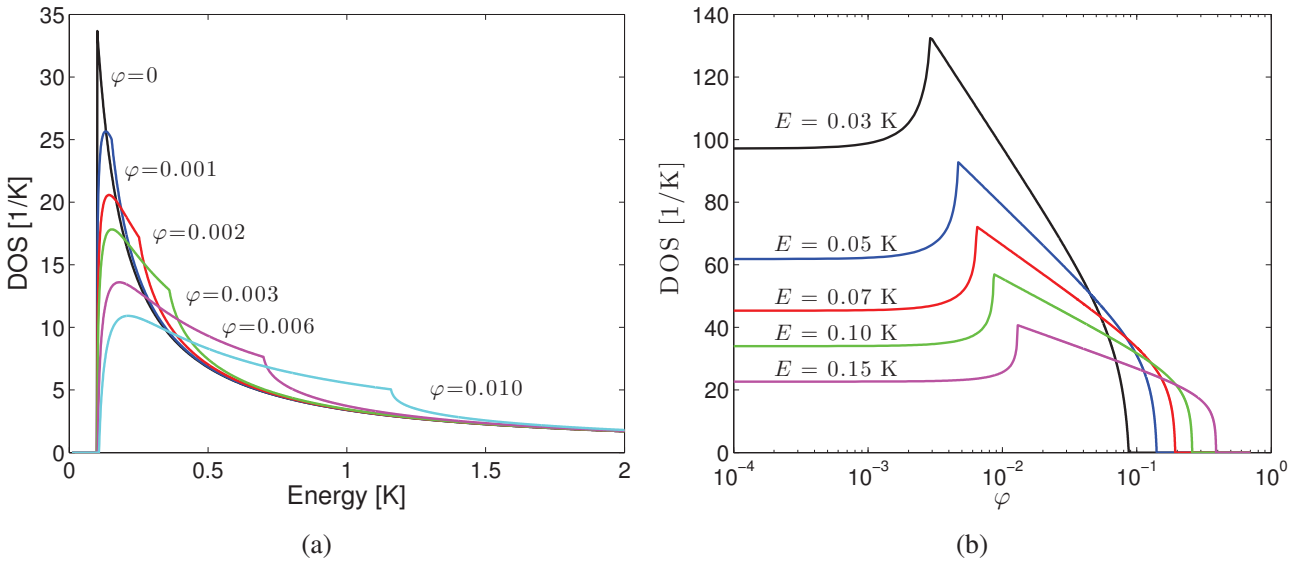

Figure 2.4: Variation of the DOS with: a) the energy gap E and different AB phases φ (which are proportional to B); b) φ for different energies. The shape of this part of the DOS (coming from the TWP with a parameter distribution (Eq. 2.5) favoring near-degeneracy) is thought to be the source of the magnetic effects. In both Figures $n_{ATS}P^*$=1 has been considered.

field dependence of just one set of dieletric constant data to understand the behavior at higher values of B and for the magnetization, as we will discuss in the following Chapters.

We remark that the incipient "crystallinity" of the RERs calls for near-degeneracy in E_1, E_2, E_3 simultaneously and not in a single one of them, hence the correlated form of Eq. 2.5. Other descriptions, with four-well potentials or modified 3D DWPs are possible for the TSs nested in the RERs and lead to the same physics as Eqs. (2.16) and (2.5) above (which describe the anomalous tunneling systems, or ATSs, nesting within the RERs).

2.3 Previously-obtained results from the ETM for T<4K

In this Section we show how with a single theoretical approach, the ETM (that can be considered as an extension of the STM based on the existence of the RERs in the otherwise homogeneously-disordered glassy network), allows for a complete explanation of the recent experiments on the physical properties of glasses at low temperatures, in the presence, but also in the absence, of a magnetic field. Here we briefly present the previous results obtained with the ETM model, where the application of standard quantum statistical mechanics and solid state theory (with the approximations for weak magnetic fields, thus $\varphi \ll 1$, and near-degeneracy, $\frac{D}{D_0} \ll 1$ which treat the ATS as an effective 2LS), yields theoretical curves in rather good agreement with

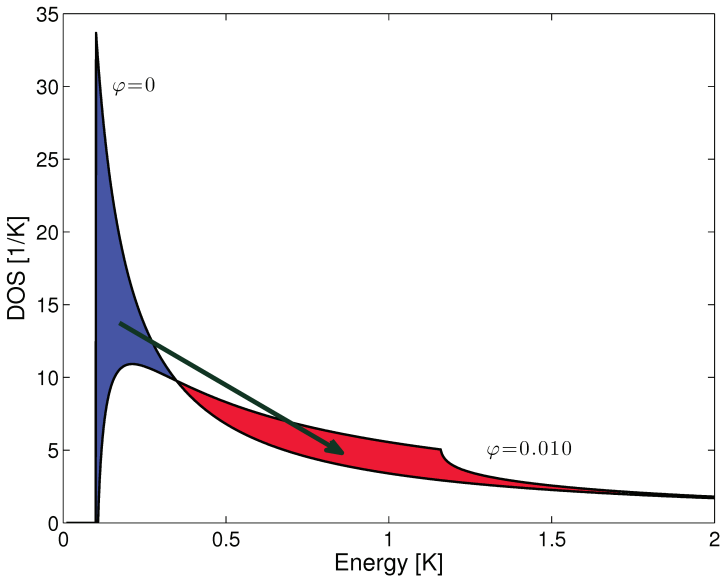

Figure 2.5: Shape of the DOS as a function of E for two different values of φ; the area under each curve represent the total number of states available (per ATS). When increasing B the states in the blue region (B=0, within a narrow energy range near the lower cutoff D_{min}) shift towards a spread band of higher energies (red region). This effect is at the origin of the magnetic field response.

the experimental measurements; the details of the theoretical calculations of the ETM leading to the explanation of the the composition-dependent anomalies are presented in [68, 71]; the derivation of the real and imaginary parts of the dielectric constant and the polarization echo amplitude for various multicomponent glasses are reported in [72]; finally a complete review can be found in [59].

2.3.1 Heat capacity

We start to look at the very first results obtained with the ETM for the heat capacity [73], that is basically given by the sum of the 2LS and the ATS contribution; as we will see from the theoretical calculations presented in the next Chapter, this latter is obtained by determining the second derivative of the free energy with respect to temperature T, neglecting the third highest energy level $\mathcal{E}_2$ (thus using the effective 2LS representation), and averaging over the parameter distribution. The fit of the experimental data for the specific heat for the $(SiO_2)_{1-x}(K_2O)_x$ glasses of Figure 1.13, thus in absence of the magnetic field, is presented in Figure 2.6(a) [70]. The fit of Stephen's data for the Pirex 9700 glass are instead reported in Figure 2.6(b) [73]; note that here the fit has been performed also for an applied magnetic field. This is a clear indication that this model provides a reasonable explanation for different phenomena using a single description.

2.3.2 Dielectric constant

For what concerns the dielectric properties of glasses at low temperature, the typical experimental measurement consists in the application of an external AC electric field (usually at radio frequencies) to the sample. The 2LS couple to such field through the electric charge or dipole moment, causing a resonant processes like absorption and emission. The dielectric constant ε usually is written as the sum of the real ε' and imaginary ε'' part, in particular this latter is also described as the dielectric loss (or loss angle $\delta = \frac{\varepsilon''}{\varepsilon'}$) which measures the dissipation of electromagnetic energy.

The real part of ε, given by the sum of the resonant and relaxation contributions, has a characteristic V-shaped form, where a minimum occurs at the temperature $T_0(\omega)$ (ω is the frequency of the electric field that is around 10^3 Hz). The STM predicts a -2:1 characteristic behavior in a semi-logarithmic plot, which actually is observed, but only in very pure *a*-SiO_2 [74]. As we have already pointed out, many multi-component glasses, like e.g. the BAS glass, have rather an almost -1:1 slope ratio, which can be explained by the ETM [71], by considering the contributions from the ATS located in the interstices among the RER. Once again, we can apply the *effective* 2LS description for weak fields considering only the lowest energy gap and extract the contributions to the polarizability tensor in agreement with the 2LS protocol.

Figures 2.7(a) and 2.7(b) report the data from Ref [75] for the real and imaginary part of the dielectric constant for different multi-silicate glasses as a function of T and B; the curves are the results of the theoretical calculations [70]. Figure 2.8 instead

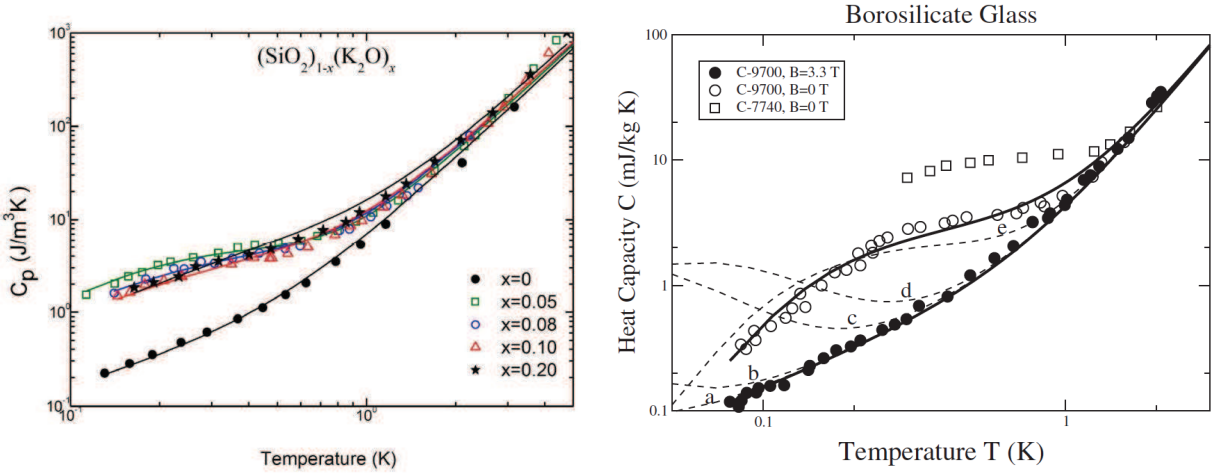

(a) (b)

Figure 2.6: a) The temperature dependence of the specific heat for a-SiO_2 (black circles) and for the $(SiO_2)_{1-x}(K_2O)_x$ glass. The lines are the theoretical curves obtained with the ETM. These data are those presented in Figure 1.13, here we plot C_p as a function of T. b) Fit of the heat capacity data of figure 1.14(b); the Corning 7740 data are represented with squares while the Pirex 9700 with empty (B=0 T) and filled (B=3.3 T) circles. The lower full line curve is fitted with the expected law for the amorphous solids. The dashed curves are the result of the heat capacity contribution of the measured concentration of paramagnetic Fe-impurities. The agreement with the data for the Pirex 9700 glass at (nominally) B=0 T is impossible for effective residual field values of B=5 mT (curve (a)), 10 mT (curve(b)), 50 mT (curve (c)) and (100 mT) (curve (d)). The agreement with the data of Pirex 9700 is achieved only for an unrealistic strong environmental field value of B=500 mT (curve(e)). The upper full line curve results from the ATS theory [13].

presents the fit of the relative dielectric loss variation; one can again see that the experimental data are very well reproduced by the ETM theory. The best-fit parameters, reported in [70], have been found to be very similar to those extracted from the study of the (real part of the) dielectric constant.

2.3.3 Polarization echo

Finally we discuss the results obtained for the electric polarization echo in glasses, which is considered a strong convincing proof of the existence of the TSs. The mechanism of the echo phenomenon in glasses is similar to that of other types of echo, like the spin echo, photon echo, etc. To measure the echo effect, a glass sample, located in a resonating cavity, is subjected to to two AC pulses at the frequency of about 1 GHz after a time interval τ_{12}. The duration of the two pulses, respectively τ_1 and τ_2, is much shorter that all relaxation processes in the system. Like in the nuclear magnetic resonance (NMR) experiments, the polarization produced by the first pulse vanishes rapidly. Then the "phase" (that represents the energy-level populations) of each TS develops till to the second pulse, that causes an effective time reversal for the

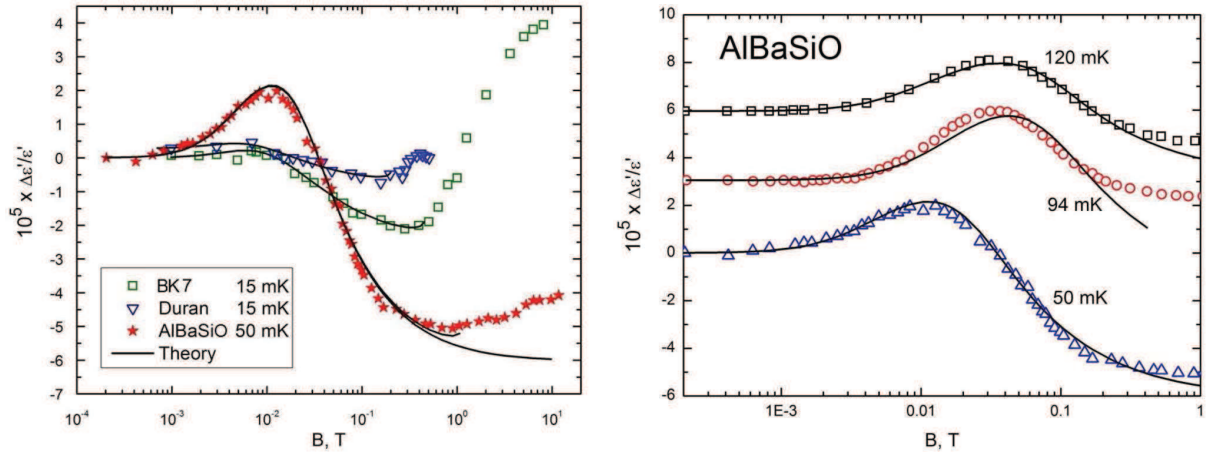

(a) (b)

Figure 2.7: Data from [76]. a) Relative dielectric constant as a function of B for the BAS glass, BK7 and Duran. b) Relative dielectric constant as a function of B and T for the BAS glass [76]. The curves are the result of the ETM theory in the "weak field" approximation (from [70]).

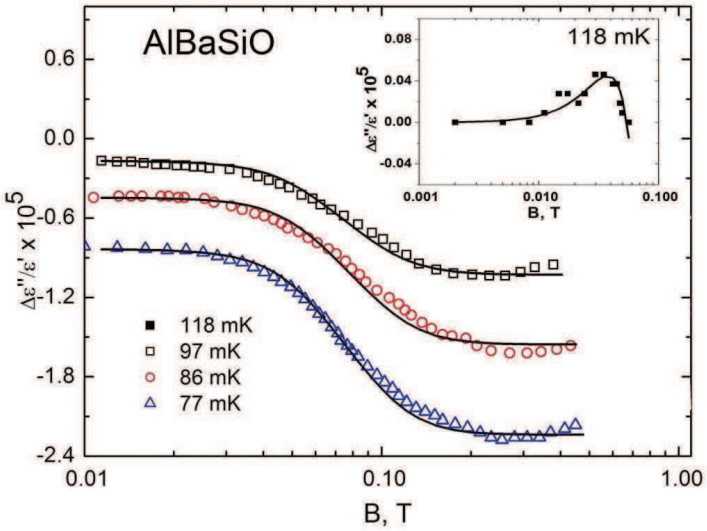

Figure 2.8: Fit of the relative dielectric loss as a function of of B and T for the a) BAS and b) BK7 glasses (from [70]).

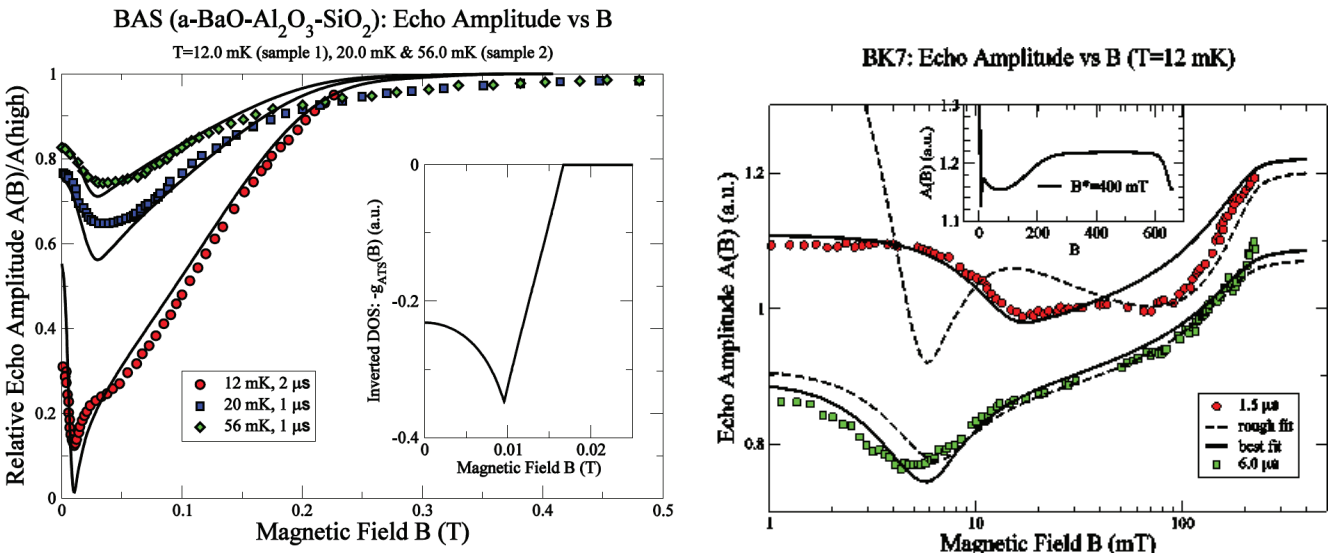

(a) (b)

Figure 2.9: a) B dependence of the echo amplitude (relative to its value at "high" fields where the saturation occurs) for the BAS glass [39]. The fits are obtained from the ETS theory [72]. The inset presents the behavior of the ATS DOS using the same parameters. b) B dependence of the echo amplitude for the BK7 glass [39]. The dashed curves (rough fit) and solid curves are derived from the theory; note that there are no more than two observable maxima or minima (no oscillations). The inset shows the prediction of the theory for higher B field.

development of the phase. The initial macroscopic polarization of the glass is finally recovered at a time τ_{12} after the second pulse.

In Figure 2.9(a) we report data for the echo amplitude of two separate samples of BAS glass as a function of the magnetic field [39], for different temperatures. The theoretical curves are the result of the ETM theory; again we can see that there is a good agreement with the experimental data, that show a minimum, followed by a linear dependence on the magnetic field and a saturating behavior (B^{-2} power law).

In Figure 2.9(b) we report data from [39], for the echo amplitude as a function of B for the multi-silicate glass BK7 at different nominal driving frequencies in the 1 GHz range. The solid curves represent the result of the fit obtained from the calculation of the theory; again, the experimental behavior is well reproduced with increasing B.

In one case the data present a double minimum (oscillations of A(B) are very rare, at most two minima are observed) and this can also be reproduced by the theory. Note that the echo amplitude seems to be rather independent of the driving frequency, and this is due to the fact that the loaded microwave re-entrant cavity used in the experiments resonates at a frequency that is set by the reacting dielectric itself [59].

Chapter 3

New results for the magnetization in non magnetic glasses

In the previous Chapters we have mentioned that the application of the ETM model, with its new form for the density of states, allows to obtain a good theoretical description of the temperature T and magnetic field B dependence for the specific heat, dielectric constant (real and imaginary part) in the linear regime, and polarization echo (linear and non-linear regime), for several non magnetic glassy systems. In this Chapter we apply the model to the available magnetization $M(T,B)$ data for some multicomponent glasses, providing a theoretical explanation for its behavior in a moderate to strong B-field values and as a function of T. The aim of this analysis is to show that the description provided by the ETM model is valid also to correctly describe this quantity, and as we will see, up to higher temperatures (to about room temperatures, 300 K). Furthermore, since a by-product of the (weak) magnetization measurements, usually preformed through SQUID magnetometry, is the paramagnetic contaminant concentration, we also determine correctly their magnitude, in the atomic ppm region. This study represents a relevant contribution to the physics of disordered solids at low and intermediate temperatures since one of the proposed explanations for the unexpected magnetic effects is indeed the presence of paramagnetic impurities. The presence of a magnetic effect in the Pyrex glass, reported long ago by Stephens [35], was e.g. entirely attributed to paramagnetic iron impurities even though the maximum effect was for $B \simeq 0$. In our opinion, the fact that the strength of the magnetic response does not scale with the concentration of the paramagnetic contaminants, excludes the possibility that they play a major role in causing such magnetic effects. However, to eventually find further confirmation of this statement, a precise determination of the impurity concentration is paramount. Traces of paramagnetic impurities, typically Fe^{2+} and Fe^{3+}, are always present in multicomponent silicate glasses, due to the fabrication process (ball-milling of chemical components etc.); their presence gives rise to nearly-ideal Langevin paramagnetism that can be exploited e.g. in the low-temperature thermometry, as suggested in [77]. We therefore intend to investigate the issue of the determination via SQUID magnetization of the concentration n_J of paramagnetic impurities [77], also in view of the fact that earlier theoretical analy-

sis [13] of the magnetic effect [41, 35] in the heat capacity C_p of some multi-silicate glasses produced values of n_J systematically much lower than those quoted in the literature [77, 41, 78, 37] (and obtained from SQUID measurements).

Exploiting the fact that for the same materials, besides the data of the specific heat, we also dispose of those for the magnetization, with the help of the model, we can now perform a cross-check of the predictions of the ETM by comparing the model parameters and concentrations obtained from the best fits of the two different types of measurements. Before introducing the new derivation of the contribution to the ATS magnetization, we present a simple procedure that allows us to evaluate only the magnetic field contribution to the specific heat (Section 3.1) and to extract the parameters of the model, including the impurities and ATS concentrations, which are relevant for our analysis. Preliminary studies on such specific heat data in the range 0.6 to 1.3 K [41] were carried out in [13]; we now intend to improve our fits in view of the latest results given by the model. In Section 3.2 we derive the contribution from the TSs in our model to the magnetization $M(T,B)$ and analyze the available data in the range 4 to 300 K [77, 41, 78] with our formula added to Langevin's contribution from the dilute paramagnetic impurities. Finally, the extracted parameters from the fits of both quantities, C_p and M, are compared and discussed in Section 3.3.

3.1 Procedure to evaluate the magnetic contribution from heat capacity data

In this Section we re-analyze the Siebert's data [41] for the magnetic effect in the heat capacity for the Duran and BAS glasses, to better estimate the concentration of Iron impurities initially for this type of measurement. The first study of the specific heat data [41] with the ETM model was performed in [13] by using a fit function given by the sum of the following four terms: the Einstein's $\gamma_{ph}T^3$ phonon and the 2LS $\gamma_{2LS}T$ non-magnetic contributions, the Langevin's paramagnetic and the ATS contributions (reported in the following). The analysis came up with concentrations $\bar{n}_J \simeq$48 ppm and, respectively, $\bar{n}_J \simeq 20$ ppm instead of the quoted [41] 126 ppm (or 180 ppm in a different study [77]) and 102 ppm for Duran and for BAS glass, respectively.

In order to better understand this large discrepancy, we implement here a new procedure to re-analyze the data for $C_p(T,B)$: we determine the single magnetic-field dependent contribution to the heat capacity, by subtracting from the data taken at the same temperatures for the same glass, the contribution given by the strongest applied magnetic field, 8 T: $\bar{C}_p(T,B) \equiv C_p(T,B) - C_p(T,\infty)$.

Fig. 3.1 presents the result of such procedure: the data of $\bar{C}_p(T,B)$, after the subtraction of the magnetic field independent data at B=8 T for the BAS glass (Fig. 3.1(a)) and for Duran (Fig. 3.1(b)).

By applying this procedure, the set of parameter to be extracted from the fit significantly reduce from the analysis in [13] and therefore we are able to get more accurate results. We apply the fit procedure to the data presented in Figure 3.1, respectively for

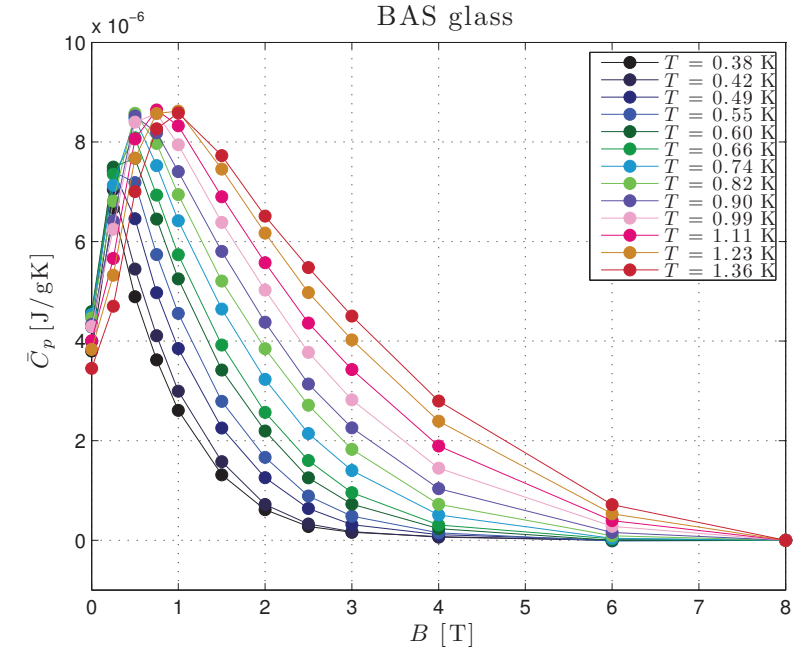

(a)

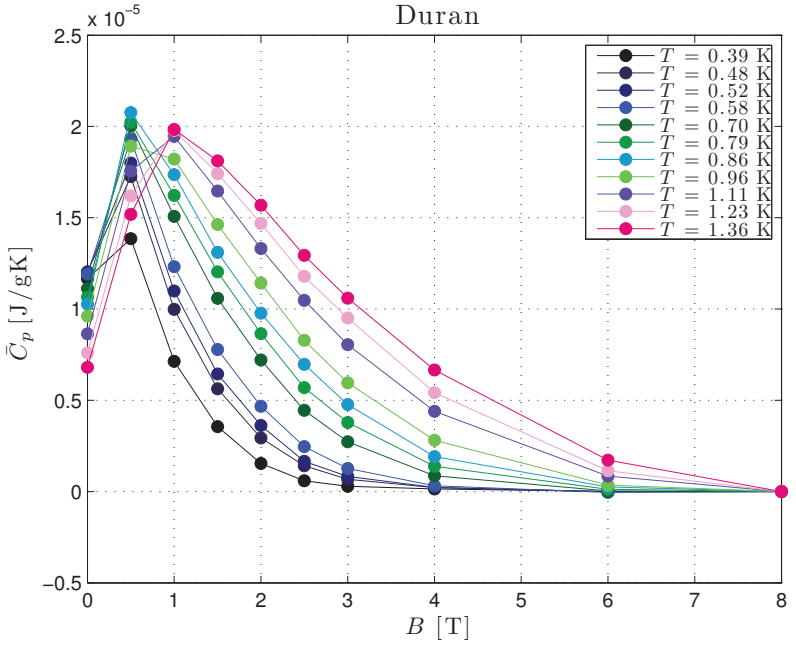

(b)

Figure 3.1: The heat capacity data $\bar{C}_p = C_p - C_p$ (8 T) as a function of the magnetic field B for different temperatures: a) for the BAS and b) Duran glasses. Data from [41] (also reproduced, upon permission, in [13]).

the BAS and Duran glasses, for the three temperatures that have the most data points around the peak of $C_p(B)$. The best fits have been obtained by using only the following magnetic dependent contributions:

1. the known Langevin contribution of the paramagnetic Fe impurities (Fe^{2+} and Fe^{3+}) having concentration n_J (J being the total angular momentum of the paramagnetic ion) :

$$C_J(T,B) = n_J \frac{k_B z^2}{4}\left(\left(\frac{1}{\sinh\frac{z}{2}}\right)^2 - \left(\frac{2J+1}{\sinh\frac{(2J+1)z}{2}}\right)^2\right) \tag{3.1}$$

where $z = \frac{g\mu_B JB}{k_B T}$ and g is Landè's factor for the paramagnetic ion in that medium, μ_B is Bohr's magneton and J the total angular momentum of the ion (in units $\hbar$=1); k_B is Boltzmann's constant. We have assumed the same values the parameters g and J take for Fe^{2+} and Fe^{3+} in crystalline SiO_2: J=2 with g=2 and, respectively, $J = 5/2$ with g=2 (we have adopted, in other words, complete quenching of the orbital angular momentum [79], consistent with other Authors' analyses [41, 78]).

2. the averaged contribution of the ATSs [13], written in terms of a sum of individual contributions from each ATS of lowest energy gap E

$$\begin{aligned} C_{ATS}(T,\varphi) &= \frac{\pi}{4}\frac{P^*\, n_{ATS}}{k_B T^2} \\ &\times\Big\{\int_{E_{c1}}^{E_{c2}} dE\ \frac{E}{\cosh^2(\frac{E}{2k_BT})}\ \ln\Big[\frac{(E^2 - D_{0min}^2\varphi^2)(E^2 - D_{min}^2)}{D_{min}^2 D_{0min}^2\varphi^2}\Big] \\ &+ \int_{E_{c2}}^{\infty} dE\ \frac{E}{\cosh^2(\frac{E}{2k_BT})}\ \ln\Big[(\frac{D_{0max}}{D_{0min}})^2\frac{E^2 - D_{0min}^2\varphi^2}{E^2 - D_{0max}^2\varphi^2}\Big]\Big\} \end{aligned} \tag{3.2}$$

or, re-written in a dimensionless form as

$$\begin{aligned} C_{ATS}(T,\varphi) &= \widetilde{C}_0(T,\varphi) + 2\pi P^* n_{ATS} k_B\Big\{\big[I(x_{c1}) - I(x_{c2})\big]\ln(x_{min}x_{0min}\varphi) \\ &+ \frac{1}{2}\big[\mathcal{I}(x_{c1},x_{min}) - \mathcal{I}(x_{c2},x_{min}) + \mathcal{I}(x_{c1},x_{0min}\varphi) - \mathcal{I}(x_{c2},x_{0max}\varphi)\big]\Big\} \end{aligned} \tag{3.3}$$

where:

- $E_{c1} = \sqrt{D_{min}^2 + D_{0min}^2\varphi^2}$ and $E_{c2} = \sqrt{D_{min}^2 + D_{0max}^2\varphi^2}$;
- $x_{c1,2} = \frac{E_{c1,2}}{2k_BT}$, $x_{min} = \frac{D_{min}}{2k_BT}$, etc.;
- $I(x) \equiv x\tanh x - \ln\cosh x$;
- $\mathcal{I}(x,a) \equiv \int_x^\infty \mathrm{d}y \frac{y}{\cosh^2 y}\ln\big(y^2 - a^2\big)$.

and with the following expression (which for $\varphi = 0$ represents the expression for the heat capacity in the absence of a magnetic field):

$$\widetilde{C}_0(T,\varphi) = 2\pi P^* n_{ATS} k_B \ln\left(\frac{D_{0max}}{D_{0min}}\right)\{\ln(2) - I(x_{c2}).\} \tag{3.4}$$

The angular average over the ATS orientations is performed by replacing $\varphi \to \frac{\varphi}{\sqrt{3}}$ (averaging $\cos^2\theta$, θ being the orientation of $S_\triangle$ with respect to $\vec{B}$).

The ATS contribution for a TWP has been obtained from the total TS heat capacity contribution:

$$C_{pTS}(T,B) = \int_0^\infty dE\ g_{tot}(E,B) C_{p0}(E,T) \tag{3.5}$$

where

$$g_{tot}(E,B) = g_{2LS}(E) + g_{ATS}(E,B) \tag{3.6}$$

is the magnetic-field dependent TS DOS, given by the sum of $g_{2LS}(E)$, the constant DOS from the STM 2LSs and $g_{ATS}(E,B)$, the near-degenerate TWPs contribution that is at the basis of the magnetic effects. The heat capacity contribution from a single TS having energy gap E is given by:

$$C_{p0}(E,T) = k_B \left(\frac{E}{2k_B T}\right)^2 \cosh^{-2}\left(\frac{E}{2k_B T}\right) \tag{3.7}$$

A full derivation of the DOS and heat capacity within the new cellular model description, in terms of a more realistic tetrahedric four-welled potential (TFWP) will be provided in Appendix A.

Note that Eq. 3.3 is actually correct only for weak magnetic fields (up to about 1 T). For higher magnetic fields one must make use of the improved form we discussed in Chapter 2 for the ATS lower energy gap of the TWP:

$$\varphi^2 \to \varphi^2\left(1 - \frac{1}{27}\varphi^2\right) \to \frac{1}{3}\varphi^2\left\{1 - \frac{1}{45}\left(\frac{B}{B^*}\right)^2\right\} \tag{3.8}$$

where now the second expression holds after orientational averaging and where B^* is the upturn value of the magnetic field that we have extract for, e.g., the B-dependence of the dielectric constant $\varepsilon'(T,B)$ [70].

3.1.1 ATS model parameter from heat capacity fit

The parameters involved when fitting data are the cutoff D_{min} and combinations of cutoffs, charge and area $D_{0min}qS_\triangle$ and $D_{0max}qS_\triangle$ [13], as well as: $n_{Fe^{2+}}$ (Fe^{2+} impurity concentration), $n_{Fe^{3+}}$ (Fe^{3+} impurity concentration) and n_{ATS} (ATS concentration, always multiplied by P^*).

BAS glass

The concentrations of the ATSs n_{ATS} and Fe-impurities extracted from the best fit of the heat capacity as a function of B, for the BAS glass, are reported in Table 3.1. After having fixed such parameters for the concentrations we extract the remaining three cutoff parameters for the BAS glass (Table 3.2). The best fit of the chosen data is reported in Fig. 3.2(a).

BAS glass	Concentration $[g^{-1}]$	Concentration [ppm]
$n_{Fe^{2+}}$	1.06×10^{17}	14.23
$n_{Fe^{3+}}$	5.00×10^{16}	6.69
$P^* n_{ATS}$	5.19×10^{16}	-

Table 3.1: Extracted parameters (from the heat capacity data) for the concentrations of ATSs and Fe-impurities for the BAS glass.

Temperature [K]	D_{min} [K]	$D_{0min}\lvert\frac{q}{e}\rvert S_{\triangle}$ [KÅ^2]	$D_{0max}\lvert\frac{q}{e}\rvert S_{\triangle}$ [KÅ^2]
0.60	0.49	4.77×10^4	3.09×10^5
0.90	0.53	5.07×10^4	2.90×10^5
1.36	0.55	5.95×10^4	2.61×10^5

Table 3.2: Extracted tunneling parameters (from the C_p data) for the BAS glass.

Duran

The concentrations of the ATSs and Fe-impurities extracted from the best fit of the heat capacity as a function of B, for Duran, are reported in Table 3.3. As done for the analysis of the BAS glass, we extract the cutoff parameters of the TWP having fixed the parameters for the Iron impurities and ATS concentrations; the fit of the chosen data is reported in Fig. 3.2(b). For both set of data we find good fits using a small set of fitting parameters which are also in agreement with those obtained in the previous analysis [13]. As we will discuss in the following, the problem with the concentrations of the Fe-impurities reported in the literature is that they do not allow for a good fit of the $\bar{C}_p(B) = C_p(B) - C_p(\infty)$ data in the small field range values. As shown in Figure 3.5, the Langevin contribution drops to zero below the peak, whilst both Siebert's and Stephens' data definitely point to a non-zero value of $\bar{C}_p(0) = C_p(0) - C_p(\infty)$ at $B = 0$ for any $T > 0$. This remarkable non-zero difference is described by the ETM

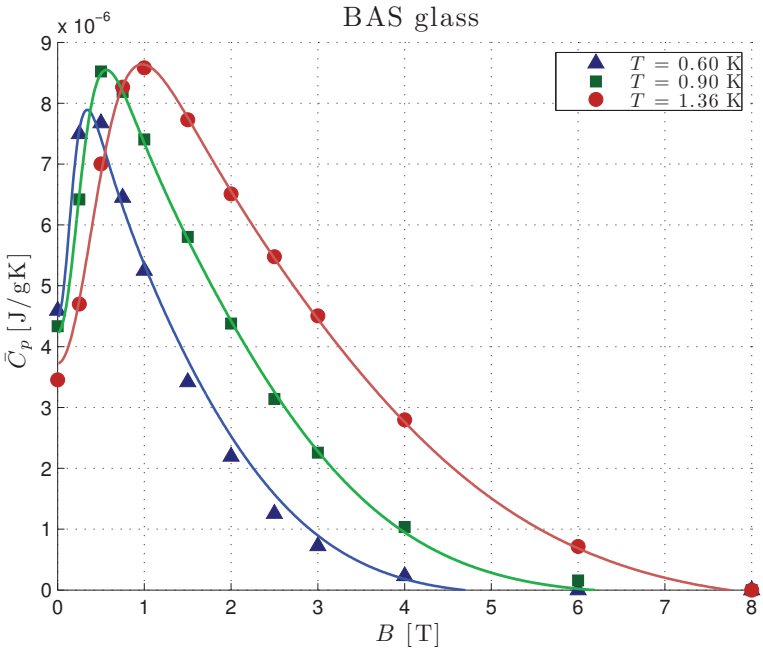

(a)

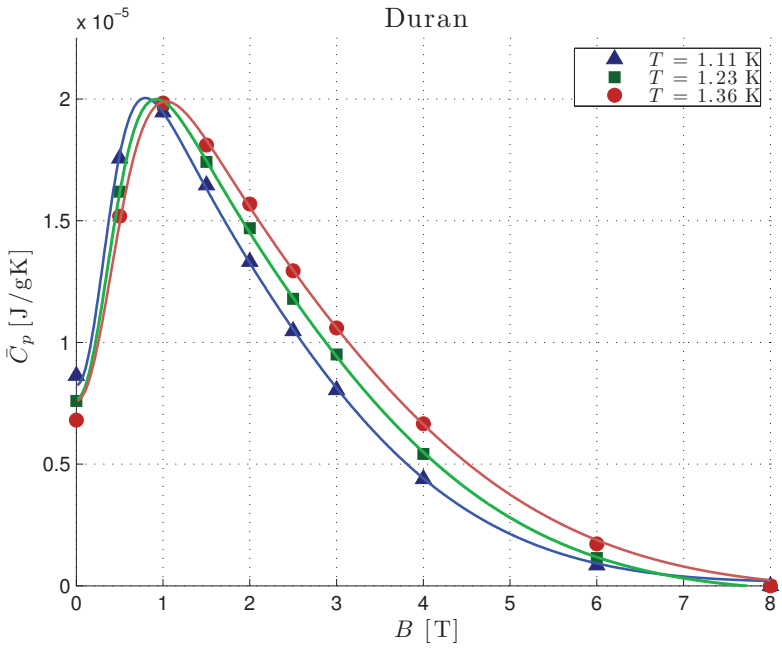

(b)

Figure 3.2: The heat capacity best fit for the a) BAS and b) Duran glasses.

and is a direct consequence of the shape of the DOS (Eq. 2.5) of the ATS contribution. The results of the C_p analysis definitely indicate that the concentration of paramagne-

Duran	Concentration [g^{-1}]	Concentration [ppm]
$n_{Fe^{2+}}$	3.21×10^{17}	33.01
$n_{Fe^{3+}}$	2.11×10^{17}	21.63
$P^* n_{ATS}$	8.88×10^{16}	-

Table 3.3: Extracted parameters (from the heat capacity data) for the concentration of ATSs and Fe-impurities for Duran.

Temperature [K]	D_{min} [K]	$D_{0min}\lvert\frac{q}{e}\rvert S_\triangle$ [KÅ^2]	$D_{0max}\lvert\frac{q}{e}\rvert S_\triangle$ [KÅ^2]
1.11	0.34	4.99×10^4	2.68×10^5
1.23	0.32	5.30×10^4	2.50×10^5
1.36	0.32	5.54×10^4	2.46×10^5

Table 3.4: Extracted tunneling parameters (from the C_p data) for Duran.

tic impurities in the multi-silicate glasses is much lower than previously thought and extracted from SQUID-magnetometry measurements of the magnetization $M(T,B)$ as a function of B and T. Having obtained good fit to the specific heat data with the ATS contribution added to the Langevin's one, we now present the results of the model applied to the magnetization data.

3.2 Magnetization theory

As a starting point we estimate the magnetic moment μ_{ATS} at $T=0$, $\mu_{ATS}=-\frac{\partial}{\partial B}\left(-\frac{1}{2}E\right)$, where $E=\sqrt{D^2+D_0^2\varphi^2}$ is the ATS lower energy gap. For not too small fields B, we get that μ_{ATS} vanishes linearly with B when $B\to 0$, but saturates at high enough B:

$$\mu_{ATS}\simeq\frac{\pi}{\Phi_0}S_\triangle D_0=\frac{\pi}{\phi_0}\left(\left|\frac{q}{e}\right|S_\triangle D_0\right). \tag{3.9}$$

Note that the very same combination $\frac{q}{e}S_\triangle D_0$ of parameters appears. Using the values extracted from the C_p best fit (e.g. those of Table 3.4) we deduce from Eq. (3.9) that (for Duran) μ_{ATS} ranges from about $3.8\mu_B$ to $27.1\mu_B$; therefore the ATS appear to carry

considerably high magnetic moments. This fact indicates that a large group of correlated charged atomic particles is involved in each single ATS and that an important ATS contribution to the magnetization of the sample is to be expected (Fe^{2+} and Fe^{3+} have magnetic moment $\mu_J = 2\sqrt{6}\mu_B$ and, respectively, $\sqrt{35}\mu_B$). We therefore expect a contribution to the measured magnetization M from the ATSs that is comparable to, or even greater than, Langevin's paramagnetism of the diluted Fe impurities.

The magnetization M of a sample containing paramagnetic impurities as well as magnetic field sensitive ATSs is, like in the case of the specific heat, also given by the sum of two different contributions:

1. Langevin's well-known contribution of the paramagnetic impurities (Fe^{2+} and Fe^{3+}, with n_J concentration of one species having spin J), given by the standard expression:

$$M_J = n_J g \mu_B J B_J(z), \quad \left(z = \frac{g\mu_B BJ}{k_B T}\right) \tag{3.10}$$

where the Brillouin function B_J is defined by:

$$B_J(z) = \frac{2J+1}{2J}\coth\left(\frac{(2J+1)}{2J}z\right) - \frac{1}{2J}\coth\left(\frac{1}{2J}z\right) \tag{3.11}$$

and its low-field susceptibility is the known Curie law:

$$\frac{M}{B} \cong \frac{n_J g^2 \mu_B^2 J(J+1)}{3k_B T} \tag{3.12}$$

2. the contribution of the ATS tunneling currents, given by the following new expression as the sum of contributions from ATSs of lowest gap E:

$$\begin{aligned} M_{ATS} = \pi\, P^* n_{ATS} \frac{1}{B}\Bigg\{ &\int_{E_{c1}}^{E_{c2}} \mathrm{d}E \tanh\left(\frac{E}{2k_B T}\right) \ln\left(\frac{E^2 - D_{0min}^2\varphi^2}{D_{min}^2}\right) \\ &+ \int_{E_{c2}}^{\infty} \mathrm{d}E \tanh\left(\frac{E}{2k_B T}\right) \ln\left(\frac{E^2 - D_{0min}^2\varphi^2}{E^2 - D_{0max}^2\varphi^2}\right)\Bigg\} \end{aligned} \tag{3.13}$$

and which can be also re-expressed (like in the case of C_{ATS}) using $y = \frac{E}{2k_B T}$ in the following form:

$$\begin{aligned} M_{ATS} = 2\pi\, P^* n_{ATS} k_B T \frac{1}{B}\Bigg\{ &\int_{x_{c1}}^{x_{c2}} \mathrm{d}y \tanh y \ln\left(\frac{y^2 - x_{0min}^2\varphi^2}{x_{min}^2}\right) \\ &+ \int_{x_{c2}}^{\infty} \mathrm{d}y \tanh y \ln\left(\frac{y^2 - x_{0min}^2\varphi^2}{y^2 - x_{0max}^2\varphi^2}\right)\Bigg\} \end{aligned} \tag{3.14}$$

where as usual

- $E_{c1} = \sqrt{D_{min}^2 + D_{0min}^2\varphi^2}$ and $E_{c2} = \sqrt{D_{min}^2 + D_{0max}^2\varphi^2}$;
- $x_{c1,2} = \frac{E_{c1,2}}{2k_B T}$, $x_{min} = \frac{D_{min}}{2k_B T}$, etc.

The above expression follows from a straightforward application of standard quantum statistical mechanics, with

$$\vec{M}_{ATS} = n_{ATS}\left\langle -\frac{\partial \mathcal{H}_{3LS}}{\partial \vec{B}}\right\rangle,$$

n_{ATS} being the ATSs' concentration The angular brackets $\langle\cdots\rangle$ denote quantum, statistical and disorder averaging.

Once again we remark that the above formula for M_{ATS} is correct for weak magnetic fields; for higher fields the usual correction has to be introduced, owing to the fact that an improved analytic expression for the lowest ATS energy gap must be used [70]. In practice, as seen in Eq. (3.8), this corresponds – where appropriate – to the replacement of B with $B\sqrt{1-\frac{1}{45}(B/B^*)^2}$. To achieve good fits for $M(T)$ in such wide temperature range (4$<T<$300 K) it is necessary to use temperature dependent fitting parameters. The underlying physical reason is that as temperature drops the RERs of the cellular structure of the glass (described in Chapter 1) begin to fuse together and adsorb atoms/ions from the interstices between them, growing at their expense [59]. This makes that the number $N(T)$ of atomic tunnelers in each interstitial ATS decreases with decreasing temperature: $T_g > T \to 0$ and a reasonable temperature-dependence is of the Arrhenius type:

$$N(T) = N_0 \exp\left\{-\frac{E_0}{k_B T}\right\}, \tag{3.15}$$

where E_0 is a suitable activation energy. Recalling that each interstitial ATS is formed by the group of $N(T)$ atomic tunnelers [68] we now use the temperature dependent parameters:

$$\begin{aligned} D_{min} &= D^{(0)}_{min}\exp\left\{-\frac{E_0}{k_B T}+\frac{E_0}{k_B T_0}\right\} \\ D_{0min}\frac{q}{e}S &= \left[D_{0min}\frac{q}{e}S\right]^{(0)}\exp\left\{-\frac{3E_0}{k_B T}+\frac{3E_0}{k_B T_0}\right\} \\ D_{0max}\frac{q}{e}S &= \left[D_{0max}\frac{q}{e}S\right]^{(0)}\exp\left\{-\frac{3E_0}{k_B T}+\frac{3E_0}{k_B T_0}\right\} \end{aligned} \tag{3.16}$$

and this holds also for B^*, that contains two parameters proportional to $N(T)$ in Eq. (3.15). T_0 is a temperature corresponding to the combinations of the parameters marked with a (0)-superscript; the values that we extract from the best fits correspond to the parameters at that temperature (typically, T_0 is the average temperature of our C_p fits). Before discussing the results regarding the magnetization, we briefly review in the next Section how we convert the Fe-concentrations thus obtained to atomic ppm concentrations (ppma).

3.2.1 Concentration conversion

The mass density of a Fe species with spin J in the sample, is given by:

$$n_J = \frac{N_J}{M} = \frac{N_J}{N_{at}} \frac{N_A}{\sum_i \xi_i A_i} \tag{3.17}$$

where

$$M = \sum_i \xi_i \frac{N_{at}}{N_A} A_i \tag{3.18}$$

is the sample's mass, and where:

N_J	number of Fe-ions in the sample with spin J
ξ_i	molar fraction of the i-th species
A_i	molar mass of the i-th species
N_{at}	total number of atoms in the sample
N_A	Avogadro's number (6.022×10^{23} mol^{-1})

for the Fe^{2+} (J=2) and Fe^{3+} (J=5/2) impurities. Table 3.5 shows parameters related to the chemical and molar composition [41] of the two multi-component silicate glasses. Therefore, using the parameters reported in Table 3.5, one gets:

$$\sum_i \xi_i A_i = \begin{cases} 80.530 \frac{\text{g}}{\text{mol}} & \text{for BAS glass} \\ 61.873 \frac{\text{g}}{\text{mol}} & \text{for Duran} \end{cases}$$

We interpret $N_J/N_{at} \equiv \bar{n}_J$ as the atomic concentration of the spin-J Fe species (to be multiplied by 10^6 to obtain the ppm) and thus we have the conversion formula:

$$n_J = \bar{n}_J \frac{N_A}{\sum_i \xi_i A_i} \tag{3.19}$$

Oxide Element	Molar Mass (A_i)	$\xi_{i,\%}$ BAS glass	$\xi_{i,\%}$ Duran
SiO_2	60.084	72.7	83.4
B_2O_3	69.620	0.72	11.6
Al_2O_3	101.961	8.8	1.14
Na_2O	61.979	0.28	3.4
K_2O	94.196	0.064	0.41
BaO	153.326	17.0	0.005
Li_2O	29.881	0.014	0.004
PbO	223.199	0.48	$<$0.01

Table 3.5: Molar mass A_i and percentage fraction $\xi_{i,\%}$ of the various oxides making up the BAS (third column) and Duran (fourth column) glasses, as reported in [41, 78].

3.2.2 Extracted parameters for the magnetization data

In this Section we report the results of the theoretical fits for the magnetization $M(B,T)$ obtained using the sum of the Langevin's contribution (Eq. 3.10) for the Fe^{2+} and Fe^{3+} impurities and the ATS contribution (Eq. (3.14). As input parameter for the fits we use the Fe^{2+}, Fe^{3+} and ATS concentrations extracted from the specific heat fits. In particular:

- The best fit for the BAS glass is reported in Fig. 3.3 and the extracted parameters in Table 3.6.
- The best fit for Duran is reported in Fig. 3.4 and the extracted parameters in Table 3.7.

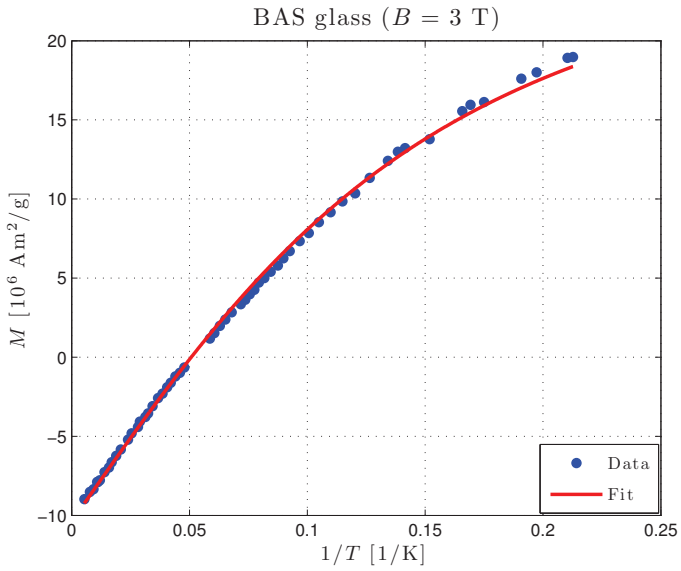

Figure 3.3: The best fit of the magnetization data [41] for the BAS glass, using Eq. (3.10) (for the Fe^{2+} and Fe^{3+} impurities) and Eq. (3.14) (for the ATSs).

3.3 Comparison of the concentrations for Iron impurities and ATSs

We now compare the parameters obtained from the two independent analysis, the heat capacity and magnetization; as we will see there is an agreement between the tunneling parameters and the concentration of the ATSs extracted from the C_p- and from the M-data.

Parameter	BAS glass
$n_{Fe^{2+}}$ [g^{-1}]	1.08×10^{17}
$n_{Fe^{3+}}$ [g^{-1}]	5.01×10^{16}
$P^* n_{ATS}$ [g^{-1}]	5.74×10^{16}
D_{min} [K]	8.01×10^{-2}
$D_{0min}\lvert\frac{q}{e}\rvert S_\triangle$ [KÅ^2]	1.31×10^{5}
$D_{0max}\lvert\frac{q}{e}\rvert S_\triangle$ [KÅ^2]	2.44×10^{5}
vert.offset [Am^{2}g^{-1}]	-1.04×10^{-5}

Table 3.6: Extracted parameters (from the magnetization data of [41]) for the concentration of ATS and Fe-impurities of the BAS glass. The vertical offset represents the residual Larmor diamagnetic contribution.

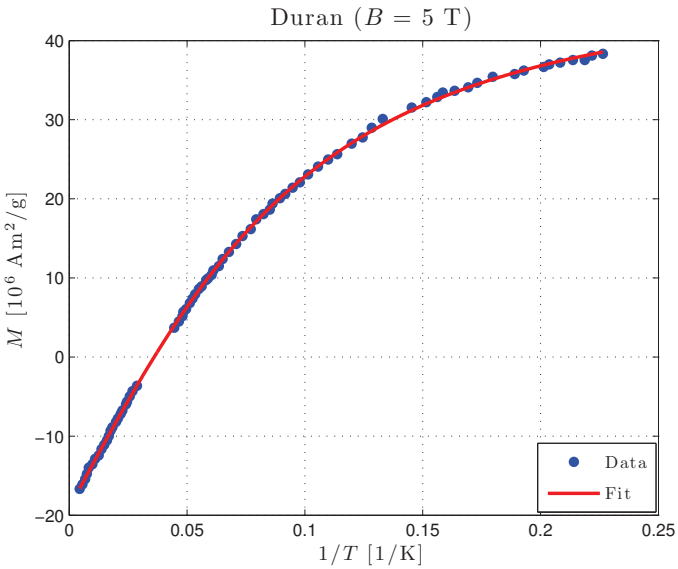

Figure 3.4: The best fit of the magnetization data [41] of Duran, using Eq. (3.10) (for the Fe^{2+} and Fe^{3+} impurities) and Eq. (3.14) (for the ATSs).

Parameter	Duran
$n_{Fe^{2+}}$ [g^{-1}]	3.07×10^{17}
$n_{Fe^{3+}}$ [g^{-1}]	2.13×10^{17}
$P^* n_{ATS}$ [g^{-1}]	8.68×10^{16}
D_{min} [K]	5.35×10^{-2}
$D_{0min}\lvert\frac{q}{e}\rvert S_\triangle$ [KÅ^2]	2.00×10^{5}
$D_{0max}\lvert\frac{q}{e}\rvert S_\triangle$ [KÅ^2]	2.81×10^{5}
vert.offset [Am^{2}g^{-1}]	-1.97×10^{-5}

Table 3.7: Extracted parameters (from the magnetization data of [41]) for the concentration of ATS and Fe impurities of Duran.

3.3.1 BAS glass

The nominal concentration of Fe^{3+} for the BAS glass is (using Eq. (3.17) or (3.19)):

$$\begin{aligned} \bar{n}_{Fe^{3+}_{nom}} &= 102 \text{ ppm} \\ n_{Fe^{3+}_{nom}} &= \frac{10^{-6} \cdot 102 \cdot 6.022 \times 10^{23} \text{ mol}^{-1}}{80.530 \frac{\text{g}}{\text{mol}}} = 7.63 \cdot 10^{17} \text{g}^{-1} \end{aligned} \tag{3.20}$$

which is inadequate to explain the behaviour of the heat capacity as a function of B presented in Figure 3.2, and as a function of T (previously studied in [13]). Table 5.1 summarizes the concentrations found from our best fits of heat capacity and magnetization data, for the BAS glass. The parameters found in [13] were $P^* n_{ATS}$=6.39×10^{16} g^{-1} and $\bar{n}_{Fe}$=20.44 ppm where this latter was for the Fe^{2+} concentration only. We therefore reach the conclusion that most of the Fe-impurities in these two glasses are of the Fe^{2+} type, in agreement with [13].

BAS glass	
Heat Capacity fit	
$n_{Fe^{2+}}$	1.06×10^{17} g^{-1} = 14.23 ppm
$n_{Fe^{3+}}$	5.00×10^{16} g^{-1} = 6.69 ppm
$P^* n_{ATS}$	5.19×10^{16} g^{-1}
Magnetization fit	
$n_{Fe^{2+}}$	1.08×10^{17} g^{-1} = 14.38 ppm
$n_{Fe^{3+}}$	5.01×10^{16} g^{-1} = 6.70 ppm
$P^* n_{ATS}$	5.74×10^{16} g^{-1}

Table 3.8: Comparison between the concentrations extracted from the two different best fitted experimental data sets for the BAS glass.

3.3.2 Duran

The nominal concentration of Fe^{3+} for Duran is (using Eq. (3.17) or (3.19)):

$$\begin{aligned} \bar{n}_{Fe^{3+}_{nom}} &= 126 \text{ ppm} \\ n_{Fe^{3+}_{nom}} &= \frac{10^{-6} \cdot 126 \cdot 6.022 \times 10^{23} \text{ mol}^{-1}}{61.873 \frac{\text{g}}{\text{mol}}} = 1.23 \cdot 10^{18} \text{g}^{-1} \end{aligned} \tag{3.21}$$

which again is inadequate to explain the behaviour of the heat capacity data as a function of B (reported in 3.5). Table 3.9 summarizes the concentrations found from our

best fits of heat capacity and magnetization data, for Duran. The parameters found in [13] were $P^* n_{ATS}$=6.92×10^{16} g^{-1} and $\bar{n}_{Fe}$=47.62 ppm where this latter was the Fe^{2+} concentration only.

Using such result we can now know the magnitude of the different contribution of the paramagnetic impurity and ATS concentrations to both the heat capacity and magnetization. In Figure 3.5 we present the behaviour of the different contributions to the heat capacity as a function of B, e.g. for the case of Duran; $C_{Fe^{2+}}$ and $C_{Fe^{3+}}$ are given by Eq. (3.1), respectively with the Fe^{2+} and Fe^{3+} parameters, C_{param} is the sum of these latter two, C_{ATS} is given by Eq. (3.3) and the green line represents the result of the best fit. The dashed line corresponds to the $\bar{C}_p(B)$ one would get from the nominal concentration $\bar{n}_{Fe}$ of 126 ppm [41] as extracted from the SQUID magnetization measurements fitted with the Langevin contribution only (no ATS contribution).

Likewise Figure 3.6 presents the behaviour of the different contributions (Eq.(3.10) and Eq.(3.14)) to the magnetization as a function of B, also for Duran. Note that the ATS contribution is in both cases *dominant*, also (in the case of the magnetization) at the higher temperatures.

Duran	
Heat Capacity fit	
$n_{Fe^{2+}}$	3.21×10^{17} g^{-1} = 33.01 ppm
$n_{Fe^{3+}}$	2.11×10^{17} g^{-1} = 21.63 ppm
$P^* n_{ATS}$	8.88×10^{16} g^{-1}
Magnetization fit	
$n_{Fe^{2+}}$	3.07×10^{17} g^{-1} = 31.58 ppm
$n_{Fe^{3+}}$	2.13×10^{17} g^{-1} = 21.86 ppm
$P^* n_{ATS}$	8.68×10^{16} g^{-1}

Table 3.9: Comparison between the concentrations extracted from the two different best fitted experimental data sets for Duran.

3.3.3 BK7

Finally we present our study of the SQUID magnetization data (also available from [41]) for the borosilicate glass BK7, for which however no substantial magnetic effect in the heat capacity C_p has been reported [41]. This glass has a nominal Fe-impurity concentration of $\bar{n}_{Fe^{3+}}$=6 ppm [41, 78, 37], yet our best fit in Fig. 3.7 with both Langevin (Eq. (3.10)) and ATS (Eq. (3.14)) contributions produces the concentrations and parameters given in Table 3.10. We conclude that our main contention is once more confirmed, in that the concentration of Fe in BK7 we extract in this way is only about 1.1 ppm and the bulk of the SQUID magnetization is due to the ATSs.

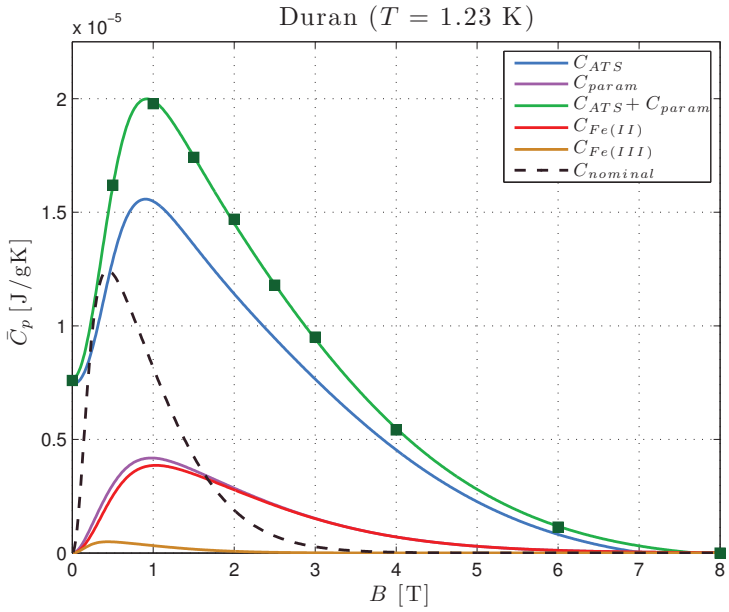

Figure 3.5: The curves represent the different terms that contribute to the heat capacity of Duran in our best fit of the data from [41]. The dashed curve is for Langevin's contribution only, but with the nominal concentration of $\bar{n}_{Fe^{3+}}$=126 ppm (no ATS).

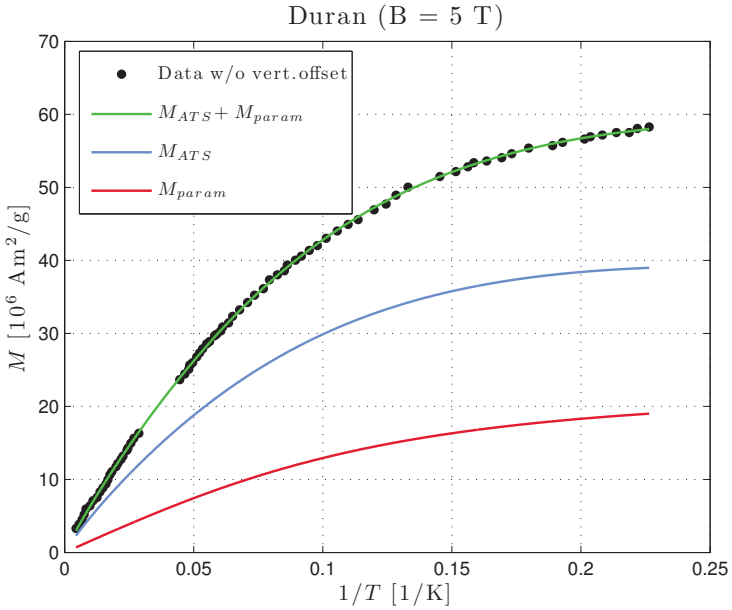

Figure 3.6: The curves represent the different contributions to the magnetization of Duran in our best fit of the data from [41].

Table 3.10 reports our very first estimate of $n_{ATS}P^*$ for BK7. Assuming P^* to be of order 1 and about the same for all glasses, we conclude that the concentration n_{ATS} of the ATSs nesting in the RERs is very similar for all of the multi-silicate glasses by us studied for their remarkable magnetic effects. From the present SQUID magnetization best fits we have obtained 5.74×10^{16} g^{-1} (BAS glass), 8.68×10^{16} g^{-1} (Duran) and 1.40×10^{16} g^{-1} (BK7). The almost negligible magnetic effect in C_p for BK7 is due, in our approach, to the low values of the cutoffs D_{0min} and D_{0max} for this system (these parameters appearing in the prefactor and in the integrals' bounds determining the ATS contribution to C_p [68]).

Parameter	BK7
$n_{Fe^{2+}}$ [g^{-1}]	6.69×10^{15} = 0,71 ppm
$n_{Fe^{3+}}$ [g^{-1}]	3.43×10^{15} = 0.36 ppm
P^*n_{ATS} [g^{-1}]	1.40×10^{16}
D_{min} [K]	5.99×10^{-2}
$D_{0min}\lvert\frac{q}{e}\rvert S_\triangle$ [KÅ^2]	8.87×10^{4}
$D_{0max}\lvert\frac{q}{e}\rvert S_\triangle$ [KÅ^2]	1.20×10^{5}
vert.offset [Am^{2}g^{-1}]	-1.08×10^{-5}

Table 3.10: Extracted parameters (from the magnetization data of [41]) for the concentration of ATSs and Fe impurities of the BK7 ($\sum_i \xi_i A_i$= 63.530 g mol^{-1} [41]). The vertical offset represents the residual Larmor diamagnetic contribution.

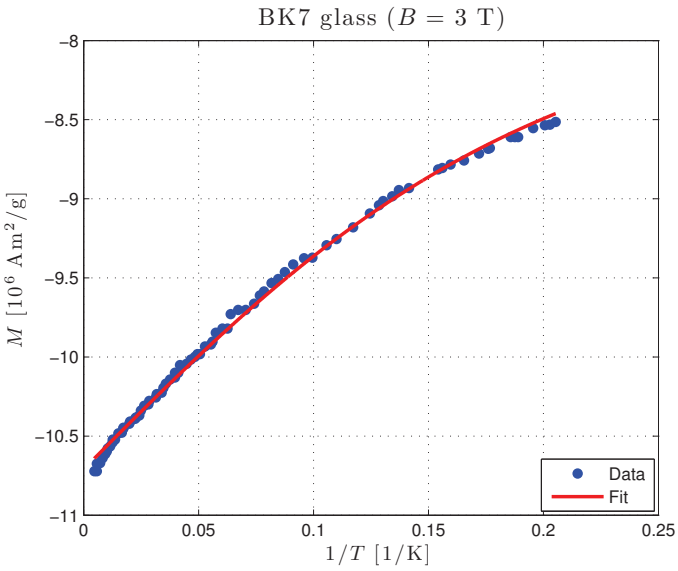

Figure 3.7: The best fit of the magnetization data [41] for BK7, using Eq. (3.10) (for the Fe^{2+} and Fe^{3+} impurities) and Eq. (3.14) (for the ATSs). Data from [41].

3.4 Conclusions

We conclude that only by allowing a contribution to the magnetization from the ATS tunneling currents as evaluated from our ETM we are able to show that the concentrations of Fe impurities (of type Fe^{2+} as well as Fe^{3+}) are in much better agreement when extracted from SQUID magnetization data or from heat capacity data with the samples in a magnetic field. The concentrations n_J that we find for the Fe impurities are, in fact, about 60 to 80% lower than those quoted in the literature for these glasses; without the inclusion of the contribution from the ATSs the extracted SQUID-measurement concentration of paramagnetic impurities will be considerably overestimated. This happened already in the case of Stephens' data [35], which have led to the Langevin-only estimate [13] $\bar{n}_{Fe} \simeq 50$ ppm in Pyrex from the C_p measurement data in a magnetic field, when in fact the mass-spectrometry analysis had given [35] $\bar{n}_{Fe}$=12 ppm.

The fact that we have established, that Langevin-only fitted SQUID-magnetization measurements considerably overestimate the concentration of paramagnetic impurities in a glassy matrix, seems to exclude the possibility that Fe-impurities and associated paramagnetic-TSs can be the possible sources of the magnetic effects in the cold glasses [50]. Indeed, Fe^{3+} would enter substitutionally to Si^{4+} only in a crystal (e.g. quartz), whilst in a multi-silicate glass the overwhelming majority of Fe-impurities would enter as network-modifiers of the SiO_4 glassy matrix [80]. This means that the amplitude of the $[FeO_4]^-$ paramagnetic TS contribution should be reduced considerably more than the 80% we claim from the overestimate of the Fe-concentration from Langevin-fitted SQUID measurements. Note that the paramagnetic-TS explanation of the magnetic effect in C_p requires concentrations n_{Fe} already some 40% greater than the nominal, Langevin-only SQUID extracted values [50]. The paramagnetic-TS approach may nevertheless retain some validity in the case of the heavily Fe- and Cr-doped multi-silicate glasses [53].

From this analysis we also find that the ATSs and the ETM employed keep giving a good description of the glass magnetization till the highest temperatures in the magnetization data, up to about 300 K[2]. We interpret this new finding with the consideration that no phonon-TS interactions are involved in the measurement of the magnetization, contrary to the case of the dielectric-constants and polarization-echo measurements, or to the case of the acoustic measurements, or that of the heat capacity, where phonons do contribute and in a complex way well above 1 K [29, 25]. The SQUID magnetization measurement in a magnetic field is therefore an ideal experiment where to study the properties of the TSs and test our ETM.

In Table 3.11 we report the paragon of the extracted tunneling parameters from the fits with the ETM for different measurements for e.g. the BAS glass. The values for the real and imaginary part of the dielectric constant have been obtained in the work of Jug and Paliienko [70]), while the specific heat C_p and the magnetization M quantities

[2]The glass transition temperature T_g is 1123 K for BAS glass and 803 K for Duran, respectively [41]).

BAS	$P^* n_{ATS}$ [g^{-1}]	D_{min} [K]	$D_{0min}\|\frac{q}{e}\|S_\triangle$ [KÅ^2]	$D_{0max}\|\frac{q}{e}\|S_\triangle$ [KÅ^2]
$\delta\varepsilon'$	-	0.02	2×10^5	3×10^5
$\delta\varepsilon''$	-	0.02	2×10^4	5×10^5
C_p	5×10^{16}	0.50	5×10^4	3×10^5
M	6×10^{16}	0.08	1×10^5	3×10^5

Table 3.11: Comparison of the extracted tunneling parameters from the fits with the ETM for different measurements for the BAS glass: the the real ε' and imaginary ε'' part of the dielectric constant (from the work of Jug and Paliienko [70]), the specific heat C_p and the magnetization M found in this analysis.

are the result of the present analysis. We can notice that there is a good agreement in the order of magnitude of the tunneling parameters extracted for the different physical quantities. This is therefore the confirmation that the assumptions of the ETM are correct and do not depend on the specific measurement.

We also remark that the tunneling parameters D_{min}, $D_{0min}|\frac{q}{e}|S_\triangle$ and $D_{0max}|\frac{q}{e}|S_\triangle$ extracted from the M data from best fits of all data in the other experiments [13, 73, 71, 72] are anomalously large. These large values have been interpreted in [68] as deriving from the correlated tunneling of a large, but not yet mesoscopic or macroscopic, number $N \sim 200$ to 600 of atomic-scale TSs. As explained in Chapter 2 the ATS is only a fictitious tunneling particle involving the correlated rearrangement of a large group of (charged) atoms.

At this stage of the analysis we can use the extracted values of $n_{ATS}P^*$ for the silicates to estimate via the ETM the size 2ξ of the mosaic cells presented in Section 1.3 in the context of the new cellular picture for glasses. From the HREM imaging we estimate the cells to be of the order of some 100 Å for the silicate and borate glasses. For example, from Figure 1.20 one estimates $\xi \approx 250$ Å (for a-SiO_2), from Figure 1.21(a) one gets $\xi \approx 300$ Å (for a-$(B_2O_3)_{0.75}$-$(PbO)_{0.25}$) and from Figure 1.21(b) one has $\xi \approx 250$ Å(for a-$LiO_2{\cdot}SiO_2$). This is completely in line with estimates of ξ that one can get from the extracted density of the ATSs that we have obtained in this work. We can in fact safely assume that on average one ATS sits in each insterstitial of the close-packed mosaic cells and then that the following approximate relationship holds for the ATS volume (x_{ATS}) and mass (n_{ATS}) densities:

$$\frac{1}{\frac{2\sqrt{2}}{3}\xi^3} = x_{ATS} = n_{ATS}\rho = \frac{P^* n_{ATS}\rho}{P^*} \tag{3.22}$$

where ρ is the mass density of the solid and P^* can be estimated from the normalization condition for the ATS parameter distribution, which reads:

$$2\pi P^* \ln\left(\frac{D_{max}}{D_{min}}\right)\ln\left(\frac{D_{0max}}{D_{0min}}\right) = 1. \tag{3.23}$$

Whilst D_{max} is unknown because it never appears in the data fitting formulae, we can safely assume it to be of such value that the quantity $\ln\left(\frac{D_{max}}{D_{min}}\right)\ln\left(\frac{D_{0max}}{D_{0min}}\right)$ is of order 1

and therefore $P^* \approx \frac{1}{2\pi}$. We then get the estimating formula:

$$\xi \approx \left[\frac{3}{4\sqrt{2}\pi(n_{ATS}P^*)\rho} \right]^{1/3} \tag{3.24}$$

so that at this point we can use the values of $n_{ATS}P^*$ obtained in this Chapter for various silicates: $n_{ATS}P^* \approx 5 \times 10^{16}$ g^{-1} (BAS glass), 8×10^{16} g^{-1} (Duran) and 1×10^{16} g^{-1} (BK7). From [41] we get: $\rho \simeq 3.1$ g cm^{-3} (BAS), 2.31 g cm^{-3} (Duran) and 2.51 g cm^{-3} (BK7). We then obtain the estimates for the crystallite's radius: $\xi \approx 1.03 \times 10^{-6}$ cm or 103 Å (BAS), 0.97×10^{-6} cm or 97 Å (Duran) and 1.89×10^{-6} cm or 189 Å (BK7), thus with little variability between the three multi-silicates. We believe this rough matching between estimates of mosaic cell's size from HRTEM imaging and ETM modeling and experimental data fitting is not coincidental and thus that the new picture of glassy atomic structure hypothesized in this work is at the very least internally consistent.

Finally we have reported that there appears to be a significant temperature dependence $N(T)$ of this number of correlated atomic tunnelers, since the parameters quoted above change slightly (or even significantly, yet remaining large) from experiment to experiment carried out at different temperature ranges, as already commented in Chapter 2.

Chapter 4

Numerical simulation study: low temperature static analysis of the PEL

As pointed out in the previous Chapters of this Thesis, the low temperature properties of glasses originate from localized quantum-mechanical tunneling systems, which couple to phonons as well as to external fields. Although a broad range of experimental observations can be explained in terms of this approach, the microscopic nature of these tunneling systems is still not completely understood. In fact today's experiments do not allow for a *direct* investigation of the relevant parameters that give rise to the low temperature quantum phenomena, i.e. the mass m, the distance of the minima d, the barrier height V_0 and the asymmetry Δ. We recall that the fundamental idea of the STM (presented in Chapter 1) is the simplification of the multidimensional PEL into double-well 1D potentials (DWPs or 2LSs). The only promising approach to make progress in this field is therefore the study of the PEL of glass-forming systems at low temperatures by means of computer simulations. The PEL is a concept of utmost importance since e.g. it is believed to give rise to the characteristic non-exponential relaxation dynamics of glassy materials [81]. Our hope is that the exploration of the shape of this surface will also permit to gain insight into the properties of glasses at intermediate, low, and very low temperatures.

The goal of the following part of the Thesis is to reach a better understanding of the link between the relevant properties of the tunneling systems and the low temperature PEL geometry through classical computer simulations. At first sight these simulation methods might appear to be contradictory since we will not make any use of quantum mechanics; but actually we are not trying to reproduce the effect of tunneling. We are instead focusing our analysis on the purely geometrical features of the PEL that could be identified with the previously described DWPs or TWPs. In fact, to assert that a DWP is a TS means that it has the necessary properties to allow tunneling in principle. Within this approach the tunneling process does not need to occur to determine a situation where it will be relevant.

After a brief introduction (Section 4.1) where we recall how the analysis of the

PEL by means of computer simulations has allowed to describe the phenomenology of glassy systems, we discuss our hypothesis of the manner in which the TSs may probe the PEL on a very local scale at low temperature (Section 4.2). In the last part of the Chapter (Section 4.3) we will then describe some basic numerical techniques that we have implemented, in order to give the reader the tools for the understanding of the new search algorithm that we developed to study the geometry of the PEL at low temperature, which will be the subject of the last Chapter of the Thesis.

4.1 The PEL framework

One of the most powerful frameworks for understanding many features of supercooled liquids and glassy materials is the so-called PEL paradigm [3]. The origin of this notion dates back to 40 years ago, when Goldstein [81] proposed a topographic description for the mapping of the high dimensional potential energy function V. Since then, this convenient concept, that is thought to control the thermodynamic and kinetic properties of the system, has been applied to a wide class of problems of interest in physics, chemistry and biology. *The PEL is the (3N+1) dimensional hyper-surface where each point of the configuration space is defined by all the atomic coordinates of the system.*

Many researchers have focused their studies on the identification of the characteristics of the PEL that are thought to be at the basis of the relevant physics phenomena, like the TSs in our case. As we shall see, our analysis concentrates on the static structure of the landscape (rather then the dynamics), where each state can be described as a point in the $3N$ dimensional ($3N$D) configuration space. To get information about the shape of the PEL we can compute the first and second derivative of V. The first derivative is given by the $3N$D vector force, which is zero at any stationary point of V, while the second derivative, the Hessian or dynamic matrix, instead provides information about the curvature of V. As we have briefly mentioned in Chapter 2, the PEL is characterized by two kind of stationary points: minima, also named *inherent structure* (IS), with a positive curvature in all directions (hence, any movement away from the point increases the potential energy) and transition states, or *saddle points* (SPs), where a movement in at least one direction corresponds to a decrease in potential energy. Only transition states with Hessian index one, i.e. one negative eigenvalue, are important in this analysis since, due to the Murrell-Laidler theorem, if two minima are connected by an index two saddle, then there must be a lower-energy path between them involving only true transition states [82].

The mapping of the PEL requires an effort that scales exponentially with the dimensionality of the system: it has been demonstrated [83] that both the number of minima $\Omega_{IS}(N)$ and SPs $\Omega_{SP}(N)$ grow with the number of atoms N in an exponential fashion

$$\begin{aligned} \Omega_{IS}(N) &\propto N! \exp(aN) \\ \Omega_{SP}(N) &\propto N! \exp(bN) \end{aligned} \tag{4.1}$$

where a, b are system-specific positive constants, independent of N. Cluster with a few dozen particles already display millions of energy minima and the number of the paths that connect them increases even faster [84]. Therefore a complete sampling of the configuration space is at present impossible with computer simulations, even for small systems [85]. "Disconnectivity graphs" have been employed to map the PEL of various Lennard-Jones (LJ) clusters, showing the partitioning of the PEL in local minima, according to a funnel structure. Figure 4.1 from [86] e.g. reports the disconnectivity graph for the case of 13 atom LJ cluster (LJ13): there is a main line that represents the superbasin of the global minimum; the branches develops directly from it at each level, meaning the gradual exclusion of the local minima as the energy is decreased.

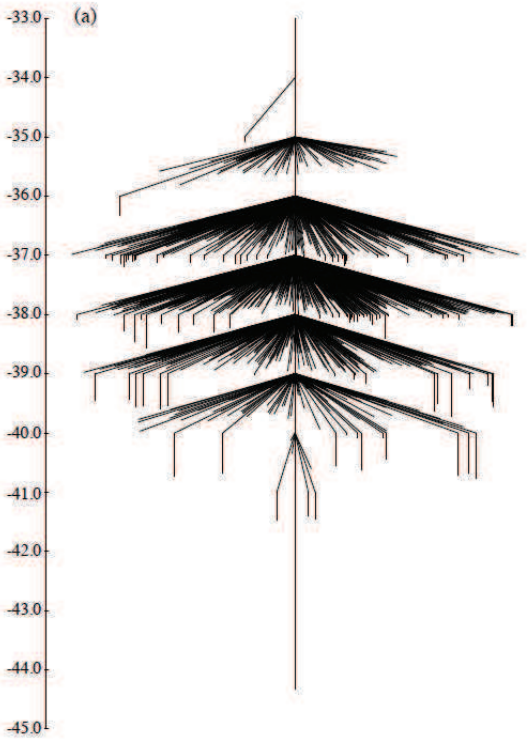

Figure 4.1: Disconnectivity graph for LJ13 cluster, from [86]. All the minima and the associated branches are displayed. The vertical axis reports the energy scale in LJ units of ε_{AA}, the pair well depth of the LJ potential).

Historically the first work that focused on the probing of the PEL of bulk glasses, studying how the system evolves and explores the various minima, was carried out by Weber and Stillinger [87]. For this they periodically quenched the configurations of MD simulations to zero temperature and identified nearby minima, as well as, the connecting transition states. Furthermore, the sampling of the PEL as a function of the temperature[3] has shown that the lower T is the more the system is stucked in deeper minima and it is unable to overcome the higher energy barriers [88]. This behavior is clearly understood by looking at Figure 4.2(a) that reports the average IS energy per particle in a Binary Mixture Lennard-Jones (BMLJ) system (defined in Chapter 6) as a function of the temperature for different cooling rates. This assumption was later confirmed [89, 90] by the discovery that below a certain temperature T_C the system samples just ISs. The same analysis also focused on the characterization of the distribution of the SPs as a function of T, obtaining the interesting result that the saddle index point increases linearly with the temperature, as shown in Figure 4.2(b).

We now come to the discussion about the techniques to identify the ISs and SPs that characterize the PEL in computer simulations. Finding minima from a given configuration is a straightforward procedure that can be accomplished using standard minimization protocols (like those described in Section 4.3.2) that allow to follow

[3] Of course the PEL is independent of T, atomic masses and coordinate system [82].

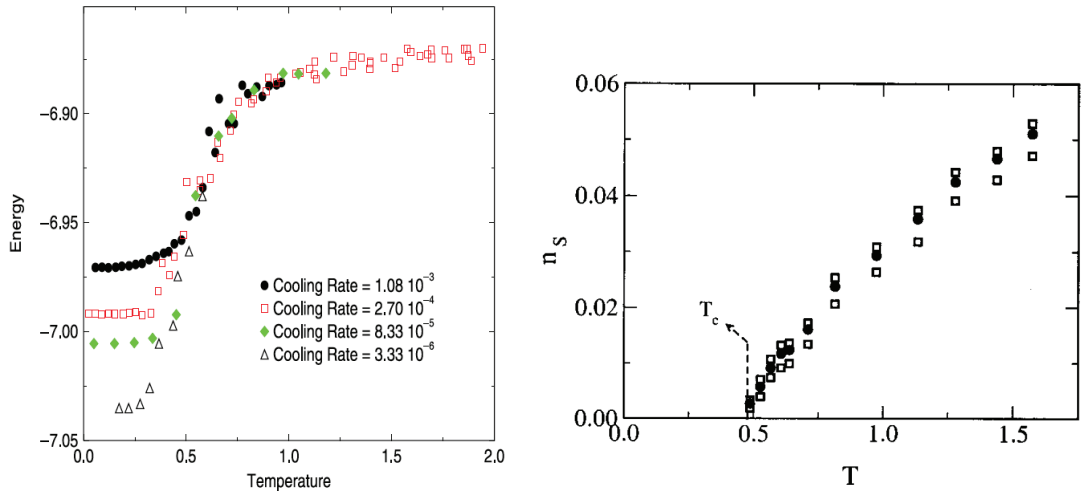

(a) (b)

Figure 4.2: Temperature dependent behavior of the a) average IS energy per particle [88] and b) SP order n_S [91] for a BMLJ model system. All the quantities are expressed in LJ reduced units.

the steepest descent direction of the PEL, walking downhill. On the other hand, in the literature, plenty of SP finding methods exist, reflecting the complexity of this task [82], not yet uniquely solved. Each method is indeed characterized by some limitations or drawbacks, as we discuss in the following paragraph.

There are mainly two classes of SP finding methods:

1. The first requires the knowledge of the initial and final minimum to identify the SP on the path that connect them [92, 93]. Such methods are based on an iterative procedure that allows to find the SP according to some given minimization conditions. However it has been pointed out in [94] that the procedure to verify that two minima are true neighbors has a relevant numerical cost and it is not always applicable.

2. The second class of methods instead is based only on the information of the initial minimum and implements a climbing up method protocol to reach the SP. Popular methods, e.g. the dimer method [95], the eigenvector-following method [96] and the Lanczos algorithm of the *ART nouveau* method [97], are based on the subsequent determination of the direction of the negative curvature of the PEL (the lowest mode of the Hessian matrix). However one of the drawback of such techniques, pointed out in [94], is that the choice of the SP path is not well controlled. The initial guess direction (generally chosen with a random displacement or through hard-sphere-like particle moves [82]) generates many SPs which are dynamically inaccessible at low temperature.

Finally, another stratagem to locate transition states, which has been extensively used in the field of supercooled liquids and glasses (see e.g. [91, 87]), is the minimization of the square gradient of the potential energy $W = |\vec{\nabla} V|^2$; SPs of the PEL of any

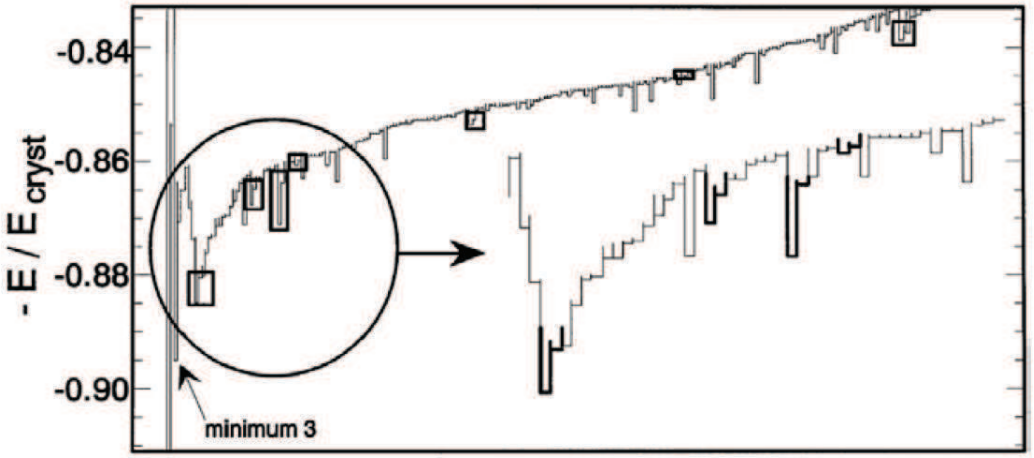

Figure 4.3: 1D representation of the PEL hyper-surface for a 32 atom BMLJ model glass. Each bin corresponds to a different configuration; on the left the crystal energy minimum can be seen. The DWPs (two adjacent minima) are highlighted. From [101].

index correspond to minima of this new function. However it was criticized [82] that such procedure locates mostly (99 % of cases, as stated in [91]) local minima of W which are not true saddles but instead "quasi-saddles", that are inflection points of V.

The SP search in the PEL was also the key point of the numerical studies related to the TSs [98, 99, 100]. The simplest approach to address these issues is the introduction of a reaction coordinate that parametrizes the motion from one local minimum to a neighboring one and from this to calculate the effective barrier height and then the tunneling parameters. Heuer and coworkers inferred [67] that the TSs indeed coincide with the DWPs (two nearby local ISs separated by a SP) in the PEL, that are relevant for the low temperature properties of glasses. In his analysis for a 32 atom BMLJ model glass [101] Heuer projected the multidimensional PEL onto a 1D potential (Figure 4.3), computing: a) the energies of the ISs using extensive quenched procedure in a similar way to Stillinger's work, and b) the Euclidean distances between these minima in configuration space. The DWPs (two adjacent minima) acting as TSs are highlighted. Note that Figure 4.3 also allows the identification of tunneling multiwelled local potentials: TWPs and TFWPs are indeed not at all rare.

The Authors of Ref. [101], due to numerical precision problems in their searching algorithm, collected the configurations of the DWPs in the $3N$D PEL in a wide range of the TSs relevant parameters (energy asymmetry Δ, distance between the wells d, and barrier height V_0); subsequently they *inferred* the information about the properties of TSs after a parametrization of these quantities with a 1D polynomial function and a not so clear interpolation procedure [100].

4.2 Sampling the PEL at low temperature

The conceptually not trivial question that we want to address in this Section is therefore how to translate the relevant 1D parameters of the model that characterize

the tunneling in the high dimensional PEL of the glass. *What are the TSs in the PEL? How can they be identified?*

The conclusions of Heuer's work regarding the nature of the DWPs in terms of configurations and parameters (asymmetry,...) indeed depend strongly on the manner they have scanned the PEL and as a consequence one does not have, in fact, at present a real good understanding of the DWPs, or more generally, of the possible atomic configurations that are mutually connected via a tunneling process. Therefore, so far, no study has yet *directly* determined the features of the PEL in the configuration space to find the presence of potential wells suitable to quantum mechanical tunneling. Actually, the most fundamental issue of what is the meaning of such DWPs or TWPs in the complex PEL of a glass has not yet been addressed in detail; the existing previous studies have in fact adjusted the results to the assumptions of the standard model without checking the possibility of other scenarios.

In this Work we intend to use an inductive argument based upon direct numerical evidence in order to find the geometries that could allow the tunneling at low temperatures. The final goal of this analysis is that once we have established a predictive microscopic characterization of the TSs and their parameters via computer simulations, we can identify the correct theoretical approach to be adopted in order to describe the experimental findings and to support the theoretical study of the microscopic properties of glasses at low temperatures T, including the ETM approach for the magnetic effects.

First of all we have to discuss the order of magnitude of the main parameters that characterize the TSs, i.e. (for the 2LSs) the tunneling matrix element Δ_0 (Chapter 2, Equation 1.10), given by

$$\Delta_0 = \frac{1}{2}\hbar\Omega\left(3 - \sqrt{\frac{8V_0}{\pi\hbar\Omega}}\right)e^{-2\frac{V_0}{\hbar\Omega}} \tag{4.2}$$

for a symmetric (Δ= 0) DWP made up by two superimposed parabolic wells, the energy of the single well $\hbar\Omega$, and the barrier height V_0. From the literature one can infer the typical range of values for the first two quantities for the most studied glasses (the multi-silicates):

- 10^{-6} K $< \Delta_0 <$ 10^{-3} K for the tunneling parameter [70],
- 10^{-5} K $< \hbar\Omega <$ 10 K for the well energy, [70, 25]

(it is thought that $\hbar\Omega$ should be the largest energy in the problem, hence of the order of the gap energy's upper cutoff E_{max}). These limits, verified also in the various applications of the present ETM theory (Chapter 2), allow us to deduce the range of variation of V_0. Figure 4.4 shows some isolines of Δ_0 as a function of V_0 and $\hbar\Omega$. The range mentioned above for Δ_0 corresponds to the region delimited by the two red bold lines. This plot shows that the typical barrier height range goes up to a maximum of 20 K or so and therefore this value represents a discriminant threshold for the relevant parameters of the TSs (2LSs, specifically). Most previous studies have found

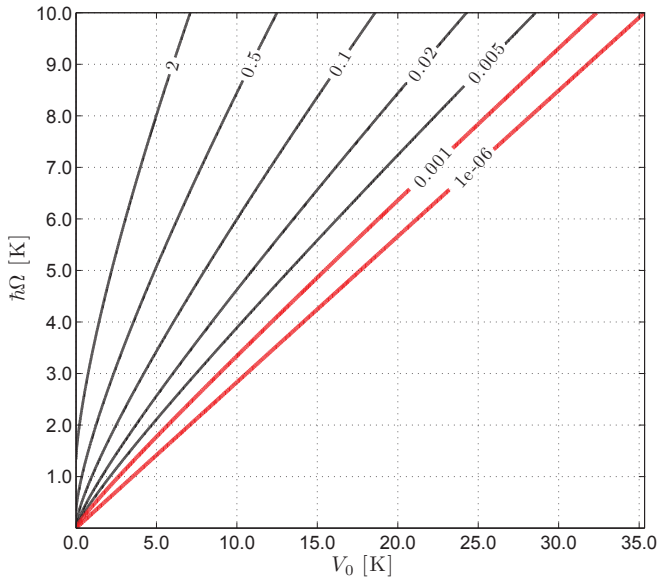

Figure 4.4: Isolines of the tunneling parameter Δ_0 as a function of the barrier height V_0 and the single-well energy $\hbar\Omega$. The physically relevant range for Δ_0 is delimited by the two bold red lines.

that the overwhelming majority of the barriers between two adjacent ISs is not that small, i.e. it is a sizable fraction of the interaction energy between the particles, thus of the order of 100 K [102]. Hence this indicates that in fact the 2LSs are *not* related to processes in which one particle changes its nearest neighborhood and thus moves a good fraction of the typical nearest neighbor distance, i.e. 0.3-2 Å. So, what other options remain for excitations that give rise to DWPs that have a small barrier height and thus a reasonable tunneling parameter? A possibility is that these excitation occur in the *interior* of the basin of attraction of an IS. In other words, the hypothesis we make is that the basin of attraction is not just a simple slightly deformed bowl, but is instead corrugated and characterized internally by small valleys. These kind of local deformations in the structure of the PEL can give rise to *effective* DWPs and therefore we believe that both the TSs and the ATSs are associated *not* with jumps of the system from one IS to a neighboring one, but rather to the motion inside the basin of attraction of a given IS. The TSs could be therefore associated with the motion from one of these valleys to a nearby one and the tunneling can occur among different channels [59].

To make this idea more specific we show in Fig. 4.5 what is intended to be an oversimplified representation of the real PEL of a glass, that we computed in order to clarify the concepts; as can be noted, the immediate surrounding of the IS is still harmonic, but as soon as one moves away (always remaining inside the same basin of attraction) different valleys (ending roughly at the North, East, South and West cardinal points in the drawing) develop (as indicated by solid lines), separated by regions in which the potential is higher and where the tunneling processes could occur (a tunneling path is marked by a bold green dashed line). We have two ISs (IS_1 and IS_2) that are connected via a reaction path (thin dashed line) that goes through a SP.

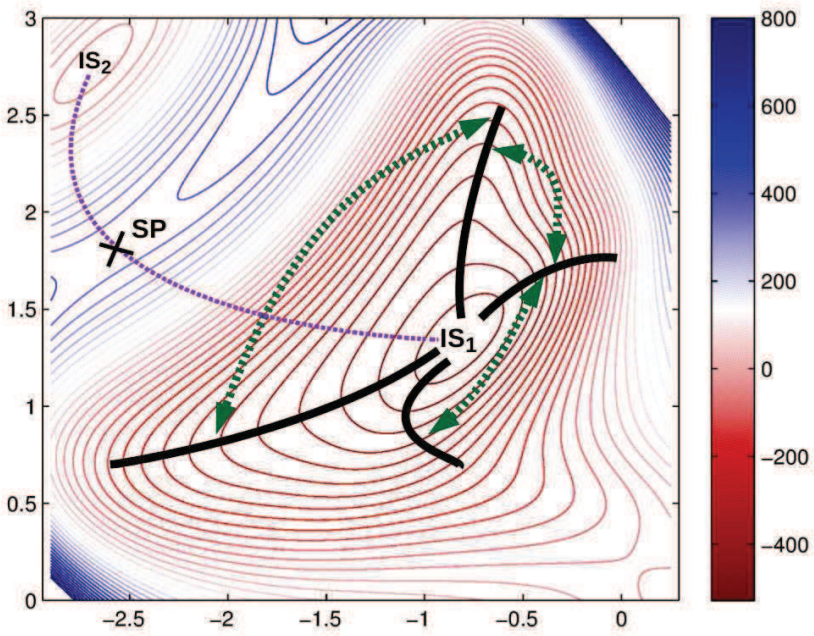

Figure 4.5: Simplified view of the PEL of a glass-forming system. We show two local minima, or ISs, that are connected by a first-order saddle point (SP). Some of the *valleys* (bold black solid lines) that emanate from the IS and often lead to a SP are also shown. The bold green dotted lines represent possible transition pathways for the tunneling effect from one valley to another. It is intended that tunneling takes place across the "reliefs" of the PEL. Note that the paths of these valleys do not necessarily lead to a saddle.

Note that this type of transition usually involves only a small number of degrees of freedom, i.e. on the order of 4-10 particles, since the excitation is localized in the 3D space. Thus the vast majority of the other particles change their position only marginally in this transition event, since they basically react only in an elastic manner, i.e. without changing their neighborhood. As mentioned above, the typical energy of the SPs is too large to permit a tunneling process with a reasonable probability and thus such processes might be irrelevant for the properties of glasses at low temperatures. We therefore conclude that the TSs should not be thought as a restricted subset of ISs forming DWPs, but rather as small irregular valleys that exist inside a single IS's basin and characterize the very bottom of the PEL. We note, however, that to each IS are connected of the order of N valleys (bold solid lines), many of which lead to one of the $O(N)$ SPs. These valleys are local minima *within* the basin of attraction of a given IS. Since these valleys start all at the IS, their energy difference is small, as long as they are close to the IS. Furthermore one can expect that also the barrier that the system has to cross when moving from one valley to another is not very large. Such processes are indicated by the bold green dotted lines with arrows. Thus such an inter-valley transition can approximately be described by a DWP in which the two wells have almost the same energy and the barrier height is not very large, i.e. the DWPs do indeed have the features that we need in order to describe the TSs. Thus in the following part of this work we intend to find the numerical evidence that the TSs

are related not to the IS-IS transitions, how it is so far believed, but to valley-valley transitions *inside* the basin of attraction of a single IS. Motivated by such hypothesis on the TS research, in the next Chapters we will explain the new computational tools (algorithms) that we develop to study directly the geometry of the basins of the ISs. We conclude this Chapter with a final Section in which we review the available numerical techniques that we employ for this research.

4.3 Numerical Methods

The analysis of PEL is accomplished by using several numerical methods tools. In particular, we perform initial molecular dynamics (MD) runs at zero temperatures (where all the particle velocities have been set to 0) to find the local minima or ISs starting from given instantaneous configurations. We then check the correctness in the determination of the IS configurations by mean of more efficient minimization techniques, the conjugate gradients, that follow the forces, thus the negative of the gradient of the potential. We briefly report in the following the basic concepts of MD simulations (Section 4.3.1) and energy minimization methods (Section 4.3.2).

4.3.1 Molecular Dynamics

Molecular Dynamics simulations are nowadays extensively used as a powerful tool in many different research fields such as chemical physics, materials science, modeling of bio-molecules and many others [103]. This numerical method allows to reproduce the properties of a system of interacting particles by solving their Newton's equations of motion that for a simple system of N atoms can be written as

$$m_i \frac{\mathrm{d}^2 \vec{r}_i}{\mathrm{d}t^2} = \vec{F}_i(\vec{r}_1, \vec{r}_2, ..., \vec{r}_N), \quad i = 1, 2, ..., N \tag{4.3}$$

where $\vec{r}_i$ are the position vectors; the forces $\vec{F}_i$ acting on the atoms and the potential energy $V(\vec{r}_1, \vec{r}_2, ..., \vec{r}_N)$ of the system for the specific arrangement of the particles are related in this way:

$$\vec{F}_i(\vec{r}_1, \vec{r}_2, ..., \vec{r}_N) = -\nabla_{\vec{r}_i} V(\vec{r}_1, \vec{r}_2, ..., \vec{r}_N) \tag{4.4}$$

If no external forces are present, the potential can often be expressed as a sum of pairwise interactions:

$$V = \sum_{i=1}^{N} \sum_{j>1}^{N} u(r_{ij}) \tag{4.5}$$

where $r_{ij} = |\vec{r}_{ij}|$ and $\vec{r}_{ij} = \vec{r}_i - \vec{r}_j$; $j > i$ means that the interactions between pair of particles are counted only once. In this case, the forces are thus expressed by counting the interaction of the individual particle with all the others in the system:

$$\vec{F}_i = \sum_{j \neq i}^{N} \vec{f}_{ij}, \quad \vec{f}_{ij} = -\frac{du(r_{ij})}{dr_{ij}} \cdot \frac{\vec{r}_{ij}}{r_{ij}} \tag{4.6}$$

and we recall that $\vec{f}_{ij} = -\vec{f}_{ji}$; the numerical effort to solve the Newton equations 4.3 varies as N^2. A basic technique to reduce the computational effort is to introduce a cutoff distance in the potential, beyond which the contributions are neglected. The microscopic information such as the atomic positions $\vec{r}$ and velocities $\vec{v}$ that describe the time evolution of the system in phase space, are then used to calculate the microscopic quantities through statistical mechanics. Such properties are then averaged along a sufficiently long trajectory to get the corresponding macroscopic quantities.

Time integration

The analytic solution of the resulting system of equations is not possible because of the many-body nature of the problem. Therefore, the strategy is to adopt discrete time step δt and numerically solve the equations. The integration of Eq. 4.3 is performed using the Velocity-Verlet numerical integrator [103] that is based on a Taylor expansion of the position vector in time:

$$\vec{r}_i(t+\delta t) = \vec{r}_i(t) + \frac{\mathrm{d}\vec{r}_i}{\mathrm{d}t}\delta t + \frac{1}{2}\frac{\mathrm{d}^2\vec{r}_i}{\mathrm{d}t^2}(\delta t)^2 + \mathcal{O}((\delta t)^3). \tag{4.7}$$

Using $\vec{F}_i(t) = m_i\frac{\mathrm{d}^2\vec{r}_i}{\mathrm{d}t^2}$ to replace the acceleration with the force we obtain the Velocity Verlet Algorithm:

$$\vec{r}_i(t+\delta t) = \vec{r}_i(t) + \frac{\mathrm{d}\vec{r}_i}{\mathrm{d}t}(t)\delta t + \vec{F}_i(t)\frac{(\delta t)^2}{2m_i} \tag{4.8}$$

$$\vec{v}_i(t+\delta t) = \vec{v}_i(t) + \frac{\delta t}{2m_i}\left[\vec{F}_i(t) + \vec{F}_i(t+\delta t)\right] \tag{4.9}$$

This algorithm is one of the most frequently used in molecular simulations because of its ease of implementation. A general strategy is the following:

1. Given the positions and the velocity at one time t, compute the forces acting on each particle.
2. Update the positions (Eq. 4.8).
3. Partial update the velocity using the current forces $\vec{v}_i = \vec{v}_i + \vec{F}_i(t)\frac{(\delta t)}{2m_i}$.
4. Compute the new forces $\vec{F}_i(t+\delta t)$ using the new positions $\vec{r}_i(t+\delta t)$.
5. Update again the velocity $\vec{v}_i = \vec{v}_i + \vec{F}_i(t+\delta t)\frac{(\delta t)}{2m_i}$.
6. Iterate 1.

The integrator that we use should be able to preserve the time reversibility property of the equation of motion, i.e. changing the sign of the velocities should result in a trajectory that re-traces itself. The Verlet algorithm and its variants satisfy this property. To start the simulations, for each particle we have to provide :

- The initial position. A possible procedure is to start from a crystalline lattice or from a configuration already equilibrated.

- The initial velocity. Generally these are obtained randomly for each of the $3N$ components from a Maxwell-Boltzmann distribution at the desired temperature T:

$$\mathcal{P}(v_i) = \left(\frac{m_i}{2\pi k_B T}\right)^{\frac{1}{2}} \exp\left(-\frac{m_i v_i^2}{2k_B T}\right) \tag{4.10}$$

  whose form is a Gaussian with zero mean.

The problem that arises by selecting the velocities in this way is that the system can have a net non zero momentum and it is drifted; therefore to remove this effect one then has to shift the velocities.

Potential Cutoff

The crucial part of a MD program involves the computation of the potential energy of a given configuration and the forces acting on all particles. Some interatomic forces decrease quickly with distance (Van der Waals, covalent interactions etc.) therefore a common strategy adopted in MD simulations is to compute a potential cutoff which is the maximum distance at which the potential is still calculated; basically interactions between atoms separated by more than the cutoff radius r_c are ignored. The main two reasons to introduce this cutoff distance are: the fact that the number of pair interactions grows as N^2 and that since periodic boundary conditions (PBC) are applied we do not want an atom to interact with itself. However such truncation of the potential gives rise to the following artifacts:

- a fraction of the potential energy is excluded;

- discontinuities in potential energy surfaces and gradient since both the energy and the gradients present jumps at the cutoff distance.

The typical solution used to overcome the latter is to shift the potential, adding an additional function that zeroes the potential exactly at r_c. The same principle is then used for the derivatives.

$$u(r_{ij}) = \begin{cases} u(r_{ij}) & \text{if } r_{ij} \leq r_c \\ 0 & \text{if } r_{ij} > r_c \end{cases} \tag{4.11}$$

As we will discuss in Section 6.3 for the purpose of this Thesis we have to be sure that the physical quantities are not affected by such truncation, therefore we will present the correction we have designed that goes to zero at r_c together with several first derivatives of the potential.

Periodic Boundary Conditions (PBC)

MD is a method to predict and study the properties of a real system in bulk. However the majority of the samples consist of more than 10^{20} particles, therefore it would be impossible to carry out such computation due to the huge amount of memory required to store all the information. Therefore a possible solution would be to track only a small number of particles in order not to slow down the calculation, but this implies that most molecules are near the edge of the sample; this is called surface effect. To be sure that the surface effect has no influence on the bulk properties, one would have to use very large system size. The size of the system should be extremely large to ensure that the surface has only a small influence on the bulk properties; however, this system would still be too large to simulate. An easy example to see this is the following: a glass of water has a very large system size with respect to its surface, on the contrary, water in a drinking straw has a much smaller system size if compared to its surface. The solution to this issue is the use of periodic boundary conditions, in which virtual copies of the simulation box are placed around the main one (that is at the center); this is a smart way to form an infinite system. Therefore each particle has a virtual image in the different simulation cells and there is no need to store its information since it can be immediately recovered knowing the box length and the periodicity. When a particle leaves the central simulation box, its virtual image will enter from the opposite face; figure 4.6 represent a 2D sketch of the idea of the PBC. Finally the number of particles in the central box is conserved and the interactions among the virtual particles are not considered. The consequence of the use of the PBC is that each particle would interact also with its images, in addition to the other particles. However, this drawback is solved with the cutoff of the potential at a distance r_c, since the interaction of two particles at distance $r_{ij} > r_c$ is neglected. So in this case the strategy is to apply the minimum image convention, for which, among all the images of the particle one considers just the interaction with the closest one. The box size L therefore is chosen to be larger then $2r_c$ along each direction, so that the particle does not interact with its images.

Neighbor list

Another method to improve the efficiency of the computation is the use of the Verlet neighbor list. The basic idea is to keep the memory of the particles within a given cutoff distance of each other, and not to update this list every time. Atoms in fact generally move within a time step only smaller than 0.2 Å, thus their neighbors remain the same for many time steps. Therefore one can limit oneself to compute the interactions among the particles within the list. Therefore the list contains for each atom i the indices of all atoms j whose distance from atom i is smaller than some chosen distance $r_m > r_c$. Care should be taken in updating the list soon enough to prevent the situation where atoms coming from outside r_m should be interacting with the central atom i, while according to the neighbor list they are not.

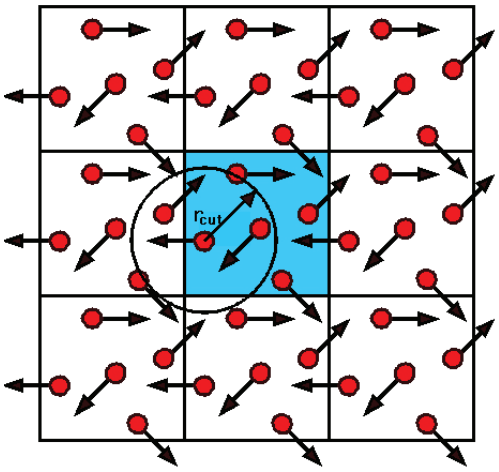

Figure 4.6: Schematic illustration of periodic boundary conditions in 2D. The calculated interaction is always with the closest image (minimum image convention): an atom can interact with one in the neighbor cell (which is an image of one of the atoms in the simulation cell) because it is within the cutoff radius r_{cut}. From [104].

4.3.2 Minimization Techniques

In order to understand the features of the TSs and verify whether they can represent a probe of the local structure of the PEL we have extensively used energy minimization algorithms. These optimization techniques are such that, given a function h depending on $3N$ independent variables (the coordinates of the particles), the value of those variables where h takes on a maximum or a minimum value is found. In particular the conjugate gradient (CG) method, described below, has been used to obtain

- the ISs configurations, starting from given low temperature istantaneous configurations $\vec{r} \equiv \{\vec{r^N}\}$ extracted from the dynamics;
- the valley and internal barriers that characterize the IS basin (Chapter 6).

In the following we give some details regarding the main concepts at the base of the implemented minimization techniques.

4.3.2.1 Steepest Descent method with line minimization

The simplest method to find the potential energy minimum is to follow the negative gradient of V through the steepest descent path of the PEL by solving the following differential equation (s is a curvilinear coordinate):

$$\frac{\mathrm{d}\vec{r}_i}{\mathrm{d}s} = -\vec{\nabla} V(\vec{r}) \tag{4.12}$$

Specifically each step of this procedure is usually implemented with a line (1D) minimization search in the direction of the negative of the gradient to determine the value x_{min} for which the energy $V(\vec{r}+x\vec{F})$ (where x is a 1D variable) is minimized. The configuration is therefore updated with the obtained minimum, $\vec{r}+x_{min}\vec{F}$, the new forces

are computed and this operation is iterated until the minimum (IS), that corresponds to the configuration for which $\vec{\nabla}V(\vec{r})$=0 is reached. The line minimization search consists of two steps:

1. *Bracketing the minimum* in an interval (0; x_{max}) where the minimum is supposed to be, using a first starting guess x_{guess} that, from the next iteration is then updated on the basis of the found minimum x_{min}. Here we briefly recall the meaning of bracketing a minimum in 1D. Suppose that we have a bracketing interval $(a;b)$; the function is then estimated in an intermediate point x to obtain a new, smaller bracketing interval, either $(a;x)$ or $(x;b)$ [105]. The iteration continues until the bracketing interval is below a certain tolerance value.

2. *Brent's Method* [106] that establishes the value of x_{min} within a certain tolerance *tol*. The idea to minimize a function h, is to generate some simple function $I(x)$ that interpolates h between its associated points. The Brent's choices for $I(x)$ are polynomials of degree 2 (parabolic approximation); this method makes the assumption that if the function is approximately parabolic near the minimum then the parabola fitted through the three points $a < x < b$ should lead to the minimum.

4.3.2.2 Conjugate Gradient (CG) method

The steepest descent method can be improved by implementing some techniques that go under the name of *conjugate gradient methods*. The basic idea is again to exploit the derivative information with line minimization to find the minimum, but this time choosing a direction that is conjugate to the old gradient (and not down to the new one) [105]. Therefore, for each minimization step j the line minimum in a direction $\vec{d}_j$ (3ND vector) is calculated taking into account the direction of the force $\vec{F}_j$ with respect to the gradients $\vec{g}_i = \vec{\nabla}V(\vec{r}_i)$ computed at the previous steps; the algorithm is here detailed:

$$\begin{cases} \vec{d}_1 = \vec{F}_1 \\ \vec{d}_j = \vec{F}_j + \beta_j \vec{d}_{j-1} \\ \vec{r}_{j+1} = \vec{r}_j + s_j \vec{d}_j \end{cases} \tag{4.13}$$

where the parameter s_j minimizes V along the direction $\vec{d}_j$ and the coefficient β keeps the information of the directions at the previous iterations. This latter can be considered as a good approximation of the Hessian if the variation of V is sufficiently small for each iteration. In our analysis we chose to implement the Polak-Ribière variant:

$$\beta_j = \frac{(\vec{g}_j - \vec{g}_{j-1}) \cdot \vec{g}_j}{\vec{g}_{j-1} \cdot \vec{g}_{j-1}} \tag{4.14}$$

that is generally recommended [105].

Chapter 5

Saddle Point finding algorithm for low dimensions

The main motivation of the numerical part of the Thesis is the search for the geometries suitable to be classified as TSs, with the features listed in Section 4.2 of the previous Chapter.
At the very first stage of this work, when the concept of tunneling *inside* the reliefs of the ISs basins was not yet establish, we also thought to study the TSs parameters by searching the DWPs of the "canonical" form, thus the sequence IS-SP-IS. As we discussed in Section 4.1, the SP search is an hard task in computer simulations, contrary to the ISs search that is accomplished by implementing steepest descent procedures (like those explained in Section 4.3.2). We discarded the possibility to set up one of the already available methods to find the SPs, because the majority of them require the full calculation of the Hessian matrix of the potential (which is computationally expensive) to evaluate the uphill path to reach the SP. Moreover we desired a method able to find the *nearest* (thus not generic) lowest saddle surrounding the local minimum, not to miss information that might be relevant to our TSs parameters search.
For this reason we decided to implement our own algorithm for the search of the SPs in bulk systems, starting with application tests on low (two) dimensional PEL, the Müller-Brown (MB) surface and a modified version (MMB). The present analysis allowed us to understand how to explore the multidimensional PEL of bulk systems and realize the search of the reliefs in the vicinity of the ISs, rather than the canonical SPs. Therefore, the concepts and results presented in this Chapter are needed to understand the very key algorithm of this Thesis: the EIS method (presented in the next Chapter) that led us to find reasonable results on the TSs search. The algorithm of this Chapter, the so-called "Biased Flattest Ascent" (BFA) method, able to find the SPs in 2D, has not yet been applied in 3*N*D for a BMLJ glass. However we believe that the BFA method has a good possibility of success also in higher dimensions. We provide the details of the novel algorithm in Section 5.1, describe the 2D employed surfaces in Section 5.2 and present the results in Section 5.3.

5.1 Method

For a given potential energy surface, the working principle of our approach is the minimization of a set of cost functions H_{BFA} built in a way that their local minima correspond to the critical points, or saddles, of V. As we will discuss in detail in the following paragraph, this method is based on the application of two main ideas:

1. Exit from the IS basin following upwards directions by adding to the local minimum a constant bias potential, hence increasing the energy. Leaving the basin of attraction of the IS in fact represents the first stage of a SP search, like e.g., in the "activation" phase of the ART method [107], where the system is pushed away from the minimum through the use of a modified force.

2. Follow the flattest ascent direction, i.e. the direction in which V increases the least, without computing the Hessian matrix. The "minimum eigenvector following method" [86] in fact assumes that the path leading to the SP point can be found by following the direction of the eigenvector corresponding to the lowest eigenvalue of the Hessian matrix of V. This method is very robust for the analysis of small clusters of LJ particles. However such method is not applicable to large system size since it requires the evaluation and inversion of the Hessian matrix ($\mathcal{O}(N^3)$ computation) at each iteration step.

The procedure that we present in this Chapter instead is similar to the "Biased Gradient Square Descent" (BGSD) method for finding transition states [108], where the selected function to minimize has the following form:

$$H_{BGSD}(r;\alpha,\beta) = \frac{1}{2}|V(r)\nabla|^2 + \frac{1}{2}\alpha(V(r)-\beta)^2 \tag{5.1}$$

α determines the bias strength and β is a selected energy level. The BGSD method is capable to find the SPs of V for a 2D system by: i) scanning over increasing values of β starting from the IS energy, and ii) simultaneously following the square gradient of the potential descent trajectory. The optimization of Eq. 5.1 is done by following the gradient of H_{BGSD}, reaching its minimum with a CG procedure. A useful approximation of the quantity $\nabla^2 V(r)\nabla V(r)$ that is needed to compute the gradient of H_{BGSD}, is performed without calculating the whole Hessian matrix. The innovative idea of the BFA is that the SP search is performed only by computing the potential energy (and not its derivative) in two distinct points of the PEL, like in the difference quotient estimation.

5.1.1 The BFA algorithm

The BFA SP finding method, exploits only the information of the spatial position of the starting minimum, or IS, and does not require the calculation of the Hessian matrix of the potential V. To understand the mechanism of the algorithm and what

we intend with the expression "flattest direction", consider a simple visualization of a basin of attraction around a 2D minimum, like the one represented in Figure 5.1. For the same isopotential line (e.g. consider the third one going up from the IS) we require that the position identified with the minimization of the cost function H_{BFA}, falls in the point A (which has the lower value of energy compared to the other points on the same isoline) and *not* in B (that represents the most unfavorable case where the potential is steepest).

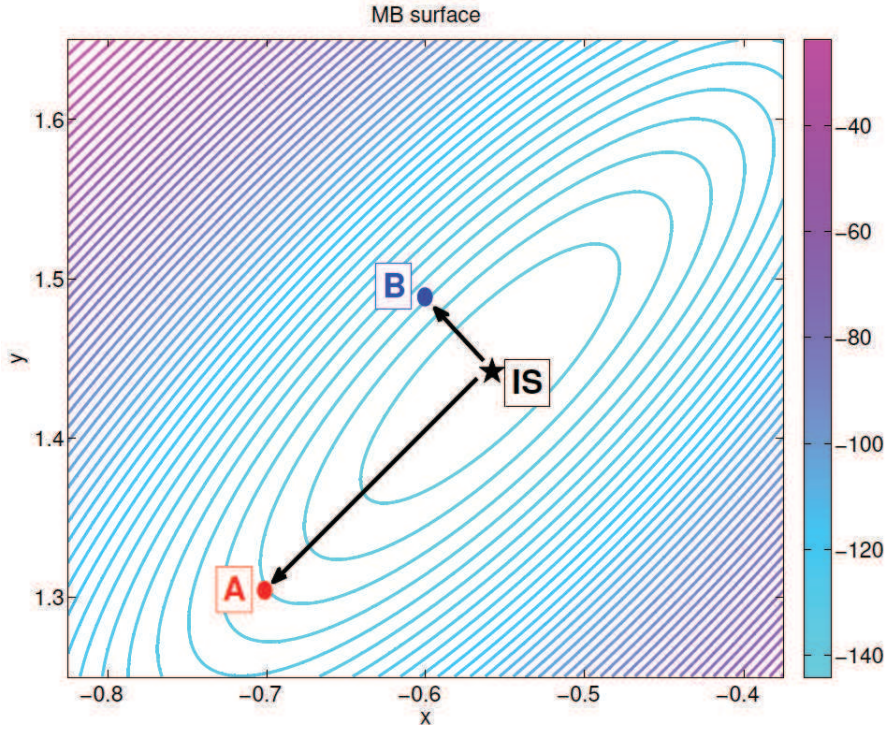

Figure 5.1: Visualization of the basin of attraction around a 2D minimum. The points A and B lie on the same isopotential line (the third one going up from the IS), but the slope at A is less than that one at B.

We can further simplify this concept using a 1D example; suppose to represent the two different profiles of the potential of Figure 5.1 associated with the A and B positions, with two parabolas 1D. The A profile is identified by the parabola with the smaller coefficient, and vice versa, the B profile is characterized by a greater coefficient (see Figure 5.2). Suppose then to select a specific height of the potential, β (which corresponds to every point belonging to a contour line in 2D), that intersects the two profiles in correspondence of the abscissa x_0: $V(x_0) = \beta$. In the following we show that our implemented 2D algorithm will select the abscissa which intersects the A profile at β height. In 1D, the function H_{BFA} has the following form:

$$H_{BFA} = (V(x) - \beta)^2 + (V(x+c) - \beta)^2 \tag{5.2}$$

where c represents a small constant. Using the approximation, $V(x_0+c) \approx V(x_0) + V'(x_0)c$ we can write

$$H_{BFA}(x) = (V-\beta)^2 + (V+V'c-\beta)^2 = 2(V-\beta)^2 + 2V'c(V-\beta) + (V')^2c^2 \quad (5.3)$$

Considering the expansion of H_{BFA} around a small interval δ we get:

$$\begin{aligned} H_{BFA}(x_0+\delta) &= 2(V(x_0+\delta)-\beta)^2 + 2(V(x_0+\delta)-\beta)V'(x_0+\delta)c + [V'(x_0+\delta)c]^2 \\ &\approx V'^2[2\delta^2 + 2\delta c + c^2] \end{aligned} \quad (5.4)$$

Therefore the derivative of H_{BFA} is minimized for $\delta = \frac{1}{2}$, thus we obtain that

$$H_{BFA}(x_0+\delta) = \frac{1}{2}c^2V'^2 \quad (5.5)$$

that means that H_{BFA} is proportional to the derivative of the potential, so that its minimization correspond to the selection of the smallest derivative.

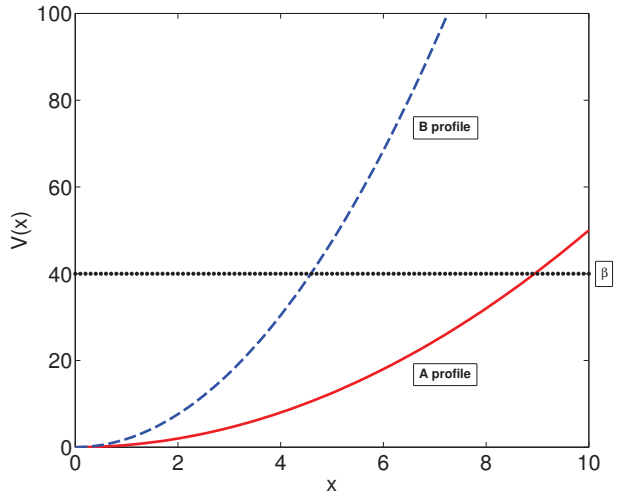

Figure 5.2: Representation of a 1D profile of the potential surface of Figure 5.1: the solid line indicates the A profile while the dashed line the B one.s

Once established that the minimization of H_{BFA}, for each level of β, follows the flattest path going out from the basin of a minimum, it is possible to extend the method to the case of more dimensions, by means of the following transformations:

$$\begin{aligned} x &\rightarrow \vec{X} \\ c &\rightarrow \Delta\hat{X} \end{aligned} \quad (5.6)$$

where $\Delta\hat{X}$ is a unit vector pointing from a reference point R, that we will specify in the following, to the current position of the configuration $\vec{X}$ in the PEL. Therefore, the general form of the H_{BFA} function is:

$$H_{BFA}(X) = \left[V(\vec{X}) - \beta\right]^2 + \left[V(\vec{X} + \Delta\vec{X}) - \beta\right]^2 \tag{5.7}$$

where the following conditions hold:

$$\begin{cases} \Delta\hat{X} = \dfrac{\vec{X} - \vec{R}}{|\vec{X} - \vec{R}|} \\ \beta = V(\vec{X}_{min}) + \Delta \end{cases} \tag{5.8}$$

The H_{BFA} function is minimized for each β value (representing the "level indicator" parameter that provides information on the height of the potential V with respect to the starting IS) which is increased each time by a constant interval Δ. At each iteration Δ is added to the value of the potential energy obtained by the previous minimization: $V(\vec{X}_{min})$ (note that for the first iteration $V(\vec{X}_{min}) = V(\vec{X}_{IS})$, where $\vec{X}_{min}$ represents the minimized configuration and $\vec{X}_{IS}$ the IS ones). In this way we minimize the energy function also keeping the memory of the spatial information; this trick ensures that, e.g. in the case of a glassy landscape, we can always check if the minimization procedure has not moved the system to a point of the configuration space "far" from the starting IS. From Equation 5.7 we expect that the resulting minimized configuration is a compromise between the minimization of the two terms. In fact:

- The first term is minimized when $V(X) = \beta$ and therefore in the 2D case this condition is verified by all the coordinates that belong to that specific potential contour isoline. As already explained this term alone does not suffice to find the SP since the identification of the flattest surface profile requires the additional information related to the gradient.

- The second term is minimized when $V(\vec{X} + \Delta\vec{X}) = \beta$, hence when $\frac{X-R}{|X-R|}$=0. This means that among the points that belong to the same isoline (condition given by the minimization of the first term), the algorithm will choose the one located at a fixed distance from the reference R, characterized by the lower value of the potential energy.

A reasonable choice for tuning H_{BFA} is to take an increment Δ sufficiently small to ensure that the β-level will not jump over the SP, missing it.

To find the coordinates of the minima we use the conjugate gradient minimization procedure described in the previous Chapter, and then we sample 16 initial points at a fixed distance from the IS. We then start the minimization procedure of the H_{BFA} function from each of these points of the space. The reason for choosing so many input points is to ensure that the success of the algorithm is independent from the starting position. We iteratively apply the BFA algorithm monitoring the values of the different

terms and the $W = |\nabla V|^2$ quantity for each value of β. When the square gradient of the potential becomes zero it means that the SP is found. A rough alternative is to stop the algorithm when the slope of square gradient of the potential starts to decrease. At this stage in fact, the basin of attraction has been overcome in the correct direction and we can proceed by performing only the minimization of the auxiliar potential W, using the approximation of the BSGD method (that does not require the calculation of the Hessian matrix). A priori the present method ensures that the climbing up in the potential with increasing β does not stop in quasi-saddles or inflection points (IP), since the probability that β is exactly equal to the SP height is very low.

5.2 2D potential surface

In this Section we introduce two different 2D potential surfaces that we can easily visualize and therefore use as test problem to compare the performance of the different variants of the local optimization algorithm. The first considered case is the Müller-Brown surface, whose properties have been extensively examined by Doye and Wales in [82]. The form of the potential is the following:

$$V_{MB}(x,y) = \sum_{i=1}^{4} A_i \exp[a_i(x-x_i^0)^2 + b_i(x-x_i^0)(y-y_i^0) + c_i(y-y_i^0)^2] \tag{5.9}$$

where

$$\begin{aligned} &A = (-200,-100,-170,15) \;\; a = (-1,-1,-6.5,0.7) \\ &b = (0,0,11,0.6) \;\; c = (-10,-10,-6.5,0.7) \\ &x^0 = (1,0,-0.5,-1) \;\; y^0 = (0,0.5,1.5,1) \end{aligned} \tag{5.10}$$

As a second test problem we use a modified Müller-Brown surface: the following function

$$V_{add}(x,y) = a_0 \sin(xy) \exp\left\{ \left(-\alpha\big((x-X_{is})^2 + (y-Y_{is})^2\big) \right\} \right. \tag{5.11}$$

with

$$\begin{aligned} &X_{IS} = -0.5582, \;\; Y_{IS} = +1.4417 \\ &a_0 = 500 \;\; \alpha = 0.1 \end{aligned} \tag{5.12}$$

was added to the original Equations (5.9), thus the total form of the analyzed modified MB potential is:

$$V_{tot}(x,y) = V_{MB}(x,y) + V_{add}(x,y) \tag{5.13}$$

The second choice for the potential surface is made in order to check that the algorithm does not depend on the size and location of the basin of the minima, therefore, we choose to shift the saddle point far away from the IS.

The contour diagrams of $V_{MB}(x,y)$ and $|\nabla V_{MB}(x,y)|^2$ are presented respectively in Figure 5.3(a) and Figure 5.3(b), while $V_{tot}(x,y)$ and $|\nabla V_{tot}(x,y)|^2$ are shown in Figure 5.3(c) and Figure 5.3(d).

5.3 Results

In the following we introduce the different versions of the algorithm that we performed to check its validity and eventual generalization to higher dimension systems. Note that the functional form of the algorithm is fixed (Equation 5.7). The versions we implement differs in the following quantities:

- $\vec{R}$: the 2D vector that indicates the reference point.
- $\vec{G}$: the 2D vector that indicates the initial guess starting configuration for the minimization.
- $\Delta\hat{X}$: the 2D vector that contains the spatial information being dependent on $\vec{X}$.

The results of the test with the different algorithms are reported in Figure 5.4 for the MB surface and in Figure 5.5 for the MMB surface.

The first version of the algorithm uses the following relations:

$$\vec{R} = \vec{X}_{IS}; \tag{5.14}$$

$$\vec{G} = \vec{X}_{min} - \frac{\Delta}{|\vec{F}(\vec{X}_{min(n-1)})|} \cdot \frac{\vec{F}(\vec{X}_{min(n-1)})}{|\vec{F}(\vec{X}_{min(n-1)})|} \tag{5.15}$$

Here a static reference point corresponding to the IS, $\vec{X}_{IS}$, is chosen, and the level β has been set to the potential energy evaluated at the minimization point found at the previous iteration. The initial configuration that we use as a guess for the optimization has been chosen in a way to exploit the information of the gradient, since we are using the forces $\vec{F}$. Note that in the optimization algorithm that we use to find the minimum configuration $\vec{X}$, we do not use $\vec{F}(\vec{X}_{min(n-1)})$ as a variable, but as a simple parameter (e.g. in the same way as $\vec{X}_{IS}$ is a parameter). This is a trick we perform so that we do not need the derivative of the forces (and hence the Hessian matrix). Finally, the prefactor $\frac{\Delta}{|\vec{F}(\vec{X}_{min(n-1)})|}$ represents a sort of difference quotient introduced to take into account the slope of the potential in that point of the configuration space. We find that this variant succeeds in the search of the SP if the shape of the basin of attraction is quite regular and smooth like for the MB case (see Figure 5.4(a)). However, if the saddle point is located in a region far from the IS, like in the MMB case, the algorithm fails (see Figure 5.5(a)).

To overcome this situation we try to set up a version with a dynamic reference point, e.g., by using the minimized configuration found at the previous iteration step. However it turns out that the climbing up trajectory overlaps the different isolines following a spiral path; we find that the algorithm is no more tunable and therefore not efficient. We therefore implement the second version:

$$\Delta\hat{X} = \left(\frac{\Delta}{|\vec{F}(\vec{X}_{min(n-k)})|} \cdot \frac{\vec{X} - \vec{R}}{|\vec{X} - \vec{R}|} \right); \quad \beta = V(\vec{X}_{min(n-1)}) + \Delta \tag{5.16}$$

$$\vec{G} = \vec{X}_{min} \tag{5.17}$$

$$\vec{R} = \begin{cases} \vec{X}_{min(n-k)} & \text{if } n > k \\ \vec{X}_{IS} & \text{if } n \leq k \end{cases} \tag{5.18}$$

introducing an "iteration parameter" k which has the following meaning: in the first set of iterations we keep the IS as the reference point, assuming an harmonic approximation of the basin of the minimum; then, after the k-th iteration we use the $(n-k)$-th previous configuration as a reference point. This second implementation of the BFA works well again for the case of a smooth potential like the MB surface (see Figure 5.4(b)), while as soon as the geometry is slightly asymmetric and irregular, like for the MMB, it fails (Figure 5.5(b)). Furthermore the choice of the k-parameter is not straightforward without the knowledge of the profile of the energy landscape, therefore this version is not suitable to be applied to high dimensional problems.

We implement the third version of the BFA method with a new definition of $\vec{R}$:

$$R = \frac{1}{k}\sum_i a_i \tag{5.19}$$

where $\vec{a}$ is a vector. At the beginning $\vec{a} = \vec{X}_{IS}$; then, after each minimization, the components a_i=a_{i+1} and $\vec{X}_{min}$ is replaced as last component of the vector.

$$\Delta\hat{X} = \left(\frac{\Delta}{|\vec{F}(\vec{X}_{min(n-1)})|} \cdot \frac{\vec{X}-\vec{R}}{|\vec{X}-\vec{R}|}\right);\ \beta = V(\vec{X}_{min(n-1)}) + \Delta \tag{5.20}$$

$$\vec{G} = \vec{X}_{min(n-1)} + \gamma_{new}\frac{\vec{Z}}{|\vec{Z}|} \ \text{ with } \ \vec{Z}\cdot\vec{F}(\vec{X}_{min(n-1)}) = 0 \tag{5.21}$$

with γ_{new}=$\gamma \cdot$ rand([-1,1]). This version is able to find the SPs for both the MB and MMB surface as shown in Figures 5.4(c) and 5.5(c).

We implement a fourth version of the BFA to check whether without the prefactor $\frac{\Delta}{|\vec{F}(\vec{X}_{min(n-1)})|}$ we could find the SPs. Therefore by using the relation

$$\Delta\hat{X} = \frac{\vec{X}-\vec{R}}{|\vec{X}-\vec{R}|};\ \beta = V(\vec{X}_{min(n-1)}) + \Delta \tag{5.22}$$

we obtain the final version of the BFA algorithm whose fraction of success (see Table 5.1) is: 16/16 (thus each of the 16 starting red points reach the saddle) for the MB surface, as shown in Figure 5.4(d), and 14/16 for the MMB surface, as presented in Figure 5.5(d).

In conclusion by using the BFA we show that the path that leads to the nearest SP does not always correspond to the path that we get following the direction of the eigenvector with the lowest eigenvalue of V. This consideration and the tools developed in the low dimensional case guide us to the next Chapter to address the issue of the TSs.

Müller-Brown surface	
Version	Success in finding SP
1	8/16
2	16/16
3	16/16
4	16/16

Modified Müller-Brown surface	
Version	success in finding SP
1	7/16
2	0/16
3	10/16
4	14/16

Table 5.1: Comparison of the fraction of success of the BFA algorithm applied to the MB and MMB surface.

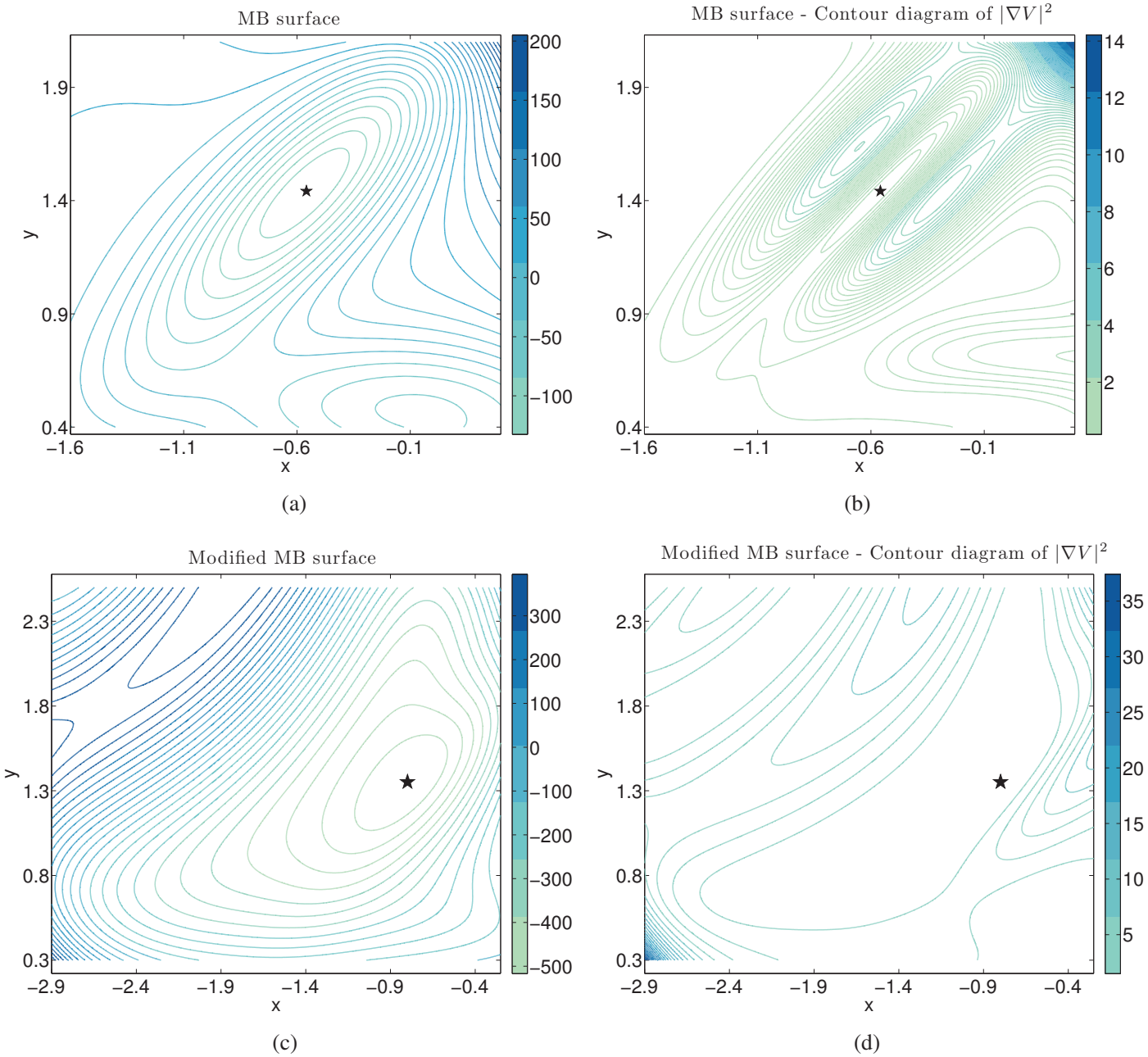

Figure 5.3: Contour diagrams of (a) $V_{MB}(x,y)$ and (b) $|\nabla V_{MB}(x,y)|^2$ for the MB surface. Contour diagrams of (c) $V_{tot}(x,y)$ and (d) $|\nabla V_{tot}(x,y)|^2$ for the MMB surface.

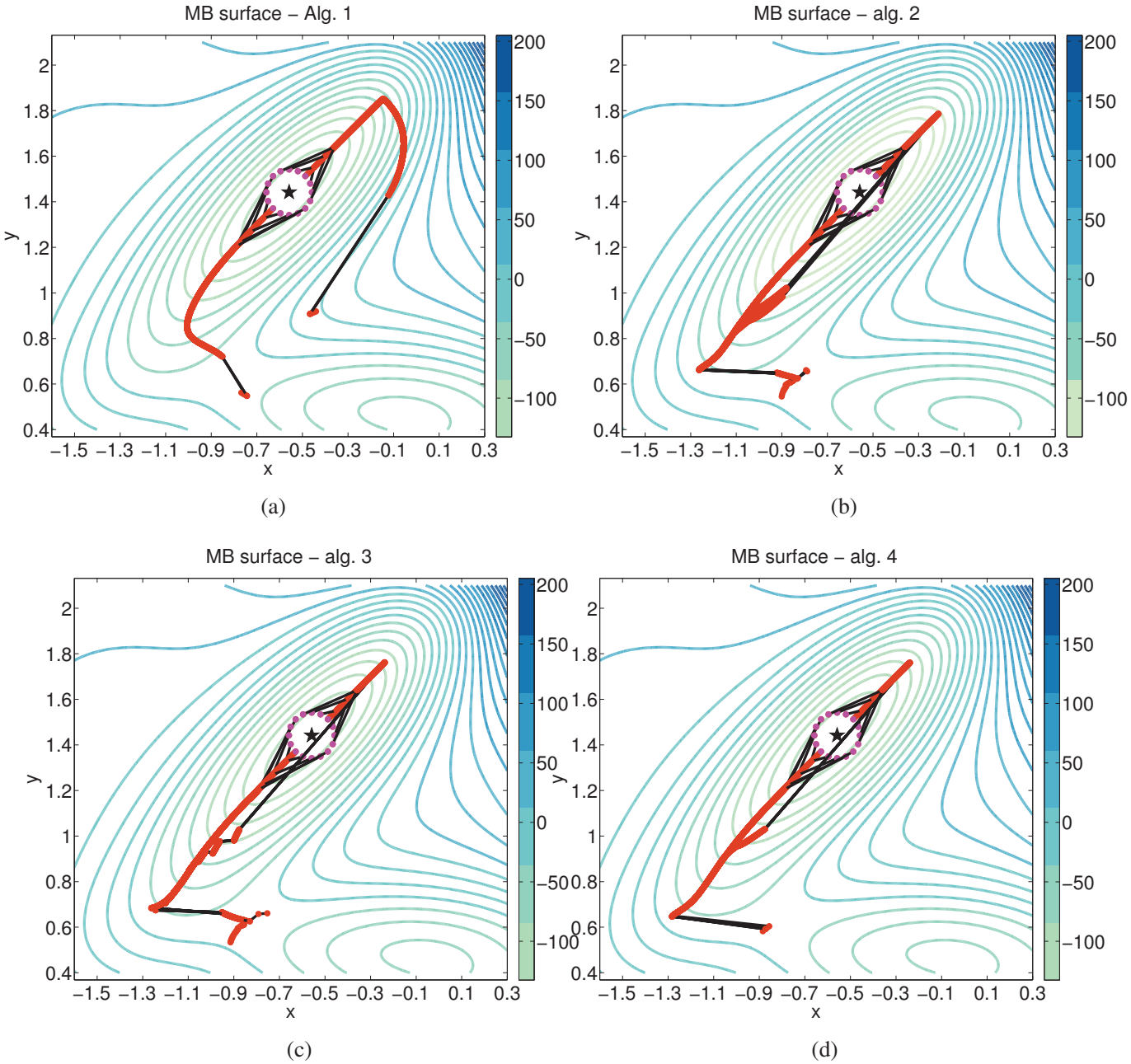

Figure 5.4: Application of the BFA method to the MB surface; the red points represent the path to reach the SP obtained for each specific variant of the algorithm.

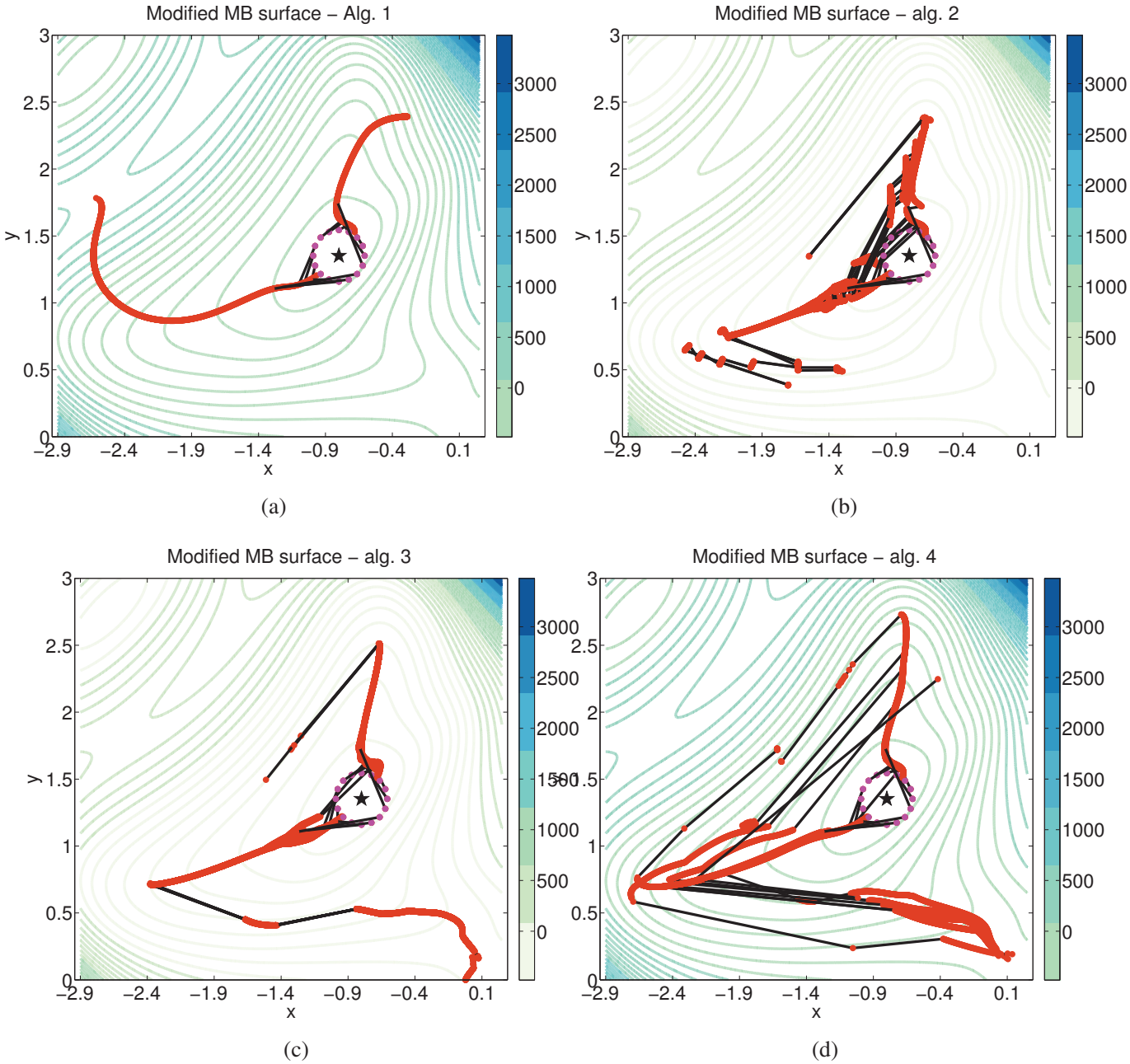

Figure 5.5: Application of the BFA method to the MMB surface; the red points represent the path to reach the SP obtained for each specific variant of the algorithm.

Chapter 6

The Effective Isopotential Surface (EIS) method

In the previous Chapters we discussed the possibility that the TSs are located in the barriers that exist within the basin of the ISs and the fact that the mere location of the SPs is not enough to characterize the PEL. As we can imagine, in fact, a given IS is associated to more than one nearby saddle and furthermore there is no guarantee to reach necessarily the SP by following the direction of the softest eigenvalue. Therefore, from the numerical point of view, in order to understand the suitable TSs geometries and thus subsequently the low temperature anomalies found experimentally, there is a need to perform local and systematic analysis of the *bottom* of the IS basin at very low temperatures. As discussed in Section 4.1, the useful information for our purposes, that we know from the literature, are that: i) around the glass transition temperature, the system moves quite close to the IS and ii) the majority of the saddles found is of order 1. Therefore, the new approach that we propose is the exploration of the ISs surrounding starting from configurations at the lowest temperature equilibrated so far (T=0.36 in LJ units, later defined) for a glassy BMLJ system. Therefore the ISs that we compute have a lower energy with respect to those analyzed in the previous investigations, allowing a more accurate low temperature study, fundamental in such analysis. We recall in fact that the PEL of a system does not depend on temperature but its exploration does: at such lower temperatures the sampling shifts to lower energies.

In Section 6.1 we describe the technical details of the new algorithm, the so-called "Effective Isopotential Method" (EIS), that allows the identification of the valleys within the basin of the ISs and their associated 3D mapping of the PEL. We report the results of the application of the EIS method for the case of i) a LJ face-centered-cubic (FCC) crystal, that we use as a starting test case (Section 6.2), and ii) a BMLJ glass at low temperature (Section 6.3). The preliminary comparison of the extracted geometrical parameters for the BMLJ glass with the experimental data is presented in Section 6.4.

The main results that we achieve with our analysis are the following:

- The hypothesis that the ISs are internally characterized by valleys is verified. In particular for the FCC crystal we find six *symmetric* valleys for a given IS

that are associated with a given particle (thus we have $6N$ valleys that start from one IS). Regarding the glass instead we discover that the majority of the particles that we looked at, have only two *asymmetric* valleys and most of them are connected to each other at an angle that is close to 180°. A smaller set of ISs is characterized by three *asymmetric* valleys that could be identified with the TWPs described by the ETM.

- The static 3D mapping of the $3N$D PEL surrounding an IS for a BMLJ glass at the lowest temperature has been performed, allowing for the first time the full visualization of the complex shape that characterize the landscape of such fragile systems.

- The order of magnitude of the extracted energy barriers among the valleys are in a good qualitative agreement with the experimental findings and therefore, in principle, we can speculate that the extracted geometries (valleys and barriers) could have the right features to allow the tunneling phenomenon.

The final goal to perform local analysis of the *bottom* of the IS basin at low temperatures to investigate its shape and systematically locate the paths/valleys has been accomplished. The next stage will be to verify whether the TSs can represent a probe of the local structure of the PEL and, therefore in this sense, contribute also to the phenomenology of the glass transition.

6.1 The working principle of EIS

The key idea of EIS to find the valleys that develop inside the IS basin is to use a minimization of a family of associated energy landscapes H with specific properties that depend on an *effective fixed distance* from two different configurations (generally the distance between a position belonging to the IS basin and the IS position itself).

But, what is a *valley*? To define this concept it is useful to refer again to the MB 2D surface example (discussed in Section 5.2) which uses "real" coordinates. We recall that the contour lines of Figure 6.1 represent the isopotential lines of the MB surface. A valley in 2D is a line that comes out from the IS and that has an energy that is lower than the energy of the surrounding, at the same distance R from the IS. Therefore, if we sample several points (marked with red dots in the Figure 6.1) equidistant from the IS (which is the only reference point we have) drawing a circle, and extracting the corresponding values of V, we are able to find the two valleys, i.e. configurations at a same distance from the local minimum that have lower energy. This means that the shape of the basin of attraction is not symmetric (because otherwise the isopotential line would be a perfect circle, which overlaps the red points) but instead, in this case, it has a stretched oval shape.

To understand qualitatively how to translate this concept in the configurational space, handling a $3N$D object, we now focus on Figure 6.2. If the basin of the IS had the shape of a symmetric paraboloid (Figure 6.2(a)) we see that the potential energy on

the black circle, that in this picture represents all the configurational points at a same distance from the IS, is constant (because it exactly coincides with the isopotential energy line). But if instead the shape of the potential basin is irregular and distorted, like the simplified case represented in Figure 6.2(b), where the symmetry is lost and there is a valley (right side of the paraboloid), then if we could be able to scan the PEL on the same black circle, we would register the presence of such channel pointing out from the IS: in correspondence of that part of the circle in fact the effective value of the potential is lower as indicated by the black arrows.

Later in the Chapter we will discuss in detail how to define the concept of fixed distance R between $3N$D configurations. All we need to know for now is that if we were able to get all the configurations of the phase space that surround the IS at a fixed distance R we could check whether each of such points would correspond effectively to an isopotential hypersurface, and thus obtain information about the topology nearby the IS. This is the basis of the *effective isopotential surface (EIS) method* that we implemented to map the basin of the PEL.

Last but not least, this type of analysis presents a practical difficulty, that is, how to get *all* the configurations of the PEL at a given distance from the IS by using a static approach. A possible solution would be to perform a statistical analysis generating a large number of random configurations e.g. starting from those obtained during the steepest descent path minimization procedure. However this way to proceed does not guarantee a complete analysis since the information on the part of the space phase we are exploring is random. The EIS method, that is presented in the next Section, is thought to systematically locate all the configurations near to the IS, and to verify the presence of valleys, getting a comprehensive view of the basin topology. To demonstrate that this method is efficient for this high dimensional mapping, we first present the results for a LJ crystal (Section 6.2) and then for a binary mixture LJ glass at low temperature (Section 6.3).

6.1.1 EIS - PART I: finding valleys

The purpose of the first part of the new developed algorithm is to locate the valleys that characterize the IS basin. In the first step we generate equilibrium configurations with parallel tempering simulations [109] at constant temperature and use them as starting configurations for a minimization procedure through the Polak-Ribière CG algorithm (presented in Section 4.3.2.2); in this way we get the corresponding set of energy minima, or ISs. In the second step the goal is to systematically generate all the configurations which can be associated with a nearby IS. Previous studies and our analysis show that the dynamics at low temperature is mainly driven by one particle that moves more than the others [9]. To get these configurations we use a local move where an atom is selected randomly from the IS configuration and slightly displaced in different fixed directions corresponding to equidistant points on a 3D sphere, thus giving new configurations. This is an approximation made to consider all possible moves of the particle in the space and the corresponding relaxation minima. In the

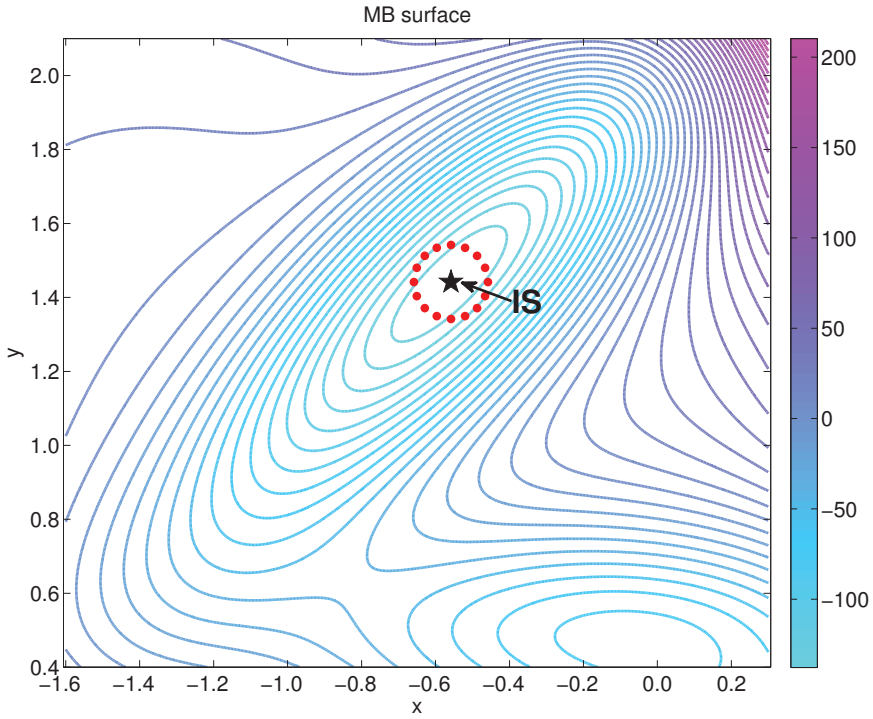

Figure 6.1: Contour diagrams for the Müller-Brown surface. The superimposed red dots represent the points equidistant from the IS minimum which is marked with a star symbol.

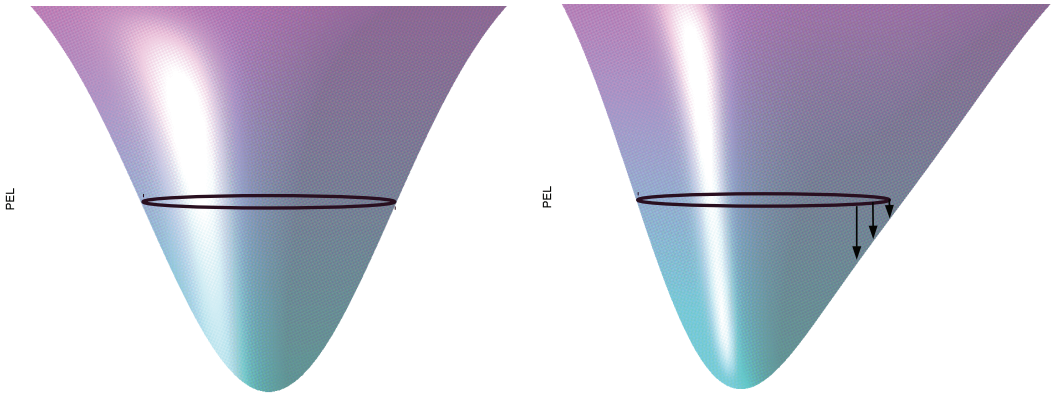

(a) (b)

Figure 6.2: Schematic representation of the basin of the IS for a system in the PEL framework. The vertical axis indicates the 3*N*D potential energy V; the minima of the two surfaces correspond to the IS energy e_{IS}; the horizontal direction represents collective configurational coordinates. a) Case of a perfectly symmetric and b) asymmetric basin. The black line represents an ideal path to scan the PEL which is at the same distance from the minimum: in b) the line is not perfectly adherent to the PEL since there is a lower valley that comes out, therefore the line of the scan falls to lower energetic points.

last phase we perform the minimization of the cost function to find the valley for each of the displaced configurations. Details:[4]

1. Select one particle M, defined by 3D vector $\vec{r}^{\,o}_{IS_M}$ from the IS configuration $\vec{X}^{o}_{IS} = \left(\vec{r}^{\,o}_{IS_1}, \vec{r}^{\,o}_{IS_2}, ..., \vec{r}^{\,o}_{IS_M}, ..., \vec{r}^{\,o}_{IS_N}\right)$; move M to the center of the simulation box: its new coordinates are $\vec{r}^{\,c}_{IS_M}=\left(\frac{L}{2}, \frac{L}{2}, \frac{L}{2}\right)$ where L indicates the box length. Arrange the positions of the other $N-1$ particles in this way:

$$\vec{r}^{\,c}_{IS_i} = \vec{r}^{\,o}_{IS_i} - \vec{dr}_{IS_M} \quad i = 1, ..., N \;\; (N \neq M) \tag{6.1}$$

where $\vec{dr}_{IS_M} = \vec{r}^{\,o}_{IS_M} - \vec{r}^{\,c}_{IS_M}$ is the displacement vector from the original $\vec{r}^{\,o}_{IS_M}$ to the centered position of M, $\vec{r}^{\,c}_{IS_M}$. Finally apply the PBC to the resulting configuration $\vec{X}^{c}_{IS} = \left(\vec{r}^{\,c}_{IS_1}, \vec{r}^{\,c}_{IS_2}, ..., \vec{r}^{\,c}_{IS_M}, ..., \vec{r}^{\,c}_{IS_N}\right)$. As we shall see, this rearrangement was made to simplify the visualization and analysis of results.

2. Construct a sphere, generating np=242 3D vectors[5] $\vec{r}^{\,k}_{sph}$, with $k = 1, ..., 242$ whose coordinates are represented by k red dots in figure 6.3. We define θ as the azimuthal angle in the xy-plane from the x-axis where $0 \leq \theta \leq 2\pi$, ϕ as the polar angle from the positive z-axis, where $0 \leq \phi \leq \pi$ and R is the radius from the origin (of coordinates (0,0,0)), which has been set to 1 in the schematic representation. Therefore using the Cartesian coordinate we have

$$\begin{cases} x = R\cos\theta\sin\phi \\ y = R\sin\theta\sin\phi \\ z = R\cos\phi \end{cases} \tag{6.2}$$

The θ and ϕ intervals are divided into 16 equal parts, respectively, $\Delta\theta$ and $\Delta\phi$: each pair of points of the sphere differs by $\Delta\theta$=22.5° and $\Delta\phi$=11.25°. In total there are: 15 xy-planes, each consisting of a circumference of 16 points, plus the two points of north and south poles that have the corresponding coordinates (0,0,1) and (0,0,-1); therefore in total there are k=(16·15)+2=242 points. The choice of such large value of k is made in order to have a good statistics in the sampling of the 3D sphere.

3. Generate 242 configurations 3ND, $\vec{X}_{IN} = \left(\vec{r}^{\,c}_{IS_1}, \vec{r}^{\,c}_{IS_2}, ..., \vec{r}^{\,c}_{IS_M} = \vec{r}^{\,1}_{sph}, \vec{r}^{\,c}_{IS_N}\right)$, with $k = 1, ..., 242$, where:

   - The $(N-1)$-th components, with $N \neq M$, are those of the IS configuration $\vec{X}^{c}_{IS}$.

[4]Note that in the following, 3ND vectors are denoted with capital letters while 3D vectors with lower-case ones.

[5]The choice np=242 is done in order to have a good statistics for the sampling of the configurations surrounding the IS.

- The M-th component takes the k-th value of $\vec{r}^{\,k}_{sph}$. This corresponds to move the particle M, from its position in the IS configuration (represented by the blue dot set at (0,0,0) in Figure 6.3) on each of the k points of the sphere, as shown by the black arrows.

4. For each of the k configurations $\vec{X}^k_{IN}$ minimize (with the CJ method described in Section 4.3.2.2) the following cost function:

$$H_1(\vec{X}_{1MIN};R) = \alpha\left(|\vec{r}_{1MIN_M} - \vec{r}^{\,c}_{IS_M}|^2 - R^2\right)^2 + V(\vec{X}_{1MIN}) \tag{6.3}$$

where α is a control parameter and $\vec{X}_{1MIN}$ is the $3N$D configuration under minimization (at the first iteration of the minimization procedure $\vec{X}_{1MIN} = \vec{X}_{IN}$; $\vec{r}^{\,c}_{IS_M}$ is fixed and $\vec{r}_{1MIN_M}$ is the 3D vector of the configuration $\vec{X}_{1MIN}$ corresponding to the particle M. Note that we use the squared modulus instead of the simple norm in order to simplify the problem, avoiding complicated calculations when computing the derivative of H_1;

$$\nabla H_1(\vec{X}_{1MIN};R)_i = 4\alpha\left(|\vec{r}_{1MIN_M} - \vec{r}^{\,c}_{IS_M}|^2 - R^2\right)\cdot(\vec{r}_{1MIN_M} - \vec{r}^{\,c}_{IS_M})_i + \nabla V(\vec{X}_{1MIN})_i \tag{6.4}$$

where $i = 1,...,N$ indicates the components of the vector (for fixed k). The basic idea behind the construction of such energy function is that the first term is minimized by those favorable coordinates that have a distance R from the IS, associated with the following condition: $|\vec{r}_{1MIN_M} - \vec{r}^{\,c}_{IS_M}| = R^2$; the second term instead makes that among these coordinates the one with the lowest potential energy is chosen. $\vec{X}_{1MIN}$ is therefore the configuration of the valley that comes out from the IS. To understand the effect of such minimization it is useful to refer again to the example of the 2D Müller-Brown surface, this time through the Figure 6.4 (which is nothing but the zoom view of the IS and the red points shown in Figure 6.1). The meaning of the red dots on the circumference and those on the 3D sphere is the same; the minimization of $H_1(\vec{X}_{1MIN};R)$ makes that each red point belonging to the 2D circumference is able to find the point of the neighborhood characterized by a lower value of the potential and a distance R from IS. Therefore, all the red points that before were equally distributed, after the minimization of $H_1(\vec{X}_{1MIN};R)$, collapse on one of the two valleys (indicated as $\vec{X}_{va}$ and $\vec{X}_{vb}$ in Figure 6.4) outgoing from the inherent structure (as schematically shown by the black arrows).

5. keep the center of mass fixed during the entire optimization.

Finally the control parameter α is proportional to the inverse of the width of the shell around the sphere scanned, i.e. α small makes that this width is large (and hence the valley is not located very precisely) and a large α makes that the width is very small. What we need is that α is large so that the first and second term are comparable. In fact, the first term should be a bit dominant, so that we have a handle on the distance.

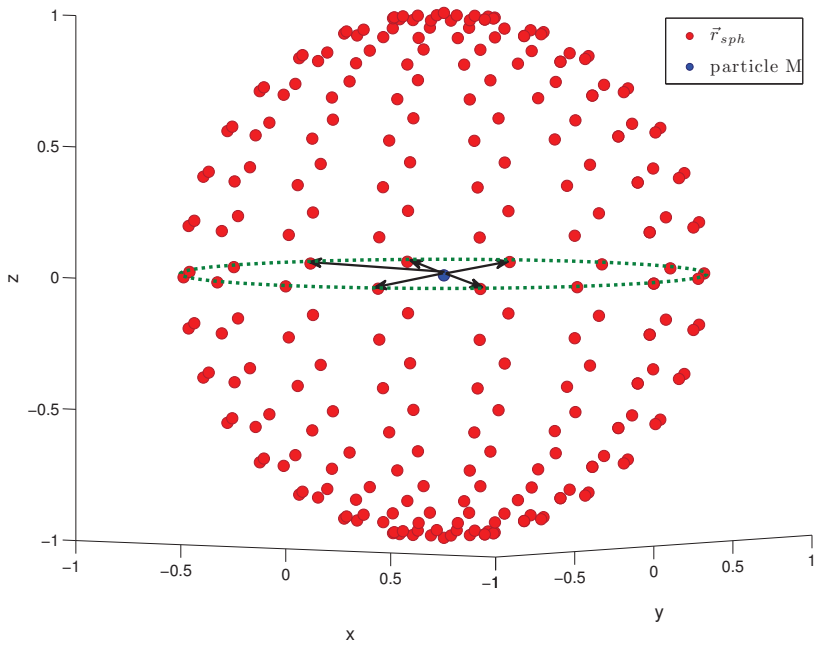

Figure 6.3: The red points represent the 242 coordinates of the sphere of radius R=1, on which the particle M (drawn in blue at the center of the sphere) will be moved.

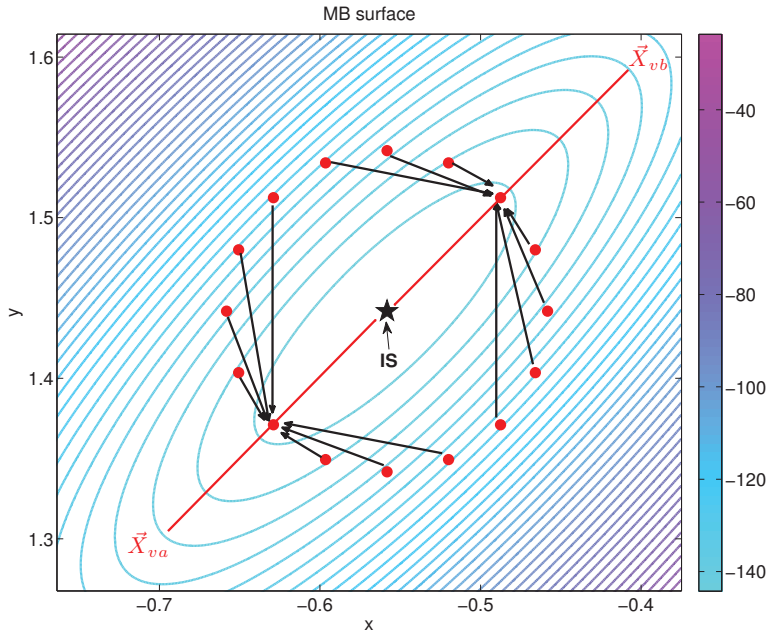

Figure 6.4: 2D schematic representation of the meaning of the minimization procedure of $H_1(\vec{X}_{1MIN};R)$: each initial red point of the circle collapses on the point of the neighborhood characterized by a lower value of the potential and a distance R from IS. As shown by the black arrows, after the minimization, the red points concentrates in two valleys $\vec{X}_{va}$ and $\vec{X}_{vb}$ outgoing from the inherent structure basin.

A good criteria to verify the correctness of the choice for α is to check that the optimal point satisfies the condition $|\vec{r}_{1MIN_M} - \vec{r}^{\,c}_{IS_M}| = R$, which means that the final point of the optimization should be R. A possible choice for α can be done in the following way: if we expand Eq. (6.3) around $|\vec{r}_{1MIN_M} - \vec{r}^{\,c}_{IS_M}| \approx R + \varepsilon$, with $\varepsilon \ll R$ we get:

$$\begin{aligned} H_1(\vec{X}_{1MIN}; R) &\approx \alpha\left(R^2 + 2R\vec{\varepsilon} + \varepsilon^2 - R^2\right)^2 + V(\vec{X}_{1MIN}) \\ &\approx 4\alpha R^2\varepsilon^2 + V(\vec{X}_{1MIN}) \end{aligned} \tag{6.5}$$

and since we know from the theory (and previous analysis) that the basin of the IS is harmonic, as a first approximation we can express $V(\vec{X}_{1MIN}) \approx V(\vec{X}^c_{IS}) + \kappa R^2$, where V_{IS} is the potential energy at the IS point and κ is the constant (which for simplicity we can take equal to $\frac{1}{2}$). Therefore the above equation can be written as:

$$H_1(\vec{X}_{1MIN}; R) \approx R^2\left(4\alpha\varepsilon^2 + \kappa\right) + V(\vec{X}^c_{IS}) \tag{6.6}$$

for the reasons we have explained we want that the first term has to be dominant; therefore by taking R=10^{-2} and $\varepsilon \approx 0.1R$ then we get that a possible choice is $\alpha = 10^9$. In particular, in our analysis, we apply twice the minimization of Eq. (6.3) using two different values of α: at the first iteration we choose an intermediate value of $\alpha = \alpha_1$, this allows us to initially roughly locate the valley; subsequently we use a large $\alpha = \alpha_2$ to find the minimum of the valley with greater precision ($\alpha_2 \gg \alpha_1$).

6.1.2 EIS - PART II: Finding barriers

In this Section we introduce the procedure to scan the energy landscape among the valleys nearby the IS that we have identified using the previous part of the algorithm (Eq. (6.3)). A priori we do not know how the shape of the neighborhood of the IS is made and how many valleys exist, ie configurations of the PEL at a distance R from the IS on which the potential has a local minimum.

For the sake of argument, suppose e.g. that the procedure described in the first part allowed us to find two different 3ND valleys in the PEL (hence characterized by different configuration and energy): $\vec{X}_{va} = (\vec{r}_{va_1}, \vec{r}_{va_2}, ..., \vec{r}_{va_M}, ..., \vec{r}_{va_N})$ and $\vec{X}_{vb} = (\vec{r}_{vb_1}, \vec{r}_{vb_2}, ..., \vec{r}_{vb_M}, ..., \vec{r}_{vb_N})$ where by construction the following relation holds:

$$|\vec{r}_{va_M} - \vec{r}^{\,c}_{IS_M}| = |\vec{r}_{vb_M} - \vec{r}^{\,c}_{IS_M}| = R. \tag{6.7}$$

How can we see if indeed these configurations correspond to local minima in the potential? The aim of the second part of the EIS method is to evaluate the structure in the neighborhood of these valleys. Always bearing in mind that moving in the landscape is not a trivial task, we intend to exploit two valleys as geometric reference to calculate the potential of all the configurations that separate them and which are situated on the effective isopotential surface, for the chosen fixed value R. If the value of the potential increases and then decreases going from $\vec{X}_{va}$ to $\vec{X}_{vb}$, ie if a local barrier is encountered, then we can assert that we have really found 3ND valleys. In the following we intend to perform a "scan" procedure of the value of V by using a geometric

construction with 3*N*D vectors between the two 3*N*D valleys, but not considering the Euclidean distance otherwise we would loose all the information regarding the location in the phase space. The strategy is to continue to exploit the constraint given by the distance *R*: for each configuration that connects the two valleys, the distance of the particle that moves the most (the one that we have shifted, *M*) from the IS should remain fixed to *R*. The technique that we propose here is to move *just* the *M* particle (thus the corresponding 3D position vector) on the shortest 3D path (an arc of a sphere) that connects its position in the 3*N*D valley $\vec{X}_{va}$ to its position in the 3*N*D valley $\vec{X}_{vb}$. The procedure is the following (refer to Figure 6.5):

1. Compute the vector connecting the two configurations of the 3*N*D valleys:

$$\vec{y}(s) = \vec{r}_{va_M} + s(\vec{r}_{vb_M} - \vec{r}_{va_M}) \tag{6.8}$$

where the parameter s varies between 0 and 1 (generally with a step equal to 10^{-3}), therefore the two extreme cases are

$$\vec{y}(s) = \begin{cases} \vec{r}_{va_M} \text{ if } s = 0 : M \text{ is in the } 3N\text{D valley } \vec{X}_{va} \\ \vec{r}_{vb_M} \text{ if } s = 1 : M \text{ is in the } 3N\text{D valley } \vec{X}_{vb} \end{cases} \tag{6.9}$$

$\vec{y}(s)$ thus corresponds to the vector that identifies the green dots (when s is increased) on the straight line that connects the two 3*N*D configurations of the valleys .

2. Compute the displacement vector $\vec{q}(s) = \vec{y}(s) - \vec{r}^{\,c}_{IS_M}$.

3. Give to such displacement the correct magnitude by normalizing the vector $\vec{q}(s)$ and multiplying it by R: $\vec{w}(s) = R \cdot \frac{\vec{q}(s)}{\| \vec{q}(s) \|}$; the norm is defined as: $\| \vec{q}(s) \| = \sqrt{\sum_{i=1}^{3} q_i^2(s)}$.

4. Sum the $\vec{w}(s)$ vector to the IS position: $\vec{l}(s) = \vec{r}^{\,c}_{IS_M} + \vec{w}(s)$; this step corresponds to the projection of the green points on the blue points on the arc.

5. Therefore, for each value of s we minimize the following cost function:

$$H_2(\vec{X}_{2MIN}; \alpha, R) = \alpha |\vec{r}_{2MIN_M} - \vec{l}(s)|^2 + V(\vec{X}_{2MIN}) \tag{6.10}$$

where $\vec{X}_{2MIN}$ is the 3*N*D configuration that is minimized, and $\vec{r}_{2MIN_M}$ are the coordinate of the corresponding particle M. At the first iteration ($s = 0$) $\vec{X}_{2MIN} = \vec{X}_{va}$ and $\vec{r}_{2MIN_M} = \vec{r}_{va_M}$; for the next iterations $\vec{r}_{2MIN_M}$ is given by the configuration minimized at the previous step. The parameter α is chosen in a way that the quantity $|\vec{r}_{2MIN_M} - \vec{l}(s)|$ is small. Therefore this function forces the system to stay on the arc of length R but at the same time choosing the minimum energy on the PEL. Here we write the derivative of Equation (6.10)

$$\nabla H_2(\vec{X}_{2MIN}; R)_i = 2\alpha \left(\vec{r}_{2MIN_M} - \vec{l}(s) \right)_i + \nabla V(\vec{X}_{2MIN})_i \tag{6.11}$$

6. Evaluate the potential energy $V(\vec{X}_{2MIN})$ corresponding to the minimized configurations as a function of the parameter s and verify if $\vec{X}_{va}$ and $\vec{X}_{vb}$ are really two valleys.

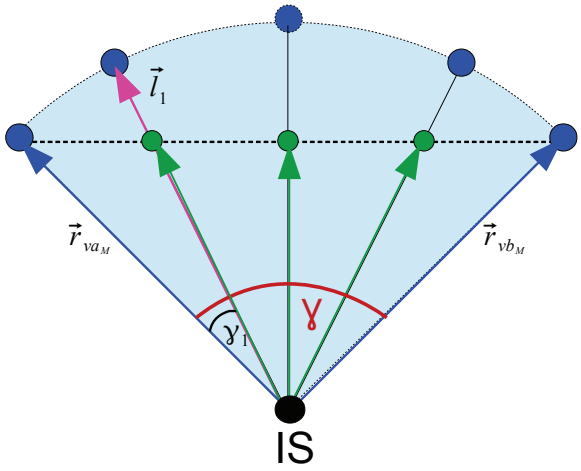

Figure 6.5: Schematic 2D representation of the EIS method part II: scan protocol between the 3*N*D configurations of the two valleys, $\vec{X}_{va}$ and $\vec{X}_{vb}$. The associated coordinates of the corresponding particle M, $\vec{r}_{va_M}$ and $\vec{r}_{vb_M}$ are indicated with blue dots. $\vec{y_1}$ is the vector corresponding to the first iteration of Equation 6.8, which for different s identifies the coordinates on the chord connecting $\vec{X}_{va}$ and $\vec{X}_{vb}$ (indicated with green dots); the displacement vector $\vec{q}(s)$ is indicated by green arrows. The orange dots, identified through the vector $\vec{l}(s)$, represent the projection of the displacement vector on the arc of circumference having radius R. Conceptually the latter dots represent the movement of M on the shortest path of the circumference (sphere in our case) that connects the two valleys. γ_1 is the angle between $\vec{X}_{va}$ and $\vec{l}_1$ (that is the value of $\vec{l}$ at the first iteration of the s parameter); the IS is located at the center of the circle.

We indicate with γ the angle between the 3D vectors $\vec{r}_{va_M}$ and $\vec{r}_{vb_M}$. The angles γ_s are defined between $\vec{r}_{va_M}$ and $\vec{l}(s)$ and are calculated using the dot product:

$$\cos(\gamma_s) = \frac{\vec{dr}_{va} \cdot \vec{dr}_l(s)}{\| \vec{dr}_{va} \| \, \| \vec{dr}_l(s) \|} \tag{6.12}$$

where the following are the displacements from the IS configuration: $\vec{dr}_{va} = \vec{r}_{va_M} - \vec{r}^{\,c}_{IS_M}$, $\vec{dr}_l(s) = \vec{l}(s) - \vec{r}^{\,c}_{IS_M}$ and $\| \ldots \|$ is the norm of the vector. By using the inverse cosine function, we determine the angles γ_s. In order to visualize the height of the barrier that separate the 3*N*D valleys, in the following plots we subtract from $V(\vec{X}_{2MIN})$ the value of $V(\vec{X}_{va})$ and we plot the scan of the potential as a function of the angle

that is formed from each vector $\vec{l}(s)$ with $\vec{r}_{va_M}$ until to reach the position defined by the vector $\vec{r}_{vb_M}$.

6.2 Results I: FCC LJ crystal

As a test case for applying the method described in the previous Sections, we have chosen a LJ FCC crystal. Partly, this choice is made because it is relatively easy to visualize the valley configurations due to the symmetry of the system and partly because we are interested to understand the choice of the magnitude of the control parameter α in order to extend our results to the case of the BMLJ glass (Section 6.3). The monoatomic A-type particles (for the sake of consistency with the later defined BMLJ system) interact via the usual LJ potential:

$$V(r_{ml}) = \underbrace{4\varepsilon_{AA}\left[\left(\frac{\sigma_{AA}}{r_{ml}}\right)^{12} - \left(\frac{\sigma_{AA}}{r_{ml}}\right)^{6}\right]}_{LJ-Potential} \underbrace{-4\varepsilon_{AA}\left(\frac{1}{r_c^{12}} - \frac{1}{r_c^{6}}\right)}_{Cutoff} \tag{6.13}$$

where r_{ml} is the distance between the particle m and l: $r_{ml} = |\vec{r}_m - \vec{r}_l|$. ε_{AA}=1.0 is the depth (i.e. the minimum) of the specific potential well, reached at r_w, and σ_{AA}=1.0 is the distance at which the inter-particle potential is zero; it can be shown that r_w=$2^{\frac{1}{6}}\sigma_{AA}$. Hereafter all the quantities will be expressed in LJ reduced units. The units of length and energy are: σ_{AA} and ε_{AA} (for more details see Table 6.1). The FCC LJ crystal (shown in Figure 6.6) is characterized by a lattice constant $a = 1.3$ and by $5\times5\times5$ unit cells (we recall that there are four atoms in the unit cell), therefore in total the simulation box contains 500 LJ atoms. (Note that the value a=1.3 has been chosen arbitrarily). We remark that the original interaction potential (Eq. 6.13) has been modified in order to ensure the continuity of the potential and its derivatives at the cutoff distance; as already discussed e.g. in [102] this is of fundamental importance to obtain a good convergence of the energy minimization procedure (presented in Section 4.3.2) that we extensively apply for the purpose of the present study. We will describe the details of this modification in Section 6.3 where we will present a general formula which is also suitable for this simplest case of the crystal. We first relax the crystal configuration through a minimization procedure to verify that corresponds to an IS, then we proceed implementing the first part of the EIS method by selecting the particle M at the center of the simulation box (marked with a red circle in Figure 6.6) and minimizing Eq. (6.3) with $\alpha_1 = 10^5$ and $\alpha_2 = 10^9$, with $R = 0.10$. These are in fact the optimal parameters that we obtained after a sequence of tests in which we varied both α and R over a wide range of values ($\alpha = 10^0 - 10^{10}$ and $R = 10^{-3} - 10^{-1}$). For the sake of brevity, we shall present the results of these tests only for the more complex case of the glass in Section 6.3.

The analysis of the results obtained with the first part of the EIS method shows that for each of the 242 minimized configurations, the particle M is the one that moves the most, satisfying the condition imposed by the algorithm: $|\vec{r}_{1MIN_M} - \vec{r}^{\,c}_{IS_M}| = R$; the

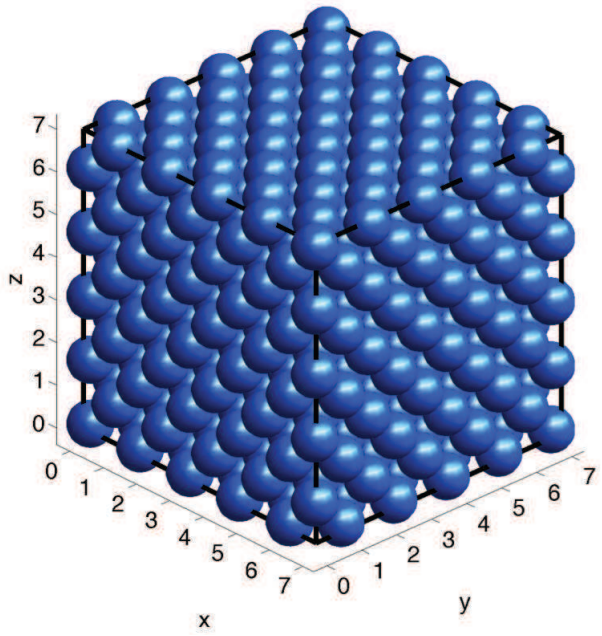

Figure 6.6: FCC LJ crystal with 500 LJ atoms; the central particle M has been selected and will be shifted on each of the 242 red points of the sphere of Figure 6.3.

other particles instead only move slightly and rearrange themselves from their starting positions. In order to understand what happened in this first stage it is useful to monitor the particle M, for example, studying the evolution of: a) its position in the 3D space and b) its energy, after the minimization. In the following we therefore present 3D plots that allow to visualize the displacement (normalized to R) of the particle M, $\vec{w}^k = R\frac{\overrightarrow{\Delta r_M}^k}{|\overrightarrow{\Delta r_M}^k|}$ (where $\overrightarrow{\Delta r_M}^k = \vec{r}^{\,k}_{1MIN_m} - \vec{r}_{M_{IS}}$), from the IS to its final position (after the minimization of H_1); in this representation the coordinates of the IS for the particle M are located at (0,0,0). An example of such plots obtained with the two step minimization (Eq. (6.3) using α_1 and α_2), is presented in Figure 6.7(a); the dots represent *all* the 242 displacement vectors $\vec{w}$ of particle M *after* the minimization. As we can see, all the initial configurations that were characterized by the displacement of the particle M on the different points of the sphere of radius R, are now relaxed (after the optimization of H_1) on just 6 symmetric regions, marked with blue dots; this is the signature of the presence of valleys in the neighborhood of the IS for a LJ crystal. Note that, as we will show in the next paragraph, the 12 green squares are not real valleys, but instead they coincide with the maximum of the barrier between the valleys. For the particular case of the crystal, the algorithm (part I) identifies these barrier points (17 % of the total cases) because of the symmetry of the problem. The identity (valley or barrier point), however, is checked also with the second part of the EIS method.

Figure 6.7(a), representing the same plot from different angles, clearly show us the symmetry of the six valleys which are located at 90 ° from each other. We will see that the path that connects this two valleys always passes through a green square, that represent the maximum of the barrier and is located at 45° from each valley, for the x, y, z directions.

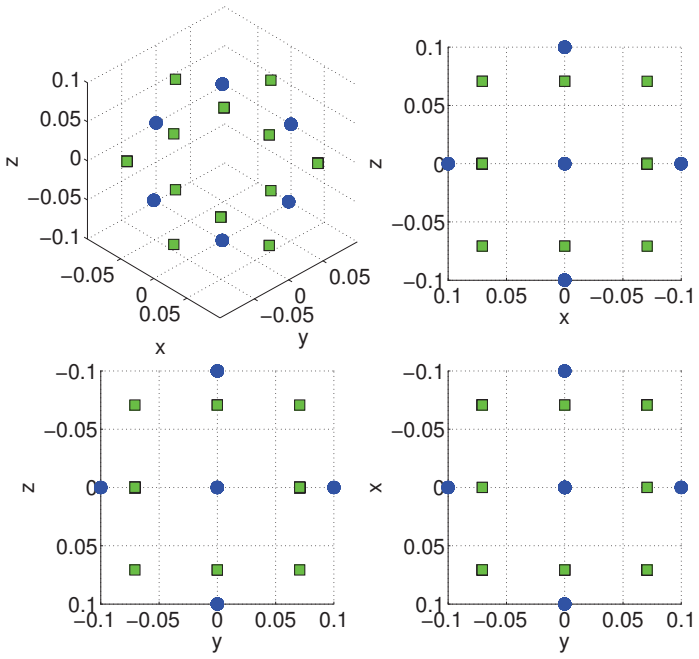

(a)

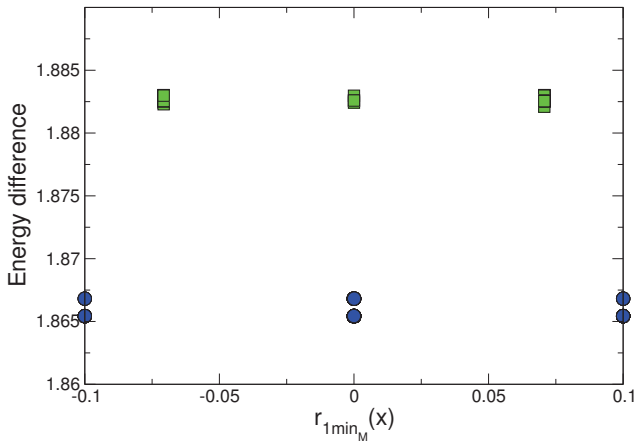

(b)

Figure 6.7: a) Position that the particle M assumes in the 3D space after the minimization of H_1 (Equation 6.3), using $R = 0.1$, $\alpha_1 = 10^5$ and $\alpha_2 = 10^9$; the 6 blue symmetric dots represent the geometrical organization of the associated valleys; in this case the 12 green squares identify instead the location of the maximum of the barriers (and not valleys) due to the symmetry of the problem. The same plot is shown from 4 different angles in order to clearly visualize the symmetry. b) Potential energy elevation from the IS value of the minimized configurations as a function of the x-coordinate of particle M for each of the 242 starting configurations; the blue dots of have lower energy than the green squares because they are valleys. All the quantities are in LJ reduced units (see Table 6.1).

By considering the corresponding plot of the total potential energy versus, e.g., the x-coordinate of the displacement of M, $\overrightarrow{\Delta r_M}$ for each value of k (Figure 6.7(b)) we find that the green dots have in fact an energy greater than the blue squares.

We now present the results obtained with the second part of the EIS method: this

procedure allows us to understand the morphology of the barriers and also to check that we found true valleys (characterized by lower energy potential than the neighborhood). For the configuration of the crystal we apply the protocol referred to in points 1. to 6. of Section 6.1.2 and we compute the value of the PEL on the path that connects each pair of consecutive valleys.

We found that not only there is symmetry with respect to the position of the valleys (as shown in Figure 6.7(a)) but also with respect to the energy. The plots of the scans of the PEL from valley to valley are symmetrical and characterized by the same initial and final energy. This is a further confirmation of the results found in Part 1, in fact, a priori it was not ensured to find such behavior. We also found that green squares actually correspond to the barriers and that are located exactly at 45° just half-way between two valleys.

This result is shown in the plot 6.8 reporting $V(\vec{X}_{2MIN})$ as a function of the angle γ_s. For clarity, we have represented just one scan from valley to valley (ie between two blue dots, black line) and one from the same initial valley to the barrier (ie between a blue dot and a green square, red line). Note that the two paths coincide exactly and also the scan of the potential energy on the paths that connect the other valleys are identical.

6.2.1 Analysis of the valleys and barriers as a function of R

We therefore analyze how these results vary with R, the distance of the particle M from the position in the IS configuration. The plot corresponding to the displacement of M after the minimization of Eq. (6.3) for R varying in the range 0.07-0.14 LJ units with a step of 0.01 LJ units is reported in Figure 6.9(a); note that there are 242 points

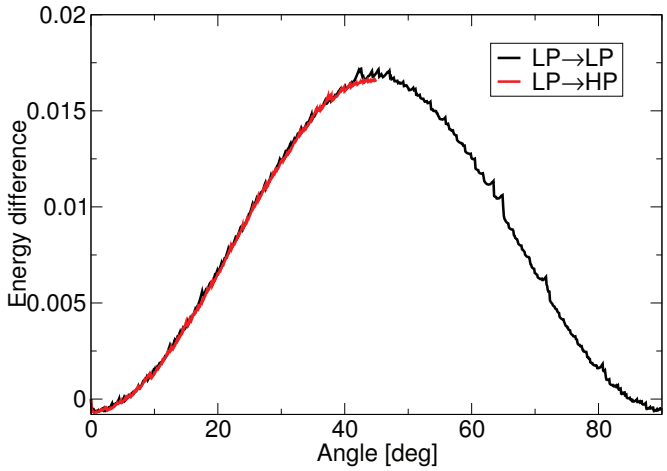

Figure 6.8: Plot of $V(\vec{X}_{2MIN})$ as a function of the angle γ_s scanning: i) the path going from the valley (or low point (LP)) to the barrier (or high point (HP)), LP→HP (the red line ends at 45 °), and ii) the path going from the same LP to the next LP, LP→LP (ie between two blue dots of Figure 6.7, black line ending at 90 °). R=0.1 and all the quantities are in LJ reduced units (see Table 6.1).

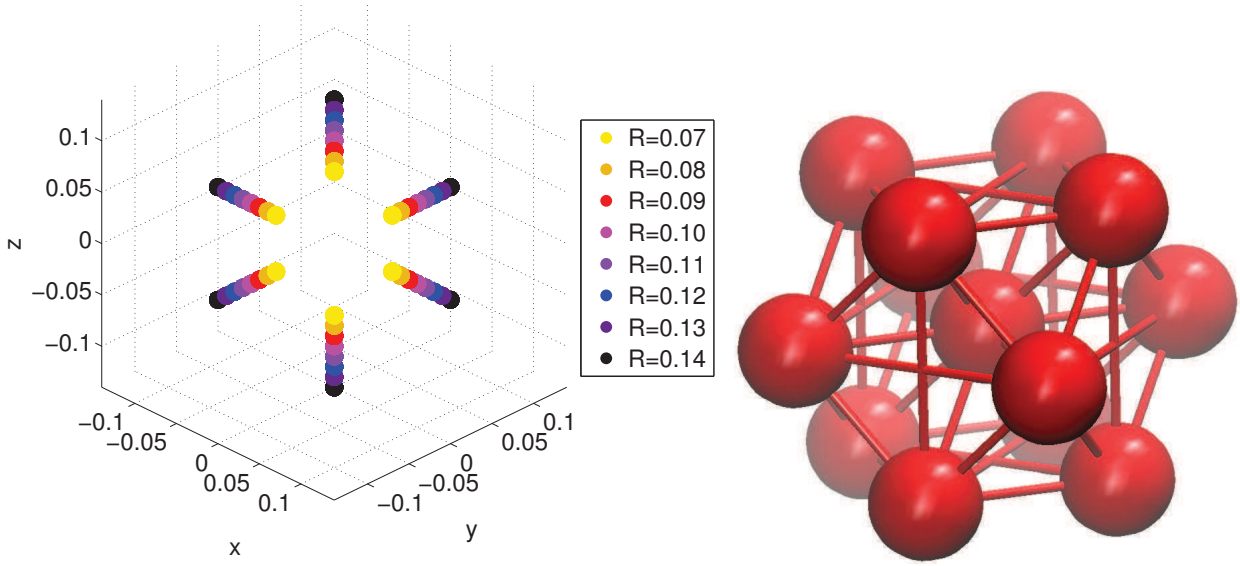

(a) (b)

Figure 6.9: a) Geometrical arrangement of the valleys for R that varies from 0.07 to 0.14; all the quantities are in LJ reduced units (see Table 6.1). b) Arrangement of the nearest neighbors (12 in a FCC) of the central particle M.

for each value of R. We can conclude therefore that there are 6 symmetric valleys that come out from the IS basin. For clarity we have just reported the valleys. In particular, for $R < 0.07$ we found no changes in the configurations, while for $R > 0.15$ we found a broadening of the cluster of particles, meaning that the valleys begin to disperse in a more complex geometry. A possible interpretation of this result is the following: we know that the valleys correspond to configurations equidistant from the minimum that have less energy on the same isoline. If we visualize the arrangement of the nearest neighbors (12 in a FCC crystal) of the particle M, we can conclude that M would prefer to move in one of the six directions in which the space between the neighbors is greater, that corresponds to lower energy configurations (represented by intersecting bonds in Figure 6.9(b)).

We now report the results of the scan between the $3N$D configurations of two of the six valleys found, $\vec{X}_{va}$ and $\vec{X}_{vb}$, performed with the second part of the EIS method (Eq. (6.10)). The vertical axis of Figure 6.10(a) reports the difference between the potential energy of the minimized configuration $V(\vec{X}_{2MIN})$ and $V(\vec{X}_{va})$, as a function of γ, the angle between the two vectors $\vec{X}_{va}$ and $\vec{X}_{vb}$, for different values of R. We report again only the result of the scan between two valleys since all the paths that connect the other ones have the same conformation due to the symmetry.

Finally in Figure 6.10(b) we report the same plot, but here the y-axis is rescaled to the peak value of each R: all the scans overlap and we find a master curve; this is an indication that the width (and the shape) of the valley is basically independent from R. Figure 6.11(a) instead presents the behavior of the potential energy difference as a function of R, for the valleys and the barriers; note the logarithmic scale. In order to better visualize such quantities, we plot the potential energy difference divided by R^2 (Figure 6.11(b)): the energy of both the barriers and the valleys has a nearly

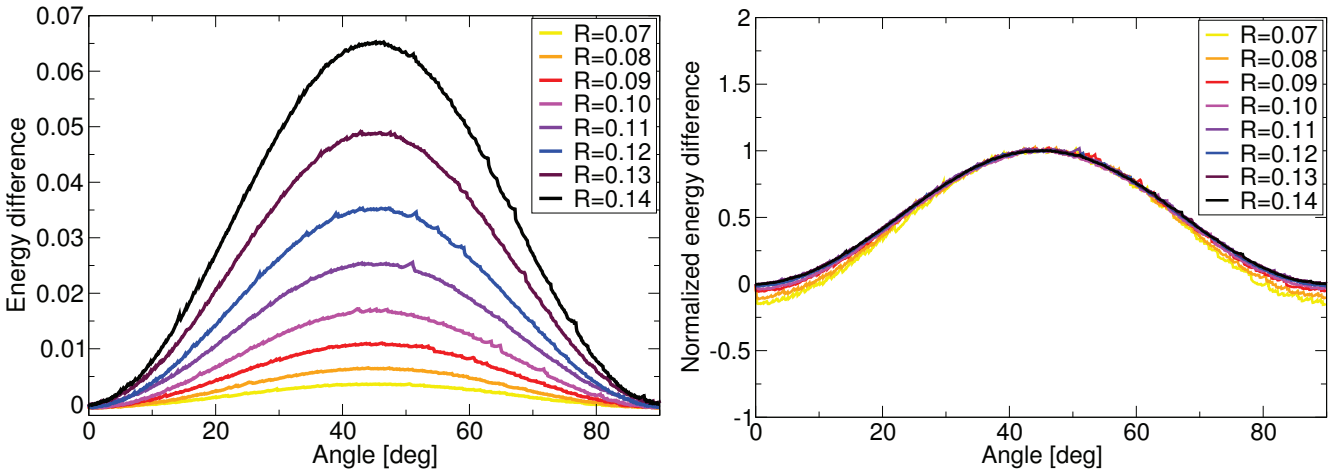

(a) (b)

Figure 6.10: a) Difference between the potential energy of the minimized configuration of the FCC crystal as a function of the angle between the two vectors, for different values of R. b) Master curve of the barrier between two different valleys. All the quantities are in LJ reduced units (see Table 6.1).

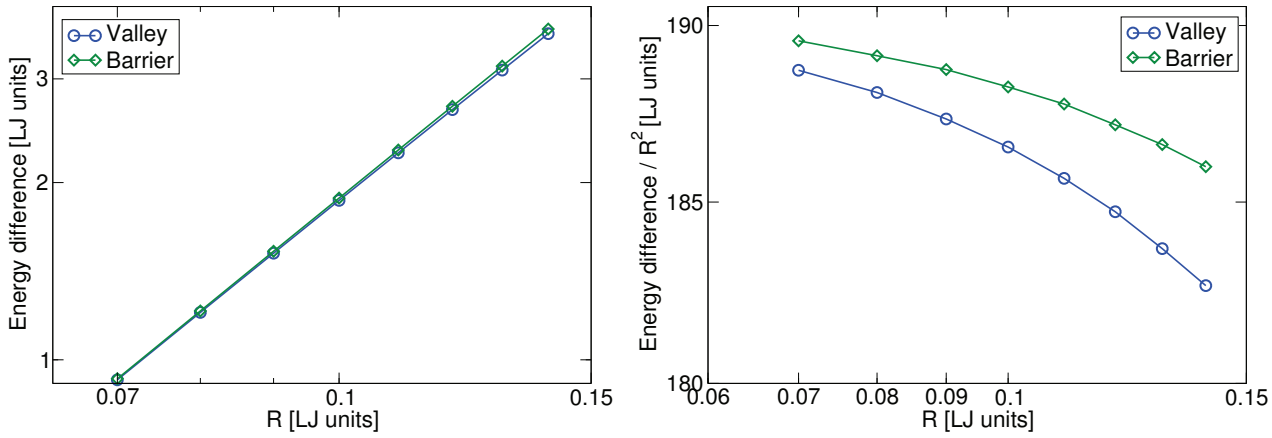

(a) (b)

Figure 6.11: a) Behavior of the potential energy difference as a function of R, for the valleys and the barriers. b) Potential energy difference rescaled for R^2. Both the vertical and horizontal axis of the two plots are scaled logarithmically. All the quantities are in LJ reduced units (see Table 6.1).

constant behavior for small values of R; for larger values the behavior of the valleys become increasingly non-constant and the barrier energy increases faster than that of the valleys. In conclusion, the EIS method allow us to analyze the energy landscape topography of a system of 500 LJ particles. We can state that the IS basin of a bulk crystalline material is characterized by 6 valleys of a single type, separated by barriers whose energy increases with R. We clearly find the evidence of the symmetry of the energy landscape since, for R fixed, all valleys are equivalent, as the barriers, located in this case midway between two valleys, in agreement with what hypothesized in [110].

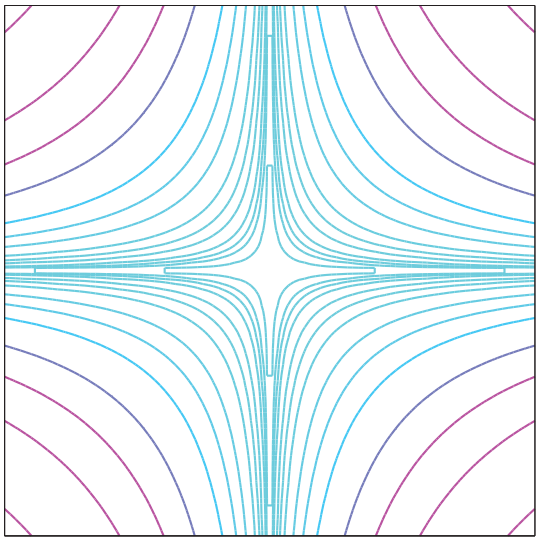

Figure 6.12: Cartoon of the contour map of a 2D energy landscape of a toy model; the IS basin is symmetric and characterized by four valleys outgoing from the IS (located at the center), and 4 barriers that connect them, with higher energy. In analogy with this plot, the 2D representation of the FCC LJ crystal landscape that we computed, is characterized by 6 equidistant valleys and barriers among them.

To better understand this result let us consider for the last time the analogy with a 2D case using the contour maps for a toy model (Figure 6.12); as we can see the inherent structure basin is completely symmetrical, characterized by four valleys that come from the IS (located at the center), and 4 barriers that connect them, with higher energy.

6.3 Results II: Binary Mixture LJ glass

The model of glass former that we consider in this Thesis is an 80:20 binary mixture of LJ particles, which has been extensively used mainly due to its ability to withstand strong supercooling without the occurrence of crystallization, together with its simple force-field formulation that allows low computational effort. This latter is a key aspect that allows faster development of new algorithms and their tests. It consists of two species of classical particles, A (80%) and B (20%) with the same mass m=1 interacting via the LJ potential:

$$V_{\alpha\beta}(r_{ml}) = \underbrace{4\varepsilon_{\alpha\beta}\left[\left(\frac{\sigma_{\alpha\beta}}{r_{ml}}\right)^{12} - \left(\frac{\sigma_{\alpha\beta}}{r_{ml}}\right)^{6}\right]}_{BMLJ-Potential} \underbrace{- 4\varepsilon_{\alpha\beta}\left(\frac{1}{r_c^{12}} - \frac{1}{r_c^{6}}\right)}_{Cutoff} \tag{6.14}$$

where α,$\beta \in \{A,B\}$ represent the indices of the type of particle and r_{ml} is the distance between the particle m and l (always considering the type α and β) $r_{ml} = |\vec{r_m} - \vec{r_l}|$; $\varepsilon_{\alpha\beta}$ is the depth (i.e. the minimum) of the specific potential well, reached at r=r_w, and $\sigma_{\alpha\beta}$ is the distance at which the inter-particle potential is zero. It can be shown that $r_{w_{\alpha\beta}}$=$2^{\frac{1}{6}}\sigma_{\alpha\beta}$. The interaction parameters that we consider are those of the classic mixture of Kob and Andersen [9], with the following set of parameters: ε_{AA}=1.0, ε_{AB}=1.5, ε_{BB}=0.5, σ_{AA}=1.0, σ_{AB}=0.8 and σ_{BB}=0.88; note the asymmetry in the diameters, $\sigma_{BB} < \sigma_{AA}$ so that particles B have a smaller diameter that particles A and energy scales: the AB interaction is stronger than both the AA and BB interactions. We report all quantities in LJ reduced units, that is, length in units of σ_{AA}, temperature T in units of ε_{AA} (setting k_B=1) and time t in units of $\sqrt{\sigma_{AA}^2 m/\varepsilon_{AA}}$. Most of the simulations have been performed for systems of N=1200 particles with a cubic simulation box of length L=10.0006, at three different temperatures T=0.36,0.37,0.40; PBC employing a cutoff radius r_c=2.5$\sigma_{\alpha\beta}$ have been implemented. The configuration of one IS at T=0.40 is presented in Figure 6.13, the A and B particles are represented respectively in blue and red color.

To extract the physical units from this model it is useful to refer to the original potential used by Stillinger and Weber that mimic the structure of the metallic Nickel Phosphorous alloy in the glassy state $Ni_{80}P_{20}$: σ_{AA}=2.218 Å, ε_{AA}=7765 J/mol and the temperature T=1 (LJ units)=933.9 K. The B particles correspond to P and the A particles to Ni. For the sake of clarity we list in Table 6.1 the conversion factors to apply the $Ni_{80}P_{20}$ units.

We now describe the modification we have made to the original interaction potential (Eq. 6.13). Since a minimization step is characterized by the movement of all the particle coordinates in the direction of the 3ND force vector, the discontinuity at r_c could cause problems in the evaluation of such a quantity, since as we know the total force acting on a particle i is given by the sum over all the forces of the particles j

$$F_i = \sum_{i}^{N} F_{i,j} \tag{6.15}$$

System of Units		
Physical quantity	LJ Units	Conversion factors for the $Ni_{80}P_{20}$ alloy
Length	σ_{AA}	2.218 Å
Energy	ε_{AA}	7765 J/mol
Temperature	ε/k_B	933.9 K

Table 6.1: System of units used in our simulations of particles interacting by the LJ potential. In LJ units k_B=1 is considered. The third column reports the conversion values for the BMLJ system [9] to the $Ni_{80}P_{20}$ metallic Nickel Phosphorous alloy in the glassy state.

In order to avoid the issues related to the convergence of the minimization algorithm, we introduce the following exponential smoothing function:

$$g_{\alpha\beta}(r_{ml}) = \mathcal{A}\exp\left(\frac{\mathcal{B}^2\sigma_{\alpha\beta}^2}{r_{ml}^2 - r_{c_{ml}}^2}\right) \tag{6.16}$$

where $\mathcal{A}$=1.1193 and $\mathcal{B}$=0.7500 are two parameters chosen in the way that the σ and ε parameters of the new potential interaction:

$$U_{\alpha\beta}(r_{ml}) = V_{\alpha\beta}(r_{ml}) \cdot g_{\alpha\beta}(r_{ml}) \tag{6.17}$$

are basically the same to those of the original form. The potential, the forces and their derivatives are continuous at r_c. Figure 6.14(a) presents the comparison of the BMLJ potential (labeled as "Potential") with the potential of Eq. 6.17 (labeled as

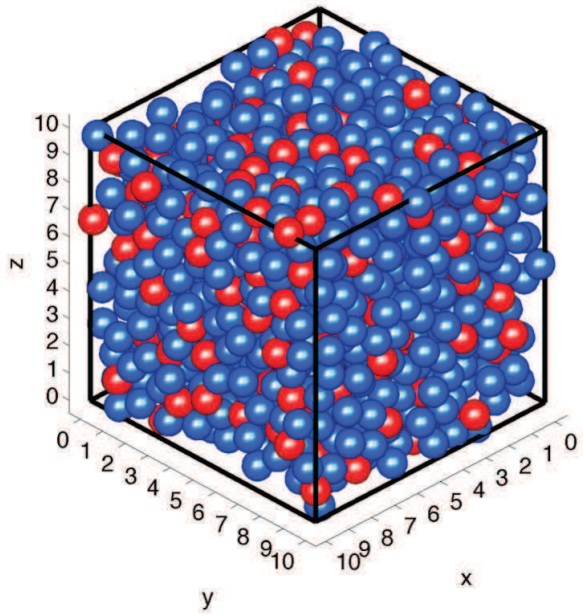

Figure 6.13: IS configuration for a BMLJ glass with 1200 atoms at $T = 0.40$; the central particle M has been selected and will be shifted on each of the 242 red points of the sphere of Figure 6.3. The A and B particles are represented respectively in blue and red color.

"New Potential") for the three types of interactions. Figure 6.14(b) is a zoom of the potentials at $r = r_c$. Figure 6.14(c) instead presents the comparison of the forces F for the two potentials and Figure 6.14(d) is the zoomed view of the forces at $r = r_c$. As we can see the two potentials match in the minima and the exponential correction affects only the vicinity of r_c, thus is a sense the implemented potential can still be thought of as BMLJ potential.

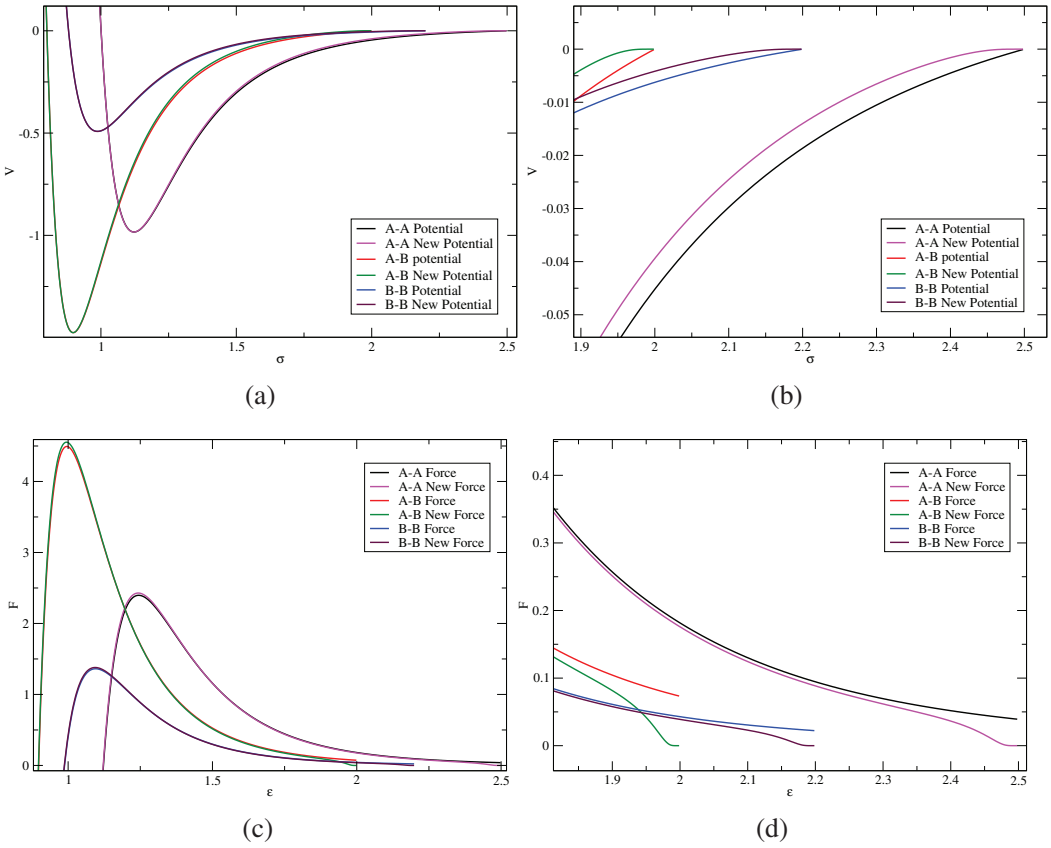

Figure 6.14: a) Comparison of the BMLJ potential ("Potential") with the potential of Eq. 6.17 ("New potential") for the three types of interactions, and b) zoomed view of the potentials at $r = r_c$. c) Comparison of the forces F for the two different potentials and d) zoomed view of the forces at $r = r_c$. All the quantities are in LJ reduced units (see Table 6.1).

Choice of α

First we report the tests implemented to study the magnitude of the control parameter α; we performed the minimization of the first part of the EIS method (Equation 6.3) for $\alpha_1 = 10^3, 10^4, 10^5, 10^6$ and fixed $\alpha_2 = 10^9$ for two different values of the radius $R = 0.04, 0.10$. The first aspect to check in order to verify the correctness of

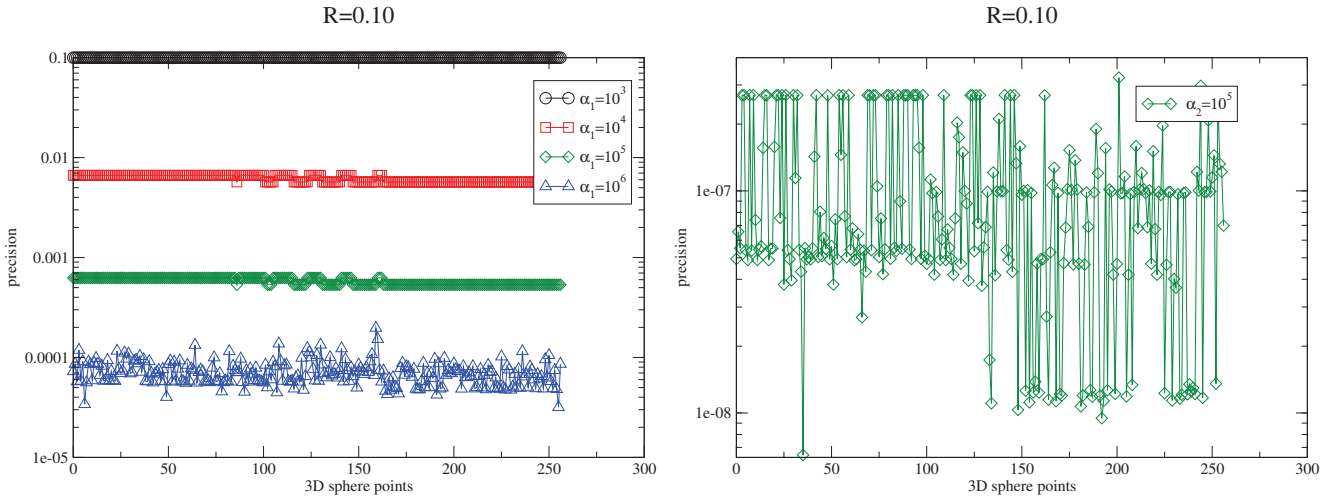

Figure 6.15: Precision of the algorithm minimization in finding the valleys that surround the IS (T=0.4). a) First minimization of Equation 6.3 where different values of α_1 are reported and b) for the values $\alpha_1 = 10^5$ and $\alpha_2 = 10^9$. All the quantities are in LJ reduced units (see Table 6.1).

the algorithm is that at the end of the minimization of Equation 6.3 we find that

$$|\vec{r}_{1MIN_M} - \vec{r}^{\,c}_{IS_M}| = R \tag{6.18}$$

Figure 6.15(a) reports the value of the precision of such quantity for $R = 0.10$, for the different α_1; as we can see the error for $\alpha_1 = 10^3$ is almost 0.10, hence of the same magnitude of R. This means that such value of α is not suitable for the algorithm since the two quantities have the same value. Increasing the value of α we can obtain a better precision, so that both $\alpha_1 = 10^5$,10^6 are reasonable to initially locate the presence of the valley. In particular we choose $\alpha_1 = 10^5$, in fact as we can see in Figure 6.15(b) the precision at the second iteration, with $\alpha_2 = 10^9$, is of the order of $5 \cdot 10^{-7}$.

Figure 6.16 reports the potential energy versus the x-coordinate of particle M for each of the 242 configurations for the different values of $\alpha_1 = 10^4, 10^5, 10^6$, for two different values of $R = 0.04$ (Figure 6.16(a)) and $R = 0.1$ (Figure 6.16(b)). We can conclude that all the points collapse in two different regions, therefore this indicates the presence of two valleys.

6.3.1 Standard cases

For the three temperatures analyzed (T = 0.36,0.37,0.40) we find that in the majority of cases each particle is associated with two almost straight valleys, like those represented in Figure 6.17; note that in the plot, all the 242 3D points obtained after the minimization of H_1 are represented for each value of R. Therefore, in the following we classify the presence of two valleys in the glass as "standard cases", in order to later distinguish all the other different geometries. Note that all 242 points for each value of R are displayed (they collapse in the two opposite green regions).

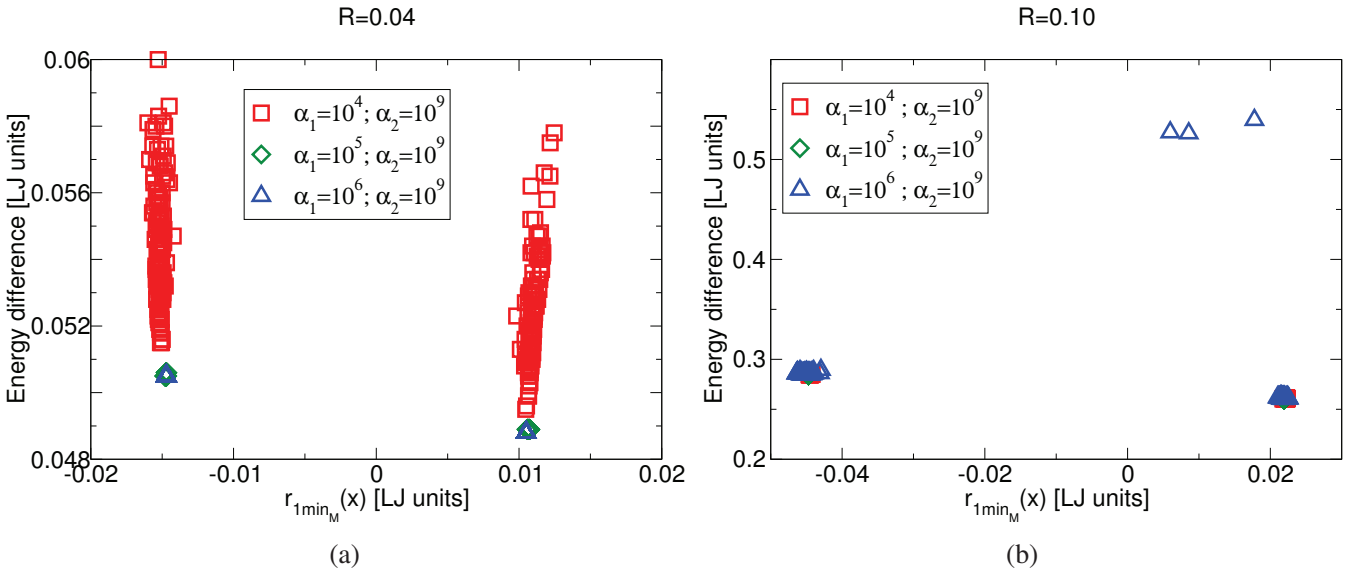

Figure 6.16: Potential energy versus the x-coordinate of particle M for each of the 242 configurations at T=0.4 for the different values of $\alpha_1 = 10^4, 10^5, 10^6$, a) for $R = 0.04$ and b) $R = 0.1$. All the quantities are in LJ reduced units (see Table 6.1).

We now report an example of scan between the 3ND configurations of two of the valleys found, $\vec{X}_{va}$ and $\vec{X}_{vb}$, performed with the second part of the EIS method (Eq. (6.10)). The vertical axis of Figure 6.18(a) reports the difference between the potential energy of the minimized configuration $V(\vec{X}_{2MIN})$ and $V(\vec{X}_{va})$, as a function of the angle between the two vectors, for different values of R by going from the valley $\vec{X}_{va}$ to $\vec{X}_{vb}$. As we can see, since the two valleys are not symmetric, for R small we have that the two paths are almost on a straight line (thus at almost 180° one from the other), while increasing R we find that the angle between the two valleys decreases by about 30° (R=0.14 with respect to R=0.02).

To verify the absence of other valleys (and so the correctness of the EIS method) we completed the scan procedure between the two valleys, considering all the configurations that lie on the circular path of radius R that connects the two valleys, associated with the complete angle (360°). The obtained closed trajectories for different values of R are presented in Figure 6.18(b). To perform the complete circumference, during the scan procedure we extract the configuration corresponding to the valley located in the middle between the two extremes; flipping the corresponding vector we obtain the reference configuration of the point $\vec{X}_c$, that a priori is not a valley. Then we perform the scan between the point $\vec{X}_{va}$ (the first valley that we consider) and $\vec{X}_c$ and between $\vec{X}_{vb}$ (the second valley that we have found) and $\vec{X}_c$; finally we merge the three trajectories and set $\vec{X}_{va}$ as the meridian 0. Note in fact that the points in the central region of Figure 6.18(b) are those of Figure 6.18(a).

Furthermore we present the dependence of the potential energy of the valleys and barriers (rescaled to the IS value) as a function of the distance R, respectively in Figures 6.19 and 6.20. In Figure 6.19(a) we show that the behavior of the potential energy

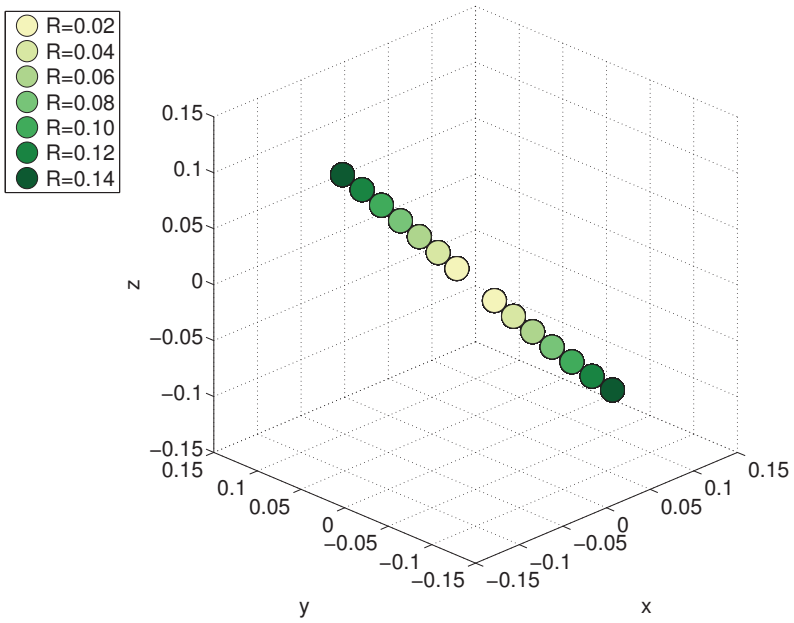

Figure 6.17: The two valleys associated to a given particle after the application of the EIS method. This is referred as the "standard case" since it represents the majority of the geometries found in our analysis.

difference $(V(\vec{X}_{1MIN}) - V(\vec{X}^c_{IS}))$ of the valleys increases quadratically with R; note the logarithmic scale on both axes. We report the same data, divided by R^2, in Figure 6.19(b), where we can see that for larger values of R, the behavior of the valleys deviates systematically from $\propto R^2$; the prefactor varies by a factor of 6, from 9 to around 60, therefore the slope of the valleys is not fixed but presents large fluctuations. We reach the same conclusions for the same plots referring to the barrier potential energy versus R. Since, as we have discussed, the valleys are not symmetric, we pick up the maximum value of the scan as the barrier value for the rescaling. Figure 6.20(a) shows that, also for the barriers, the potential energy difference increases quadratically with R. Reporting the same data divided by R^2 in Figure 6.20(b), we observe again that the behavior of the barriers is no longer constant for larger values of R; the range of the prefactor is smaller compared with the case of the valleys.

Displacement vector

We now want to understand what is the meaning of the presence of two valleys found for the case of the glass; therefore we compute the displacement vector from the configuration of a valley with respect to the IS and attach it to each particle in the IS configuration. For the sake of clarity we will show just the zoomed view on the cluster of particle that undergo the greater displacement (the particle M which is the one moved, is characterized by the largest magnitude of the vector and is represented at the center of figure), hence the nearest neighbors of particle M. The displacement vectors obtained after the minimization of H_1 are presented in Figure 6.21 and Figure 6.22 depending on whether the moved particle is of type A or of type B. In both Figures

T=0.40. The left side shows a side view, while the right side shows a top view where the vector corresponding to the particle M is perpendicular to the plane of the paper. The A and B particles are represented respectively in blue and red color. In both cases:

- We confirm that the shifted particle M is really the one that moves the most during the relaxation.
- The rest of the surrounding particles move less and almost in a transversal manner.
- The particles behind M (e.g., to its right in Figure 6.21(a) and 6.22(a)) move in order to occupy the space that is being freed up.

The main difference with the case of the FCC crystal is that now the relaxation after the particle displacement and the minimization of H_1, causes the movement of the particle towards another one, and not towards the empty spaces existing among them. This behavior suggests the possible existence of correlated 3ND vector fields, eventually associated with the gradient flow of the landscape.

6.3.2 Special cases

Approximately 10% of the cases analyzed so far[6] with the minimization of H_1, do not belong to the class of the "two standard valleys". Different geometries, or "special cases" have been found, also characterized by three valleys. In the following we report the "zoology" of the most significant cases, which mainly differ from the two, almost straight, geometric valleys. Figure 6.23 presents two different cases where one of the branches of the two main valleys further divides, following a λ-shape; note that in this case the third valley does not originate from the IS but only from a given distance R, a concept that is new and never observed so far.

Another type of valley arrangement is shown in Figure 6.24(a); we consider this as a special case due to the particular U-shape of the two branches. Performing the scan procedure with the minimization of the H_2 function (Figure 6.24(b)) in fact we find that the barrier among the two valleys, when traveling the shortest distance, has lower energy, with respect to the standard cases. Note the way in which the minimum of the second valley $\vec{X}_{vb}$ shifts towards the minimum of the first valley ($\vec{X}_{va}$), located at 0°.

Finally in Figure 6.24(c) we show the circular scan that we perform for different values of R (note that the scan between the two valleys is the same represented in Figure 6.24(b)). In this case we can also notice that the presence of a higher valley (that seems to develop at $R = 0.12$) is captured by the energy scan implemented with our method. A small barrier is in fact starting around 180°, whose signature is evident also from the isolated point of Figure 6.24(a).

[6]The goal is to apply the EIS method to all the particles of the sample to obtain the complete statistics. Such simulations (at the lowest temperature ever achieved for the BMLJ glass, T=0.36) are currently in progress and the results will be presented in the near future.

In the list of special cases, we add also the "right-angle" shape valleys characterized by two bent branches (the angle between the valleys is around 90°, smaller than the standard cases); one such example is shown in Figure 6.25(a). Also in this case the energy of the barrier is lower than the standard case (Figure 6.25(b)) when traveling the shortest distance on the arc of radius R connecting the two valleys. We report the result of the scan along the circle for different values of R in Figure 6.25(c).

Finally Figure 6.26(a) reports the special case of three valleys coming out from the IS for different values of R; to better understand this category we show also the circular scan that we perform for R =0.08-0.14 with a step of 0.02 (Figure 6.26(b)). As expected the highest energy barrier ($\sim$0.4 LJ units) is located in correspondence of the path going from the two farthest valley branches. The variation of the potential energy difference (rescaled to the value of one of the three valleys for the specific value of R) as a function of the angle presents three distinct minima.

6.4 Comparison with the experimental findings

In this Section we paragon the results of our low temperature numerical analysis with the experimental findings. From the Equation 4.2 of the tunneling matrix element that we present at the beginning of Chapter 4 (Section 4.2) we derived that the discriminant threshold for the TSs barrier height V_0 in multi-silicate glasses is $\sim$20 K. The BMLJ system model, that we chose to use due to its numerous advantages, mimics a fragile metallic glass and not a strong glass (like the multi-silicates). However, due to the scarcity of experimental values for the TS parameters for fragile glasses, we can consider valid the value of $\sim$20 K as the upper limit for the energy barriers heights. By using Table 6.1 we have that 20 K=0.02 LJ units, therefore this is the barrier limit value that we have to look for in our computer simulation results. We therefore can fix a reasonable small value of R and look at the corresponding potential energy barrier heights. In Figure 6.27 we thus report the circular scans of: i) the two valleys standard case corresponding to Figure 6.18 and ii) the special cases of Figures 6.24, 6.25, only for R=0.04. As we can notice, the geometries of the special cases have the suitable energy barrier parameters to allow the tunneling ($<$0.02 LJ units) in principle; in particular, the right-angle valleys seem to be the most promising TS candidates. On the contrary, the standard case valley geometries are characterized by higher barriers ($\sim$0.065 LJ units=65 K). We can conclude that the TS DWPs might coincide with the geometries of the special case category since their energy barriers are compatible with the experimental findings. The very good agreement with the experimental values for the energy barriers tells us that our analysis is promising in order to get essential information on the TSs. Moreover we find the evidence of the TWPs, that are characterized by three minima with lower energy barriers with respect to the DWPs. We report in Figure 6.28 the circular scan (corresponding to Figure 6.26) of the PEL, showing that for a reasonable distance of R=0.08, one can identify two small barriers. This is a further confirmation of the existence of multi-well geometries in the low temperature landscape of glasses.

6.5 Conclusions

We end this Chapter with the plot of a very special configuration extracted from parallel tempering simulations, after the equilibration at T=0.37, where we find for the first time in the BMLJ glass the spontaneous formation of a small crystallite. In Figure 6.29 we highlight with bigger blue spheres the particles that form the FCC-like crystallite (all of them are type A particles) in the configuration of the BMLJ system. For the sake of clarity we decided not to distinguish with different color the type A and B particles. The formation of such better ordered region therefore points to the fact that indeed the RER could exist in some concentration and extent in real glasses.

We finally show an ensemble view of some of the valleys found with the part I of the EIS method for the glassy configuration (Figure 6.30) and the configuration containing the tiny crystallite (Figure 6.31). The magenta dots represent the different values of R that vary from 0.02 to 0.14 with a step of 0.02. As we can see, the valleys belonging to the glass sample have a regular shape, some are perpendicular to the central valley and other are parallel. On the contrary, the valleys in the vicinity of the crystallite (the FCC stucture is still visible in Figure 6.31), are characterized by a strongly irregular shape. This fact might be probably related to the difference in the intermediate-range structure. We are currently carrying out further analysis on this peculiar case to gain more insight.

In conclusion, The EIS method allows us to carry out for the first time a detailed study of the geometry of the bottom of the PEL at low temperature, very near to the IS of the glass sample. We find that the basin of attraction is characterized by internal valleys whose energy increases quadratically with the distance from the local minimum. With respect to the previous numerical studies on the TSs, that were based on parameters of DWPs coinciding with IS-SP-IS geometry, characterized by very high energy barrier values, ~ 0.5 LJ units=500 K in [67], we give a new viewpoint on the possible nature of the TSs in the PEL at very low temperature. We present in fact direct evidence for low energy barriers with the correct parameters to allow in principle the tunneling phenomena. Whether the extracted geometries could be identified with the TSs is still a speculation, that need to be verified and this will be the object of future work. Furthermore the presence of better ordered structures and the three valleys geometries could support in some way the existence of the TWPs of the ETM. The next step of our analysis will be the verification of the probability distributions of the extracted parameters, according to the STM and/or to the ETM. We plan to carry on the same analysis for more realistic glassy system, e.g. the silica or sodium-silicates, to study the properties of the low temperature geometries and compare the PEL topology.

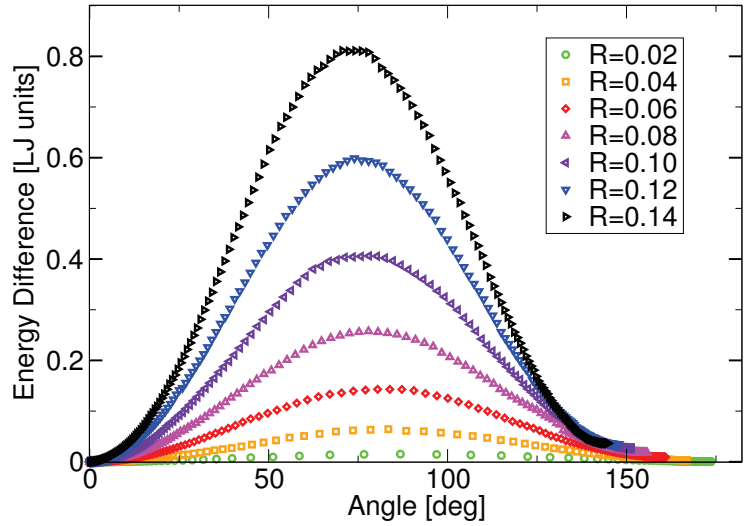

(a)

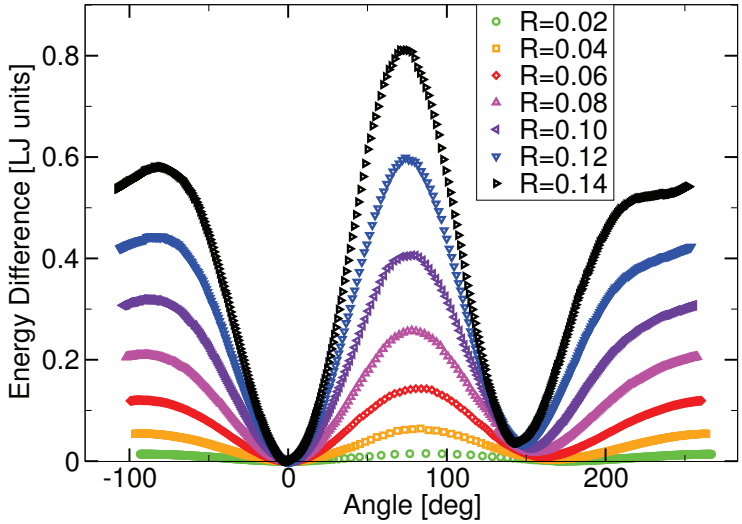

(b)

Figure 6.18: a) Example of potential energy barrier between two valleys (belonging to the standard cases category) as a function of the angle between them. The vertical axis has been rescaled to the value of the lowest valley for the specific value of R. b) Variation of the potential energy difference (rescaled to the value of the lowest valley for each value of R) as a function of the angle. The points correspond to the configurations that lie on the circular path of radius R (the closed-loop trajectory associated with the complete angle of 360°) connecting the two valleys of a) (here also shown at 0° and ∼150°).

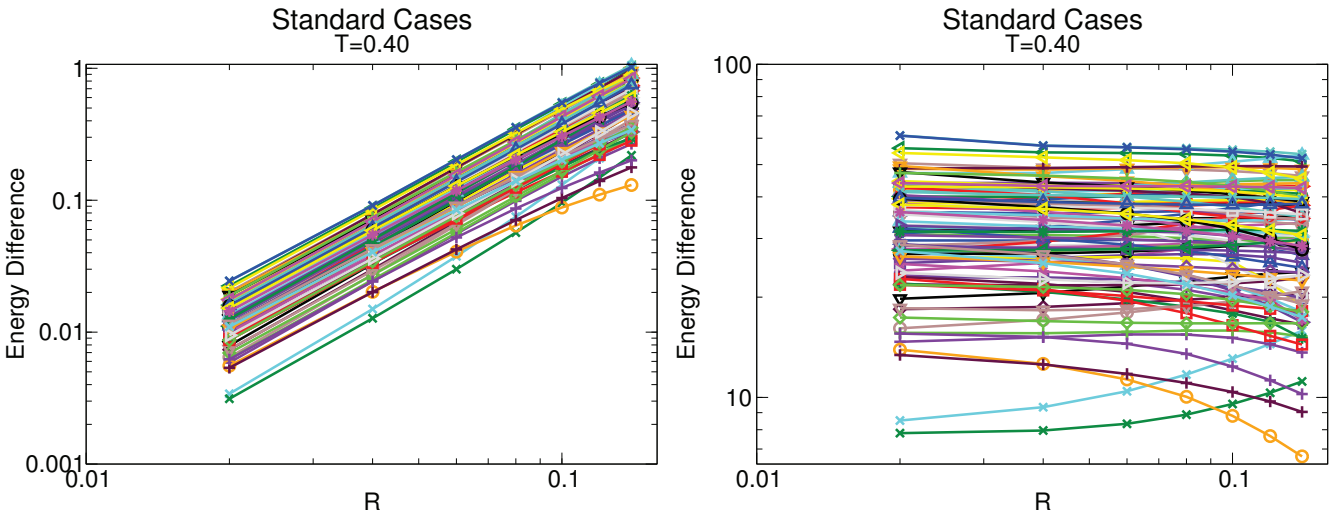

(a) (b)

Figure 6.19: a) Behavior of the potential energy rescaled to the energy of the IS as a function of R for the valleys that belong to the standard cases category. b) Same data of a) but with the vertical axis divided by R^2 (note the logarithmic scale on both axis). All the quantities are in LJ reduced units (see Table 6.1); $T = 0.40$.

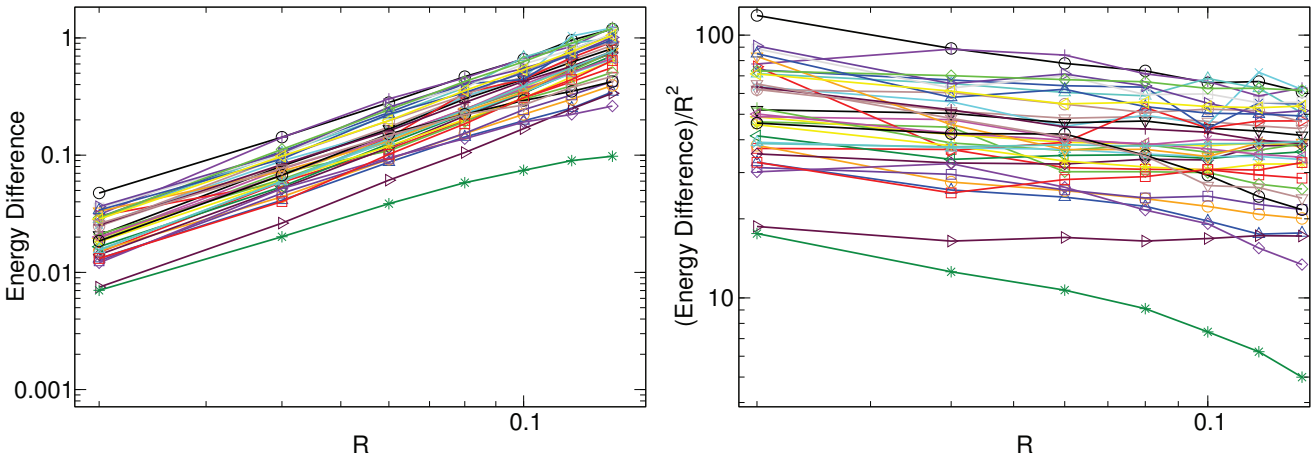

(a) (b)

Figure 6.20: a) Behavior of the potential energy rescaled to the energy of the IS as a function of R for the barriers that belong to the standard cases category. b) Same data of a) but with the vertical axis divided by R^2 (note the logarithmic scale on both axis). All the quantities are in LJ reduced units (see Table 6.1); $T = 0.40$.

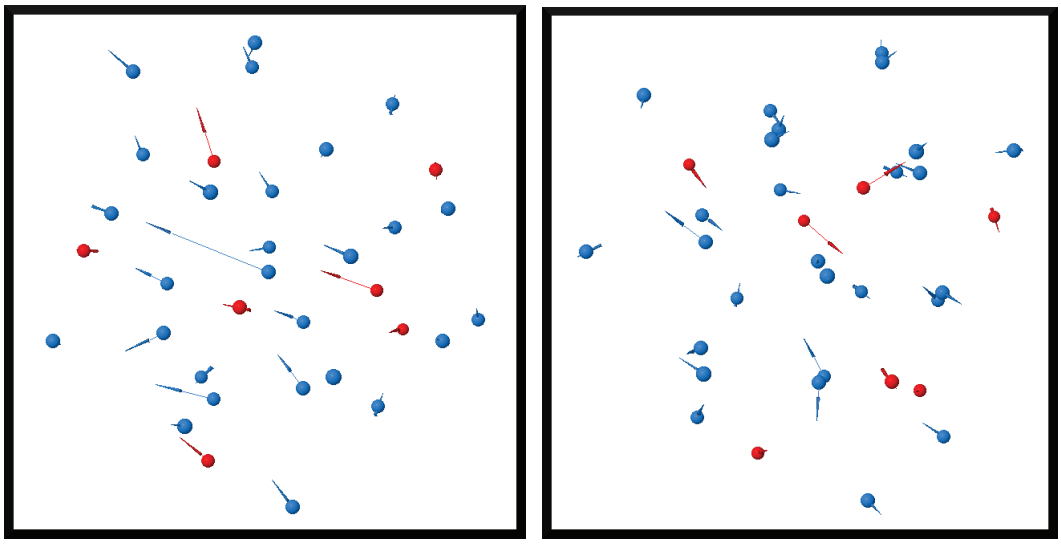

(a) (b)

Figure 6.21: Side and top view of the displacement vectors when the displaced central particle is of type A. The A and B particles are represented respectively in blue and red color.

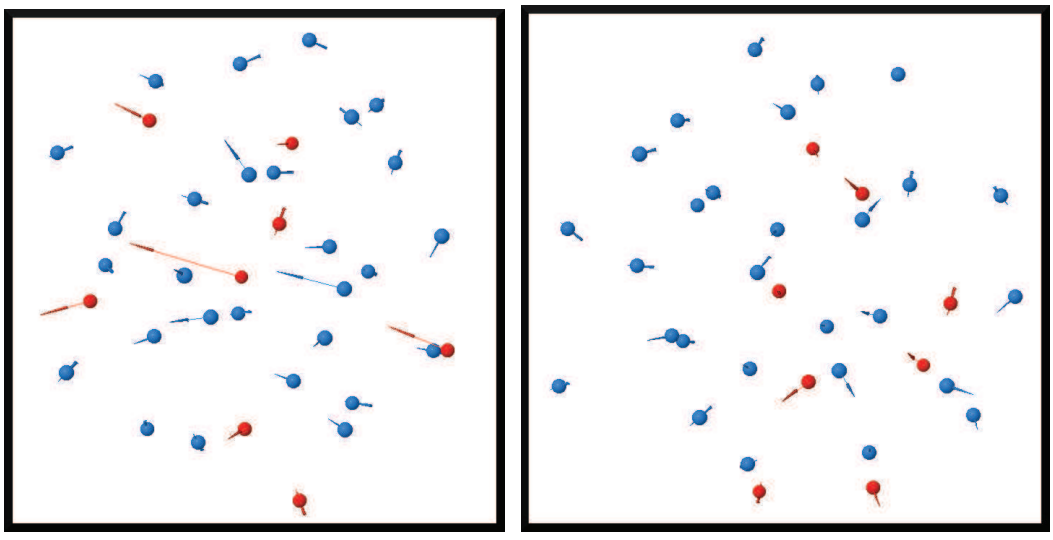

(a) (b)

Figure 6.22: Side and top view of the displacement vectors when the displaced central particle is of type B. The A and B particles are represented respectively in blue and red color.

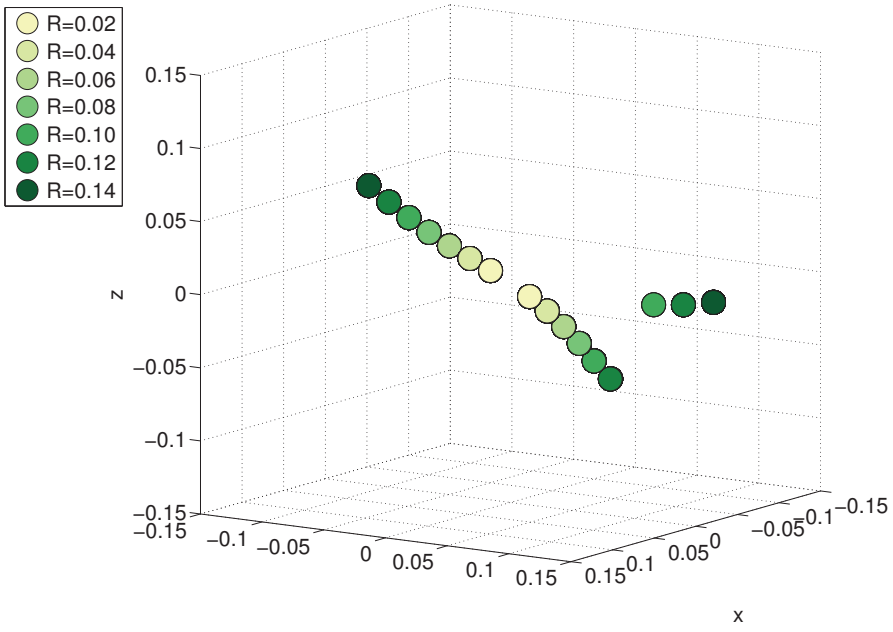

(a)

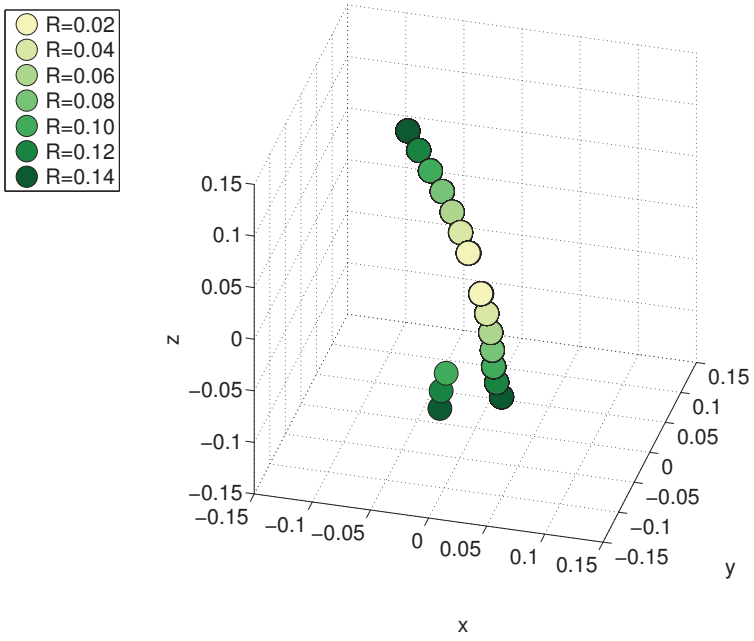

(b)

Figure 6.23: λ-shape valleys associated to two different particles after the application of the EIS method. This kind of valley shape has been classified in the "special case" category since it represents a minor subset of the geometries found for a given IS.

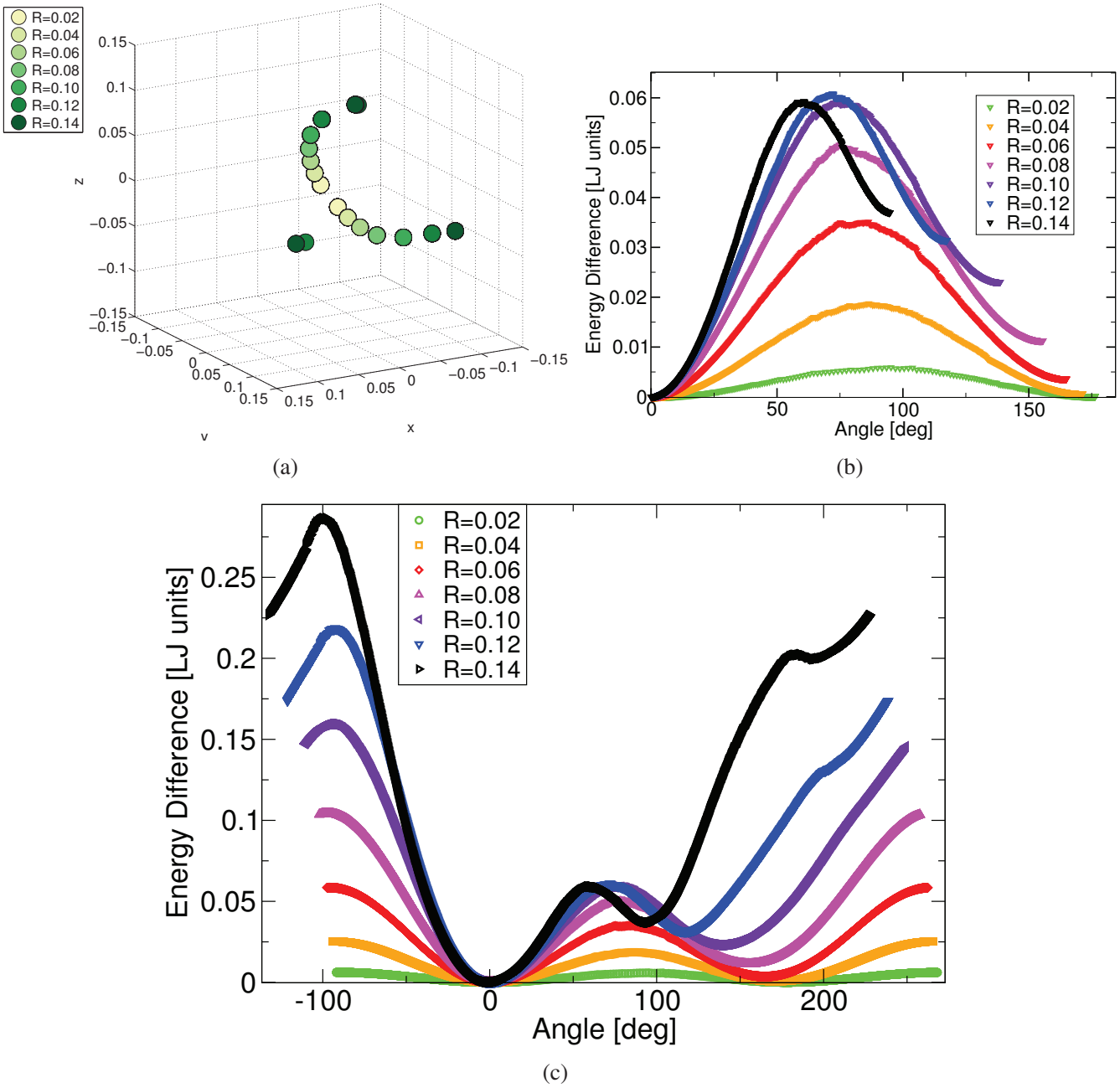

Figure 6.24: a) U-shape valleys associated to a given particle after the application of the EIS method. This kind of valley shape has been classified in the "special case" category since it represents a minor subset of the geometries found for a given IS. b) Potential energy barrier between the two valleys of a) as a function of the angle between them. The vertical axis has been rescaled to the value of the lowest valley for the specific value of R. c) Variation of the potential energy difference (rescaled to the value of the lowest valley for each value of R) as a function of the angle. The points correspond to the configurations that lie on the circular path of radius R (the closed-loop trajectory associated with the complete angle of 360°) connecting the two valleys of a) (here also reported). Note that the valley points at R=0.12 and R=0.14 in a) are captured by the scan procedure through the "bumps" at $\sim 120°$ in c). All the quantities are expressed in LJ reduced units (see Table 6.1); $T = 0.40$.

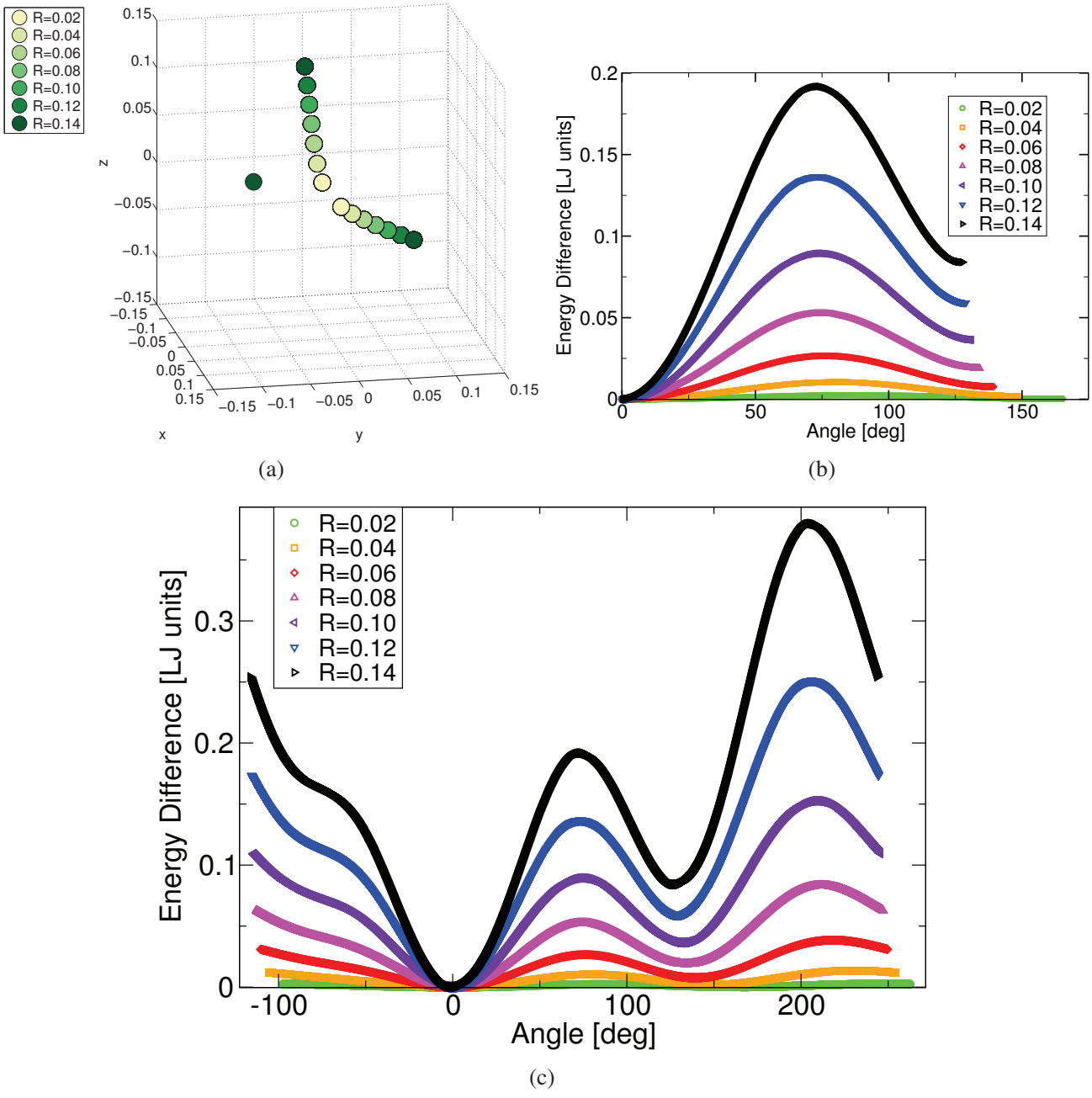

Figure 6.25: a) Right-angle shape valleys associated to a given particle after the application of the EIS method. This kind of valley shape has been classified in the "special case" category since it represents a minor subset of the geometries found for a given IS. b) Potential energy barrier between the two valleys of a) as a function of the angle between them. The vertical axis has been rescaled to the value of the lowest valley for the specific value of R. c) Variation of the potential energy difference (rescaled to the value of the lowest valley for each value of R) as a function of the angle. The points correspond to the configurations that lie on the circular path of radius R (the closed-loop trajectory associated with the complete angle of 360°) connecting the two valleys of a) (here also reported). Note that the valley points at R=0.12 and R=0.14 in a) are captured by the scan procedure through the "bumps" at $\sim -70°$ in c). All the quantities are expressed in LJ reduced units (see Table 6.1); $T = 0.40$.

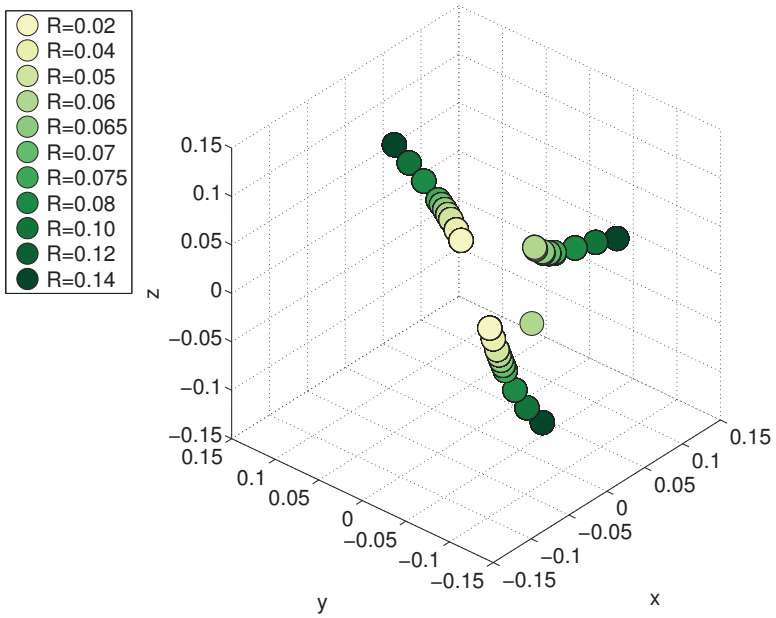

(a)

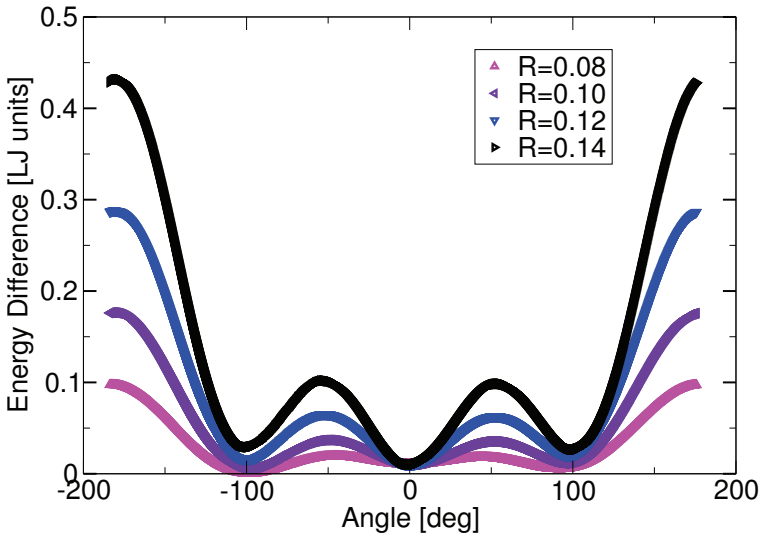

(b)

Figure 6.26: a) Three valleys associated to a given particle after the application of the EIS method. This kind of valley shape has been classified in the "special case" category since it represents a rare case of the geometries found for a given IS. b) Potential energy barrier between the two of the three valleys of a) as a function of the angle between them. The vertical axis has been rescaled to the value of one of the three valleys for the specific value of R. c) Variation of the potential energy difference (rescaled to the value of one of the three valleys for the specific value of R) as a function of the angle. The points correspond to the configurations that lie on the circular path of radius R (the closed-loop trajectory associated with the complete angle of 360°) connecting the two nearest valleys of a). Note the presence of three distinct minima. All the quantities are expressed in LJ reduced units (see Table 6.1); $T = 0.40$.

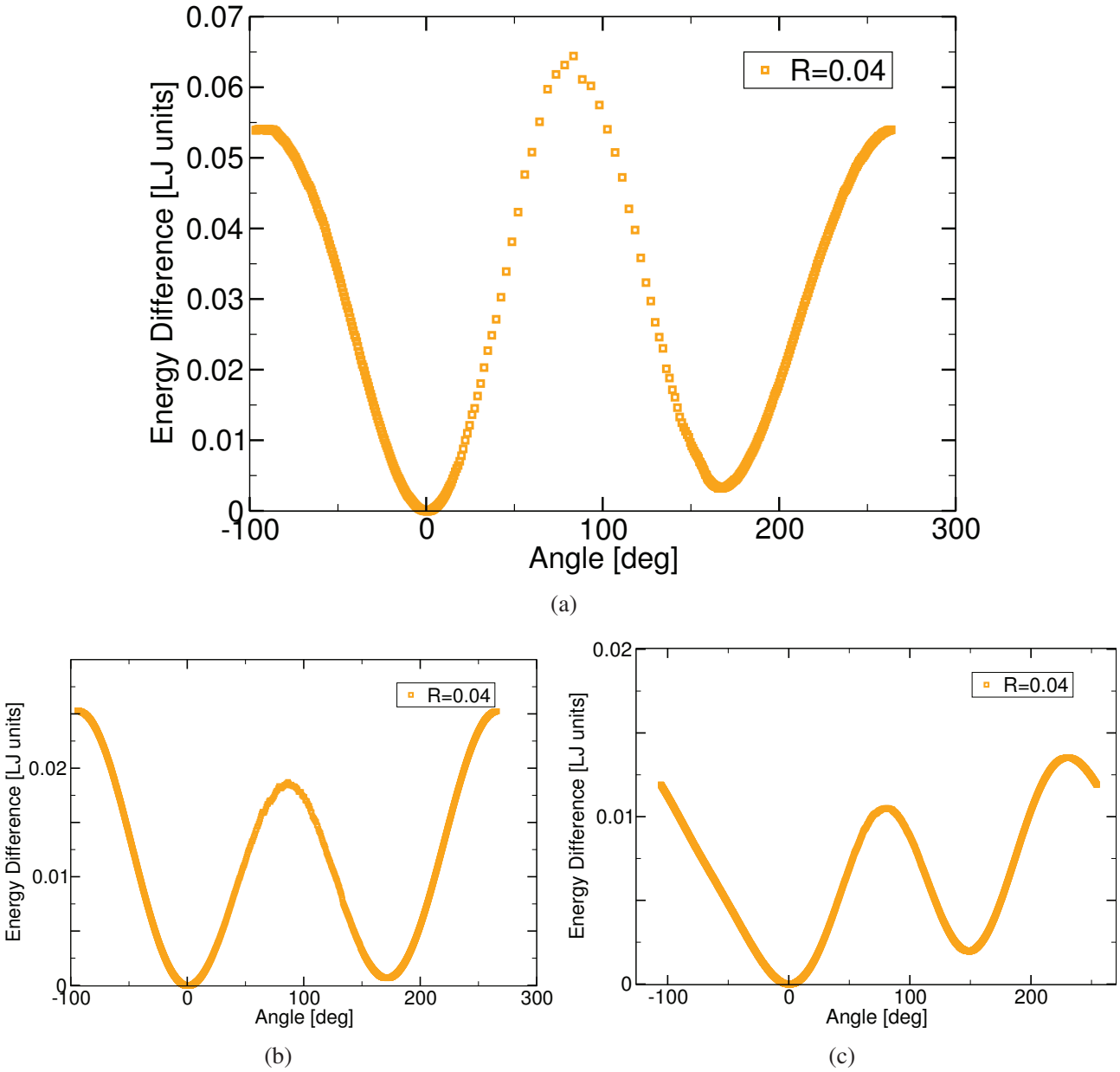

Figure 6.27: Comparison of the variation of the potential energy difference (rescaled to the value of the lowest valley) as a function of the angle for $R = 0.04$, a) for the standard case (corresponding to Figure 6.18), b) the U-shape valley (corresponding to Figure 6.24) and c) the right-angle valley (corresponding to Figure 6.25). The standard case geometry cannot be considered as a TS-like geometry since the barrier height is greater than the expected value of <0.02 LJ units (derived from the literature); the barriers of the special cases instead present the right order of magnitude and therefore we expect that they could be regarded as the TSs. $T = 0.40$.

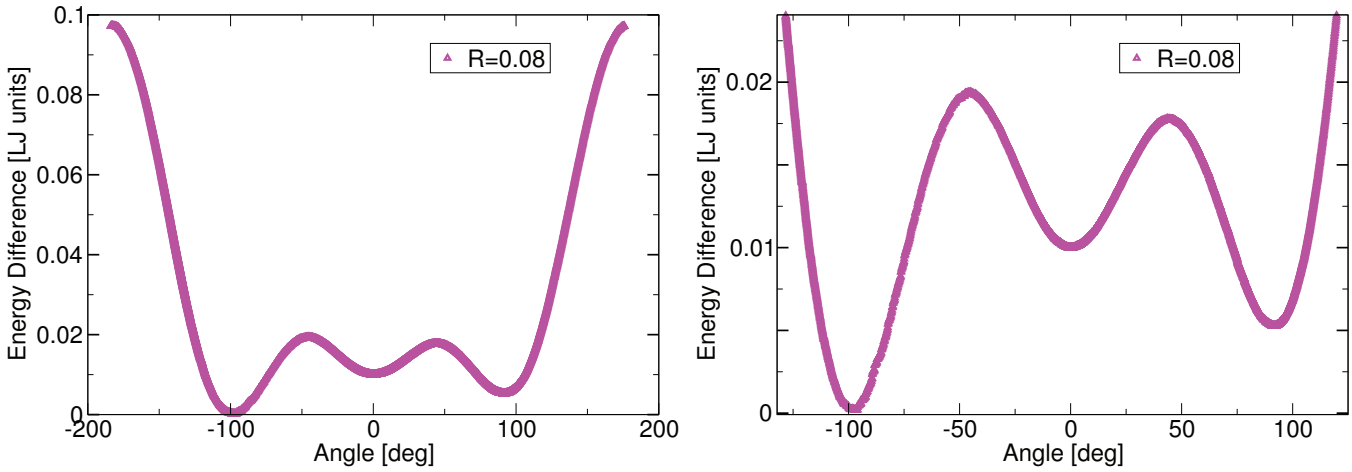

(a) (b)

Figure 6.28: Potential energy difference (rescaled to the value of the lowest valley) as a function of the angle for $R = 0.08$, for the three valleys special case (corresponding to Figure 6.26), a) entire and b) zoomed view. $T = 0.40$.

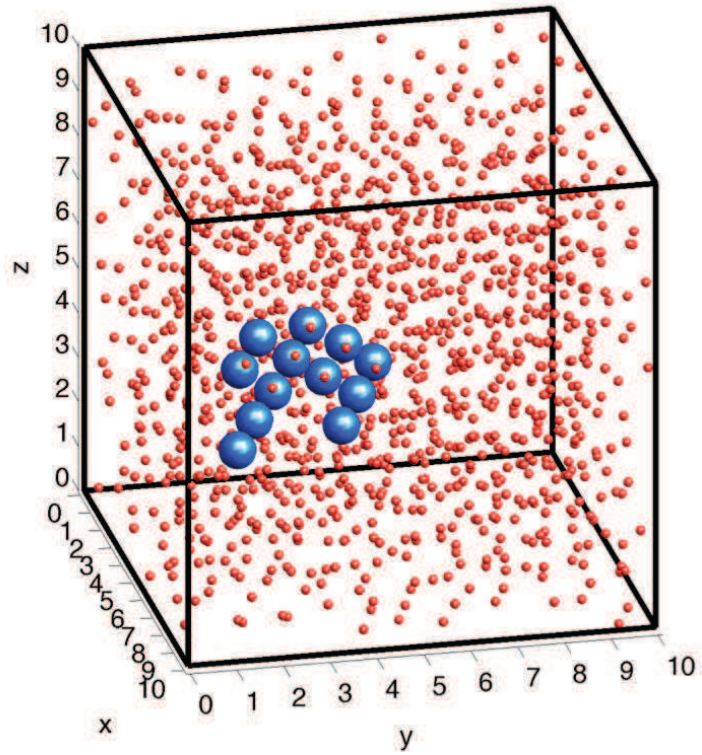

Figure 6.29: The crystallite particles (highlighted as larger blue spheres) spontaneously generated during parallel tempering simulations at T=0.37 inside a BMLJ glass sample. For the sake of clarity we decided not to distinguish with different color the type A and B particles.

Figure 6.30: Cluster of valleys for a BMLJ glassy configuration at $T = 0.4$. The majority of the valleys has a "standard" two-valleys geometry.

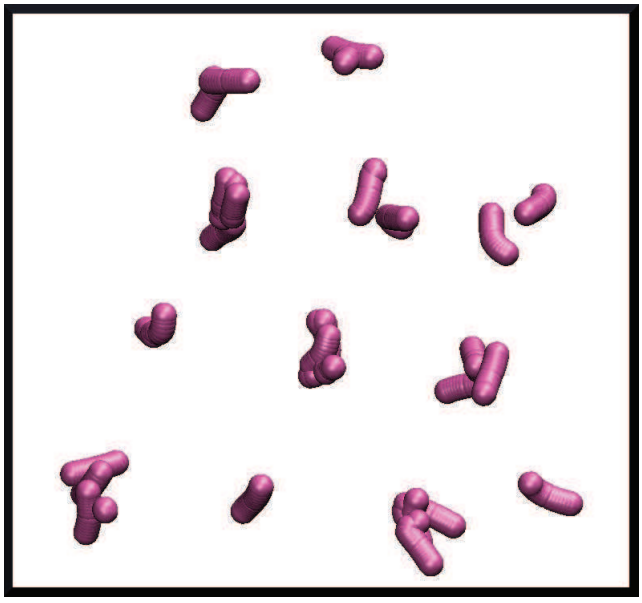

Figure 6.31: Cluster of valleys for the particles corresponding to the crystallite (marked with blue spheres in Figure 6.29) in the glass sample at $T = 0.37$. Many of the valleys have an irregular shape; the FCC planes of the crystallite are still distinguishable.

General Conclusions and Outlook

In this work we have investigated the limitations of the Zachariasen-Warren "classic" picture for the intermediate range atomic structure of glasses (in real and computer model systems). Formulated in the early 1930s [16, 111], the Zachariasen-Warren picture of glass structure has dominated glass science for almost a century, however other points of view developed, starting from the "crystallites" hypothesis of Lebedev of 1937 [112] and then continuing all the way to the "polyclusters" concept of Bakai [11]. In recent times the alternative picture of the glass structure has found support notably with the "paracrystals" concept of J.C. Phillips [17], further advocated by Treacy and Borisenko for the structure of a-Si films [53]. A similar concept has been proposed for the structure of metallic glasses by Hwang *et al.* [54] in the context of the observed "devitrification" phenomenon in systems like a-$Zr_{50}Cu_{45}Al_5$. Wright [18] has introduced the term "cybotactic groupings" to denote the crystallite regions as regions of enhanced ordering with respect to the surrounding fully disordered matrix, coming to the conclusion that all of the network glasses, particularly when multicomponent, should contain crystallite-like structures in contrast to the standard homogeneous random-network Zachariasen-Warren picture. A mosaic type structure was also suggested by de Gennes [61] for the glassy state and it forms the core of the description of the glass transition and of the glassy state due to Wolynes [52, 51].

The mosaic alternative picture for the intermediate-range structure of the glass is now found to be the basic justification for a mathematical model (the ETM) explaining the magnetic effects recently discovered in multicomponent silicate and organic glasses, notably in the heat capacity, in the real and imaginary part of the dielectric constant and in the polarization echo at sub-Kelvin temperatures. The ETM is an extension of the standard tunneling model of W.A. Phillips and of P.W. Anderson, Halperin and Varma formulated in 1972 which accounts for many of the low-temperature anomalies discovered by Zeller and Pohl and then by Hunklinger and collaborators in the 1970s. Whilst the STM relies heavily on the classical Zachariasen-Warren picture of glass structure for the distribution of the tunneling parameters, the ETM relies on the full implementation of the mosaic, or cellular model of glass structure where crystallites, but not necessarily micro-crystals, are invoked. The ETM is also an extension of the 3D version of the STM by Kettemann, Fulde and Strehlow used to explain the magnetic effects, but it relies on two distinct types of tunneling systems induced by the cellular picture: The standard two-level systems, sitting mostly at crystallite defects and at the cell boundaries, where the atomic arrangement

is strongly discontinuous, and the newly advocated anomalous TSs that sit in the interstitials between the close-packed crystallites. Owing to the proximity of better-ordered regions, the ATSs are taken to have a near-degenerate distribution of the energy asymmetries that characterize the tetrahedral (or to simplify, triangular) topology of the newly advocated tunneling potentials. The TSs sitting in each interstitial are thought to be charged, strongly interacting and probably coherently-tunneling atomic defects, hence each ATS is characterized by a single fictitious tunneling particle with highly renormalized parameters: charge, and also magnetic-field threaded area and tunneling amplitude. In this way, each ATS is a tunneling quasi-particle characterized by parameters that scale with the number N of coherent microscopic TSs in each interstitial of the mosaic or cellular atomic arrangement. The ETM needs a number N of coherently tunneling atomic particles of the order of 10^2 [70] rather than 10^6 as originally advocated. This is in line with the value of about 200 proposed by the theory of Lubchenko and Wolynes [52, 51].

The ETM was found to be very useful to explain a large number of experimental sets of low-temperature data, for a variety of different glasses, and with the combinations of the renormalized parameters that are of the same order of magnitude for most of the investigated glasses. Though broad oversimplification and approximations are involved in the mathematical modeling, the ETM has been able to show that the investigated magnetic effects are a consequence of a highly non-uniform, highly magnetic sensitive form of the ATS DOS that directly reflects the advocated non homogeneous atomic structure of glasses. Beside the magnetic effects, the ETM has been shown to explain also the composition dependent effects [70] discovered by A.C. Anderson and collaborators in the mixed alkali-silicates at low temperatures.

In the first part of this work we have addressed the question of the paramagnetic impurities concentration, which the ETM has systematically underestimated in explaining the heat capacity data at low temperatures. These paramagnetic impurities give a contribution of the same order of magnitude as the ATSs, thus a careful determination of their number is crucial. We therefore resolved to re-analyze the SQUID-magnetization data for the studied glasses, since the paramagnetic impurity concentration is nominally determined in the literature from such measurements, which are done between 4 and 300 K with a SQUID magnetometer and then assuming a pure Langevin description of the e.g. Fe-ion paramagnetism. We calculated the contribution from the magnetic sensitive ATSs to the sample magnetization using the ETM, a contribution which we found to be large because of the large number N of coherently tunneling TSs in each interstitial ATS. Adding both Langevin and ATS contributions we have found we could fit very well the SQUID-data in the whole of the 4-300 K range when a simple Arrhenius form of the temperature dependence of N is used, justified by means of the consolidation of the mosaic structure at the expense of the atomic species in the interstitials as the temperature is lowered. This mathematical description of the magnetization produces concentrations of the various species involved and of the tunneling parameters that are in very good agreement with those extracted from the fits of the heat capacity data using the ETM. From the practical

point of view these findings imply that the paramagnetic impurity concentrations are grossly overestimated in a SQUID measurement when only the Langevin contribution is considered. In turn, this means that non magnetic silicate glasses could be (weakly) *per se* paramagnetic: a most unexpected result. A second unexpected result is that the tunneling model continues to give a reasonable description - for the interstitial ATSs only - all the way to room temperatures. We speculate this is connected to the fact that phonon interactions are kept simple for the "protected" ATSs sitting in the interstitial cages between the crystallites.

To put the ETM further to the test, and to investigate the nature of the TSs from a computer simulation standpoint, we have begun - in the second part of this work - a newly-conceived numerical analysis of the potential energy landscape of a model glassy system, since the TSs ought to represent the lowest energy features of this PEL. We have thus first determined from the experimental situation that, at least for the multi-silicate strong glasses, the energy barriers separating the tunneling potential wells ought to be in the region of maximum 20 K [59]. This is in contrast with the typical potential energy barriers between the inherent structures of the PEL found in computer simulations of the binary-mixture Lennard-Jones glass: around 100 K [102]. We have chosen the BMLJ fragile glass as a first model to investigate numerically for reasons of simplicity and versatility. However, since we speculate that the mosaic structure of the glassy state could be the thermal history continuation from the dynamical heterogeneities of the supercooled regime (the slow DH regions becoming the better ordered cells of the mosaic and the faster regions giving rise to the ATS coherently tunneling particles in the interstitials), the BMLJ glass is also a very natural choice. Indeed, at least in 2D, the DH with their slower and faster regions are very well characterized and confirmed by many simulations of this model [113]. In turn, in the metallic glasses (for which the BMLJ model is a paradigm, at least for the a-NiP system) the TSs have also been found and seen to be characterized by similar tunneling parameters as for the strong glasses [114].

We therefore became convinced that the TSs are features of the PEL to be found most likely *inside* each single 3*N*D basin of the IS, rather than features of the PEL consisting of two or more IS minima. With this new scenario, we have developed a systematic algorithm for the search of "valleys" within a single IS basin of the PEL corresponding to parallel tempering simulation configurations at the lowest possible temperatures in the glassy regime that can be currently obtained and equilibrated. Starting with the LJ FCC crystal, we have identified, with this new algorithm, the existence of six valleys inside each IS basin and that are to be expected from the symmetry of the crystal. Moving over to the numerical analysis of ISs corresponding to the BMLJ glass at temperatures (0.36 in LJ units) well below the glass transition temperature (T_g=0.44) we have been able to find that typically each IS is characterized by two, and occasionally three "valleys" inside its basin. Many of such PEL topologies seems to have the right energy characteristics to be identified with double-well and, less frequently, three-well local potentials. We speculate that these could be the DWPs and TWPs (or ATSs) that have been advocated in the mathematical modelization in real

space that characterizes the first part of this work, namely the tunneling features of the ETM. The systematic search for these key configurations of the PEL and their statistics in terms of energy asymmetries and tunneling amplitudes is currently underway and promises to be the way to see what the TSs might look like. We have also found glassy configurations that contain partially crystallized regions (with evidence of some faceting) and that appear to have a lower energy than similar configurations that are totally disordered; these may be tentatively identified with the cells of the ETM. Further analysis is underway, but it looks as if the numerical analysis we have conducted with the new search algorithm is poised to confirm many of the assumptions of the ETM. A model which, as also shown in the first part of this work, is the minimal tunneling model capable to explain in a consistent way many unusual experimental findings in the low temperature physics of real, multicomponent and contaminated single-component glasses. The low temperature magnetic and composition anomalies have now been linked to the question of the true intermediate-range atomic structure of glasses, a question that remains open and that is paramount for the development of good mathematical models of the physical properties of amorphous solids which do not benefit from simplifications like Block's theorem for crystals. Moreover, a mosaic structure of glass, with the cells represented by better ordered regions, would provide a reasonable new rationale for the mechanism of glass formation.

Appendix A

The realistic tetrahedric four-well tunneling potential

In Chapter 2 of this Thesis we described our theoretical extension of the STM, assuming that a subset of tunneling quasi-particles is moving in a TWP associated with the inhomogeneities of the glassy atomic structure. However the triangular three-well version employed to fit the experimental data is nothing else than the semplification of the more realistic situation of a tetrahedric four-well tunneling potential (TFWP) within the cellular model picture we presented in Chapter 1. Here we present the mathematical description of the TFWP showing that, in fact, we obtain the same physics of the TWP version, which is probably also very realistic. In Section A.1 we define the geometry of the problem, then in Section A.2 we study the effect of a magnetic field directed along the z-axis of a tetrahedron. We derive the Peierl's phase contributions when the particle moves in the four wells and we obtain the formula for the energy levels and gaps. The new findings for the DOS and the specific heat are also reported. We end this Appendix with the evaluation of the case where $\vec{B}$ has a generic direction (Section A.3), showing that we find the same results of the simplified case, confirming the correctness of the derivation. We remark that a previous study, considering 4 energy levels but in a square-well geometry, has been carried out in [68].

A.1 Definition of the tetrahedric geometry

In this Section we define the geometry of the problem for the case of a TFWP. We first show how the TFWP Hamiltonian, is similar to that of the TWP Hamiltonian. We write the TFWP Hamiltonian in the presence of a magnetic field, coupled orbitally to the charged tunneling particle:

$$H_0 = \begin{pmatrix} E_1 & D_0 e^{i\varphi_{12}} & D_0 e^{i\varphi_{13}} & D_0 e^{i\varphi_{14}} \\ D_0 e^{i\varphi_{21}} & E_2 & D_0 e^{i\varphi_{23}} & D_0 e^{i\varphi_{24}} \\ D_0 e^{i\varphi_{31}} & D_0 e^{i\varphi_{32}} & E_3 & D_0 e^{i\varphi_{34}} \\ D_0 e^{i\varphi_{41}} & D_0 e^{i\varphi_{42}} & D_0 e^{i\varphi_{43}} & E_4 \end{pmatrix}$$

where $\sum_{i=1}^{4} E_i = 0$ is imposed and φ_{ij} are the Peierls phases one gets when the particle moves in the corresponding wells and that have to be evaluated according to the direction of the magnetic field. Here is the definition of the equilateral tetrahedron (l is the length of the edge), presented in Figure A.1:

- vertex 1: $(0,\frac{\sqrt{3}}{3}l,0)$;
- vertex 2: $(+\frac{l}{2},-\frac{\sqrt{3}}{6}l,0)$;
- vertex 3: $(-\frac{l}{2},-\frac{\sqrt{3}}{6}l,0)$;
- vertex 4: $(0,0,\frac{\sqrt{6}}{3}l)$;

Parameterization of the edges:

- Edge 12: $y = -\sqrt{3}x + \frac{\sqrt{3}}{3}l$, z=0;
- Edge 23: $y = -\frac{\sqrt{3}}{6}l$, z=0;
- Edge 31: $y = +\sqrt{3}x + \frac{\sqrt{3}}{3}l$, z=0;
- Edge 14: $z = +\frac{\sqrt{6}l}{3} - \sqrt{2}y$, x=0;
- Edge 24: $x = -\frac{\sqrt{6}}{4}z + \frac{1}{2}l$, $y = \frac{\sqrt{2}}{4}z - \frac{\sqrt{3}}{6}l$;
- Edge 34: $x = +\frac{\sqrt{6}}{4}z - \frac{1}{2}l$, $y = \frac{\sqrt{2}}{4}z - \frac{\sqrt{3}}{6}l$;

The values of the unit vectors, perpendicular to the 4 faces of a tetrahedron, are:

- $\hat{n}_{213}$=(0,0,1);
- $\hat{n}_{243}$=$(0,-\frac{2\sqrt{2}}{3},+\frac{1}{3})$;
- $\hat{n}_{134}$=$(-\frac{\sqrt{6}}{3},+\frac{\sqrt{2}}{3},+\frac{1}{3})$;
- $\hat{n}_{142}$=$(+\frac{\sqrt{6}}{3},+\frac{\sqrt{2}}{3},+\frac{1}{3})$;

A.2 Derivation in the presence of a magnetic field directed along z

In the following we assume that the magnetic field is directed along z ($\vec{B}$=(0,0,B)). recalling that the area of one face of the tetrahedron is $S_{\triangle} = \frac{\sqrt{3}}{4}l^2$ and the unit vectors are described in Section A.1, the flux across the face 213 is e.g.: φ_{tot}^{213}=$\frac{e}{\hbar}S\vec{B}\cdot$

$\hat{n}_{213}=\frac{e}{\hbar}\frac{\sqrt{3}}{4}l^2B$. The calculation of the flux for the other faces gives
$\varphi_{tot}^{243}=\varphi_{tot}^{134}=\varphi_{tot}^{142}=\frac{e}{\hbar}\frac{\sqrt{3}}{12}l^2B=\frac{1}{3}\varphi_{tot}^{213}$.

The starting point of the derivation of the DOS for a TFWP when $\vec{B}$ is directed along the z-axis is the calculation of the Peierls phases. We proceed in this way:

$$\varphi_{ij}=\frac{e}{\hbar}\int_a^b\left(A_x\mathrm{d}x+A_y\mathrm{d}y+A_z\mathrm{d}z\right)=\frac{e}{\hbar}\int_a^b\mathrm{d}t\left(A_x\frac{\mathrm{d}x}{\mathrm{d}t}+A_y\frac{\mathrm{d}y}{\mathrm{d}t}+A_z\frac{\mathrm{d}z}{\mathrm{d}t}\right) \tag{A.1}$$

where t parameterizes the straight line.
The vector potential, when $\vec{B}$ is directed along $\vec{z}$, is $\vec{A}=\left(-\frac{1}{2}By,+\frac{1}{2}Bx,0\right)$; the Peierls phases are therefore:

- $\varphi_{12}=\frac{e}{\hbar}\int_0^{l/2}\left(-\frac{1}{2}B(-\sqrt{3}t+\frac{\sqrt{3}}{3}l)+\frac{1}{2}Bt\left(-\sqrt{3}\right)\right)\mathrm{d}t=-\frac{e}{\hbar}\frac{\sqrt{3}}{12}Bl^2$
  in fact for edge 12: z=0, $x=t$ and $y=-\sqrt{3}t+\frac{\sqrt{3}}{3}l$;

- $\varphi_{23}=\frac{e}{\hbar}\int_{+l/2}^{-l/2}-\frac{1}{2}B\left(-\frac{\sqrt{3}}{6}l\right)\mathrm{d}t=-\frac{e}{\hbar}\frac{\sqrt{3}}{12}Bl^2$
  in fact for edge 23: z=0, $x=t$ and $y=-\frac{\sqrt{3}}{6}l$;

- $\varphi_{31}=\frac{e}{\hbar}\int_{-l/2}^{0}\left(-\frac{1}{2}B\left(\sqrt{3}t+\frac{\sqrt{3}}{3}l\right)+\frac{1}{2}Bt\left(\sqrt{3}\right)\right)\mathrm{d}t=-\frac{e}{\hbar}\frac{\sqrt{3}}{12}Bl^2$
  in fact for edge 31: z=0, $x=t$ and $y=+\sqrt{3}t+\frac{\sqrt{3}}{3}l$

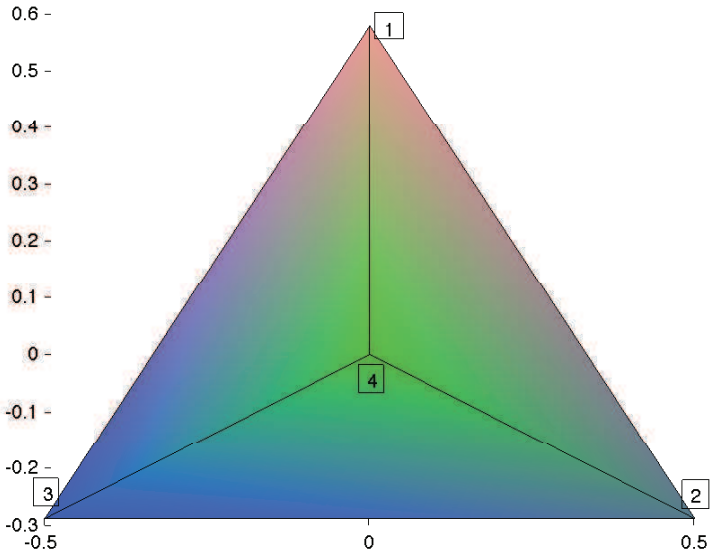

Figure A.1: Equilateral tetrahedron.

- $\varphi_{14}=\frac{e}{\hbar}\int_{\sqrt{3}l/3}^{0}\left(-\frac{1}{2}Bt(0)+\frac{1}{2}B(0)\right)\mathrm{d}t=0$
  in fact for edge 14: x=0, $y=t$, $z=\frac{\sqrt{6}l}{3}-\sqrt{2}t$
- $\varphi_{24}=\frac{e}{\hbar}\int_{0}^{\sqrt{6}l/3}\left(-\frac{1}{2}B\left(-\frac{\sqrt{2}}{4}t-\frac{\sqrt{3}}{6}l\right)\left(-\frac{\sqrt{6}}{4}\right)+\frac{1}{2}B\left(-\frac{\sqrt{6}}{4}t+\frac{1}{2}l\right)\left(\frac{\sqrt{2}}{4}\right)\right)\mathrm{d}t=0$
  in fact for edge 24: $z=t$, $x=-\frac{\sqrt{6}}{4}t+\frac{1}{2}l$, $y=\frac{\sqrt{2}}{4}t-\frac{\sqrt{3}}{6}l$;
- $\varphi_{34}=\frac{e}{\hbar}\int_{0}^{\sqrt{6}l/3}\left(-\frac{1}{2}B\left(+\frac{\sqrt{2}}{4}t-\frac{\sqrt{3}}{6}l\right)\left(+\frac{\sqrt{6}}{4}\right)+\frac{1}{2}B\left(+\frac{\sqrt{6}}{4}t-\frac{1}{2}l\right)\left(\frac{\sqrt{2}}{4}\right)\right)\mathrm{d}t=0$
  in fact for edge 34: $z=t$, $x=+\frac{\sqrt{6}}{4}t-\frac{1}{2}l$, $y=\frac{\sqrt{2}}{4}t-\frac{\sqrt{3}}{6}l$;

Therefore, by the sum of the closed paths, we have:

- face 213: $\varphi_{21}+\varphi_{13}+\varphi_{32}=3\left(\frac{e}{\hbar}\frac{\sqrt{3}}{12}Bl^2\right)=\frac{e}{\hbar}\frac{\sqrt{3}}{4}\mathrm{l}^2\mathrm{B}=\varphi_{tot}^{213}$;
- face 243: $\varphi_{24}+\varphi_{43}+\varphi_{32}=0+0+\left(\frac{e}{\hbar}\frac{\sqrt{3}}{12}Bl^2\right)=\frac{e}{\hbar}\frac{\sqrt{3}}{12}Bl^2=\frac{1}{3}\varphi_{tot}^{213}$;
- face 134: $\varphi_{13}+\varphi_{34}+\varphi_{41}=\left(\frac{e}{\hbar}\frac{\sqrt{3}}{12}Bl^2\right)+0+0=\frac{e}{\hbar}\frac{\sqrt{3}}{12}Bl^2=\frac{1}{3}\varphi_{tot}^{213}$;
- face 142: $\varphi_{14}+\varphi_{42}+\varphi_{21}=0+0+\left(\frac{e}{\hbar}\frac{\sqrt{3}}{12}Bl^2\right)=\frac{e}{\hbar}\frac{\sqrt{3}}{12}Bl^2=\frac{1}{3}\varphi_{tot}^{213}$.

A.2.1 Calculation of the energy levels and the gaps

Therefore, following the definition of Equation A.1 we have that the matrix, in the case of orthogonal $\vec{B}$, is:

$$H_0=\begin{pmatrix} E_1 & D_0e^{-i\frac{\varphi}{3}} & D_0e^{i\frac{\varphi}{3}} & D_0 \\ D_0e^{i\frac{\varphi}{3}} & E_2 & D_0e^{-i\frac{\varphi}{3}} & D_0 \\ D_0e^{-i\frac{\varphi}{3}} & D_0e^{i\frac{\varphi}{3}} & E_3 & D_0 \\ D_0 & D_0 & D_0 & E_4 \end{pmatrix}$$

Note that if E_1=E_2=E_3=E_4=0 the eigenvalues are $\lambda_{1,2,3}=-D_0$, $\lambda_4=3D_0$. The plot of the eigenvalues of H_0, numerically calculated, for φ which varies between 0 and π is represented in Figure A.2. The eigenvalue equation is the following:

$$\begin{aligned}
&3D_0^4-3D_0^4e^{-\frac{2}{3}i\varphi}-3D_0^4e^{\frac{2}{3}i\varphi}+D_0^3e^{-\frac{1}{3}i\varphi}E_1+D_0^3e^{\frac{1}{3}i\varphi}E_1+D_0^3e^{-\frac{1}{3}i\varphi}E_2\\
&+D_0^3e^{\frac{1}{3}i\varphi}E_2-D_0^2E_1E_2+D_0^3e^{-\frac{1}{3}i\varphi}E_3+D_0^3e^{\frac{1}{3}i\varphi}E_3-D_0^2E_1E_3-D_0^2E_2E_3\\
&+D_0^3e^{-i\varphi}E_4+D_0^3e^{i\varphi}E_4-D_0^2E_1E_4-D_0^2E_2E_4-D_0^2E_3E_4+E_1E_2E_3E_4\\
&-3D_0^3e^{-\frac{1}{3}i\varphi}\lambda-3D_0^3e^{\frac{1}{3}i\varphi}\lambda-D_0^3e^{-i\varphi}\lambda-D_0^3e^{i\varphi}\lambda+3D_0^2E_1\lambda+3D_0^2E_2\lambda\\
&+3D_0^2E_3\lambda-E_1E_2E_3\lambda+3D_0^2E_4\lambda-E_1E_2E_4\lambda-E_1E_3E_4\lambda-E_2E_3E_4\lambda\\
&-6D_0^2\lambda^2+E_1E_2\lambda^2+E_1E_3\lambda^2+E_2E_3\lambda^2+E_1E_4\lambda^2+E_2E_4\lambda^2+E_3E_4\lambda^2\\
&-E_1\lambda^3-E_2\lambda^3-E_3\lambda^3-E_4\lambda^3+\lambda^4=0
\end{aligned}\tag{A.2}$$

Applying the relation

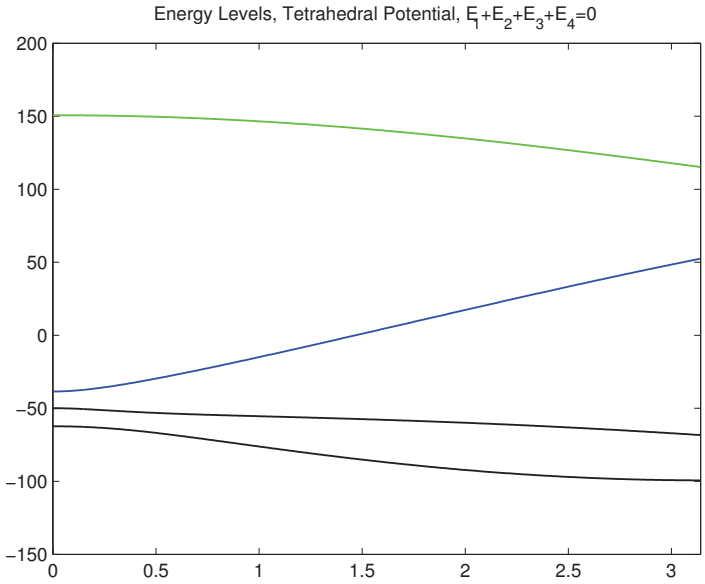

Figure A.2: Plot of the energy levels for φ varying between 0 and π.

- $\sum_{i=1,4} E_i = 0$

the Equation (A.2) becomes:

$$3D_0^4\left(1-2\cos\left(\frac{2}{3}\varphi\right)\right)+2D_0^3\cos\left(\frac{1}{3}\varphi\right)(E_1+E_2+E_3)+2D_0^3\cos(\varphi)E_4 - \left(\sum_{i<j}E_iE_j\right)D_0^2-2D_0^3\left(3\cos\left(\frac{1}{3}\varphi\right)+\cos(\varphi)\right)\lambda+\left(\sum_{i<j}E_iE_j-6D_0^2\right)\lambda^2 + \lambda^4 \approx 0 \tag{A.3}$$

In case of φ=0 and E_i=0, the equation reduces to:

$$-3D_0^4-8D_0^3\lambda-6D_0^2\lambda^2+\lambda^4=0 \tag{A.4}$$

whose eigenvalues are $\lambda_{1,2,3}=-D_0$ and $\lambda_4=3D_0$.
From the definition $D=\sqrt{E_1^2+E_2^2+E_3^2+E_4^2}$ and by an expansion of the cosines for small φ, the approximation of the characteristic polynomial (Equation (A.3)) becomes:

$$\lambda^4-\frac{1}{2}D^2\lambda^2-6D_0^2\lambda^2-8D_0^3\lambda+\frac{4}{3}D_0^3\varphi^2\lambda-3D_0^4+\frac{4}{3}D_0^4\varphi^2+\frac{1}{2}D_0^2D^2=0 \tag{A.5}$$

This equation can be factored in the following way:

$$\frac{1}{6}(D_0+\lambda)\left(+6\lambda^3-6D_0\lambda^2-3D^2\lambda-30D_0^2\lambda+8D_0^3\varphi^2+3D_0D^2-18D_0^3\right)=0 \tag{A.6}$$

Therefore, one solution is $\lambda_3=-D_0$ while the other three solutions are obtained by the resolution of the cubic equation:

$$\left(\lambda^3-D_0\lambda^2-\frac{1}{2}D^2\lambda-5D_0^2\lambda+\frac{4}{3}D_0^3\varphi^2+\frac{1}{2}D_0D^2-3D_0^3\right)=0 \tag{A.7}$$

where $a = 1$, $b = -D_0$, $c = -(\frac{1}{2}D^2 + 5D_0^2)$, $d = +\frac{4}{3}D_0^3\varphi^2 + \frac{1}{2}D_0D^2 - 3D_0^3$ indicate the coefficients. Through the transformation $\lambda = t - (b/3a)$ one obtains the depressed cubic:

$$\left(t^3 - \frac{1}{2}D^2t - \frac{16}{3}D_0^2t + \frac{4}{3}D_0^3\varphi^2 + \frac{1}{3}D_0D^2 - \frac{128}{27}D_0^3\right) = 0 \tag{A.8}$$

Defining the coefficients $p = -(\frac{1}{2}D^2 + \frac{16}{3}D_0^2)$ e $q = (\frac{4}{3}D_0^3\varphi^2 + \frac{1}{3}D_0D^2 - \frac{128}{27}D_0^3)$ one can find the solutions of Equation (A.8), of the form:

$$t_k = 2\sqrt{-\frac{p}{3}}\cos\left(\frac{1}{3}\arccos\left(\sqrt{-\frac{27q^2}{4p^3}}\right) - \frac{2\pi}{3}k\right) \tag{A.9}$$

with $k = 0, 1, 2$. Therefore, developing the coefficients we get:

$$\begin{aligned}
t_0 &= \frac{1}{\sqrt{3}}\left(2\sqrt{\frac{16D_0^2}{3} + \frac{D^2}{2}}\cos\left(\frac{1}{3}\Theta\right)\right) \\
t_1 &= \frac{1}{\sqrt{3}}\left(2\sqrt{\frac{16D_0^2}{3} + \frac{D^2}{2}}\cos\left(\frac{1}{3}\Theta - \frac{2\pi}{3}\right)\right) \\
t_2 &= \frac{1}{\sqrt{3}}\left(2\sqrt{\frac{16D_0^2}{3} + \frac{D^2}{2}}\cos\left(\frac{1}{3}\Theta - \frac{4\pi}{3}\right)\right)
\end{aligned} \tag{A.10}$$

where it holds that

$$\Theta = \arccos\left(\frac{3\sqrt{3}}{2}\sqrt{-\frac{(-\frac{128D_0^3}{27} + \frac{D_0D^2}{3} + \frac{4D_0^3\varphi^2}{3})^2}{(-\frac{16D_0^2}{3} - \frac{D^2}{2})^3}}\right) \tag{A.11}$$

The solutions of the quartic (Equation (A.5)) are therefore:

$$\begin{aligned}
\lambda_0 &= \frac{D_0}{3} + \frac{1}{\sqrt{3}}\left(2\sqrt{\frac{16D_0^2}{3} + \frac{D^2}{2}}\cos\left(\frac{1}{3}\Theta\right)\right) \\
\lambda_1 &= \frac{D_0}{3} + \frac{1}{\sqrt{3}}\left(2\sqrt{\frac{16D_0^2}{3} + \frac{D^2}{2}}\cos\left(\frac{1}{3}\Theta - \frac{2\pi}{3}\right)\right) \\
\lambda_2 &= \frac{D_0}{3} + \frac{1}{\sqrt{3}}\left(2\sqrt{\frac{16D_0^2}{3} + \frac{D^2}{2}}\cos\left(\frac{1}{3}\Theta - \frac{4\pi}{3}\right)\right) \\
\lambda_3 &= -D_0
\end{aligned} \tag{A.12}$$

and we obtain that

$$\cos\Theta = \sqrt{2}\sqrt{\frac{D_0^2(9D^2 + 4D_0^2(-32 + 9\varphi^2))^2}{(32D_0^2 + 3D^2)^3}} \approx \frac{1}{8}\sqrt{64 - 27\left(\frac{D}{D_0}\right)^2 - 36\varphi^2} \tag{A.13}$$

if $\varphi \to 0$ e $\frac{D}{D_0} \to 0$, one has that $\cos\Theta = 1$. Therefore, if $\Theta \to 0$, it is possible to expand the cosine ($\cos\Theta \sim 1 - \frac{\Theta^2}{2}$) and the sine ($\sin\Theta \sim \Theta$) for small Θ angles. The plot of

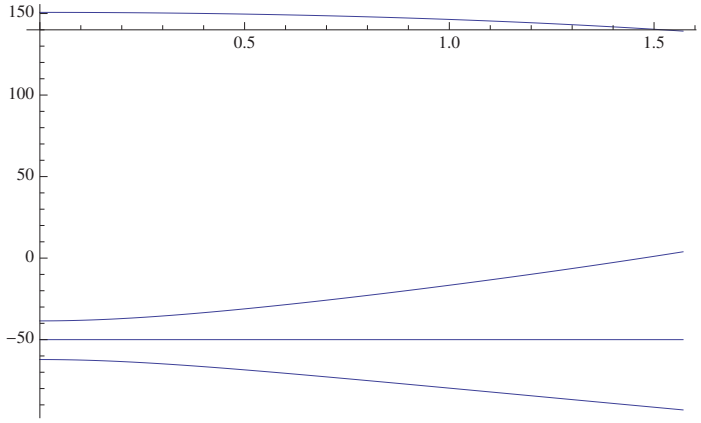

Figure A.3: Plot of the approximated energy levels (Equation (A.12)) as a function of φ which varies between 0 and $\pi/2$.

the approximate eigenvalues is shown in Figure A.3. From the Equation (A.12) it is possible to get the behavior of the two lower energy gaps:

$$\begin{aligned}\Delta\mathcal{E}' &= \lambda_2 - \lambda_3 = -\frac{4}{3}D_0 + \frac{2}{\sqrt{3}}\sqrt{\frac{16D_0^2}{3} + \frac{D^2}{2}}\sin\left(\frac{\pi}{6} + \frac{\Theta}{3}\right) \\ \Delta\mathcal{E}'' &= \lambda_1 - \lambda_3 = +\frac{4}{3}D_0 - \frac{2}{\sqrt{3}}\sqrt{\frac{16D_0^2}{3} + \frac{D^2}{2}}\sin\left(\frac{\pi}{6} - \frac{\Theta}{3}\right)\end{aligned} \tag{A.14}$$

However, in the limit $\varphi \to 0$ e $\frac{D}{D_0} \to 0$, the two gaps are equal and equal to:

$$\Delta\mathcal{E}' = \Delta\mathcal{E}'' \approx \frac{1}{2}\sqrt{D^2 + \frac{4}{3}\varphi^2 D_0^2} \tag{A.15}$$

A.2.2 Calculation of the density of states

The considered distribution function to obtain a DOS behavior like $1/E$, is the following:

$$P(E_1, E_2, E_3, E_4, D_0) = \frac{P^*}{(E_1^2 + E_2^2 + E_3^2 + E_4^2)^{\frac{3}{2}} D_0} = 4\pi\frac{P^*}{D^3 D_0} \tag{A.16}$$

Note that when another energy level is included in the analysis we have to increase the exponent of D. The reduced DOS (considering only the two lower energy gaps) is defined as:

$$\begin{aligned}n(E) &= 4\pi\int_{D_{min}} dD D^2 \int_{D_{0min}}^{D_{0max}} dD_0 \frac{P^*}{D^3 D_0}\delta(E - \Delta\mathcal{E}_1)\delta(E' - \Delta\mathcal{E}_2) \\ &= 4\pi P^* \int_{D_{min}} \frac{dD}{D}\int_{D_{0min}}^{D_{0max}} \frac{dD_0}{D_0}\delta\left(E - \frac{1}{2}\sqrt{D^2 + \frac{4}{3}\varphi^2 D_0^2}\right)\delta\left(E' - \frac{1}{2}\sqrt{D^2 + \frac{4}{3}\varphi^2 D_0^2}\right)\end{aligned} \tag{A.17}$$

Using the representation:

$$\delta(f(x)) = \sum_i \frac{\delta(x-x_i)}{|f'(x_i)|} \tag{A.18}$$

where x_i are the points in which $f(x)$=0, whith $x = D_0$, one finds that:

$$2\sqrt{3}\int_{D_{0min}}^{D_{0max}} \frac{dD_0}{D_0}\frac{E}{\varphi\sqrt{4E^2-D^2}}\delta\left(D_0 - \frac{\sqrt{3}}{\varphi}\sqrt{E^2-\frac{D^2}{4}}\right) = \frac{4E}{4E^2-D^2} \tag{A.19}$$

This integral is non-zero if $D_{0min} \leq D_{0+} = \frac{\sqrt{3}}{\varphi}\sqrt{E^2-\frac{D^2}{4}} \leq D_{0max}$, ie if

$$\begin{cases} D_1 \leq D \leq D_2 \\ D \geq D_{min} \end{cases}$$

with $D_1 = 2\sqrt{E^2 - \frac{1}{3}\varphi^2 D_{0max}^2}$ and $D_2 = 2\sqrt{E^2 - \frac{1}{3}\varphi^2 D_{0min}^2}$.
Expressing the other energy gap as a function of D_{0+} one obtains:

$$\delta(E' - \Delta\mathcal{E}_2) = \delta(E'-E) \tag{A.20}$$

which confirms the fact that the two gaps are equal in the limit $\varphi \to 0$ e $\frac{D}{D_0} \to 0$.
We can therefore distinguish the two intervals:

1. $D_1 < D_{min}$ for which the DOS becomes

$$n(E,E') = 4\pi P^* \int_{D_{min}}^{D_2} \frac{dD}{D}\frac{4E}{4E^2-D^2}\delta(E'-E) \tag{A.21}$$

With the change of variables $x = \frac{D}{2E}$, the integral becomes:

$$n(E,E') = \frac{4\pi P^*}{E}\int_{x_{min}}^{x_2}\frac{dx}{x}\frac{1}{(1-x^2)}\delta(E'-E) \tag{A.22}$$

and its solution has the form:

$$\begin{aligned} n(E,E') &= \frac{4\pi P^*}{E}\ln\left[\frac{x}{\sqrt{1-x^2}}\right]_{x_{min}}^{x_2}\delta(E'-E) \\ &= \frac{4\pi P^*}{E}\ln\left[\frac{\sqrt{(3E^2-D_{0min}^2\varphi^2)(4E^2-D_{min}^2)}}{D_{0min}D_{min}\varphi}\right]\delta(E'-E) \end{aligned} \tag{A.23}$$

2. $D_1 > D_{min}$; therefore the DOS is calculated as

$$n(E,E') = 4\pi P^* \int_{D_1}^{D_2} \frac{dD}{D}\frac{4E}{4E^2-D^2}\delta(E'-E) \tag{A.24}$$

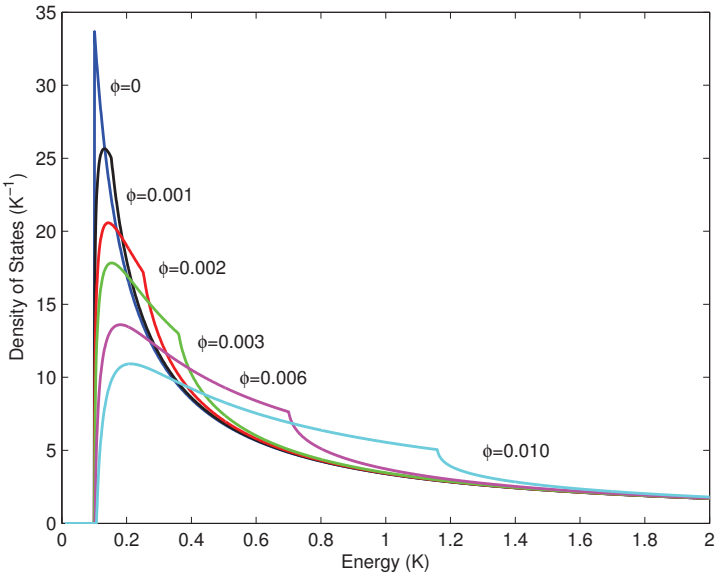

Figure A.4: Behavior of the DOS as a function of energy.

Proceeding as in point 1. one finds:

$$\begin{aligned} n(E,E') &= \frac{4\pi P^*}{E} \ln\left[\frac{x}{\sqrt{1-x^2}}\right]_{x_1}^{x_2} \delta(E'-E) \\ &= \frac{4\pi P^*}{E} \ln\left[\frac{D_{0max}}{D_{0min}}\sqrt{\frac{3E^2 - D_{0min}^2\varphi^2}{3E^2 - D_{0max}^2\varphi^2}}\right]\delta(E'-E) \\ &= \frac{4\pi P^*}{E} \ln\left[\sqrt{\frac{\frac{3E^2}{(D_{0min}\varphi)^2}-1}{\frac{3E^2}{(D_{0max}\varphi)^2}-1}}\right]\delta(E'-E) \end{aligned} \tag{A.25}$$

Therefore the complete form for the DOS is the following:

$$n(E,E',\varphi) = \begin{cases} 0 & \text{if } E < E_{c1} \\ n_+ = \frac{4\pi P^*}{E} \ln\left[\frac{\sqrt{(3E^2 - D_{0min}^2\varphi^2)(4E^2 - D_{min}^2)}}{D_{0min}D_{min}\varphi}\right]\delta(E'-E) & \text{if } E_{c1} < E < E_{c2} \\ n_- = \frac{4\pi P^*}{E} \ln\left[\sqrt{\frac{\frac{3E^2}{(D_{0min}\varphi)^2}-1}{\frac{3E^2}{(D_{0max}\varphi)^2}-1}}\right]\delta(E'-E) & \text{if } E > E_{c2} \end{cases}$$

where the critical values for which the DOS changes are $E_{c1} = \sqrt{\frac{1}{4}D_{min}^2 + \frac{1}{3}D_{0min}^2\varphi^2}$ and $E_{c2} = \sqrt{\frac{1}{4}D_{min}^2 + \frac{1}{3}D_{0max}^2\varphi^2}$. The plots of the DOS as a function of the energy and the AB phase, for a single ATS, are shown in Figures A.4 and A.5. We clearly notice that the shape of the DOS that we find is identical to the previously analyzed case of the TWP. The main consequence we expect from this result is that, since as we said, the shape of the DOS appears to give rise to the magnetic effect, we have the

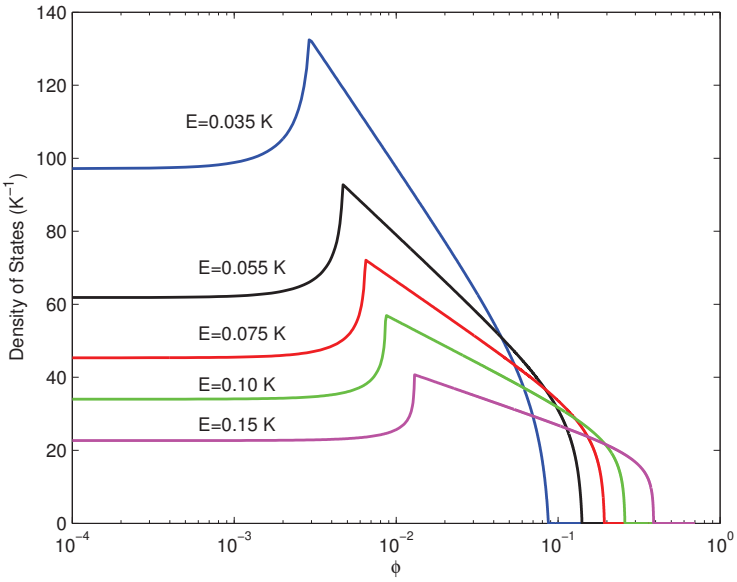

Figure A.5: Behavior of the DOS as a function of the AB phase φ.

confirmation that the TWP is the correct potential, suitable to describe real glasses. To obtain further confirmation we thus compute the contribution from the ATS to the heat capacity, using the present result.

A.2.3 Calculation of the specific heat

The aim of this Section is to check whether with the TFWP we obtain the same behavior of the ATS contribution to the specific heat, found for the TWP. From the solution of the eigenvalue equation, one gets four eigenvalues such that $\mathcal{E}_1 < \mathcal{E}_2 < \mathcal{E}_3 << \mathcal{E}_4$. Therefore, considering this low temperature regime, we can think about working with an *effective* three level system. The four-level model reduces to a three-level system with two equal energy gaps: $E = |\mathcal{E}_2 - \mathcal{E}_1| = |\mathcal{E}_3 - \mathcal{E}_2| = E'$ which depend on the phase $\varphi(B)$. It is necessary to calculate the contribution to the specific heat of each tunneling unit. The partition function can be written, with $\beta = \frac{1}{k_B T}$, as:

$$Z = \mathrm{e}^{-\beta\mathcal{E}_1} + \mathrm{e}^{-\beta\mathcal{E}_2} + \mathrm{e}^{-\beta\mathcal{E}_3} \tag{A.26}$$

It is now possible to express the energy levels as a function of the energy gap E and E':

$$\begin{aligned} \mathcal{E}_1 &= -\frac{E+E'}{2} + x \\ \mathcal{E}_2 &= +\frac{E-E'}{2} + x \\ \mathcal{E}_3 &= +\frac{E+E'}{2} + x \end{aligned} \tag{A.27}$$

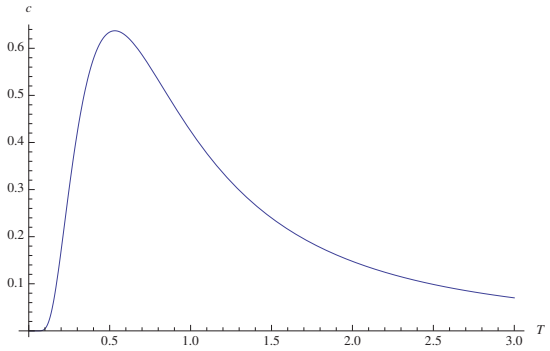

Figure A.6: Behavior of $c_0(E,E',T)$ as a function of T.

where $x = \frac{\mathcal{E}_1+\mathcal{E}_3}{2}$ represents the average between the two outer levels $\mathcal{E}_1$, $\mathcal{E}_3$. By calculating:

$$\begin{aligned} F(T) &= -\frac{1}{\beta}\ln Z = -\frac{1}{\beta}\ln\left[e^{-\beta x}\left(e^{\frac{\beta(E+E')}{2}}+e^{-\frac{\beta(E-E')}{2}}+e^{-\frac{\beta(E+E')}{2}}\right)\right] \\ &= x-\frac{1}{\beta}\ln\left[e^{\frac{\beta(E+E')}{2}}+e^{-\frac{\beta(E-E')}{2}}+e^{-\frac{\beta(E+E')}{2}}\right] \\ &= x-k_BT\ln\left[2\cosh\left(\frac{E+E'}{2k_BT}\right)+e^{\frac{-E+E'}{2k_BT}}\right] \end{aligned} \tag{A.28}$$

we obtain the specific heat per tunneling unit:

$$c_0(E,E',T) = -T\frac{\partial^2 F(T)}{\partial T^2} = \frac{1}{k_BT^2}\frac{e^{\frac{E'}{k_BT}}\left(E'^2+e^{\frac{E}{k_BT}}\left((E+E')^2+E^2e^{\frac{E'}{k_BT}}\right)\right)}{\left(1+e^{\frac{E'}{k_BT}}+e^{\frac{E+E'}{k_BT}}\right)^2} \tag{A.29}$$

The behavior of $c_0(E,E',T)$ is shown in Figure A.6. Using the form found for the contribution to the specific heat of each tunneling unit, $c_0(E,E',T)$, and the form of the DOS calculated in Section A.2.2, the specific heat in the presence of magnetic field is:

$$\begin{aligned} C(T,\varphi) &= \int dE' \int dE\; c_0(E,E',T)n(E,E',\varphi) \\ &= \int dE' \int dE\; c_0(E,E',T)n(E,\varphi)\delta(E'-E) = \int dE\; c_0(E,E',T)n(E,\varphi) \end{aligned} \tag{A.30}$$

where

$$c_0(E,E',T) = \frac{4E^2+E^2e^{-\frac{E}{k_BT}}+E^2e^{+\frac{E}{k_BT}}}{k_BT^2\left(1+2\cosh\left(\frac{E}{k_BT}\right)\right)^2} \tag{A.31}$$

Therefore, the integral can be written as:

$$C(T,\varphi) = \int_{E_{c1}}^{E_{c2}} c_0(E,E',T)\frac{4\pi P^*}{E}\ln\left[\frac{\sqrt{(3E^2 - D_{0min}^2\varphi^2)(4E^2 - D_{min}^2)}}{D_{0min}D_{min}\varphi}\right]\mathrm{d}E + \int_{E_{c2}}^{\infty} c_0(E,E',T)\frac{4\pi P^*}{E}\ln\left[\sqrt{\frac{\frac{3E^2}{(D_{0min}\varphi)^2} - 1}{\frac{3E^2}{(D_{0max}\varphi)^2} - 1}}\right]\mathrm{d}E \tag{A.32}$$

It should be noted that the expressions $E_{c1} = \sqrt{\frac{1}{4}D_{min}^2 + \frac{1}{3}D_{0min}^2\varphi^2}$ and $E_{c2} = \sqrt{\frac{1}{4}D_{min}^2 + \frac{1}{3}D_{0max}^2\varphi^2}$ depend on φ.
By using the following change of variables $y = \frac{E}{k_BT}$, and considering the following relations:

$$\int \frac{y\cdot(2+\cosh y)}{(1+2\cosh y)^2}\mathrm{d}y = \left[\frac{y\sinh y}{1+2\cosh y} - \frac{1}{2}\ln(1+2\cosh y)\right] \tag{A.33}$$

in particular:

$$\int_0^{\infty} \frac{y\cdot(2+\cosh y)}{(1+2\cosh y)^2}\mathrm{d}y = \frac{\ln 3}{2} \tag{A.34}$$

it is possible to rewrite the form of the specific heat (Equation (A.32)) in the following way:

$$\begin{aligned} C(T,\varphi) = 8\pi P^* k_B\Bigg\{ &\ln\left(\frac{x_{0max}}{x_{0min}}\right)\cdot\left(\frac{1}{2}\ln(1+2\cosh x_{c2}) - \frac{x_{c2}\sinh x_{c2}}{1+2\cosh x_{c2}}\right) \\ &+ \ln(x_{min}x_{0min}\varphi)\cdot[\mathcal{I}(x_{c1}) - \mathcal{I}(x_{c2})] + \frac{1}{2}\Big[\mathfrak{I}(x_{c1},x_{min},4) - \mathfrak{I}(x_{c2},x_{min},4) \\ &+ \mathfrak{I}(x_{c1},x_{0min}\varphi,3) - \mathfrak{I}(x_{c2},x_{0max}\varphi,3)\Big]\Bigg\} \end{aligned} \tag{A.35}$$

where $x_{c1,2} = E_{c1,2}/k_BT$, $x_{min} = D_{min}/k_BT$, etc., and the following quantities have been defined:

$$\begin{aligned} \mathcal{I}(x) &\equiv \left[\frac{x\sinh x}{1+2\cosh x} - \frac{1}{2}\ln(1+2\cosh x)\right] \\ \mathfrak{I}(x,a,b) &\equiv \int_x^{\infty}\mathrm{d}y\ \frac{y\cdot(2+\cosh y)}{(1+2\cosh y)^2}\ln\left(by^2 - a^2\right) \end{aligned} \tag{A.36}$$

Table A.1 reports the parameters used to numerically calculate $C(T,\varphi)$ (Equation (A.35)) as a function of φ, which depends on the magnetic field $\vec{B}$ through the usual relations:

$$\varphi = 2\pi\frac{\Phi(\vec{B})}{\Phi_0}, \quad \Phi(\vec{B}) = \vec{S}\cdot\vec{B} \tag{A.37}$$

The behavior of $C(T,\varphi)$ as a function of $\vec{B}$ for the parameters reported in Table A.1 is presented in Figure A.7. We therefore find that the characteristic behavior of the ATS

contribution to the specific heat has a qualitative agreement with the one give by the TWP version. We can therefore conclude that the TWP suffices to fit the experimental data and obtain a suitable approximation of the more realistic TFWPs advocated by the cellular model (Chapter 1, Section 1.3).

$n_{ATS}P^*$	D_{min}	$D_{0min}\lvert\frac{q}{e}\rvert S$	$D_{0min}\lvert\frac{q}{e}\rvert S$	$\Phi_0 = \frac{h}{e}$	T	B	E
g^{-1}	K	KÅ^2	KÅ^2	TÅ^2	K	T	K
3.0×10^{15}	0.02	1.98×10^{4}	4.96×10^{5}	4.3×10^{5}	0.35	0-1	0.01-2

Table A.1: Parameters used to calculate the specific heat.

A.3 Derivation in the presence of a generic magnetic field

This Section deals with the derivation of the energy levels for the more general case of a $\vec{B}$ directed randomly. We therefore describe the magnetic field (using the polar coordinates) in this way, $\vec{B} = (B\sin\theta\cos\phi, B\sin\theta\sin\phi, B\cos\theta)$. The area of a face of the tetrahedron is $S = \frac{\sqrt{3}}{4}l^2$; the unit vectors are described in Section A.1. The total fluxes are:

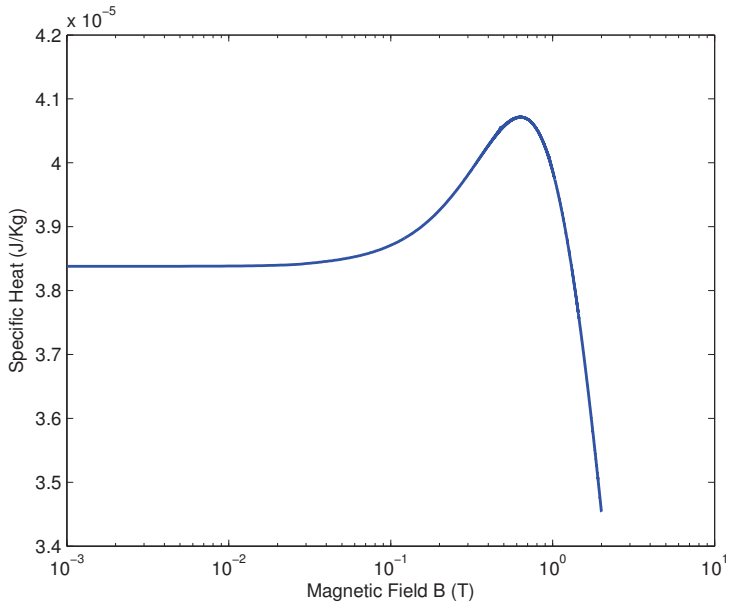

Figure A.7: Behavior of the specific heat as a function of the magnetic field, calculated with the parameters in the table A.1.

- $\varphi_{tot}^{213}=\frac{e}{\hbar}S\vec{B}\cdot\hat{n}_{213}=\frac{e}{\hbar}\frac{\sqrt{3}}{4}l^2B\cos\theta$.
- $\varphi_{tot}^{243}=\frac{e}{\hbar}S\vec{B}\cdot\hat{n}_{243}=\frac{e}{\hbar}\frac{\sqrt{3}}{4}l^2B\big(-\frac{2\sqrt{2}}{3}\sin\theta\sin\phi+\frac{1}{3}\cos\theta\big)$.
- $\varphi_{tot}^{134}=\frac{e}{\hbar}S\vec{B}\cdot\hat{n}_{134}=\frac{e}{\hbar}\frac{\sqrt{3}}{4}l^2B\big(-\frac{\sqrt{6}}{3}\sin\theta\cos\phi+\frac{\sqrt{2}}{3}\sin\theta\sin\phi+\frac{1}{3}\cos\theta\big)$.
- $\varphi_{tot}^{142}=\frac{e}{\hbar}S\vec{B}\cdot\hat{n}_{142}=\frac{e}{\hbar}\frac{\sqrt{3}}{4}l^2B\big(+\frac{\sqrt{6}}{3}\sin\theta\cos\phi+\frac{\sqrt{2}}{3}\sin\theta\sin\phi+\frac{1}{3}\cos\theta\big)$.

A.3.1 Calculation of the Peierls phases

To calculate the Peierls phases one proceeds as before:

$$\varphi_{ij}=\frac{e}{\hbar}\int_a^b\big(A_x\mathrm{d}x+A_y\mathrm{d}y+A_z\mathrm{d}z\big)=\frac{e}{\hbar}\int_a^b\mathrm{d}t\left(A_x\frac{\mathrm{d}x}{\mathrm{d}t}+A_y\frac{\mathrm{d}y}{\mathrm{d}t}+A_z\frac{\mathrm{d}z}{\mathrm{d}t}\right)\tag{A.38}$$

where t parameterizes the straight line.
The vector potential, when $\vec{B}$ is generic, is:
$\vec{A}=\big(\frac{1}{2}B\big(-\cos\theta\ y+\sin\theta\sin\phi\ z\big),+\frac{1}{2}B\big(\cos\theta\ x-\sin\theta\cos\phi\ z\big),\frac{1}{2}B\big(-\sin\theta\sin\phi\ x+\sin\theta\cos\phi\ y\big)\big)$; the Peierls phases are then:

- $\varphi_{12}=-\frac{e}{\hbar}\frac{\sqrt{3}}{12}l^2B\cos\theta$;
- $\varphi_{23}=-\frac{e}{\hbar}\frac{\sqrt{3}}{12}l^2B\cos\theta$;
- $\varphi_{31}=-\frac{e}{\hbar}\frac{\sqrt{3}}{12}l^2B\cos\theta$;
- $\varphi_{14}=+\frac{e}{\hbar}\frac{\sqrt{2}}{6}l^2B\sin\theta\cos\phi$;
- $\varphi_{24}=+\frac{e}{\hbar}l^2B\big(-\frac{\sqrt{6}}{12}\sin\theta\sin\phi-\frac{\sqrt{2}}{12}\sin\theta\cos\phi\big)$;
- $\varphi_{34}=+\frac{e}{\hbar}l^2B\big(+\frac{\sqrt{6}}{12}\sin\theta\sin\phi-\frac{\sqrt{2}}{12}\sin\theta\cos\phi\big)$;

Therefore, by the sum of the closed paths, we have:

- face 213: $\varphi_{21}+\varphi_{13}+\varphi_{32}=\frac{e}{\hbar}\frac{\sqrt{3}}{4}l^2B\cos\theta$;
- face 243: $\varphi_{24}+\varphi_{43}+\varphi_{32}=\frac{e}{\hbar}l^2B\big(+\frac{\sqrt{3}}{12}\cos\theta-\frac{\sqrt{6}}{6}\sin\theta\sin\phi\big)$;
- face 134: $\varphi_{13}+\varphi_{34}+\varphi_{41}=\frac{e}{\hbar}l^2B\big(+\frac{\sqrt{3}}{12}\cos\theta+\frac{\sqrt{6}}{12}\sin\theta\sin\phi-\frac{\sqrt{2}}{4}\sin\theta\cos\phi\big)$;
- face 142: $\varphi_{14}+\varphi_{42}+\varphi_{21}=\frac{e}{\hbar}l^2B\big(+\frac{\sqrt{3}}{12}\cos\theta+\frac{\sqrt{6}}{12}\sin\theta\sin\phi+\frac{\sqrt{2}}{4}\sin\theta\cos\phi\big)$;

A.3.2 Calculation of the energy levels and the gaps

The matrix in the case of generic $\vec{B}$ is:

$$H_0 = \begin{pmatrix} E_1 & D_0 e^{-i\frac{\varphi}{3}\cos\theta} & D_0 e^{+i\frac{\varphi}{3}\cos\theta} & D_0 e^{+i\frac{2\sqrt{6}}{9}\varphi\sin\theta\cos\phi} \\ D_0 e^{+i\frac{\varphi}{3}\cos\theta} & E_2 & D_0 e^{-i\frac{\varphi}{3}\cos\theta} & D_0 e^{-i\frac{\sqrt{2}}{3}\varphi\sin\theta\left(\sin\phi+\frac{\sqrt{3}}{3}\cos\phi\right)} \\ D_0 e^{-i\frac{\varphi}{3}\cos\theta} & D_0 e^{+i\frac{\varphi}{3}\cos\theta} & E_3 & D_0 e^{+i\frac{\sqrt{2}}{3}\varphi\sin\theta\left(\sin\phi-\frac{\sqrt{3}}{3}\cos\phi\right)} \\ D_0 e^{-i\frac{2\sqrt{6}}{9}\varphi\sin\theta\cos\phi} & D_0 e^{+i\frac{\sqrt{2}}{3}\varphi\sin\theta\left(\sin\phi+\frac{\sqrt{3}}{3}\cos\phi\right)} & D_0 e^{-i\frac{\sqrt{2}}{3}\varphi\sin\theta\left(\sin\phi-\frac{\sqrt{3}}{3}\cos\phi\right)} & E_4 \end{pmatrix} \tag{A.39}$$

The characteristic polynomial is:

$$\begin{aligned}
&+3D_0^4 - D_0^2\left(\sum_{i<j} E_i E_j\right) + E_1E_2E_3E_4 + 3D_0^2\left(\sum_i E_i\right)\lambda \\
&-\left(\sum_{i<j<k} E_iE_jE_k\right)\lambda - 6D_0^2\lambda^2 + \left(\sum_{i<j} E_iE_j\right)\lambda^2 - \left(\sum_i E_i\right)\lambda^3 + \lambda^4 \\
&+2D_0^3\Bigg[(E_1-\lambda)\cos\left(\frac{1}{3}\varphi\left(\cos\theta - 2\sqrt{2}\sin\phi\sin\theta\right)\right) + (E_4-\lambda)\cos(\varphi\cos\theta) \\
&+(E_2-\lambda)\cos\left(\frac{1}{3}\varphi\left(\cos\theta + \sqrt{2}\sin\theta\left(-\sqrt{3}\cos\phi + \sin\phi\right)\right)\right) \\
&+(E_3-\lambda)\cos\left(\frac{1}{3}\varphi\left(\cos\theta + \sqrt{2}\sin\theta\left(+\sqrt{3}\cos\phi + sin\phi\right)\right)\right)\Bigg] \\
&-2D_0^4\Bigg[\cos\left(\frac{1}{3}\varphi\left(2\cos\theta + \sqrt{2}\sin\theta\left(+\sqrt{3}\cos\phi - \sin\phi\right)\right)\right) \\
&-\cos\left(\frac{1}{3}\varphi\left(2\cos\theta - \sqrt{2}\sin\theta\left(+\sqrt{3}\cos\phi + \sin\phi\right)\right)\right) \\
&-\cos\left(\frac{2}{3}\varphi\left(\cos\theta - \sqrt{2}\sin\phi\sin\theta\right)\right)\Bigg]
\end{aligned} \tag{A.40}$$

Applying:

- $\sum_{i=1,4} E_i = 0$

- $\sum_{i<j<k} E_iE_jE_k = 0$

the eigenvalue equation becomes:

$$
\begin{aligned}
&+3D_0^4 - D_0^2\left(\sum_{i<j} E_iE_j\right) - 6D_0^2\lambda^2 + \left(\sum_{i<j} E_iE_j\right)\lambda^2 + \lambda^4 \\
&+2D_0^3\Bigg[(E_1-\lambda)\cos\left(\frac{1}{3}\varphi\Big(\cos\theta - 2\sqrt{2}\sin\phi\sin\theta\Big)\right) + (E_4-\lambda)\cos(\varphi\cos\theta) \\
&+(E_2-\lambda)\cos\left(\frac{1}{3}\varphi\Big(\cos\theta + \sqrt{2}\sin\theta\big(-\sqrt{3}\cos\phi + \sin\phi\big)\Big)\right) \\
&+(E_3-\lambda)\cos\left(\frac{1}{3}\varphi\Big(\cos\theta + \sqrt{2}\sin\theta\big(+\sqrt{3}\cos\phi + sin\phi\big)\Big)\right)\Bigg] \\
&-2D_0^4\Bigg[\cos\left(\frac{1}{3}\varphi\Big(2\cos\theta + \sqrt{2}\sin\theta\big(+\sqrt{3}\cos\phi - \sin\phi\big)\Big)\right) \\
&-\cos\left(\frac{1}{3}\varphi\Big(2\cos\theta - \sqrt{2}\sin\theta\big(+\sqrt{3}\cos\phi + \sin\phi\big)\Big)\right) \\
&-\cos\left(\frac{2}{3}\varphi\Big(\cos\theta - \sqrt{2}\sin\phi\sin\theta\Big)\right)\Bigg] \approx 0
\end{aligned}
\tag{A.41}
$$

If ϕ=0 e θ=0, the characteristic polynomial is reduced exactly to that of the case of orthogonal B:

$$
\begin{aligned}
&+3D_0^4\left(1-2\cos\left(\frac{2}{3}\varphi\right)\right) + 2D_0^3\cos\left(\frac{1}{3}\varphi\right)(E_1+E_2+E_3) + 2D_0^3\cos(\varphi)E_4 \\
&-\left(\sum_{i<j} E_iE_j\right)D_0^2 - 2D_0^3\left(3\cos\left(\frac{1}{3}\varphi\right) + \cos(\varphi)\right)\lambda + \left(\sum_{i<j} E_iE_j - 6D_0^2\right)\lambda^2 \\
&+\lambda^4
\end{aligned}
\tag{A.42}
$$

We define the following quantities:

- $\alpha \equiv \frac{1}{3}\cos\theta$;
- $\beta \equiv \frac{2\sqrt{6}}{9}\sin\theta\cos\phi$;
- $\gamma \equiv \frac{\sqrt{2}}{3}\sin\theta\sin\phi$;
- $\delta \equiv \frac{\sqrt{2}}{3}\sin\theta\frac{\sqrt{3}}{3}\cos\phi$;

Through an expansion of the cosines for small φ, Equation (A.41) reduces to:

$$
+\lambda^4 - \frac{1}{2}D^2\lambda^2 - 6D_0^2\lambda^2 - 8D_0^3\lambda + \zeta D_0^3\varphi^2\lambda - 3D_0^4 + \zeta D_0^4\varphi^2 + \frac{1}{2}D_0^2D^2 = 0 \tag{A.43}
$$

that has the same form of the Equation (A.5), which refers to the case of the orthogonal tetrahedric potential; ζ denotes an expression that depends from θ e ϕ in the following manner:

$$
\begin{aligned}
\zeta &= 2\big(6\alpha^2 + \beta^2 + \gamma^2 + \beta(\gamma-\delta) + \gamma\delta + \delta^2\big) \\
&= \frac{4}{3}\cos^2\theta + \frac{2}{27}\Big(10 + 4\cos(2\phi) + 5\sqrt{3}\sin(2\phi)\Big)\sin^2\theta
\end{aligned}
\tag{A.44}
$$

Equation (A.43) can be factored in the following way:

$$\left(D_0+\lambda\right)\left(\lambda^3-D_0\lambda^2-\frac{1}{2}D^2\lambda-5D_0^2\lambda+\zeta D_0^3\varphi^2+\frac{1}{2}D_0D^2-3D_0^3\right) \tag{A.45}$$

Therefore, one solution is $\lambda_3=-D_0$, while the other three solutions are obtained by the resolution of the cubic equation:

$$\left(\lambda^3-D_0\lambda^2-\frac{1}{2}D^2\lambda-5D_0^2\lambda+\zeta D_0^3\varphi^2+\frac{1}{2}D_0D^2-3D_0^3\right)=0 \tag{A.46}$$

where $a=1$, $b=-D_0$, $c=-(\frac{1}{2}D^2+5D_0^2)$, $d=+\zeta D_0^3\varphi^2+\frac{1}{2}D_0D^2-3D_0^3$ indicate the coefficients. Through the transformation $\lambda=t-(b/3a)$ one gets the depressed cubic:

$$\left(t^3-\frac{1}{2}D^2t-\frac{16}{3}D_0^2t+\zeta D_0^3\varphi^2+\frac{1}{3}D_0D^2-\frac{128}{27}D_0^3\right)=0 \tag{A.47}$$

Defining the coefficients $p=-(\frac{1}{2}D^2+\frac{16}{3}D_0^2)$ and $q=(\zeta D_0^3\varphi^2+\frac{1}{3}D_0D^2-\frac{128}{27}D_0^3)$ one finds the solutions of the Equation (A.47) of the usual form (Equation (A.9)). Thus developing the coefficients, one gets the three solutions of the cubic equation (as in Equation (A.10)):

$$\begin{aligned}
t_0&=\frac{1}{\sqrt{3}}\left(2\sqrt{\frac{16D_0^2}{3}+\frac{D^2}{2}}\cos\left(\frac{1}{3}\Theta\right)\right)\\
t_1&=\frac{1}{\sqrt{3}}\left(2\sqrt{\frac{16D_0^2}{3}+\frac{D^2}{2}}\cos\left(\frac{1}{3}\Theta-\frac{2\pi}{3}\right)\right)\\
t_2&=\frac{1}{\sqrt{3}}\left(2\sqrt{\frac{16D_0^2}{3}+\frac{D^2}{2}}\cos\left(\frac{1}{3}\Theta-\frac{4\pi}{3}\right)\right)
\end{aligned} \tag{A.48}$$

but in this case:

$$\Theta\approx\arccos\left(\frac{1}{8}\sqrt{64-27\left(\frac{D}{D_0}\right)^2-27\zeta\varphi^2}\right) \tag{A.49}$$

The solutions of the quartic (Equation (A.43)) are therefore:

$$\begin{aligned}
\lambda_0&=\frac{D_0}{3}+\frac{1}{\sqrt{3}}\left(2\sqrt{\frac{16D_0^2}{3}+\frac{D^2}{2}}\cos\left(\frac{1}{3}\Theta\right)\right)\\
\lambda_1&=\frac{D_0}{3}+\frac{1}{\sqrt{3}}\left(2\sqrt{\frac{16D_0^2}{3}+\frac{D^2}{2}}\cos\left(\frac{1}{3}\Theta-\frac{2\pi}{3}\right)\right)\\
\lambda_2&=\frac{D_0}{3}+\frac{1}{\sqrt{3}}\left(2\sqrt{\frac{16D_0^2}{3}+\frac{D^2}{2}}\cos\left(\frac{1}{3}\Theta-\frac{4\pi}{3}\right)\right)\\
\lambda_3&=-D_0
\end{aligned} \tag{A.50}$$

and we obtain that

$$\cos\Theta\approx\left(\frac{1}{8}\sqrt{64-27\left(\frac{D}{D_0}\right)^2-27\zeta\varphi^2}\right) \tag{A.51}$$

if $\varphi \to 0$ and $\frac{D}{D_0} \to 0$, we obtain $\cos\Theta = 1$. Therefore, if $\Theta \to 0$ one can expand the cosine for small Θ angles:

$$\Theta \approx \sqrt{\frac{27}{64}\left(\frac{D}{D_0}\right)^2 + \frac{27}{64}\zeta\varphi^2} \tag{A.52}$$

From Equation (A.50), it is possible to obtain the behavior of the two lower energy gaps:

$$\begin{aligned}
\Delta\mathcal{E}' &= \lambda_2 - \lambda_3 = -\frac{4}{3}D_0 + \frac{2}{\sqrt{3}}\sqrt{\frac{16D_0^2}{3} + \frac{D^2}{2}}\sin\left(\frac{\pi}{6} + \frac{\Theta}{3}\right) \\
\Delta\mathcal{E}'' &= \lambda_1 - \lambda_3 = +\frac{4}{3}D_0 - \frac{2}{\sqrt{3}}\sqrt{\frac{16D_0^2}{3} + \frac{D^2}{2}}\sin\left(\frac{\pi}{6} - \frac{\Theta}{3}\right)
\end{aligned} \tag{A.53}$$

However, as in the case of the orthogonal tetrahedric potential, in the limit $\varphi \to 0$ e $\frac{D}{D_0} \to 0$, the two gaps are equal and equal to:

$$\Delta\mathcal{E}' = \Delta\mathcal{E}'' \approx \frac{1}{2}\sqrt{D^2 + \zeta\varphi^2 D_0^2} \tag{A.54}$$

It should be noted that the variable ζ, which depends on θ and ϕ, is defined in Equation (A.44); in particular in the case where ϕ=0 and θ=0, one has that $\zeta = \frac{4}{3}$ and hence the gap reduces exactly to that of the case of perpendicular B (Equation (A.15)).
The orientational average value of ζ^2 is different from zero, in fact we have:

$$\begin{aligned}
\overline{\zeta^2} &= \int_0^\pi d\theta \sin\theta \int_0^{2\pi} d\phi \frac{\zeta^2}{4\pi} \\
&= \frac{1}{4\pi}\int_0^\pi d\theta \sin\theta \int_0^{2\pi} d\phi \left(\frac{4}{3}\cos^2\theta + \frac{2}{27}\left(10 + 4\cos(2\phi) + 5\sqrt{3}\sin(2\phi)\right)\sin^2\theta\right)^2 \\
&= \frac{1}{4\pi}\int_0^\pi d\theta \sin\theta \left(\frac{\pi}{486}\left(1179 + 476\cos(2\theta) + 73\cos(4\theta)\right)\right) \\
&= \frac{3808}{3645} = 1.045 = 119.8^\circ
\end{aligned} \tag{A.55}$$

where 4π is the total solid angle. We therefore find that also in the case of a generic direction of the magnetic field, the energy gaps and levels still have the same behavior described by the TWPs.

A.4 Conclusion

In conclusion in this Appendix we have shown that within the cellular structure of glasses the TWP is the 2D version (suitable for very thin films) of a more realistic potential characterized by four near-degenerate wells with a 3D tetrahedric geometry, as implied by the cellular picture [59]. Having shown that the basic physics is rather similar to that of the (much simpler) triangular version we can consider this latter like the simplest working model to describe real glasses.